Theses and Dissertations   Theses and Dissertations

1-1-2011

Coupled Sequential Process-Performance Simulation and Multi-Attribute Optimization of Structural Components Considering Manufacturing Effects

Ali Najafi

Follow this and additional works at: https://scholarsjunction.msstate.edu/td

COUPLED SEQUENTIAL PROCESS-PERFORMANCE SIMULATION AND

MULTI-ATTRIBUTE OPTIMIZATION OF STRUCTURAL COMPONENTS

CONSIDERING MANUFACTURING EFFECTS

By

Ali Najafi

A Dissertation
Submitted to the Faculty of
Mississippi State University
in Partial Fulfillment of the Requirements
for the Degree of Doctor of Philosophy
in Computational Engineering
in the Department of Aerospace Engineering

Mississippi State, Mississippi

August 2011

COUPLED SEQUENTIAL PROCESS-PERFORMANCE SIMULATION AND

MULTI-ATTRIBUTE OPTIMIZATION OF STRUCTURAL COMPONENTS

CONSIDERING MANUFACTURING EFFECTS

By

Ali Najafi

Approved:

<table>
<tr><td>Masoud Rais-Rohani
Professor of Aerospace Engineering
Director of Dissertation</td><td>Douglas Bammann
Professor of Mechanical Engineering
Committee Member</td></tr>
<tr><td>Mark Horstemeyer
Professor of Mechanical Engineering
Committee Member</td><td>Esteban Marin
Research Professor
Committee Member</td></tr>
<tr><td>Tomasz Haupt
Research Associate Professor
Committee Member</td><td>Seth Oppenheimer
Professor of Mathematics
Committee Member</td></tr>
<tr><td>Roger King
Professor of Electrical Engineering
Graduate Coordinator</td><td>Sarah Rajala
Professor of Electrical Engineering
Dean of the School/College</td></tr>
</table>

Name: Ali Najafi

Date of Degree: August 6, 2011

Institution: Mississippi State University

Major Field: Computational Engineering

Major Professor: Dr. Masoud Rais-Rohani

Title of Study: COUPLED SEQUENTIAL PROCESS-PERFORMANCE SIMULATION AND MULTI-ATTRIBUTE OPTIMIZATION OF STRUCTURAL COMPONENTS CONSIDERING MANUFACTURING EFFECTS

Pages in Study: 221

Candidate for Degree of Doctor of Philosophy

Coupling of material, process, and performance models is an important step towards a fully integrated material-process-performance design of structural components. In this research, alternative approaches for introducing the effects of manufacturing and material microstructure in plasticity constitutive models are studied, and a computational framework is developed for coupled process-performance simulation and optimization of energy absorbing components made of magnesium alloys. The resulting mixed boundary/initial value problem is solved using nonlinear finite element analysis whereas the optimization problem is decomposed into a hierarchical multilevel system and solved using the analytical target cascading methodology. The developed framework is demonstrated on process-performance optimization of a sheet-formed, energy-absorbing component using both classical and microstructure-based plasticity models. Sheet-forming responses such as springback, thinning, and rupture are modeled and used as manufacturing process attributes whereas weight, mean crush force, and maximum crush force are used as performance attributes. The simulation and optimization results show

that the manufacturing effects can have a considerable impact on design of energy absorbing components as well as the optimum values of process and product design variables.

DEDICATION

To my beloved Parents

ACKNOWLEDGEMENTS

support has enabled me to achieve so many wonderful things that I could not have done on my own.

TABLE OF CONTENTS

LIST OF TABLES

LIST OF FIGURES

xiv

xvi

CHAPTER I

INTRODUCTION AND LITERATURE SURVEY

Computer simulation has become a useful tool to predict the structural response under different boundary conditions and to help explore the design space to find the optimum design while minimizing the need for physical testing. In finite element analysis (FEA) of a boundary-value problem in structural mechanics, response predictions depend on the selected set of boundary conditions, structural geometry, and mechanical behavior of the material as represented by the constitutive relations. Both the manufacturing process and performance attributes can be simulated separately using FEA. However, to more accurately model the structural performance in design, it is essential to consider the manufacturing effects, particularly the changes that can occur in both the material as well as the manufactured product (e.g., configuration variation). The scope of this dissertation, as delineated further in Section 1.5, is to investigate the effect of manufacturing on performance and optimum design of energy absorbing structural components that are produced using the sheet stamping process.

1.1   Energy Absorption and Crush Simulation

Safety is one of the most important criteria in design of vehicle structures. In general, a crashworthy vehicle must meet the impact energy management criteria that require the passenger compartment structure to sustain crash loads without excessive deformation while absorbing and dissipating the kinetic energy of impact. Some automotive structural components such as the side rails play a vital role in absorbing the

bulk of impact energy in the full- and offset-frontal crash conditions (Chung 1996). With the goal of minimizing injury to the vehicle occupants, as defined by the head injury criteria (Mahmood 2000), the design of side rails requires a proper balance between intrusion distance and peak acceleration. While the component has to be stiff enough to limit intrusion, it has to accommodate sufficient plastic deformation to attenuate the impulsive force and associated acceleration transferred to the occupants. In addition, the requirement for energy absorption must be balanced by other design criteria such as weight efficiency. Traditionally, structural performance simulations are performed by using the initial component geometry from the CAD model with material properties obtained from coupon-level tests on the stock material.

Over the past thirty years, numerous experimental, analytical, and numerical studies have been conducted to gain better understating of the crush mechanism of thin-walled tubular components and evaluation of their characteristics in terms of the buckling, mean crush force, folding deformation, and energy dissipation associated with progressive plastic collapse under static and dynamic axial compression. These studies have principally focused on prismatic tubes made of steel and aluminum alloys with some having foam-filled cavities (Chen 2001; Kim 2002; Abramowicz 2003; Karagiozova 2008; Jones 2003; Reid 1996).

Due to the complex nature of the deformation behavior and the evolving properties of the material, experimental validations of the crushing process is still an active area of research. The effect of dynamic load on the material properties is often ignored in analytical solutions. In 1989, Abramovicz and Weirzbicki (1989) modified their analytical formulation to capture the strain rate effect in strain rate sensitive materials through the work of Calladine and English (1984), which explicitly showed the

relation between the initial velocity of impact and strain rate based on some engineering assumptions. They used the empirical relationship that was previously proposed by Symonds (1965) based on testing of steel tubes at various strain rates. This phenomenological relationship, which modifies the yield stress for different strain rates, has also been incorporated into many nonlinear finite element analysis (FEA) codes such as LS-DYNA and ABAQUS for including the effect of strain rate on classical plasticity models.

Langseth and Hopperstad (1996) performed extensive experiments on different heat-treated square aluminum tubes under both static and dynamic loadings, and showed that in static testing, most of the mode shapes are symmetric whereas in dynamic cases, the mode shape tends to vary during the crush deformation. They also observed that the mean crush force for dynamic cases are higher than the static ones, and concluded that by introducing imperfection, the ratio between dynamic and static mean crush force can be kept constant. Hansen et al. (2000) experimentally showed that the dynamic effect, causing an increase in the mean crush force of strain-rate-insensitive aluminum, is because of inertial force arising from the acceleration of tube walls introduced by dynamic loading.

Although the distinction between static and dynamic load cases also depends on the material and geometric properties of the tube, the dynamic plastic buckling (Lindberg 1987) occurs for impact velocities higher than 100 m/s and mass ratio of 600. In most of the studies related to automotive crashworthiness, the behavior is in the range of dynamic progressive buckling due to the use of trigger mechanism. The problem is more complicated for tubes without trigger mechanism where there is interaction between

elastic/plastic buckling, stress wave propagation and the folding initiation (Karagiozova 2004a,b).

By the late 1980's and the development of nonlinear FEA codes such as LS-DYNA and PAM-CRASH, it became possible to analyze the crash phenomenon (Abramowicz 2003; Otubushin 1998) as a non-smooth, highly nonlinear problem based on the explicit time integration technique (Belytschko 2000). Most of the element models used in these codes originally developed by Belytschko et al. (2000) and Hughes et al. (1981, 2000)with subsequent modifications aimed at correcting the problem of zero energy (hourglass modes), enhancing the computational efficiency, and objectivity of stress rate, to pass a wide range of patch tests. In the case of contact-impact analysis for dynamic progressive buckling simulations, the penalty method is often used for rigid body and self-contact calculations (Belytschko 1991;Wriggers 2002). To include material nonlinearity, many previous studies have used classical elastic-plastic models with kinematic and/or isotropic hardenings (Simo 1998). These methods can also include the Cowper-Symonds (1965) model to account for strain rate sensitive materials (Halquist 1998, 2006).

1.2   Effects of Microstructure and Manufacturing on the Crush Behavior

In the studies mentioned above, the effects of manufacturing or material microstructure were not considered until Dipaolo et al. (2007, 2008) conducted a series of controlled experiments focused on the symmetric quasi-static axial crush response of welded stainless steel square tubes. They first investigated different control methods in the form of tube end constraints and collapse initiators (triggers) to control the so-called configuration response (combination of collapse geometry and the shape of the load-

4

displacement curve). This was then followed by examination of the effects of alloy composition and microstructure on the configuration response. Their results showed that the combination of greater carbon content and smaller grain size enhanced both the peak crush load as well as energy absorption for the secondary fold formation. This study showed that both the composition and microstructure, as the two main consequences of manufacturing process, can affect the crushing behavior. Therefore, the crush behavior becomes more accurate if the microstructural information can be included in the simulations.

Researchers at the Norwegian University of Technology SIMLab studied the effect of heat treatment, as a manufacturing process, on the quasi-static and dynamic crush behavior of energy absorbing components. (Langseth et al. 2001, 2006, 2009)

Multiscale simulation can provide a proper tool to include the microstructural information of material. One method is to include detailed microstructural information to explicitly account for the effect of microstructure (Najafi et al 2011),which is computationally expensive. Even if the computational limitations are resolved, the bridging of information between different length scales is challenging and requires many advancements. Another practical approach to include the multiscale information is by the use of advanced material models that represent the material behavior in a physically motivated (phenomenological) manner at the continuum level (McDowel 1998, 2001; Horstemeyer et al. 2001, 2004; Bammann et al. 1996, 2001; Marin et al. 2006) using the framework of internal state variable (ISV) theory. Such a material model can keep track of the homogenized evolution of microstructure. The main feature of such physically motivated models is the simultaneous modeling of the effects of strain rate and temperature on material behavior. Hence, the microstructural evolution is implicitly

5

considered in ISV models. The level of details provided by the state variables depends upon the physics considered in the material modeling procedure. Olivera et al (2010) showed that inclusion of isotropic and kinematic hardening as well as anisotropy can affect the crush simulation predictions.

Manufacturing effects also play an important role in proper prediction of the crushing behavior. Studies show that the manufacturing process and the choice of process parameters can cause significant changes in material microstructure and, thus, the macro-level behavior of structural component (Kellicut et al. 1999; Simunovic 2002; Williams et al. 2005; Oliveira et al. 2006). Therefore, material characterization experiments are required to find the in-situ properties of the material in samples taken from different regions of the manufactured component. However, such experiments may not be possible in the early design stage prior to component manufacturing. A practical solution to this problem is to perform coupled sequential process-performance simulations whereby both material properties and component geometry can evolve from one stage to the next for a more accurate prediction of the structural performance measures. This framework also helps to guide the manufacturing process in a way that process parameters are evaluated against both process objectives and performance criteria. Coupling of the material, process, and performance models is an important step in capturing the actual physical behavior of the material and structure while facilitating integrated material-process-performance design (Olsen et. al. 1997; McDowell et al. 2007; Acar et al. 2009). The main theme in this framework is to find information that can couple the manufacturing effects with performance analysis. Both material (micro-level) and structure (macro-level) will be affected by the manufacturing processes involved. At micro-level, the material state including microstructure, defect, and stresses evolve subject to different

6

loading paths, whereas at macro-level, the geometry deforms permanently to form the desired shape.

Traditional engineering design practices usually focus on separate boundary-value problems for product fabrication or performance analysis. Therefore, a sequence of separate experimental and/or computational studies is performed to evaluate each scenario based on the set of experimental characterizations. This separate analysis approach may prove inefficient in design space exploration when part geometry and/or process control parameters are subject to change.

There have been some limited investigations on the coupled process-product (performance) simulations. For example, the effect of material deformation history from forming simulation was studied by using classical plasticity constitutive relations found from the stress-strain curves (Oliveira et al. 2006; Kaufman 1998; Kellicut 1999). Kellicut et al. (1999) performed a comparative study on hydroformed tube bending-crush simulations by considering springback, thinning, as well as material parameters such as plastic strain and residual stresses (both separately and combined) and showed that the plastic strain has the most significant effect on the crush behavior. Mayer (2004) and Williams et al. (2005) performed integrated hydroform-crush simulations, whereas Ryou et al. (Ryou 2005) extracted the stress and strain responses from forming process using ideal forming solution and a hybrid membrane/shell method to pass the information to impact simulation. They improved the computation time by preserving the accuracy of the model as compared to FE simulations. Simunovic and Aramayo (2002) showed that by including the history effects, the crash response of energy absorbing components of the UltraLight Steel Auto Body (ULSAB) vehicle models can change despite the relatively modest difference in the overall response. They also argued that the thicknesses

7

of regions that are work hardened in the component are reduced by the stamping process. Oliveira et al. (2006) performed experimental and computational study of s-rail tubes considering the forming process, and found that the maximum crush force and the mean crush force will change as a result of the manufacturing process effects. Bottcher and Frik (2003) did a similar study and showed that metal forming data is required in crash simulation of front rail panel of an Opel model, especially in high strength dual phase steel due to its rapidly hardening characteristic. Krusper (2003) and Dagson (2001) performed their analysis on a simple bar while considering the springback response of the material. As mentioned earlier, most of these studies considered a material with isotropic hardening with limited number of studies modeling the effect of kinematic hardening or combined isotropic/kinematic hardening on crush response.

1.3   Sheet Metal Forming Simulation

In recent years, FE simulation has been used to study extensively the sheet metal forming process from different aspects such as material modeling and implementation, element formulation, contact formulation, numerical solution techniques, and coupled loading-unloading problems (Wang et al. 1978; Chung et al. 1998; van den Boogaard et al. 2003; Stephan et al. 2009; Zhuang 2008; Cheng and Kikuchi 1985; Tang 1976, 1981; Bathe and Chaudhary 1985, 1986; Rebel et al. 2002; Oden and Kikuchi 1982; Oden and Pires 1983; Bayram and Nied 2000; Simo and Laursen 1992; Yang et. al. 1994; Kim and Yang 1985; Hibbitt et al. 1970). The recent developments in numerical simulation of sheet metal forming processes have evolved into a very powerful design and analysis tool in the automotive industry by facilitating the design of complex stamped parts while

8

preventing manufacturing induced failures such as cracking and wrinkling, thus, reducing the need for expensive tooling adjustments and modifications.

Both explicit and implicit FEA are used for forming simulation. The first complete and consistent FE formulation for large deformation-large strain problem was developed by Hibbitt et al. in 1970. In order to perform simulation on large-scale problems, shell elements are more efficient than continuum (solid) elements from both computational and modeling standpoints. Hybrid models that incorporate both membrane and bending stresses and strains could help improve tremendously the results of FE simulations.

Springback is a common problem in the sheet metal forming process. It is represented by the elastically driven change of shape of the workpiece once the forming tools are removed. Springback presents problems during assembly because of the emerging mismatch between the components. Once the stamped sheet components and die sets are removed from the forming tools, the resulting internal stresses from the stamping process, known as residual stresses, will relax and cause the part to deviate from the shape imposed by the forming tool.

Although there have been many improvements in the area of sheet metal forming simulation, accurate springback prediction continues to be a difficult task. Since springback (or tool removal) analysis is the last step in the forming simulation, all the errors accumulated during the previous stamping/deep drawing simulations will influence the springback results. There have been many research studies in recent years on the numerical factors affecting the springback analysis (Xu et al. 2004; Lin and Liu 2000) Factors considered include element formulation, explicit versus implicit solvers and their related solution time steps, constitutive relations, hardening formulations, element size

9

and density, number of integration points through the shell thickness, and the influence of considering the draw beads in FE models (Xu et al. 2004; Lin and Liu 2000; Jetteur 1986; Dhia et al. 1995; Yang et al. 1995; Noels et al. 2004).

1.4   Mathematical Optimization of Process and Performance Systems

Numerical optimization techniques may be used to find the best set of process control parameters and/or component geometry to optimize the specified set of objectives defined in the optimization problem. Numerical optimization has been used for both manufacturing process optimization as well as energy absorption performance optimization as separate simulations. The most common objectives considered in sheet forming problems are rupture (Sun et al. 2010) and wrinkling (Wei and Yuying 2008), which is measured by comparing the principal strain distribution at each element integration point with forming limit diagrams and forming limit curves, thinning as a measure of thickness change, and plastic strain affecting springback in the components. Other objectives such as uniform thickness distribution (Ohata 1996) by considering the draw bead and restraining force as the design variables, optimum blank shape design (Azaouzi 2008; Guo 2000) as well as reducing the cost associated with forming in terms of punch speed (Tamasco et. al. 2011) have also been considered.

Energy absorption management in thin-walled crush tubes is enhanced through mathematical optimizations. The goal of design optimization is to determine the proper geometric attributes that minimize or maximize a selected objective by considering the limitations imposed by manufacturing and performance considerations . Previous studies in design optimization of structural components for energy absorption have focused on the component's cross-sectional geometry (Kim 2001; Rais-Rohani et al. 2005), stiffener

10

geometry (Salehghaffari et al. 2011), and the multi-cell configuration (Sun et al. 2011) . The optimizer could be directly coupled with an FEA code, where repeated high fidelity simulations are performed during the optimization process, tied to analytical formulations for energy absorption evaluation (e.g., using superfolding element representation and associated modifications) (Kim 2001; Chen 2002; Najafi 2011), or integrated with surrogate models that are developed using metamodelling techniques (Fang et al. 2005; Rais-Rohani et al. 2010).

As sheet metal forming process simulation is computationally expensive and some responses are non-smooth (noisy), its direct coupling with numerical optimization is impractical. To alleviate this problem, metamodels are used as surrogates for high fidelity simulations (Wei and Yuying 2008; Sun et al. 2010).

1.5   Scope of the Dissertation

The goal of this research is to capture the manufacturing process effects in design optimization of energy absorbing components, especially those made of magnesium alloys. To achieve this goal, the following objectives are pursued: (1) investigating alternative approaches for introducing the effects of manufacturing and material microstructure in plasticity constitutive models; (2) modeling of the mixed boundary / initial value problem for energy absorption in components made of a magnesium alloy; (3) developing a computational framework for coupled sequential process-performance simulations; (4) designing a multilevel decomposition and optimization scheme suitable for coupled process-performance systems; (5) applying the developed computational framework to design optimization of an energy absorbing component produced using a

11

sheet forming process. Contributions in pursuit of these objectives are highlighted in the dissertation.

The coupling of process and performance simulations should have the flexibility of supporting both the all-at-once optimization considering a single design group as well as the decomposed multilevel optimization when manufacturing design and product design are done by separate groups.

Enhancing the energy absorption capability of a double-hat tube by considering the stamping process effects is used as an application problem. The deep drawing, springback, and crush events are all modeled. Depending upon the material model or constitutive relations used, the coupling level between the stamping process and axial crush changes. In this research, both classical plasticity and a physically based phenomenological ISV model are investigated in the coupled simulation and optimization. The incorporation of an ISV material model in the coupled process-performance simulations and its integration in design optimization using a multilevel framework represent the principal contributions of this research.

The remaining portion of this dissertation is organized as follows. Chapter II discusses the plasticity formulations used to couple the process-performance simulations. The coupling terms that are available in classical plasticity and physically based ISV plasticity models are shown. This chapter ends by brief introduction of the crystal plasticity model used to incorporate material grain orientations. Chapter III discusses both the cold and hot forming simulations. For cold forming simulations, classical plasticity model is used and for hot forming case, ISV model is used. Sensitivity analysis of the effect of manufacturing process variables and geometric attributes on the manufacturing quality responses are addressed and discussed. Chapter IV introduces the

12

coupled simulation using classical plasticity and ISV models followed by a study of the effect of texture on the crushing behavior. In this chapter the effect of manufacturing process parameters on energy absorption is discussed. Chapter V discusses the all-at-once and analytical target cascading (ATC) formulations used for coupled process-performance optimization. Metamodeling strategy used in this research is also discussed in this chapter. Chapter VI provides two all-at-once optimization problems solved using classical plasticity and ISV models and followed by a multi-level decomposed optimization of a coupled process-performance problem, which is solved using the ATC formulation. Chapter VII discusses the general computational framework designed for process-performance simulation and optimization. Chapter VIII summarizes the studies performed in this research and offers some insights for future work.

CHAPTER II

CONSTITUTIVE MODELING OF DUCTILE METALS

Plastic deformation in polycrystalline ductile metals is influenced by the arrangement of atoms and the larger microstructural features. Constitutive models are used to describe the stress-strain relationship for a given material. This relationship can be influenced by such factors as temperature and strain rate. The plastic deformation requires having some variables that define the past history of stress and temperature at a point besides the current stress and temperature. The past history can be precisely defined through functional analysis and mathematical theories known as theory of material with memory (Lubliner 2008). One alternative way to consider this past history is by introducing a set of variables, in addition to stress and temperature, known as internal or hidden variables. Therefore, the strain calculation will have a dependency on these new variables. Consequently, the addition of these variables requires introducing additional constitutive relations.

The state variables can be categorized into two major types including a mathematical construct and physically based state variables. In the following sections two material models including a classical plasticity model and another model based on the internal state variable (ISV) theory will be introduced. Finally, this chapter discusses a crystal plasticity model which also a state variable model but it is used in the mesoscale level to consider the grain orientation effects in the boundary value problems.

14

2.1 Classical Plasticity Model with Rate effects

In the classical plasticity model the total strain is written as an additive decomposition of elastic strain and plastic strain where the elastic strain is an infinitesimal strain. It is assumed that linear isotropic hardening holds for the constitutive equations. The linear isotropic hardening slope is derived from the slope of stress strain data in piecewise linear plasticity model. In this case the one-dimensional representation of rate independent plasticity is expressed in the following set of equations (Simo& Hughes 1998) written in:

Elastic stress-strain relationship:

$$\sigma = E\left(\varepsilon - \varepsilon^p\right) \tag{2.1}$$

Flow rule and isotropic hardening law

$$\dot{\varepsilon}^p = \dot{\lambda}\, sign\left(\sigma\right) \tag{2.2}$$

$$\dot{\kappa} = \dot{\lambda} \tag{2.3}$$

$\dot{\kappa} = |\dot{\varepsilon}^p|$ can be defined based on the choice of equivalent plastic strain as the simplest form of evolutionary equation for isotropic hardening.

Yield surface

$$f(\sigma, \kappa) = |\sigma| - \left(\sigma_y + H\kappa\right) \le 0 \tag{2.4}$$

Kuhn-Tucker complementary conditions

$$\lambda \ge 0,\, f(\sigma, \kappa),\, \lambda f(\sigma, \kappa) = 0 \tag{2.5}$$

Consistency condition

$$\dot{\lambda}\dot{f}(\sigma, \kappa) = 0 \text{ if } f(\sigma, \kappa) = 0 \tag{2.6}$$

Numerical integration of the rate-independent plasticity model in one dimension is summarized within the following equations given a (σ_n, κ_n):

$$\sigma_{n+1}^{tr} = E\left(\varepsilon_{n+1} - \varepsilon_n^p\right) \tag{2.7}$$

15

$$f_{n+1}^{tr} = |\sigma_{n+1}^{tr}| - [\sigma_y + H\kappa] \tag{2.8}$$

IF $f_{n+1}^{tr} \leq 0$ THEN

$$(\blacksquare)_{n+1} = (\blacksquare)_{n+1}^{tr} \tag{2.9}$$

ELSE

$$\Delta\lambda = \frac{f_{n+1}^{tr}}{(E+K)} > 0 \tag{2.10}$$

$$\varepsilon_{n+1}^p = \varepsilon_n^p + \Delta\lambda \, \text{sign}(\sigma_{n+1}^{tr}) \tag{2.11}$$

$$\kappa_{n+1} = \kappa_n + \Delta\lambda \tag{2.12}$$

$$\Delta\sigma = E(\varepsilon_{n+1} - \Delta\lambda \, \frac{\sigma_{n+1}^{tr}}{|\sigma_{n+1}^{tr}|}) \tag{2.13}$$

$$\sigma_{n+1} = \sigma_n + \Delta\sigma \tag{2.14}$$

the yield surface at the beginning of the analysis is considered as the initial yield stress

and as the material experiences plastic deformation, the instantaneous yield value is

captured based on the yield surface expansion as a result of isotropic hardening.

Therefore, in this formulation, manufacturing effects can be transferred in terms of

residual stresses and equivalent plastic strains as initial values of (σ_1, κ_1). In a piecewise

linear plasticity model, the slope related to isotropic hardening H is derived considering

the state of stress and plastic strain based on the stress strain curve and therefore the

hardening slope gets updated as a result of slope change.

The main difference between the rate-independent plasticity and rate-dependent

plasticity lies in the definition of the flow rule describing the evolution of ε_n^p. This

evolution equation can be postulated with a similar format of rate-independent plasticity

in equation (2.2). However, despite of this similarity, evolution equation for ε_n^p deferrers

fundamentally from rate-independent flow rule; in the rate-independent plasticity, the

plastic strain rate is a pseudo-time rate to solely describe the sequence of events and the

time scale is irrelevant. Moreover, rate-dependent model uses a given constitutive law

that explicitly relate the instantaneous stress σ and the static yield stress σ_y to the plastic multiplier or $\dot{\lambda}$ in spite of rate-independent formulation that has . The rate dependency of the J2 plasticity material is established based on the interpolation of strain rate between the rate dependent stress-strain curves entered or through a phenomenological model for flow rule such as

$$\dot{\lambda}(\sigma, \kappa) = \begin{cases} \frac{1}{c}\left[\left(\frac{|\sigma|}{\sigma_y}\right)^{1/P} - 1\right] & if \ f(\sigma, \kappa) \geq 0 \\ 0 & if \ f(\sigma, \kappa) < 0 \end{cases} \tag{2.15}$$

Where C and P are material constants. Therefore, the rate-dependent material model for linear isotropic hardening can be derived from following equations:

- Elastic stress-strain relationships in 3D space

$$\boldsymbol{\sigma} = \mathbb{C} : (\boldsymbol{\varepsilon} - \boldsymbol{\varepsilon}^{vp}) \tag{2.16}$$

- Yield surface (closure of elastic domain in the stress space):

$$f(\boldsymbol{\sigma}, \kappa) = |\boldsymbol{\sigma}| - (\sigma_y + H\kappa) \leq 0 \tag{2.17}$$

- Flow rule and hardening law:

$$\dot{\boldsymbol{\varepsilon}}^{vp} = \dot{\lambda} \frac{\partial f(\sigma, \kappa)}{\partial \sigma} \tag{2.18}$$

$$\dot{\kappa} = \dot{\lambda}$$

$$\dot{\lambda}(\boldsymbol{\sigma}, \kappa) = \begin{cases} \frac{1}{c}\left[\left(\frac{|\sigma|}{\sigma_y}\right)^{1/P} - 1\right] & if \ f(\boldsymbol{\sigma}, \kappa) \geq 0 \\ 0 & if \ f(\boldsymbol{\sigma}, \kappa) < 0 \end{cases} \tag{2.19}$$

where the bold letters representing second ranked tensor of stress $\boldsymbol{\sigma}$ and stain $\boldsymbol{\varepsilon}$ and $\mathbb{C}$ is the forth rank tensor for isotropic elasticity. The integration scheme in the deviatoric space is

$$\boldsymbol{e}_{n+1} = \boldsymbol{\varepsilon}_{n+1} - \frac{1}{3}tr(\boldsymbol{\varepsilon}_{n+1})\boldsymbol{I} \tag{2.20}$$

$$\boldsymbol{s}_{n+1}^{tr} = 2\mu(\boldsymbol{e}_{n+1} - \boldsymbol{e}_n^p) \tag{2.21}$$

IF $f_{n+1}^{tr} = \|\boldsymbol{s}_{n+1}^{tr}\| - \sqrt{\frac{2}{3}}[\sigma_y + H\kappa] \leq 0$ THEN

$$(\blacksquare)_{n+1} = (\blacksquare)_{n+1}^{tr} \tag{2.22}$$

17

ELSE

$$n_{n+1} = s_{n+1}^{tr}/\|s_{n+1}^{tr}\| \tag{2.23}$$

Compute $\Delta\lambda_{n+1}$ based on Newton-Raphson scheme (Simo&Hughes 1998, Neto et al 2008)

$$\kappa_{n+1} = \kappa_n + \sqrt{\frac{2}{3}}\,\Delta\lambda_{n+1} \tag{2.24}$$

$$\varepsilon_{n+1}^{vp} = \varepsilon_n^{vp} + \Delta\lambda_{n+1}\,n_{n+1} \tag{2.25}$$

$$\sigma_{n+1} = \overline{\lambda}\,tr(\varepsilon_{n+1})I + s_{n+1}^{tr} - 2\mu\,\Delta\lambda_{n+1}\,n_{n+1} \text{ or} \tag{2.26}$$

$$\Delta\sigma_{n+1} = \overline{\lambda}\,tr(\Delta\varepsilon_{n+1})I + 2\mu(\Delta\varepsilon_{n+1}^e) = \overline{\lambda}\,tr(\Delta\varepsilon_{n+1})I + \Delta s_{n+1}^{tr} - 2\mu\,\Delta\lambda_{n+1}\,n_{n+1}$$

$$\sigma_{n+1} = \sigma_n + \Delta\sigma_{n+1} \tag{2.27}$$

By having $\kappa_n = \varepsilon_n^{vp}$ the manufacturing effect can be considered through a non-zero state of σ_n and ε_n^{vp}.

2.2 Internal State Variable Model

The original kinematics of deformation is defined based on the deformation gradient which is decomposed into three maps including isochoric plastic F_d^p (continuous distribution of dislocations with permanent volume preserving deformation), dilational inelastic F_v^p (continuous distribution of voids causing volume change) and elastic F^e (lattice displacement from equilibrium) parts with the following relation (Bilby 1960, Kröner 1961, Bammann&Aifantis 1989, Davison 1977)

$$F = F^e F_v^p F_d^p \tag{2.28}$$

In this study, we ignore the continuum damage assumption and focus on the plasticity aspect of deformation i.e.

$$F = F^e F_v^p \tag{2.29}$$

and the velocity gradient L is

18

$$L = \dot{F}F^{-1} \tag{2.30}$$

Mathematically, the selection of internal state variables (ISVs) are somewhat arbitrary, but in the present ISV model which is an extension of BCJ plasticity, the kinematic hardening, isotropic hardening, static and dynamic recovery are physically motivated. The elastic stress strain relation is defined as:

$$\overset{\circ}{\sigma} = \dot{\sigma} - W^e \sigma - \sigma W^e = \lambda \, tr(D^e)I + 2\mu D^e \tag{2.31}$$

where λ and μ are Lame constants, I is the second rank identity tensor and D^e is the symmetric part of elastic velocity gradient calculated as subtraction of inelastic velocity gradient D^p from total rate D through

$$D^e = D - D^p \tag{2.32}$$

The asymmetric part of the velocity gradient is defined through $W = \frac{1}{2}(L - L^T)$ and it is assumed that the continuum spin is equal to elastic spin $W = W^e$

Keeping the similar form of power law equations, for the inelastic rate of deformation D^p considers the stress, temperature, and internal variables (Bammann et al 1996).

$$D^p = f(T) \, sinh\left[\frac{\|s-\alpha\| - (R+Y(T))}{V(T)}\right] \frac{s-\alpha}{\|s-\alpha\|} \tag{2.33}$$

the flow rule for the symmetric part of the plastic velocity gradient is depend on deviatoric stress s, kinematic hardening internal variable α, isotropic hardening variable R. There are three functions related to yielding which has Arrhenius-type temperature dependency including f(T) which determines the regime of initial yielding rate dependency, Y(T) is the rate independent yield stress, and V(T) determines the magnitude of rate dependence on yielding. Each of the three equations is defined with exponential form as shown as

19

$$f(T) = C_5 \exp(-C_6/T),$$

$$Y(T) = C_3 / 2 \left(C_{21} + \exp^{-C_4/T} \right) \times [1 + \tanh(C_{19}(C_{20} - T))], \qquad (2.34)$$

$$V(T) = C_1 \exp(-C_2/T)$$

where constants C_1 through C_6 are considered to be material parameters.

The relationships of the thermodynamic conjugates of kinematic and isotropic hardening are defined based on the following equations:

$$\boldsymbol{\alpha} = \frac{2}{3} h(T) \boldsymbol{\beta} \qquad (2.35)$$

$$\kappa = H(T) \, \epsilon_{ss} \qquad (2.36)$$

The evolution equation for the in deformation conjugates for kinematic and isotropic hardening are

$$\dot{\boldsymbol{\beta}} = \dot{\boldsymbol{D}}^P - \lfloor r_d(T) \, \dot{\varepsilon}^P + r_s(T) \rfloor \, \|\boldsymbol{\beta}\| \, \boldsymbol{\beta} \qquad (2.37)$$

$$\dot{\epsilon}_{ss} = \dot{\varepsilon}^P - \lfloor R_d(T) \, \dot{\varepsilon}^P + R_s(T) \rfloor \kappa \, \epsilon_{ss} \qquad (2.38)$$

Equations 2.20 and 2.21 are cast in the hardening recovery format such that the anisotropic hardening is represented through $h(T)$, the isotropic hardening function is $H(T)$, the static recovery is presented with $r_s(T)$ and $R_s(T)$, and the dynamic recovery is described through $r_d(T)$ and $R_d(T)$. It is worth noting that the D^{in} is replace with D in the recovery terms for implementation to resolve some computational difficulty of numerical integration. The hardening and recovery equations have the following temperature dependency relations based on Horstemeyer (1995) motivated from McDowell 1992 in the most general form:

$$r_d(T) = C_7 \exp\left(-C_8/T\right) \qquad (2.39)$$

$$h(T) = C_9 - C_{10}T \qquad (2.40)$$

20

$$r_s(T) = C_{11} \exp\left(-C_{12}/_T\right) \tag{2.41}$$

$$R_d(T) = C_{13} \exp\left(-C_{14}/_T\right) \tag{2.42}$$

$$H(T) = C_{15} - C_{16}T \tag{2.43}$$

$$R_s(T) = C_{17} \exp\left(-C_{18}/_T\right) \tag{2.44}$$

Similarly, C_i's are considered to be material constants. For problems with high strain rates, it is assumed that the material undergoes adiabatic conditions and 90% of the plastic work is dissipated into heat. Hence, the thermal dissipation equation resulting in temperature changes is then written:

$$\dot{T} = \frac{0.9}{\rho c_v} \, \boldsymbol{s} \colon \boldsymbol{D}^p \tag{2.45}$$

where ρ and c_v are the material density and specific heat capacity of the material. The specific heat capacity is also changes due to temperature (Chen 2009) but this effect is ignored in the present formulation. Thus, specific heat capacity is specified based on the initial temperature. $\boldsymbol{s}$ is the deviatoric Cauchy stress and $\boldsymbol{D}^p$ is the symmetric part of the plastic velocity gradient.

The numerical integration is on the equations 2.37 to 2.38 applying Newton-Raphson solution to the nonlinear set of equations for specified temperature

$$F_y = q - \kappa - Y - V \sinh^{-1}\left[\frac{\Delta\lambda}{f\Delta t}\right] \tag{2.46}$$

$$F_\alpha = \omega_\alpha - \frac{h}{1+(r_d\Delta\lambda+r_s\Delta t)\omega_\alpha} \|\boldsymbol{\beta}_n + \Delta\lambda \, \boldsymbol{n}\| = 0 \tag{2.47}$$

$$F_\kappa = \omega_\kappa - \frac{H}{1+(R_d\Delta\lambda+R_s\Delta t)\omega_\kappa} [\epsilon_{ss}^n + \Delta\lambda] = 0 \tag{2.48}$$

$$F_\varepsilon = \frac{\left|(-p_e+s_{33}^e)q_e - 3G\Delta\lambda \, z_{33}^d\right|}{2G} = 0 \tag{2.49}$$

with

$$q = q_e - \Delta\lambda\left[3G + \frac{h}{1+(r_d\Delta\lambda+r_s\Delta t)\omega_\alpha}\right] \tag{2.50}$$

21

$$q_e = \sqrt{\frac{3}{2}\mathbf{Z}^d : \mathbf{Z}^d} \tag{2.51}$$

$$\mathbf{Z}^d = \mathbf{s}^e - \frac{2}{3}\frac{h}{1+(r_d\Delta\lambda+r_s\Delta t)\omega_\alpha}\boldsymbol{\beta}_n \tag{2.52}$$

$$p_e = -\frac{1}{3}\,tr(\boldsymbol{\sigma}) \tag{2.53}$$

$$\mathbf{s}^e = \boldsymbol{\sigma}^e + p_e\mathbf{1} \tag{2.54}$$

$$\mathbf{n} = \frac{3}{2}\frac{\mathbf{Z}^d}{q_e} \tag{2.55}$$

The unknowns in these coupled equations are equivalent plastic strain increment $\Delta\lambda$, norm of back stress tensor $\omega_\alpha = \|\boldsymbol{\alpha}\|$, isotropic hardening stress, and third diagonal component of strain due to the plane stress assumption s_{33}.

Once the unknowns are identified, they will be used in the following equations to calculate the state variables at the current increment:

$$\varepsilon^p = \varepsilon_n^p + \theta\,\Delta\lambda\,\mathbf{I}:\mathbf{n} \tag{2.56}$$

$$\boldsymbol{\beta} = \frac{1}{1+\theta(r_d\Delta\lambda+r_s\Delta t)\omega_\alpha}[\boldsymbol{\beta}_n + \theta\,\Delta\lambda\,\mathbf{I}:\mathbf{n}] \tag{2.57}$$

$$\epsilon_{ss} = \frac{1}{1+\theta(R_d\Delta\lambda+R_s\Delta t)\omega_\kappa}[\epsilon_{ss}^n + \theta\,\Delta\lambda\,] \tag{2.58}$$

$$\Delta\boldsymbol{\sigma}_{n+1} = \bar{\lambda}\,tr(\Delta\boldsymbol{\varepsilon}_{n+1})\mathbf{I} + 2\mu(\Delta\boldsymbol{\varepsilon}_{n+1}^e) \tag{2.59}$$

$$\boldsymbol{\sigma}_{n+1} = \boldsymbol{\sigma}_n + \Delta\boldsymbol{\sigma}_{n+1} \tag{2.60}$$

At the beginning of the simulations ε_1^p, $\boldsymbol{\beta}_1$ and ϵ_{ss}^1 are assumed to be zero if there is no manufacturing effect prescribed in the material. However, if the intention is to include the manufacturing effects, these values along with the stress states should be extracted and used as the initial value for the sequential simulations.

2.3   Crystal Plasticity Finite Element Modeling

Almost all materials in nature are anisotropic either due to their inherent properties and/or the manufacturing processes and loading/deformation histories. What we observe at the macroscale is a phenomenological anisotropy that is associated with

22

specific structures and orientations at the microscale level. The anisotropy originates from the anisotropic elastic behavior and the orientation-dependent activation of crystallographic deformation mechanisms such as dislocation, twins and martensitic transformation. Subsequently, the mechanical behavior such as deformation, yield, strength, hardening and damage will be influenced by this anisotropic behavior. Continuum mechanics has provided a viable framework to represent anisotropy through tensorial calculus. From the macro-scale standpoint, anisotropic plasticity is ignored in most material models by the assumption of random grain orientation in material aggregates. There have been early attempts to model the anisotropic behavior in polycrystalline materials (Taylor 1938, Bishop and Hill 1951a&b, Kröner1961, Kocks et al 1975&1998, Meyers 2002, Kothari and Anand 1998), with some extensions of these early approaches (Regueiro et al 2002, Barlat et al 1994, Barlat and Chung 1993, Dafalias 2000&2001, Francois 2001) to represent the anisotropic behavior in macroscale continuum models. However, the macro-level continuum models do not consider the microstructural features within a polycrystalline material. In contrast, crystal plasticity FE models account explicitly for discrete grains and slip systems, considering then the anisotropy of single crystal properties and crystallographic texture. This approach to materials modeling is typically more predictive and robust than macroscopic plasticity since it directly addresses evolution of crystallographic texture and models both anisotropic elasticity and plasticity, while using phenomenological models at the crystal level to represent its plastic flow kinetics and hardening behavior (Horstemeyer et al 2005).

In this work, we used the formulation of a crystal plasticity model to describe the isothermal, quasi-static, large deformation of polycrystalline metals developed by Marin

23

(Marin 2006). The model is formulated based on the multiplicative decomposition of the deformation gradient into elastic and plastic components; a description physically motivated by mechanisms underlying plastic slip in single crystals (Marin 2006). Therefore, the elasto-plastic response of single crystal is modeled considering the crystallographic slip is the dominant deformation mechanism and other mechanism such as twining, grain boundary sliding and diffusion are not considered in this developments. The deformation gradient F in single crystal is decomposed into an elastic F^e and a plastic F^p components having the following relationship:

$$F = F^e F^p = V^e R^e F^p = V^e F^*$$

(2.61)

where F^p described the plastic slip (dislocation motion) on the crystallographic planes leaving the crystal lattice unchanged and R^e and V^e model the rotation through proper orthogonal tensor and elastic stretching through left elastic stretch tensor respectively. As it is shown in figure 2.1, the present decomposition introduces four configurations for the deformation having two intermediate configurations. In the present formulation, we used relaxed configuration $\tilde{B}$ to write the crystal constitutive equation.
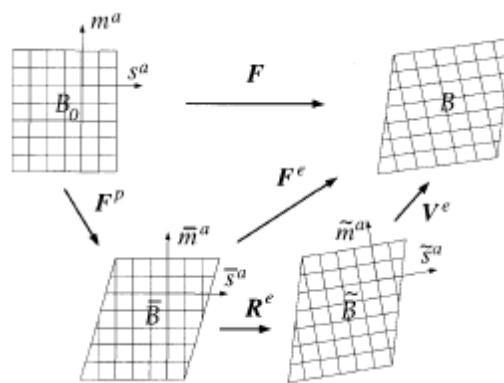
Figure 2.1   Kinematics of deformation (Marin 2006)

24

The plastic velocity gradient in current configuration $\boldsymbol{l} = \dot{\boldsymbol{F}}\boldsymbol{F}^{-1}$ can be written in the relaxed configuration $\tilde{B}$ by pre and post multiplication of the left elastic stretch tensor $\boldsymbol{V}^{e-1}(\blacksquare)\boldsymbol{V}^{e}$ operator:

$$\tilde{\boldsymbol{L}}^{*} = \dot{\boldsymbol{R}}\,\boldsymbol{R}^{eT} + \boldsymbol{R}^{e}\bar{\boldsymbol{L}}^{p}\boldsymbol{R}^{eT} \tag{2.62}$$

where dotted variables representing the time derivative and $\bar{\boldsymbol{L}}^{p} = \dot{\boldsymbol{F}}^{p}\boldsymbol{F}^{p-1}$ as pure plastic velocity gradient in $\bar{B}$ configuration that can be related to a dyadic product $\otimes$ of unit vectors ($\bar{\boldsymbol{s}}^{\alpha}$, $\bar{\boldsymbol{m}}^{\alpha}$) known as Schmid tensor ($\bar{\boldsymbol{Z}}^{\alpha} = \bar{\boldsymbol{s}}^{\alpha}\otimes\bar{\boldsymbol{m}}^{\alpha}$) for α slip system via a plastic shearing rate of $\dot{\gamma}$:

$$\bar{\boldsymbol{L}}^{p} = \dot{\gamma}\bar{\boldsymbol{Z}}^{\alpha} \tag{2.63}$$

The velocity gradient can be decomposed into symmetric and skew symmetric to account for the plastic spine and plastic stretch as it is discussed in detail by Marin (2006).

The state variable model of crystal plasticity in the context of thermodynamics is proposed by Coleman and Gurtin (1967) using Clasius-Duhem inequality per unit volume of the unloaded intermediate configuration $\tilde{B}$:

$$-\dot{\tilde{\psi}}_{v} + \boldsymbol{\tau}:\boldsymbol{l} \geq 0 \tag{2.64}$$

Where $\dot{\tilde{\psi}}_{v}$ is the rate Helmholts free energy per unit volume in unloaded intermediate configuration $\tilde{B}$ and τ is the Kirchhoff stress. In this treatment, the free energy is defined to be dependent on applied elastic strain $\widetilde{\boldsymbol{E}}^{e}$, and a set of strain like internal state variables for each α-slip system $\tilde{X}^{\alpha}$ (Marin 2006) that represent the state of evolving structure of the material generated during plastic slip:

$$\tilde{\psi}_{v} = \hat{\tilde{\psi}}_{v}(\widetilde{\boldsymbol{E}}^{e},\tilde{X}^{\alpha}) \tag{2.65}$$

In this article, the reduced set of $\tilde{X}^{\alpha}$ are considered to just include lattice strain fields around the dislocation generated or accumulated on α-slip system as $\tilde{X}^{\alpha} = \{\varepsilon_{s}^{\alpha}\}$ by

25

taking the material time derivative of the free energy and substituting it in the free energy equation, and applying the internal state variable treatment of Coleman and Gurtin (1965), two definition for the force conjugates of the strains appeared in the free energy is derived i.e. (Marin 2006)

$$\tilde{S} = \frac{\partial \tilde{\psi}_v}{\partial \tilde{E}^e} \text{ and } \kappa_s^\alpha = \frac{\partial \tilde{\psi}_v}{\partial \varepsilon_s^\alpha} \tag{2.66}$$

Where $\tilde{S}$ is the 2nd Piola-Kirchhoff stress in $\tilde{B}$ and κ_s^α is the flow strength representing the internal lattice stress field generated by dislocation structures during plastic deformation. Having these definitions in equation 2.52, the Clasius-Duhem inequality reduces to

$$\sum_{\alpha=1}^{N} \tau^\alpha \dot{\gamma}^\alpha - \sum_{\alpha=1}^{N} \kappa_s^\alpha \dot{\varepsilon}_s^\alpha \geq 0 \tag{2.67}$$

The first term is associated with the plastic dissipation due to slip processes and the second term is the power due to the accumulation of dislocations. By assuming a quadratic form for the Helmholtz free energy related to $\tilde{E}^e$ and ε_s^α the material capability to do work is determined

$$\tilde{\psi}_v = \frac{1}{2} \tilde{E}^e : \mathbb{C}^e : \tilde{E}^e + \frac{1}{2} \sum_{\alpha=1}^{N} \mu_E c_\kappa \varepsilon_s^{\alpha^2} \tag{2.68}$$

where $\mathbb{C}^e$, μ_E and c_κ are fourth order anisotropic tensor then the constitutive equations 2.51 can be obtained as

$$\tilde{S} = \mathbb{C}^e : \tilde{E}^e \text{ and } \kappa_s^\alpha = \mu_E c_\kappa \varepsilon_s^\alpha \tag{2.69}$$

to complete the model equations, considering small elastic strain that reduces V^e to a infinitesimal strain ϵ^e ($V^e = 1 + \epsilon^e$) after neglecting the higher order terms in the Taylor expansion, it is required to define evolution equations for γ^α and ε_s^α known as flow rule

26

and hardening law respectively. The kinetics of slip is based on the empirical relationship know as power law model given by

$$\dot{\gamma}^\alpha = \gamma_0 \left[\frac{|\tau^\alpha|}{\kappa_s^\alpha}\right]^{1/m} sign(\tau^\alpha) \tag{2.70}$$

where τ^α is the resolved shear stress on the α-slip system and m is a rate sensitivity parameters varies with the rate and temperature (Anad&Kothary 1998). In this study, we assume that the strain rate and temperature does not vary too much and m is considered as a constant parameter. The dislocation based hardening rule is formulated based on the evolution equation of Cocks and Mecking (1979) for the dislocation density with a slight modification (Marin 2006) and assuming that all the slip systems harden with the same rate (Marin 2006). Therefore, the evolution equation for κ_s^α is

$$\dot{\kappa}_s^\alpha = h^\alpha |\dot{\gamma}^\alpha| \text{ and } h^\alpha = h_0^\alpha \left(1 - \frac{\kappa_{s,S} - \kappa_S}{\kappa_{s,S} - \kappa_{s,0}}\right) \sum_{\alpha=1}^N |\dot{\gamma}^\alpha| \tag{2.71}$$

and the saturation strength $\kappa_{s,S}$ is given by Follansbee and Cocks (1988) in the room temperature

$$\kappa_{s,S} = \kappa_{s,S0} \left[\frac{\sum_{\alpha=1}^N |\dot{\gamma}^\alpha|}{\dot{\gamma}_{S0}}\right]^{m'} \tag{2.72}$$

where $\kappa_{s,S0}$, $\dot{\gamma}_{S0}$ and m' are material parameters.

The numerical integration of the present constitutive model is implicit and developed for both implicit and explicit FE codes (i.e., ABAQUS STANDARD and EXPLICIT) as UMAT and VUMAT, respectively (Marin 2006). The elastic part is capable of considering anisotropic elastic crystals. Effective elastic properties can be defined for cubic and hexagonal crystals in terms of elastic constants appeared in $\tilde{\mathbb{C}}^e$ elements. For the constitutive integration scheme, the coupled first order ordinary differential equations for variables ($\epsilon^e, R^e, \varepsilon_s^\alpha$) are discretized to form a coupled

27

nonlinear algebraic equations and solved using a two-level iteration scheme (Marin-Dawson 1998) method. The detail of the model implementation is given by Marin (2006).

CHAPTER III

SHEET METAL FORMING SIMULATION

In recent years, the sheet metal forming using FE simulation has been studied extensively using both explicit and implicit simulations. These significant developments in numerical simulation of sheet metal forming processes have become a very powerful tool in the automotive industry. This helps to facilitate the design to prevent failures in the trial out process and reduce design cost by predicting cracking and wrinkling tendencies.

In this study, forming of single hat tubes is taken into consideration. The final desired geometry is the assembly of two single hat tubes that are joined together. In this chapter, the process of stamping simulation and the responses are being studied.

Two sets of blank/holder/die geometries should be defined in the FE model. Figure 3.1 shows the FE model of a single hat blank/holder/die set. The same die set is mirrored with respect to blank plane considering the thickness of the blank that offsets the model to have a clearance of blank sheet thickness between two sheets. The forming simulations for each single hat are performed so that the punch and holding forces are applied in opposite directions to produce the actual cross-section of the closed double-hat tube assembly.

29
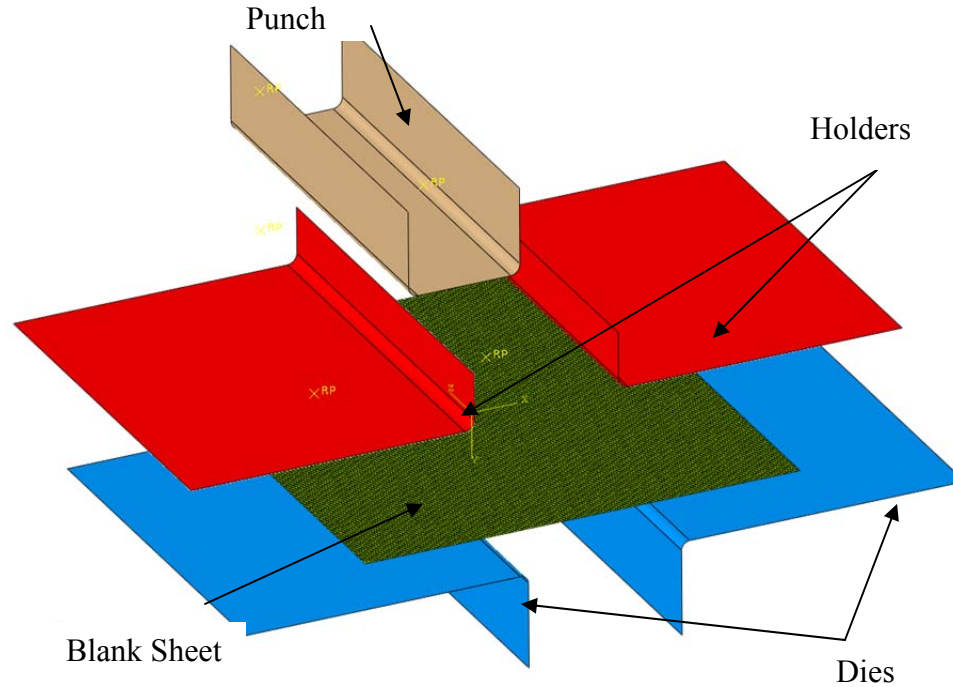
Figure 3.1   Finite element model for forming a single hat section

The forming simulation for each single hat section contains two basic steps in explicit FEA that are distinguished based on the boundary conditions:

Gripping the blank between die and holder: The holding forces are increased linearly from zero to the desired holding force specified as one of the manufacturing process parameters. In this step, both punch and dies are kept fixed in their respective positions. By increasing the holding force, the contact between the holders and dies with the blank is increased. In this stage, the kinematic contact formulation is used because of the computational efficiency of the formulation (Wriggers 2006). The simplicity of the geometry enabled us to define meshless die and holder surfaces through standard analytical rigid surfaces. Therefore, in this explicit solution step as well as in the next step (the deep drawing step), punch, dies and holders are defined by analytical rigid surfaces. Contact surfaces are defined on both surfaces of the blank by considering the surface offset due to the blank thickness. Penalty formulation is used in tangential contact

30

and a friction coefficient is defined as a manufacturing process parameter for an equivalent representation of both surface roughness and draw beads.

Deep drawing simulation: After the gripping step, the deep drawing stage is modeled by applying a constant velocity to the punch with a shape that matches the final geometry of the product (excluding the springback effect). Hence, the results of the previous step are directly transferred to this step where the boundary conditions on the fixed punch in the direction normal to the blank surface are removed and a constant velocity is applied to the punch to form the single hat section. The amount of punch displacement representing the height of the single-hat section is extracted from the termination time and the punch velocity. In this study, the punch velocity is assumed to be constant for a linear displacement. It should be noted that this setup does not impose a uniform strain rate in all the elements. Thus, rate sensitivity of the material will not have a uniform effect on the structure. In this step, dies remain clamped and the holders are fixed in all degrees of freedom except the direction perpendicular to the blank surface. In this direction, the constant holding force is applied to preserve the constant gripping force throughout the drawing process.

The state variables and geometric information from the deep drawing simulation are transferred and treated as the initial state in the unloading stage (i.e., removal of all the tooling parts from the workpiece) for springback analysis. Springback process is considered to be a quasi-static problem considering the stress distribution captured from deep drowning, dynamic effects, and the contact conditions. Additionally, all the rigid surfaces including punch, dies, and holders are removed from the FE model, which makes the model more suitable for implicit FEA considering the quasi-static nature of the springback phenomenon and the absence of highly nonlinear factors in the model. The

31

springback deformation stems from the initial state resulting from the deep drawing simulation. In order to guarantee convergence and stability of the non-linear implicit FEA, boundary conditions are defined such that the two edges of the hat section are held fixed perpendicular to the actual normal surface. As shown in Fig. 3.2, the equilibrium condition is achieved by constraining the model in all the transverse directions. The boundary condition defined in this stage is designed such that the effect of the force required to assemble a non-fitted double-hat section is already considered. In this stage, residual stresses and geometric attributes are updated during quasi-static analysis while the other computational state variables such as plastic strain remain unchanged. It is worth mentioning that similar to the deep drawing simulation, the springback analysis is performed separately and simultaneously on two identical single hat sections. There is no interaction between the two hat sections, however, in both the deep drawing and springback simulations. The two hat sections are then assembled in the next stage to produce a double-hat crush tube.
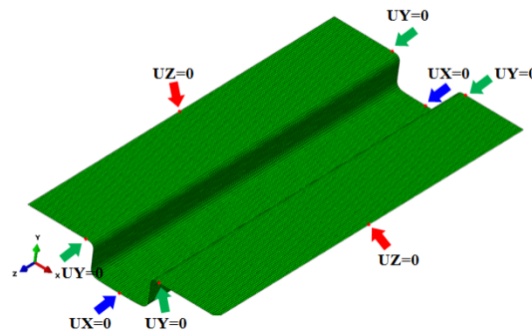
Figure 3.2   Boundary conditions defined in the springback analysis

3.1   Definitions of responses in stamping simulation

In this study, six responses are assigned and defined as objective/constraint in the optimization problem. *Rupture* and *thinning* are the responses extracted from the deep

32

drawing simulations, *springback* is a response calculated from the springback simulation and the *maximum crush force* and the *mean crush force* are the responses calculated from the crush simulation as the main two parameters to evaluate the energy absorption behavior of the double hat tubes.

Rupture is found by extracting the principal major and minor plastic strains in each element, which are compared against the forming limit diagram reported in the literature (Lee 2008). Based on the definition, rupture is a measure of accumulated plastic major strains from simulation and FLD diagram (Fig. 3.3). FLD that is used in this study is assumed to behave linearly in both compressive and tensile plastic strains. Rupture is calculated by taking the difference between the major strain calculated in FE simulation and that extracted from the FLD using the following equation

$$R = \begin{cases} \sum_{i=1}^{n} R_i{}^2 = \sum_{i=1}^{n}(\varepsilon_1^i - \phi(\varepsilon_2^i))^2 & \varepsilon_1^i > \phi(\varepsilon_2^i) \\ 0 & \varepsilon_1^i \le \phi(\varepsilon_2^i) \end{cases} \tag{3.1}$$

where $\phi(\varepsilon_2)$ is the equation representing FLD curve and ε_1^i and ε_2^i are the principal major and minor strains at each integration point through the thickness calculated in the FE-based deep drawing simulations when the termination time reaches the limit.
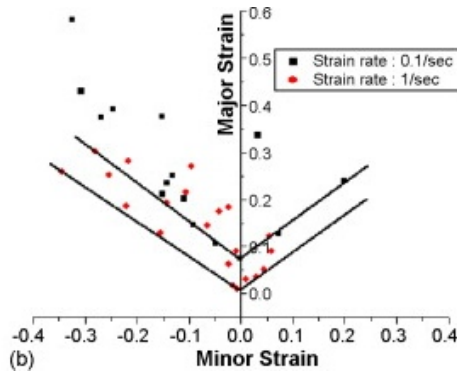
Figure 3.3   Forming limit diagrams for AZ31 in two strain rates (Lee 2008)

Thinning is extracted by comparing the final thickness of each element against its initial value and is found using a single metric defined as

$$T = \sum_{i=1}^{n} T_i^2 = \sum_{i=1}^{n} (\frac{t_i - t_o}{t_o})^2 \qquad (3.2)$$

where t_o and t_i are the initial and final shell thicknesses, respectively. Since the shell thickness in the blank is assumed to be constant for all the elements, t_o is always equal to the shell thickness assigned to the elements.

Springback is calculated by comparing the nodal coordinates extracted from the last step of the deep drawing simulation with those in the last step of springback. A single springback metric representing the deviation of the nodal coordinates is calculated as

$$S = Max(D_i) = Max(\sqrt{(X_i - X_o)^2 + (Y_i - Y_o)^2 + (Z_i - Z_o)^2}) \qquad (3.3)$$

where X, Y, Z are the Cartesian coordinates with indexes i and o representing the result at the end of springback and deep drawing, respectively.

An automated procedure through a developed FORTRAN code is used to extract the rupture and thinning results from the ABAQUS binary file, calculate the principal strains, and incorporate the equations mentioned above without using ABAQUS CAE in deep drawing and springback simulations.

3.2 Sensitivity of cold forming simulation responses using classical plasticity model:

A sensitivity analysis is performed to investigate the sensitivity of the selected responses to variations in each design variable. The upper and lower bounds for the selected seven design variables are shown in Table 3.1. An FE simulation is performed by perturbing a single design variable by ±15% from its average value while keeping the

www.manaraa.com

other design variables fixed at their corresponding average (baseline) values shown in the first row of Table 3.1 in bold.

Table 3.1   The values assigned to design variables for sensitivity analysis

Sensitivity	Width (mm)	Height (mm)	Corner Radius (mm)	Thickness (mm)	Holding Force (kN)	Punch Velocity (m/s)	Friction Coefficient
Friction Coefficient ±15%	**55**	**27.5**	**5**	**1.75**	**30**	**6**	**0.225**
	55	27.5	5	1.75	30	6	0.16875
	55	27.5	5	1.75	30	6	0.25875
Punch Velocity ±15%	55	27.5	5	1.75	30	6	0.225
	55	27.5	5	1.75	30	4.5	0.225
	55	27.5	5	1.75	30	6.9	0.225
Holding Force ±15%	55	27.5	5	1.75	30	6	0.225
	55	27.5	5	1.75	22.5	6	0.225
	55	27.5	5	1.75	34.5	6	0.225
Thickness ±15%	55	27.5	5	1.75	30	6	0.225
	55	27.5	5	1.3125	30	6	0.225
	55	27.5	5	2.0125	30	6	0.225
Corner Radius ±15%	55	27.5	5	1.75	30	6	0.225
	55	27.5	3.75	1.75	30	6	0.225
	55	27.5	5.75	1.75	30	6	0.225
Height ±15%	55	27.5	5	1.75	30	6	0.225
	55	20.625	5	1.75	30	6	0.225
	55	31.625	5	1.75	30	6	0.225
Width ±15%	55	27.5	5	1.75	30	6	0.225
	41.25	27.5	5	1.75	30	6	0.225
	63.25	27.5	5	1.75	30	6	0.225
Upper Bound	70	35	7.5	2.5	50	10	0.35
Lower Bound	40	20	2.5	1	100	2	0.1

Figures 3.4 to 3.10 show the results of the sensitivity analysis. The sensitivity values are normalized and shown separately in each figure. Each bar chart is divided into two groups, the responses shown on the left side are derived as a result of a -15% perturbation in a design variable while the responses shown on the right are derived from a +15% perturbation. As it is clearly shown, the springback is very sensitive to changes with the design variables. Figure 3.4 shows the effect of changes in friction coefficient on the responses. Increasing the friction coefficient decreases material flow leading to greater rupture and thinning in the structure. Decreasing the friction coefficient also introduces less plastic deformation but higher springback.

35

Friction Coefficient

	Decrease (-15%)	Increase (+15%)
◼ Rupture	-4.69%	4.25%
◼ Thinning	-7.95%	5.06%
◼ Springback	28.57%	-34.83%
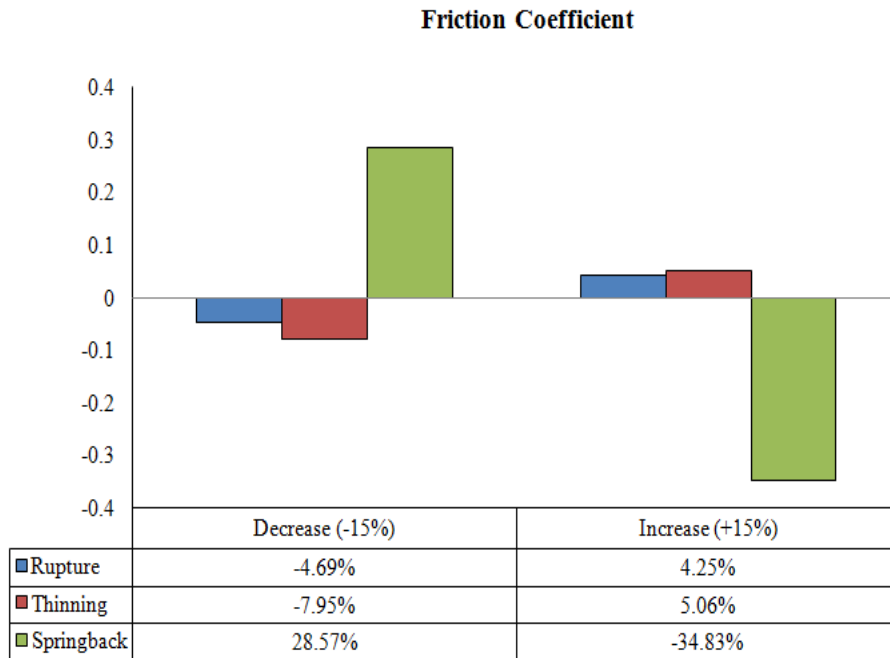
Figure 3.4   Sensitivity of responses to changes in the friction coefficient

Varying the holding force has a small overall effect on the manufacturing process responses as the scale of values shown in Fig. 3.5. Increasing the holding force introduces very slight rupture increase in the component. Springback has an inverse nonlinear relationship with the holding force. The effect is much greater when the holding force is reduced than when it is increased by the same incremental amount. A reduction in holding force would reduce plastic deformation causing greater springback in the workpiece.
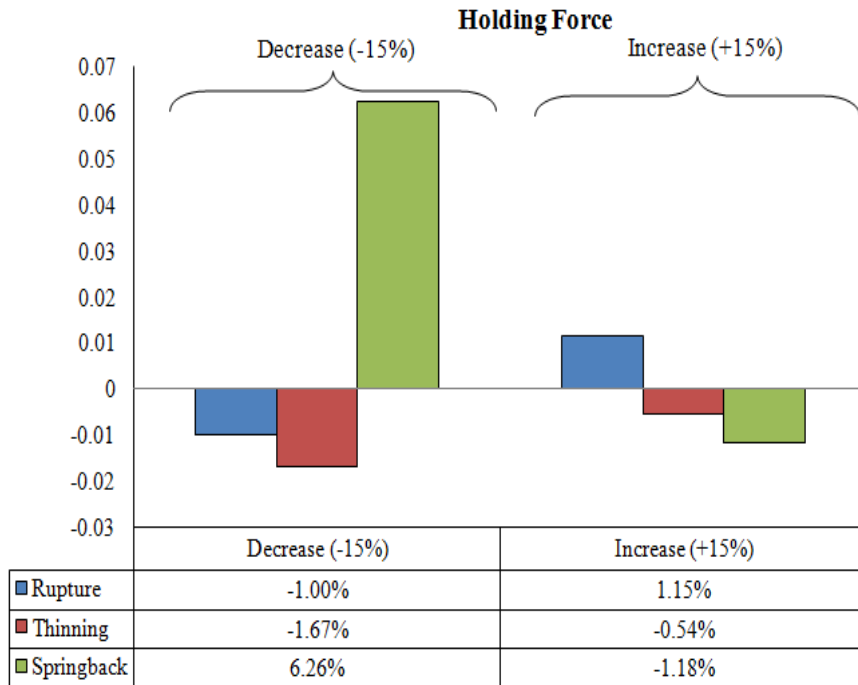
Figure 3.5   Sensitivity of responses to changes in the holding force

Punch velocity can affect the result because of the strain rate dependency of the material as well as imposing different dynamic properties on the material. It can be seen in Fig. 3.6 that the punch velocity can affect the thinning response more than the rupture. Increasing the punch velocity decreases springback because of increase in plastic deformation.

37

	Decrease (-15%)	Increase (+15%)
■ Rupture	-4.14%	3.86%
■ Thinning	-7.31%	5.80%
■ Springback	-2.72%	-11.45%
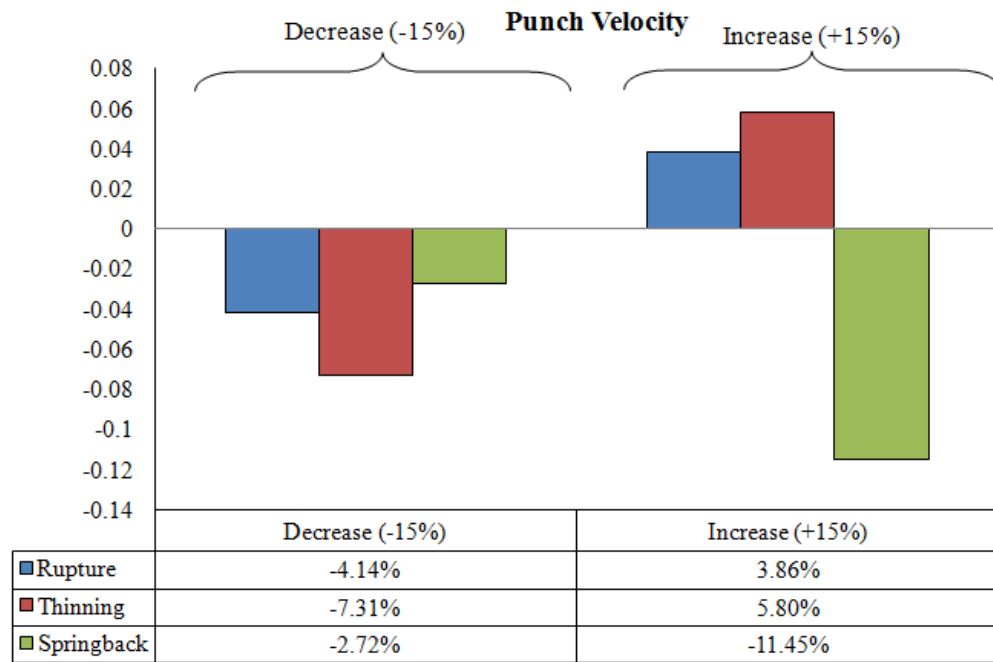
Figure 3.6   Sensitivity of responses to changes in the punch velocity

Change in the corner radius affects the manufacturing process as illustrated in Fig. 3.7. Both thinning and plastic deformations are affected by the change in the corner radius. Increasing the corner radius also affects the springback response in a significant way by reducing plastic deformation.
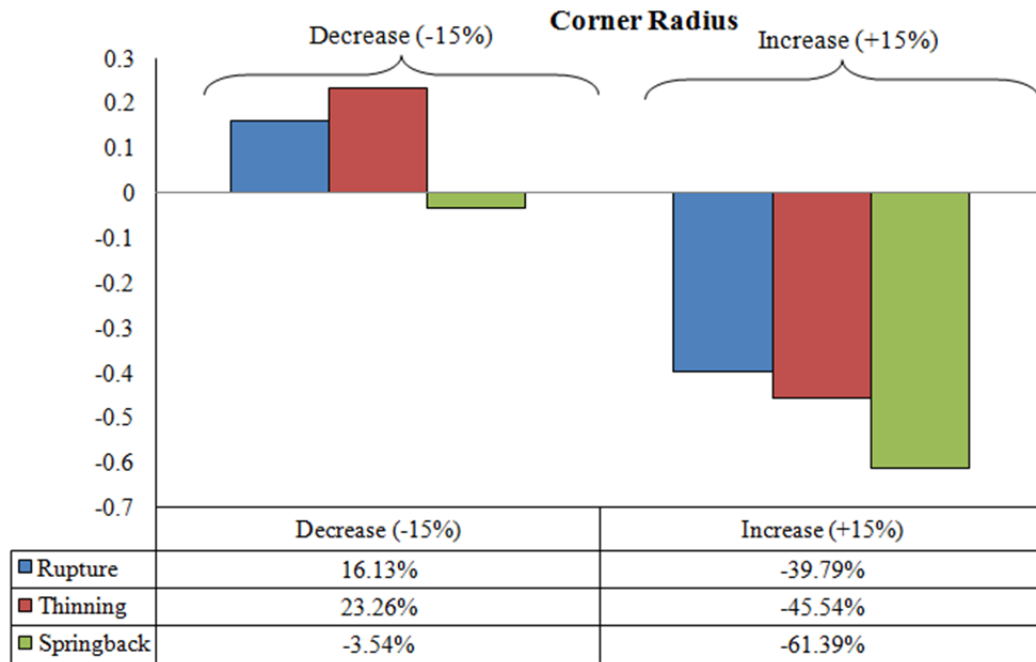
Figure 3.7   Sensitivity of responses to changes in the corner radius

The change in the geometry of the tube also affected manufacturing responses of the tube as shown in Figs. 3.8 and 3.9. The cross-sectional geometry of the tube can change by width, height, and the thickness of the tube. As the width and height of the tube change, the amount of material that remains under the holders changes resulting in more friction area between the blank and the forming tools. Since the plastic strain changes considerably in the height region, the effect of change in height is more considerable than that in the width.

	Decrease (-15%)	Increase (+15%)
Rupture	4.98%	-6.36%
Thinning	0.18%	-4.90%
Springback	6.02%	-21.37%
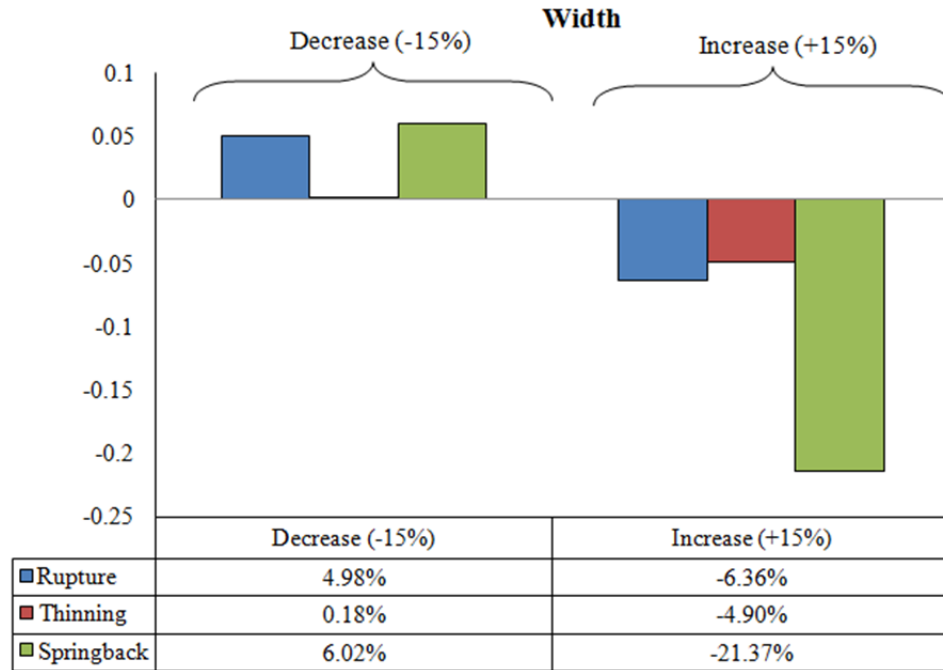
Figure 3.8   Sensitivity of responses to changes in width

	Decrease (-15%)	Increase (+15%)
Rupture	-10.18%	-1.24%
Thinning	-14.87%	7.56%
Springback	1.53%	9.21%
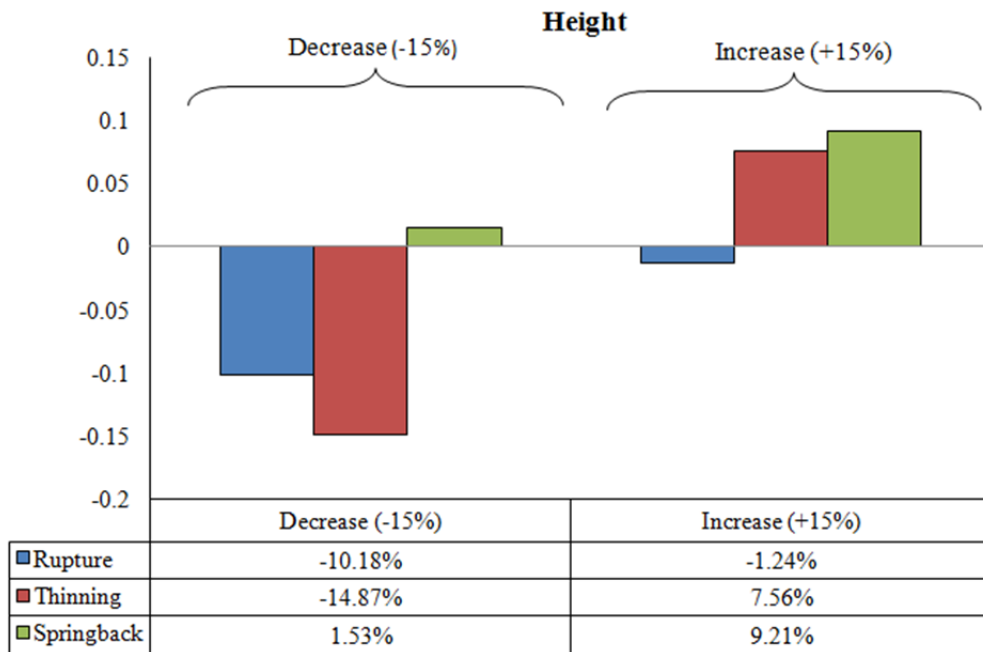
Figure 3.9   Sensitivity of responses to changes in height

40

Change in the sheet thickness has the most impact on the responses in both manufacturing and crush as indicated by the scale of values in Fig. 3.10. The stress distribution, plastic deformation, and flexural stiffness are highly affected by thickness resulting in a significant impact on the manufacturing responses.
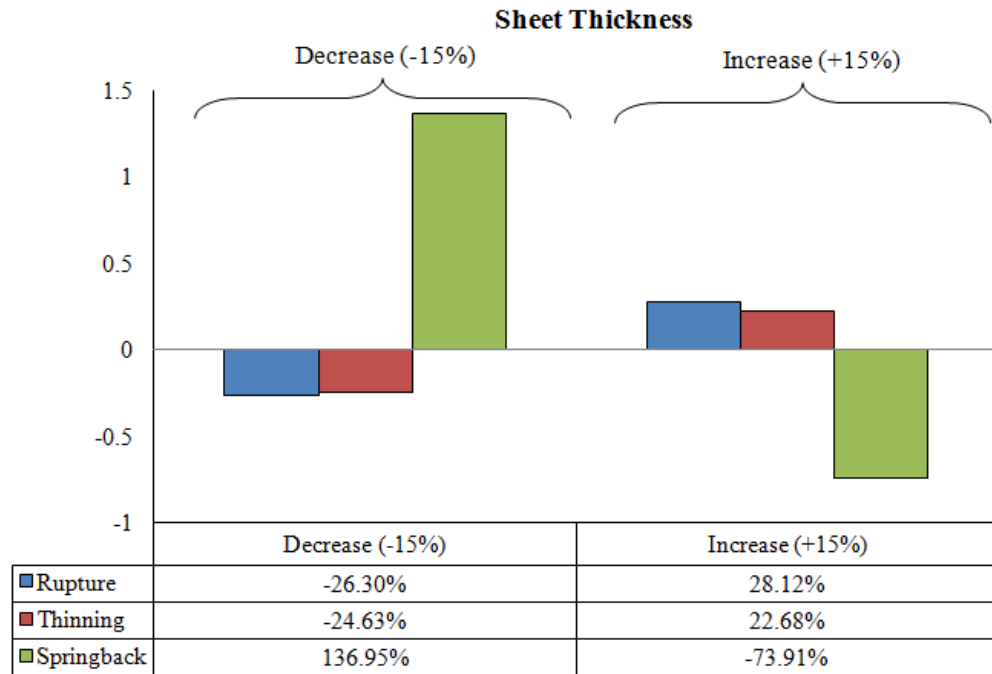
Figure 3.10   Sensitivity of responses to changes in sheet thickness

The sensitivity results are also presented differently in Figs. 3.11 to 3.13. In Fig. 3.12, sheet thickness and corner radius are shown to have significant effect on rupture response as defined by Eq. (3.1), with friction coefficient, punch velocity, and holding force having minimal effect. Figure 3.12 also shows that rupture has a direct relationship with some parameters such as thickness and punch velocity and inverse relationship with others, with corner radius being the most notable.

	Friction Coefficient	Punch Velocity	Holding Force	Thickness	Corner Radius	Height	Width
■ Decrease (-15%)	-4.69%	-4.14%	-1.00%	-26.30%	16.13%	-10.18%	4.98%
■ Increase (+15%)	4.25%	3.86%	1.15%	28.12%	-39.79%	-1.24%	-6.36%
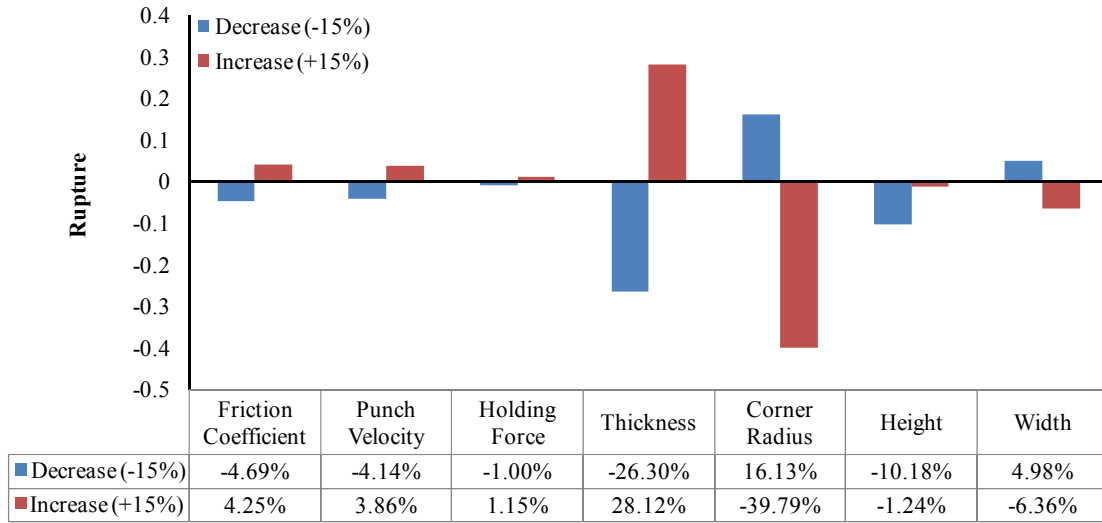
Figure 3.11   Sensitivity of rupture to design variables

Figure 3.12 shows that the global measure of thinning as defined in Eq. (3.2) is affected the most by changes in the corner radius, followed by blank thickness and height. In comparison, the manufacturing process parameters appear to be less influential.

	Friction Coefficient	Punch Velocity	Holding Force	Thickness	Corner Radius	Height	Width
■ Decrease (-15%)	-7.95%	-7.31%	-1.67%	-24.63%	23.26%	-14.87%	0.18%
■ Increase (+15%)	5.06%	5.80%	-0.54%	22.68%	-45.54%	7.56%	-4.90%
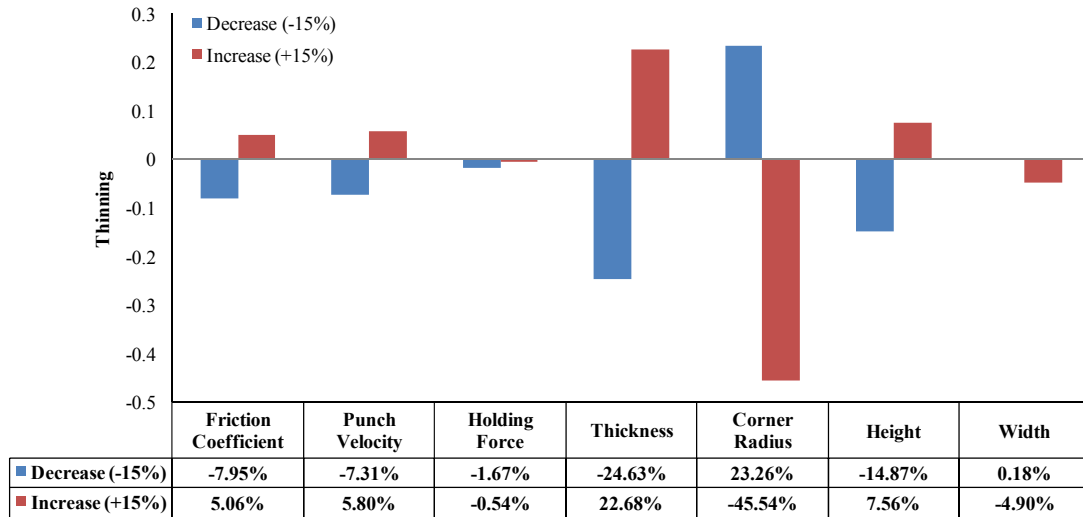
Figure 3.12   Sensitivity of Thinning to design variables

Springback response appears to be most sensitive to changes in blank thickness as shown in Fig. 3.13. While decreasing blank thickness by 15% causes the springback

42

value to more than double, an increase of 15% causes a relatively smaller decrease in springback. It is interesting to note that springback goes down by both increasing and decreasing the corner radius, although the former has a greater impact. Of all the process parameters, friction coefficient has the highest impact on springback.

	Friction Coefficient	Punch Velocity	Holding Force	Thickness	Corner Radius	Height	Width
Decrease (-15%)	28.57%	-2.72%	6.26%	136.95%	-3.54%	1.53%	6.02%
Increase (+15%)	-34.83%	-11.45%	-1.18%	-73.91%	-61.39%	9.21%	-21.37%
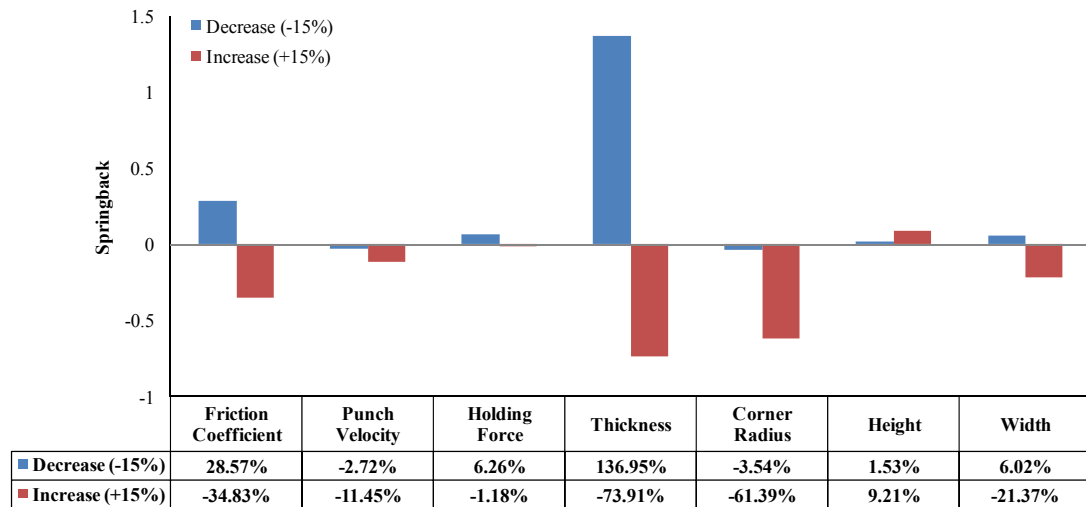
Figure 3.13   Sensitivity of springback to design variables

3.3   Sensitivity analysis of hot forming simulations using ISV model:

In the internal state variable constitutive model presented in chapter 2, all the material parameters are defined to be temperature dependent. This capability allows us to incorporate the temperature changes into the material constants. Since the practical applications showed that magnesium alloys should be formed at the elevated temperature, this part of work is devoted to sensitivity study of the same process parameters mentioned in the previous section.

In this study, magnesium AZ 31 is used for simulation the constants are listed in table 1. The data is calibrated based on the experimental results in the literature for

43

tension-compression-tension (Agnew 2006), elevated temperature (Lee 2008)as well as strain rates (Lee 2008).

Table 3.2   Material constants for AZ 31 magnesium alloys

ID #	constants	Value	ID #	constants	Value
1	ρ (kg/m^3)	1660	14	C_{10} (MPa/ºK)	2.98
2	$^*C_v$ (J/(kg K))	105	15	C_{11} (1/Mpa s)	0.0002
3	E_v (MPa)	45000	16	C_{12} (ºK)	102
4	υ	0.35	17	C_{13}	0.0022
5	C_1 (MPa)	15.103	18	C_{14} (ºK)	5E-07
6	C_2 (ºK)	796.36	19	C_{15} (MPa)	1050
7	C_3 (MPa)	15.103	20	C_{16} (MPa/ºK)	2
8	C_4 (ºK)	821	21	C_{17} (MPa)	0.02
9	C_5 (1/s)	1E-05	22	C_{18} (ºK)	9E-05
10	C_6 (ºK)	300	23	C_{19} (1/ºK)	0.0001
11	C_7 (1/MPa)	0.0525	24	C_{20} (ºK)	20
12	C_8 (ºK)	0.9234	25	C_{21}	0
13	C_9 (MPa)	1590			

*Reported at room temperature (Chen et al. 2009)

The perturbation value for the sensitivity analysis is similar to the values mentioned in previous section and is equal to ±15%. Eight variables are defined as the parameters in this study, four geometric attributes including: width, height, thickness, and corner radius, along with three manufacturing process parameters including, friction coefficient between forming tools and the blank sheet, punch velocity, and holding force. The effect of change in the workpiece temperature is also studied separately in this section. Table 3.3 provides the parameters used for the sensitivity study.

44

Table 3.3   The values assigned to design variables for sensitivity analysis

Sensitivity	Width (mm)	Height (mm)	Corner Radius (mm)	Thickness (mm)	Holding Force (kN)	Punch Velocity (m/s)	Friction Coefficient	Workpiece Temperature (k)
Friction Coefficient ±15%	**55**	**27.5**	**5**	**1.75**	**30**	**6**	**0.055**	**475**
	55	27.5	5	1.75	30	6	0.04675	475
	55	27.5	5	1.75	30	6	0.06325	475
Punch Velocity ±15%	55	27.5	5	1.75	30	6	0.055	475
	55	27.5	5	1.75	30	4.5	0.055	475
	55	27.5	5	1.75	30	6.9	0.055	475
Holding Force ±15%	55	27.5	5	1.75	30	6	0.055	475
	55	27.5	5	1.75	22.5	6	0.055	475
	55	27.5	5	1.75	34.5	6	0.055	475
Thickness ±15%	55	27.5	5	1.75	30	6	0.055	475
	55	27.5	5	1.3125	30	6	0.055	475
	55	27.5	5	2.0125	30	6	0.055	475
Corner Radius ±15%	55	27.5	5	1.75	30	6	0.055	475
	55	27.5	3.75	1.75	30	6	0.055	475
	55	27.5	5.75	1.75	30	6	0.055	475
Height ±15%	55	27.5	5	1.75	30	6	0.055	475
	55	20.625	5	1.75	30	6	0.055	475
	55	31.625	5	1.75	30	6	0.055	475
Width ±15%	55	27.5	5	1.75	30	6	0.055	475
	41.25	27.5	5	1.75	30	6	0.055	475
	63.25	27.5	5	1.75	30	6	0.055	475
Workpiece Temperature (k) ±15%	55	27.5	5	1.75	30	6	0.055	475
	55	27.5	5	1.75	30	6	0.055	404
	55	27.5	5	1.75	30	6	0.055	546
Upper Bound	70	35	7.5	2.5	50	10	0.01	600
Lower Bound	40	20	2.5	1	100	2	0.1	300

Figures 3.14 to 3.21 show the results of the sensitivity analysis using ISV model in hot forming simulation. The sensitivity values are normalized and shown separately in each figure. Each bar chart is divided into two groups, the responses shown on the left side are derived as a result of a -15% perturbation in a design variable while the responses shown on the right are derived from a +15% perturbation.

It is shown that the friction coefficient effect affects the response results. However, due to the elevated temperature, this sensitivity analysis is performed in lower friction coefficient compare to the cold forming simulation. Both rupture and thinning shown a linear change due to the friction coefficient and the springback behavior is also keeps the reverse relation closer to linear behavior.

45

	Decrease (-15%)	Increase (+15%)
■ Rupture	-1.60%	1.78%
■ Thinning	-1.66%	1.91%
■ Springback	5.88%	-4.90%
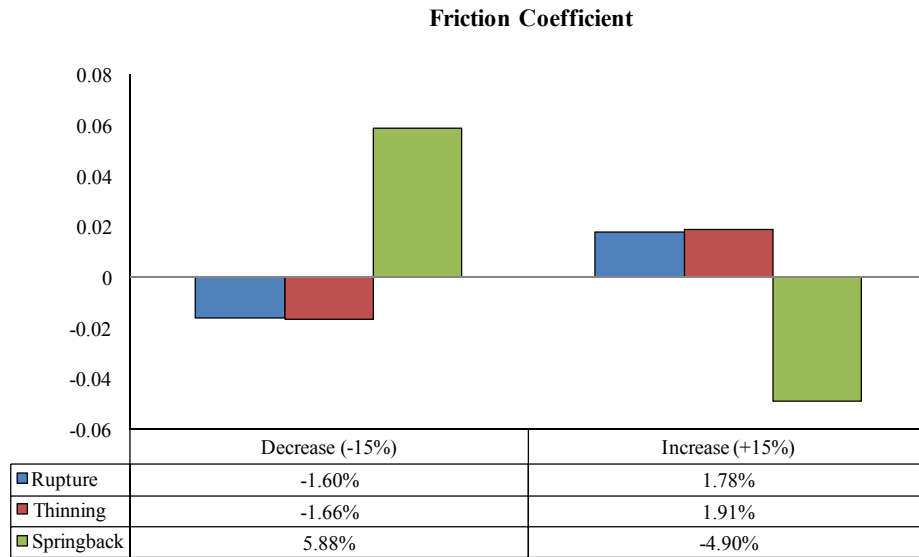
Figure 3.14   Sensitivity of responses to changes in friction coefficient.

	Decrease (-15%)	Increase (+15%)
■ Rupture	-29.77%	32.92%
■ Thinning	-30.76%	30.31%
■ Springback	135.29%	-37.75%
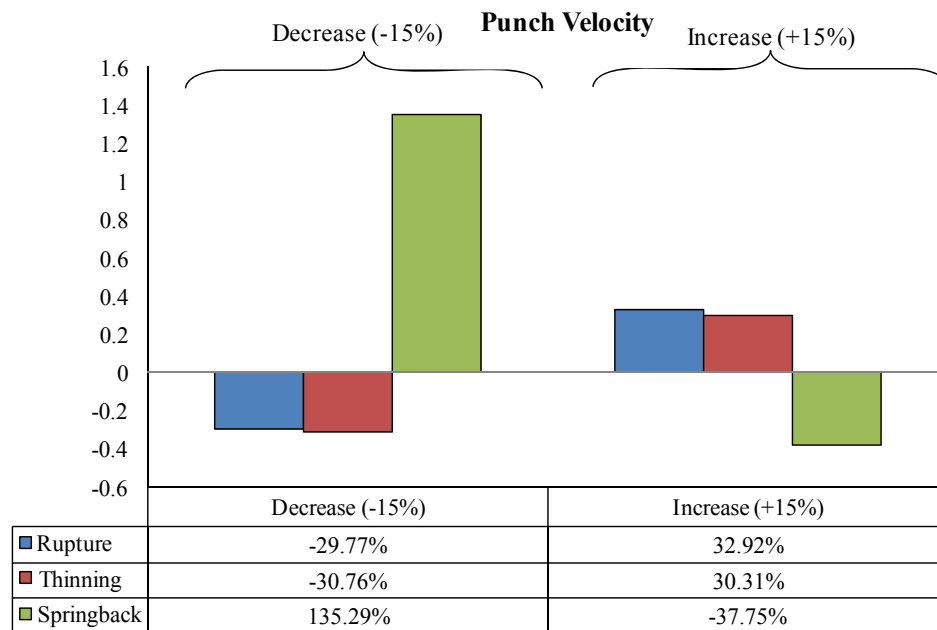
Figure 3.15   Sensitivity of responses to changes in punch velocity.

The punch velocity changes affect the rupture and thinning inversely. As the punch velocity increases, the rate dependent yield increased and therefore the plastic

46

deformation decreased. Decrease in plastic deformation will result into decrease in the plastic strain that is the major parameter in the rupture and thinning responses.

	Decrease (-15%)	Increase (+15%)
■ Rupture	-0.88%	0.93%
■ Thinning	-0.76%	0.85%
■ Springback	1.47%	-1.96%
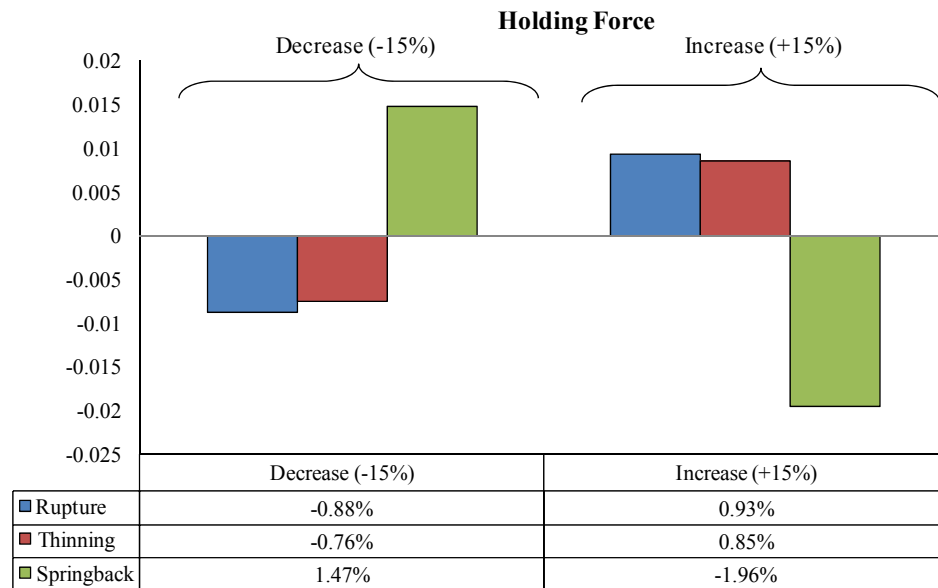
Figure 3.16   Sensitivity of responses to changes in holding force.

As the holding force increases, there is more plastic deformation imposed in the blank sheet during drawing process. This effect increases the rupture and thinning in the workpiece.

47

Workpiece Temperature

	Decrease (-15%)	Increase (+15%)
■ Rupture	272.06%	-31.17%
■ Thinning	142.55%	-39.99%
■ Springback	62.75%	263.73%
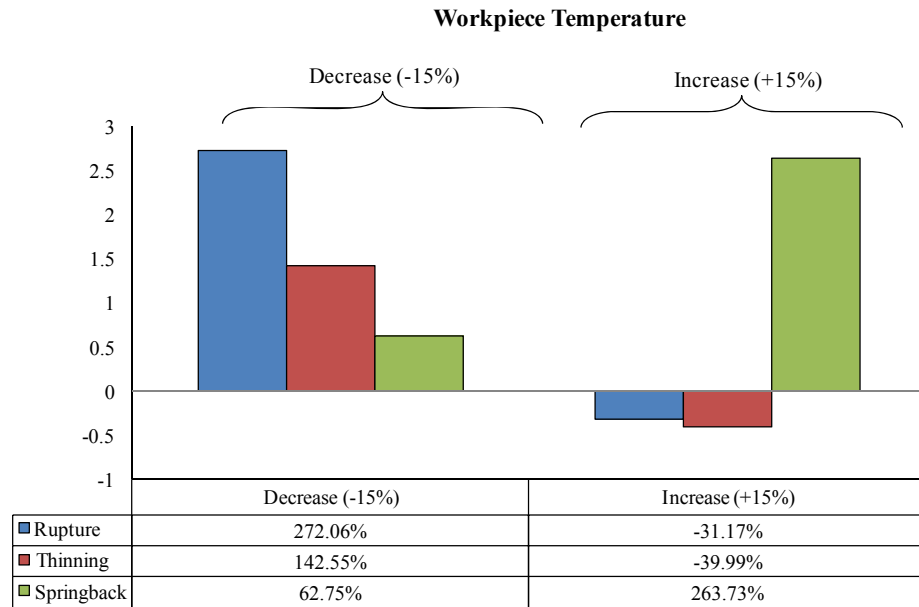
Figure 3.17   Sensitivity of responses to changes in workpiece temperature.

Since the ISV plasticity model is a temperature dependent model, it is important to explore the effect of workpiece temperature on the response parameters in forming simulation. As it is has been shown experimentally, magnesium has a less degree of ductility compare to other metallic alloys such as aluminum and steel. Therefore, it is required to perform the drawing process at elevated temperature. The selectivity study illustrates that by decreasing temperature of 15% the level of rupture and thinning changes drastically whereas by increasing the temperature by 15% the level of rupture and thinning varies less. There also a very considerable nonlinearity on all the response is observed.

Changes in the geometric attribute of the product also affect the responses in the manufacturing process responses meaning that in order to reach to an optimum manufacturing qualities, it is required to adjust the process parameters based on the geometry.

48

Width

	Decrease (-15%)	Increase (+15%)
■ Rupture	5.50%	-6.30%
■ Thinning	5.88%	-7.67%
■ Springback	77.45%	-16.67%
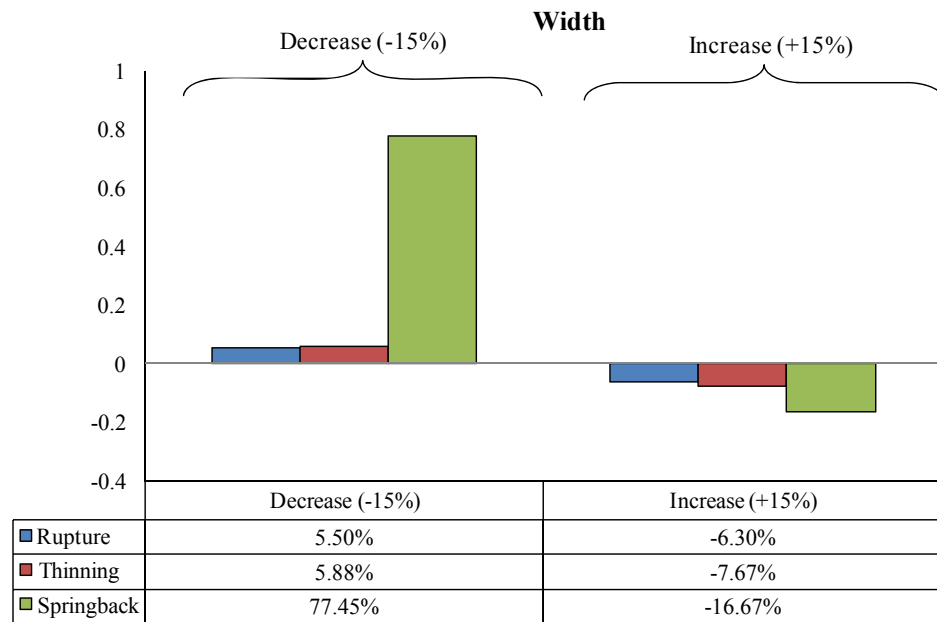
Figure 3.18   Sensitivity of responses to changes in width in hot forming.

The total width of the blank sheet is always assumed to be twice the perimeter of the desired shape. The width of the tube in this drawing process does not experience plastic deformation. Therefore, decreasing the width decreases the area that undergoes the plastic deformation resulting in the higher value for rupture and thinning. Simultaneously, the residual stresses increased in the tube due to the increase in the plastically deformed area and result into the higher springback.

The tube height that determines the size of the side walls of the single hat tubes has a direct relationship with the manufacturing responses. Decreasing the height decreases the area of plastic deformation on the side walls and also decreases the residual stresses resulting in decrease in rupture, thinning and springback responses.

49

Workpiece Temperature

	Decrease (-15%)	Increase (+15%)
▪ Rupture	272.06%	-31.17%
▪ Thinning	142.55%	-39.99%
▪ Springback	62.75%	263.73%
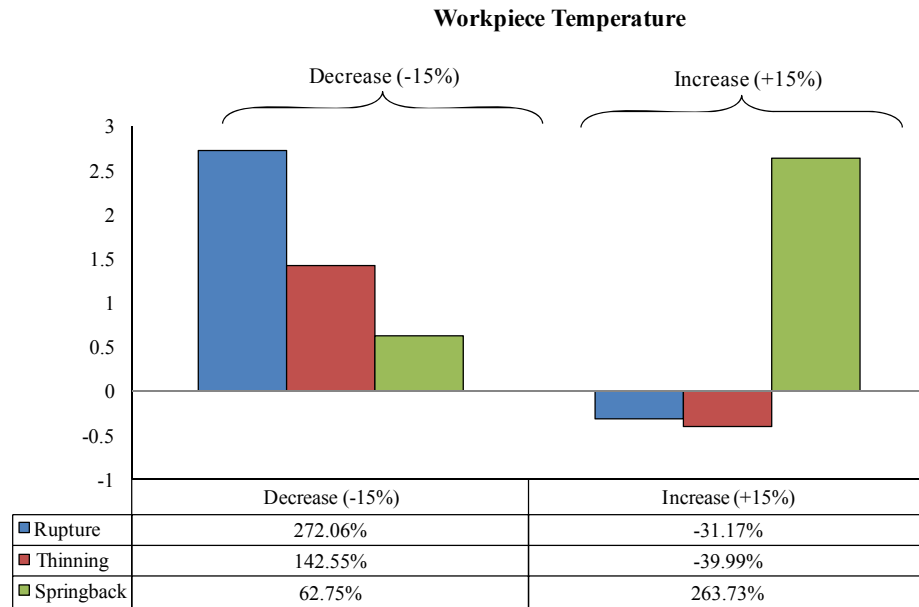
Figure 3.19   Sensitivity of responses to changes in workpiece temperature in hot forming.

Height

	Decrease (-15%)	Increase (+15%)
▪ Rupture	-10.99%	9.28%
▪ Thinning	-13.03%	10.96%
▪ Springback	-15.69%	12.75%
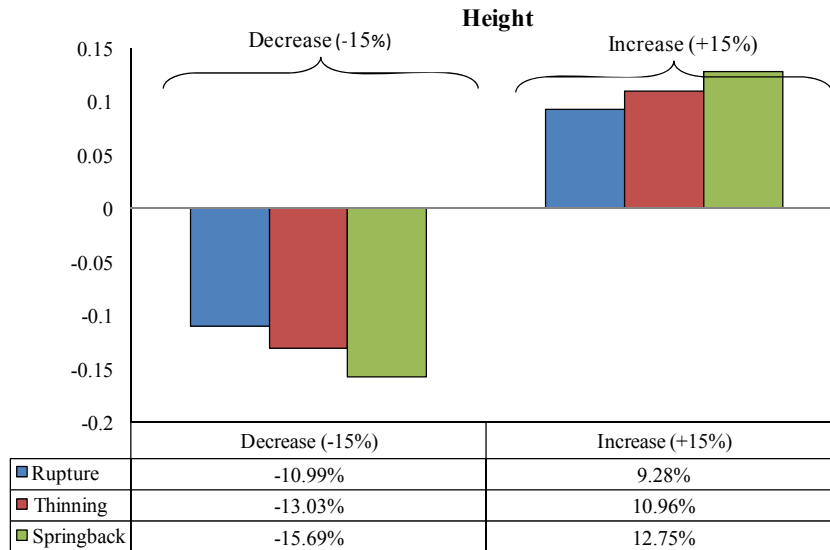
Figure 3.20   Sensitivity of responses to changes in height in hot forming.

50

Sheet Thickness

	Decrease (-15%)	Increase (+15%)
■ Rupture	-4.90%	5.36%
■ Thinning	-3.63%	3.22%
■ Springback	-15.20%	24.51%
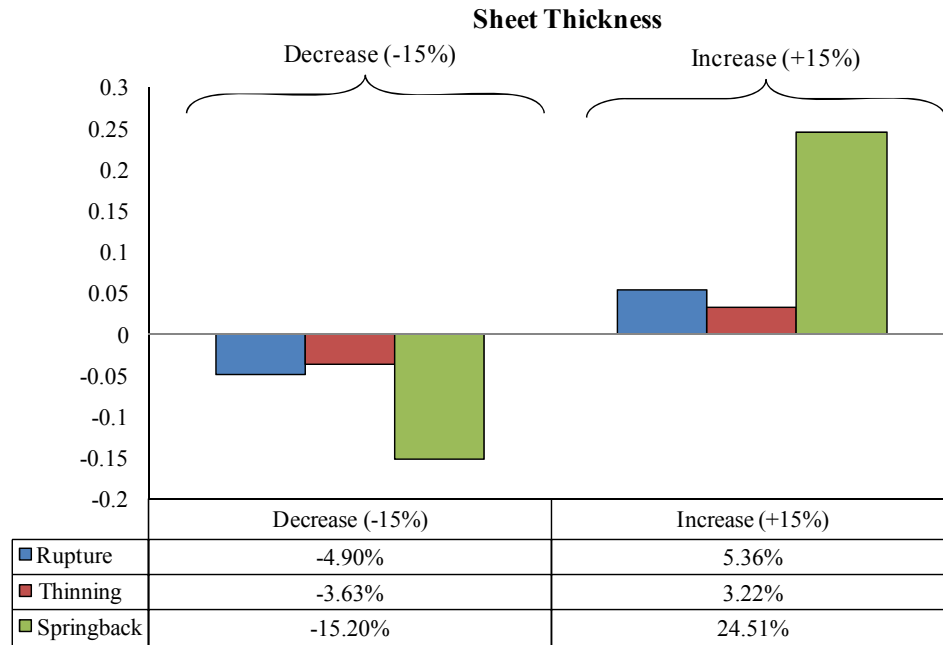
Figure 3.21   Sensitivity of responses to changes in sheet thickness in hot forming.

The manufacturing response sensitivity due to the change in the sheet thickness in hot forming simulation is less than the cold forming simulation as the material can carry more ductility and plastic deformation. The relation between the changes in the blank thickness and the manufacturing response are direct as the increase and thickness results in to increasing in the responses. In order to find the most effective variables on the manufacturing process responses the data of selectivity analysis are shown for each responses separately. As it is shown the punch velocity is considered to be the most effective manufacturing design variable. It is also seen that the thickness effect is changed compare to the cold forming simulations. The rupture and springback varying similarly with respect to changes of the manufacturing process variables. The springback response showed severe nonlinearity as the variables in the forming simulation changes.

51

	Friction Coefficient	Punch Velocity	Holding Force	Thickness	Corner Radius	Height	Width
■ Decrease (-15%)	-1.60%	-29.77%	-0.88%	-4.90%	15.33%	-10.99%	5.50%
■ Increase (+15%)	1.78%	32.92%	0.93%	5.36%	-10.37%	9.28%	-6.30%
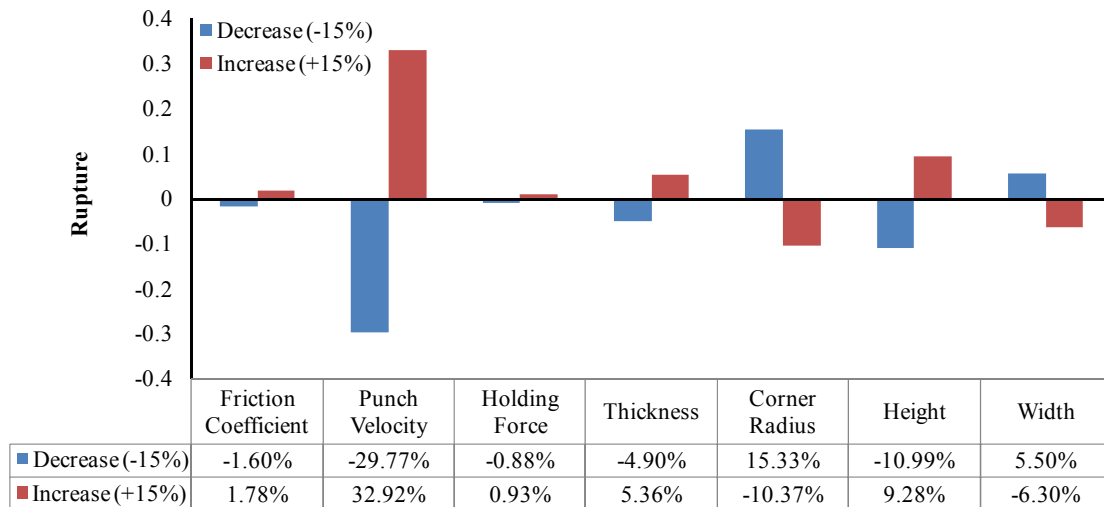
Figure 3.22   Sensitivity of rupture to design variables in hot forming

	Friction Coefficient	Punch Velocity	Holding Force	Thickness	Corner Radius	Height	Width
■ Decrease (-15%)	-1.66%	-30.76%	-0.76%	-3.63%	15.87%	-13.03%	5.88%
■ Increase (+15%)	1.91%	30.31%	0.85%	3.22%	-11.09%	10.96%	-7.67%
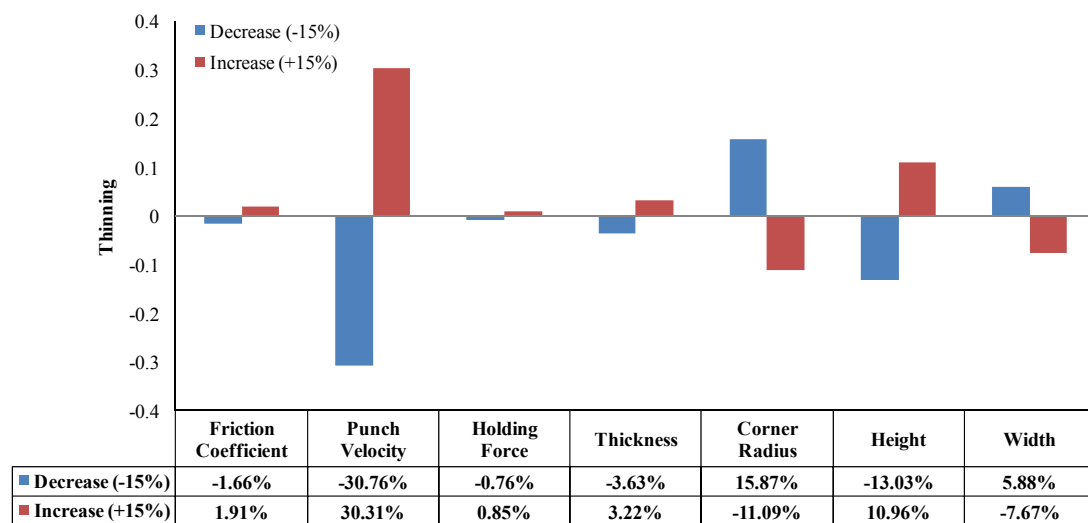
Figure 3.23   Sensitivity of thinning to design variables in hot forming

	Friction Coefficient	Punch Velocity	Holding Force	Thickness	Corner Radius	Height	Width
Decrease (-15%)	5.88%	135.29%	1.47%	-15.20%	-15.20%	-15.69%	77.45%
Increase (+15%)	-4.90%	-37.75%	-1.96%	24.51%	39.22%	12.75%	-16.67%
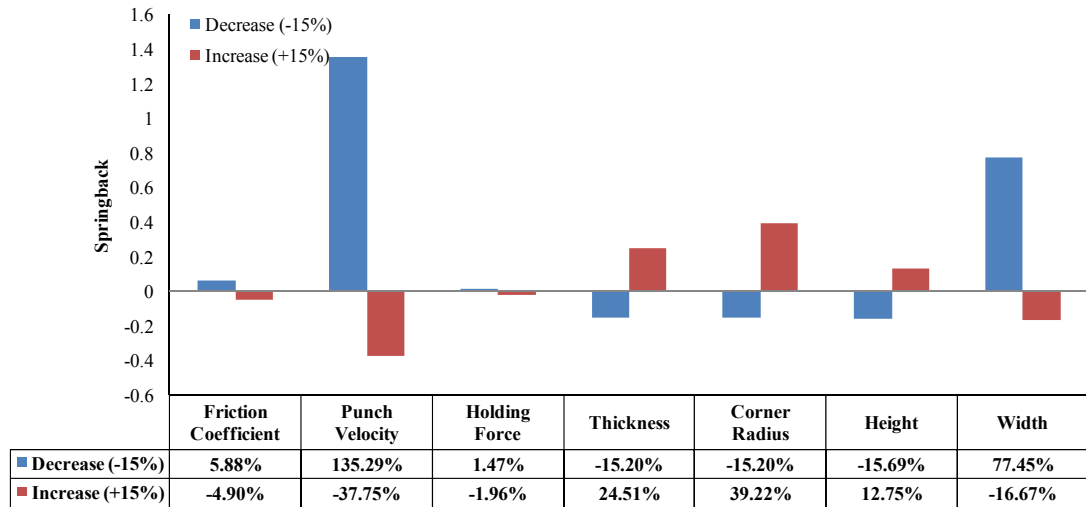
Figure 3.24   Sensitivity of springback to design variables in hot forming

CHAPTER IV

EFFECT OF MANUFACTURIN ON THE ENERGY ABSORPTION

During product fabrication using the sheet forming process, material and the part geometry are both influenced by the manufacturing process parameters and manifested through residual stresses, springback, and thinning. The material microstructure is also affected by the forming process due to the extensive plastic deformation; consequently, work hardening and the dislocation density, grain orientation and texture pattern, as well as the amount of micro damage in the material can change. This evolution during the manufacturing process can affect both springback and the actual performance of the product such as energy absorption and crash/crush behavior. In order to include the changes in material and geometry from one process stage to another, it is necessary to store the analysis output from one simulation stage and transfer it as input to or initial condition for the next simulation.

Coupled quasi-static analysis is available in some implicit FE codes such as ABAQUS/STANDARD by defining all the loading scenarios (analysis procedures) in one step or using the restart option to initialize a new solution using information from the previous steps (ABAQUS manual 2010). In each step, the boundary conditions can be changed and the material state can be passed to the next step. The same strategy is also available in some hydro codes or explicit solvers such as LS-DYNA or ABAQUS/EXPLICIT that can perform a coupled sequential simulation under dynamic environment (Xu et al 2004, ABAQUS manual 2010). The increasing demand for

54

coupled simulations motivated most commercial software codes to provide tools to map some solutions as initial state in the problems (Lin and Liu 2000, ABAQUS manual 2010, MD NASTRAN manual 2008). This capability is limited, however, to some specific material models, solution types, and nonlinear iterative solving procedures.

The implicit integration scheme is usually more suitable to solve quasi-static problems with geometric and material nonlinearity, whereas dynamic and high rate problems are more easily solved using explicit integration scheme. However, there are other factors that come into play as problem nonlinearity becomes more severe. In explicit integration scheme, convergence is always guaranteed but it is achieved by using very small (stable) time steps. Therefore, the computations become more expensive and the storage volume should be controlled carefully to enhance the efficiency of the solution. Because of using small time steps, round off error is accumulated as the time progresses, and some simplifications such as the use of diagonalized mass matrix can make the simulation results noisy requiring filtering.

The main challenge in using explicit solvers for quasi-static problems is their time step which can be improved by using some computational artifacts and model adaptation such as mass scaling techniques or carefully increasing the loading rate for rate insensitive materials. These parameters should be used carefully as they may affect the structural response due to the change in the dynamic and inertia properties of the structure analyzed. Selecting a proper solution strategy to tackle a boundary value problem is a very challenging task and requires proper understanding of the physics of the problem as well as the software capabilities and limitations, element formulations, contact formulations, and numerical solution parameters.

55

In general, a coupled simulation is achieved by the ability to transfer effectively the results from one simulation to another. The data transfer includes geometric attributes and the material state. Tracking the geometric attributes includes the deformation state and the thickness change while removing or disabling elements in the fractured regions. Material state can be tracked by some parameters including the residual stresses, damage, and other model related state variables that represent the physical state of the material and structure. Since some implementations of the constitutive models require zero state as the initial condition, the evolution of state variables and stresses should be carefully tracked to confirm the ability of the solver to use the mapped solutions as the initial values for the subsequent analyses.

4.1 Classical Plasticity Material Model

In order to show the significance of including the manufacturing effects on the axial crushing behavior of double-hat tubes, two simulation cases are compared, one using a separate stand-alone performance simulation that does not include any history effects or information from the manufacturing process and the other using a coupled sequential process-performance simulation that includes residual stresses, plastic strains, thinning, and springback information from process simulation together with a piecewise linear isotropic hardening material model in performance simulation. Tubes are modeled using plane-stress shell element formulation. They are held fixed at one end and axially loaded with a flat rigid wall at the other end that is moving with a constant speed of 5 m/s. Both self-contact and surface-to-surface contact between rigid wall and tube are used. A classical multi-linear kinematic hardening material model is used for this simulation.

56

Figure 4.1 shows the curves of crush force versus crush distance at the top as well as the crush modes for both the cases. It appears that both the crush response and the crush mode change due to the inclusion of the history effects. The maximum crush force drops from 95 kN to 89 kN by considering the history effects. Similarly, the mean crush force changes from 20 kN to 18 kN when history effects are considered. This comparison shows the importance of incorporating the history effects to find more realistic response predictions, and presents an opportunity to enhance the performance responses by guiding process parameters in a way that produces acceptable product from the manufacturing standpoint as well as the optimized performance characteristics.
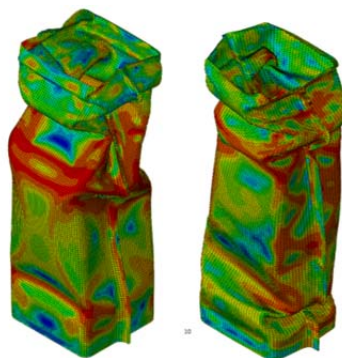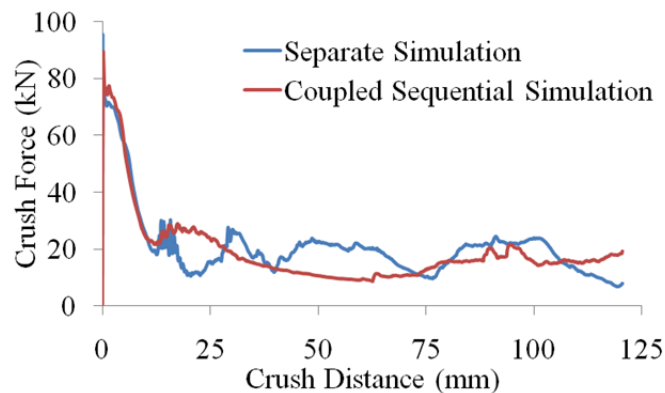
Separate Simulation   Coupled Sequential Simulation

Figure 4.1   Comparison between crushing behavior of two double-hat tubes by including and excluding the history effects (deformation is shown with the scale factor of 0.6).

4.1.1   Coupled Sequential Process-Performance Simulation Procedure

A coupled sequential process-performance simulation is conducted by using
ABAQUS/EXPLICIT for the deep drawing (loading) simulation,
ABAQUS/STANDARD for the springback (unloading) simulation under isothermal
condition at room temperature, followed by ABAQUS/EXPLICIT simulation for the
crush analysis. The procedure of forming and springback simulation is similar to what is
been discussed in chapter II. In this section, in order to produce the double hat tube, it is
required to perform the forming simulation for both single hat tubes simultaneously to be
able to perform the one-to-one mapping from the integration points, nodal coordinates
and element attributes. The two hat sections are required to be trimmed by removing the
outer flange elements in order to shape the actual double hat tube. In this research no
attempt is made to simulate the cutting process therefore, the residual stresses related to
the cutting process is ignored. However, it is worth noting that the prismatic geometry
result into a very negligible plastic deformation in the wing as it can be seen in figure 4.3.
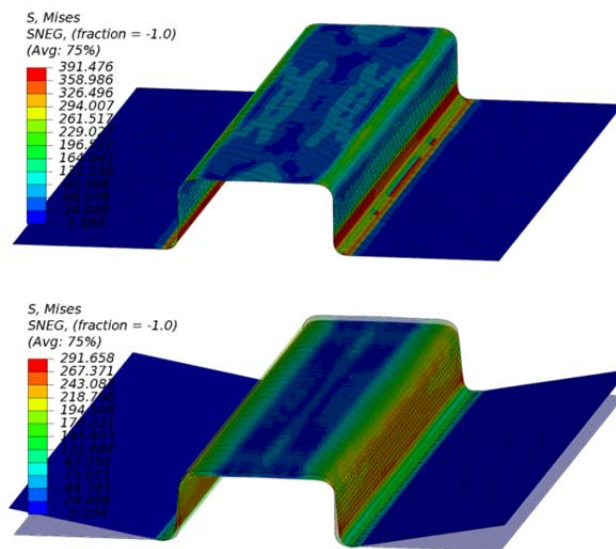
Figure 4.2   The von-Misses stress distribution on the tube before (top) and after
springback (bottom).

58
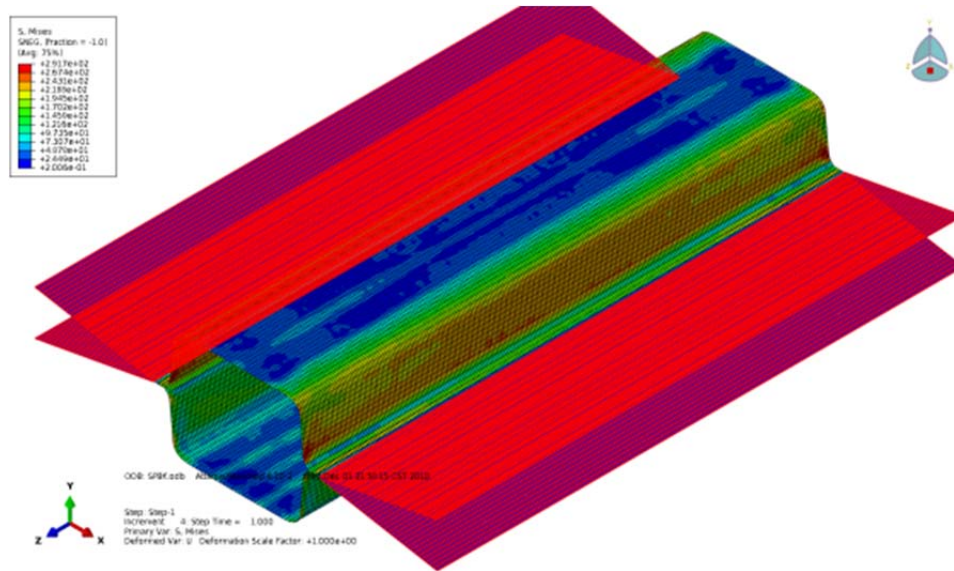
Figure 4.3   Trimming of single hat sections after the springback simulation. The red area is removed from the model.

Then two single-hat tubes are joined together as shown in Fig. 4.3. In this research the effect of joining or welding is ignored and it is assumed that the joining is perfect and the material in this region will not be affected due to the joining process. The single hat sections are connected through the highlighted edges shown in Fig. 5 using tie contact formulation. The tie contact constrains the master and slave surfaces similar to the multiple constraint points when the clearance between two surfaces is below the tolerance defined as an input variable. If the surfaces are out of prescribed tolerance, the interaction becomes a contact formulation. A preliminary study showed that switching the master and slave surfaces would not affect the crushing behavior of the tube. Once the distance between the two surfaces becomes more than the clearance tolerance, constraints are removed and contact formulation is activated similar to the conventional contact definition. It is worth noting that this kind of joining is a very crude representation of welding the two single hat sections together as no attempt is made to model the thermo-mechanical process involved.

59
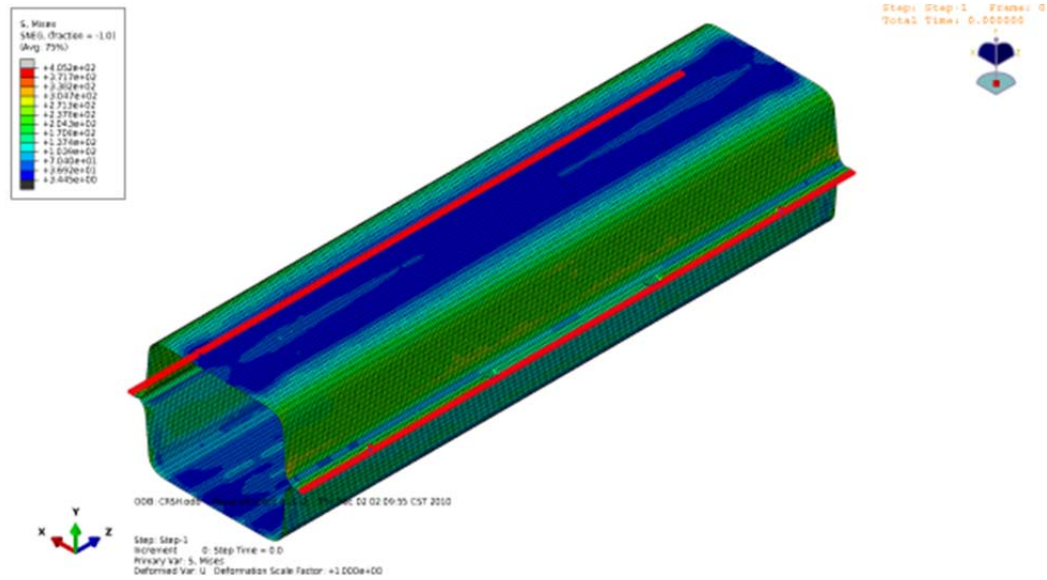
Figure 4.4   Trimming of single hat sections after the springback simulation. The red area is removed from the model.

Crush simulation of the double-hat tube is performed using the geometry, residual stresses, and state variables from the previous deep drawing and springback analyses. An explicit solver is used for crush simulation because the crush process is highly nonlinear. Owing to the geometry of the double-hat tube and presence of the initial condition imported from the previous steps, selecting a proper contact formulation to perform the crush simulation is critical. Six contact interaction sets between elements are defined in the crush simulation including interactions between the lower hat section and the rigid wall, the upper hat section and the rigid wall, interaction between the upper and lower hat sections, tie contact between the assembly edge of the upper and lower surfaces, and separate self contact interaction for the upper and lower hat sections. For all of the aforementioned contact interaction sets, penalty function formulation in both normal and tangential directions is used. Despite the computational cost, using penalty function provides a proper flexibility for the explicit code to find a stable time step that is affected by severity of the contacts. Moreover, the maximum ratio of thickness-to-element length

60

is used to overcome the difficulty of the fine mesh density that results in relatively thick shell elements. This option is used to enhance the computational stability of the contact by adjusting the element thickness and, consequently, reducing the mesh distortion that can lead to an unsuccessful simulation.

Crush simulation is done by fixing the tube at one end and applying an axial load through a moving rigid wall defined with a prescribed displacement at the other end. The rigid wall moves with a constant speed to simulate constant loading rate as shown in Fig. 4.5.
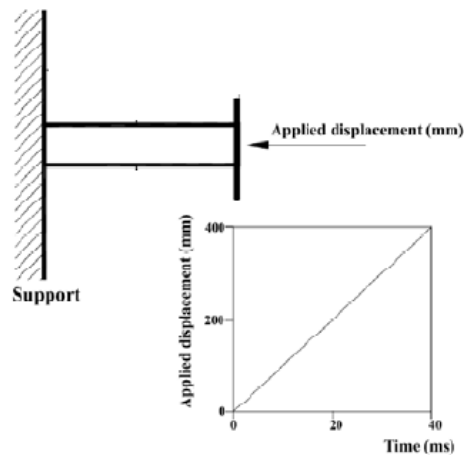
Figure 4.5   Description of the boundary conditions and loading for the crush
              simulation

The material model used in this study is piecewise linear isotropic hardening. The constant for the linear kinematic hardening is calculated based on the slope of a line connecting two adjacent points on the stress-strain curve. The material model uses von Misses yield surface and the one-dimensional stress-strain input is considered as equivalent von Misses stress versus effective plastic strain. Coupling scheme is utilized by transferring residual stresses and the equivalent plastic strains as the material state

61

variables. The yield surface expands due to the isotropic hardening assumption in the model; therefore, the instantaneous yield point varies during the loading process. The yield point at the end of the forming simulation is captured by finding the plastic strain. In this study, material data for AZ31 magnesium alloy sheet at room temperature is used for all the simulations. In order to account for the rate dependency, the stress-strain curves for two extreme rates are considered with those for the other rates found through interpolation. The elastic modulus, Poisson's ratio, and density are chosen to be 45 GPa, 0.33, and 1.738 kg/m3, respectively. The material behavior in terms of true stress versus true strain is plotted in Fig. 4.6 for the two extreme strain rates. Adiabatic heating is not considered in any of the simulations.
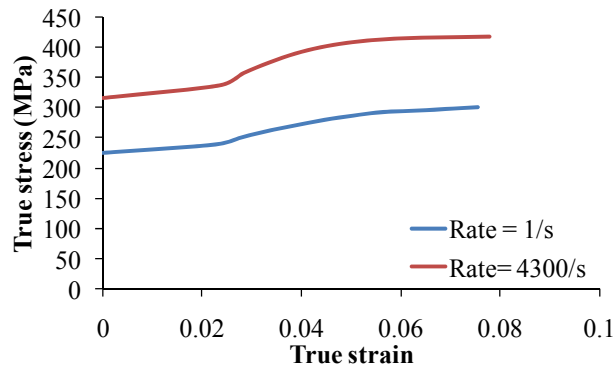
Figure 4.6   AZ31 magnesium alloy sheet stress-strain curves for two different strain rates

4.1.2   Definitions of Performance Responses

In this study, two responses are extracted from crush simulation including the *maximum crush force* and the *mean crush force* that are the responses calculated from the crush simulation as the main two parameters to evaluate the energy absorption behavior of the double hat tubes.

62

From the crush simulation, the maximum crush force is calculated from the contact force history of the rigid wall and the mean crush force is calculated from the area under the crush force versus crush distance divided by the effective crush distance. These results are extracted and filtered using a Python scripting application available in ABAQUS and a FORTRAN code to calculate the mean crush force values. The mean crush force is the amount of total energy absorbed in each increment in the axial direction divided by the effective cross-head displacement of the rigid wall with the equation expressed as

$$P_m = \frac{1}{\delta_{eff}} \int_0^t F(t)D(t)dt \qquad (4.1)$$

where $F(t)$ is the amount of the instantaneous contact force normal to the rigid wall surface and $D(t)$ is the instantaneous cross-head axial displacement of the rigid wall. SAE filtering of 60 Hz is used to smooth out the noise in the force results. For this analysis, the final cross-head displacement of the rigid wall is assumed to be 125 mm, which is 50% of the tube length, thus, $\delta_{eff} = 125\ mm$. The maximum crush force is the largest value of $F(t)$ after performing SAE filtering.

The specific energy absorption (SEA), or energy absorbed per unit mass, is calculated for the first 50% of the tube length using the equation

$$SEA = \frac{E}{m} = \frac{\int_0^t F(t)D(t)dt}{\rho\,A\,\delta_{eff}} \qquad (4.2)$$

where ρ and A are material density and cross-sectional area, respectively.

4.1.3   Effect of manufacturing process and geometric attributes on crush

In order to study the effect of manufacturing process as well as geometrical attributes on the crushing behavior, a sensitivity analysis is performed. The upper and

lower bounds for the selected seven design variables are shown in Table 4.1. An FE

simulation is performed by perturbing a single design variable by ±15% from its average

value while keeping the other design variables fixed at their corresponding average

(baseline) values shown in the first row of Table 4.1 in bold.

Table 4.1　　The values assigned to design variables for sensitivity analysis

Sensitivity	Width (mm)	Height (mm)	Corner Radius (mm)	Thickness (mm)	Holding Force (kN)	Punch Velocity (m/s)	Friction Coefficient
Friction Coefficient ±15%	**55**	**27.5**	**5**	**1.75**	**30**	**6**	**0.225**
	55	27.5	5	1.75	30	6	0.16875
	55	27.5	5	1.75	30	6	0.25875
Punch Velocity ±15%	55	27.5	5	1.75	30	6	0.225
	55	27.5	5	1.75	30	4.5	0.225
	55	27.5	5	1.75	30	6.9	0.225
Holding Force ±15%	55	27.5	5	1.75	30	6	0.225
	55	27.5	5	1.75	22.5	6	0.225
	55	27.5	5	1.75	34.5	6	0.225
Thickness ±15%	55	27.5	5	1.75	30	6	0.225
	55	27.5	5	1.3125	30	6	0.225
	55	27.5	5	2.0125	30	6	0.225
Corner Radius ±15%	55	27.5	5	1.75	30	6	0.225
	55	27.5	3.75	1.75	30	6	0.225
	55	27.5	5.75	1.75	30	6	0.225
Height ±15%	55	27.5	5	1.75	30	6	0.225
	55	20.625	5	1.75	30	6	0.225
	55	31.625	5	1.75	30	6	0.225
Width ±15%	55	27.5	5	1.75	30	6	0.225
	41.25	27.5	5	1.75	30	6	0.225
	63.25	27.5	5	1.75	30	6	0.225
Upper Bound	70	35	7.5	2.5	50	10	0.35
Lower Bound	40	20	2.5	1	100	2	0.1

The sensitivity values are normalized for both mean crush force and maximum

crush force responses and shown separately based on the variable considered to be

changed in each figure. Each bar chart is divided into two groups, the responses shown

on the left side are derived as a result of a -15% perturbation in a design variable while

the responses shown on the right are derived from a +15% perturbation. It appears that

the manufacturing process variables such as holding force and punch velocity can affect

considerably the performance of the crush tube as measured by the maximum and mean

values of the crush force. Fig 4.7 shows the effect of changes in friction coefficient on the

energy absorption characteristics. Changing the friction coefficient during manufacturing

64

process has a nonlinear effect on the mean and maximum crush forces. As it has been shown in chapter III, friction coefficient changes the amount of plastic strain, element thickness as well as spring back. The combination of these effects transferred from manufacturing process changes the crush behavior in terms of folding size and results into a nonlinear behavior.

Friction Coefficient

	Decrease (-15%)	Increase (+15%)
■ Max Crush Force	1.83%	1.88%
■ Mean Crush Force	1.03%	4.45%
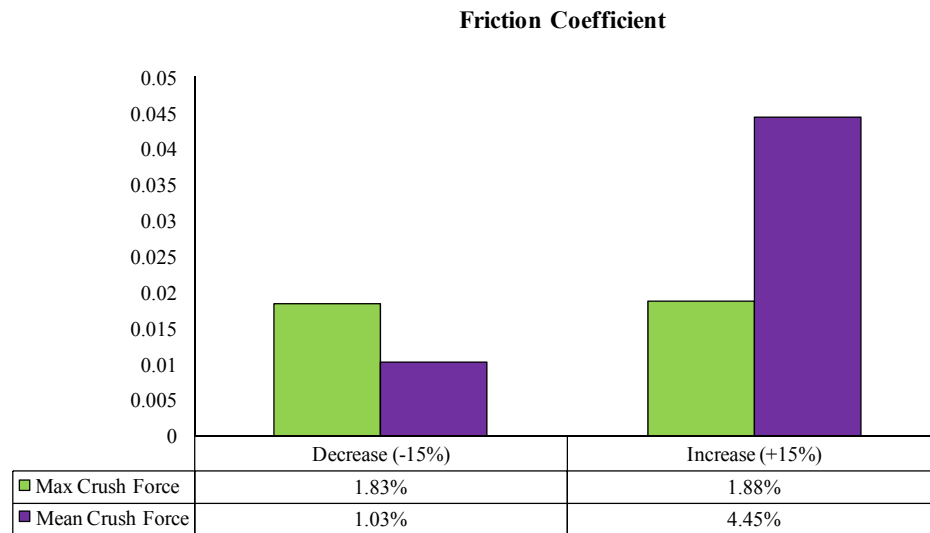
Figure 4.7   Sensitivity of responses to changes in the friction coefficient

Varying the holding force has a strong and reverse influence on the mean crush force mainly due to the work hardening and thinning as shown in Fig. 4.8.

65
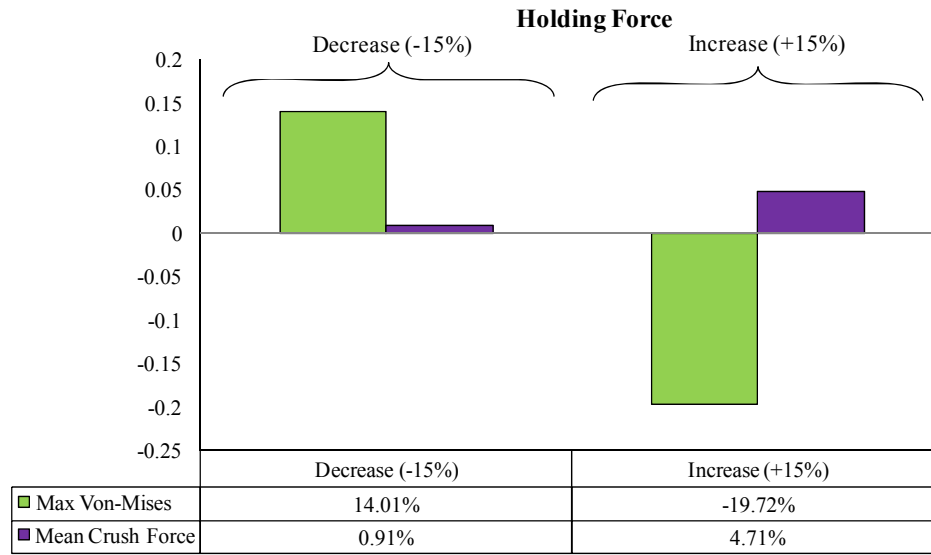
Figure 4.8   Sensitivity of responses to changes in the holding force

Punch velocity can affect the result of energy absorption because of the strain rate dependency of the material. It can be seen in Fig. 4.9 that the mean crush force is affected mainly due to the work hardening effect imposed by the plastic deformation and strain rates. The maximum crush force is also increased due to the increasing in the yield point resulted from the equilibrium state of material that affected due to manufacturing process.
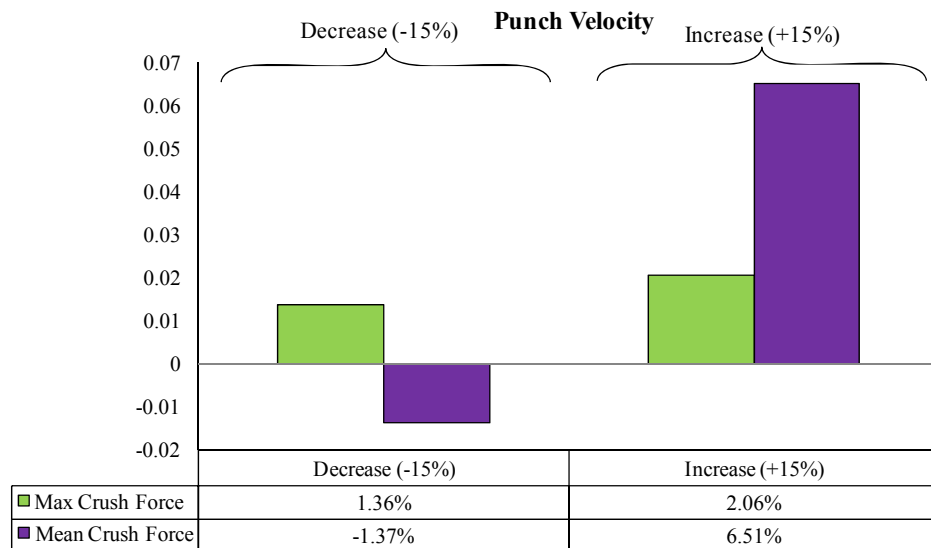
Figure 4.9   Sensitivity of responses to changes in the punch velocity

66

Change in the corner radius as a geometric attribute does not influence the crush behavior considerably as illustrated in Fig. 4.10. However, the sharper corner introduces a reduction in the maximum crush force.

	Decrease (-15%)	Increase (+15%)
■ Max Crush Force	1.86%	1.95%
■ Mean Crush Force	-16.92%	-1.71%
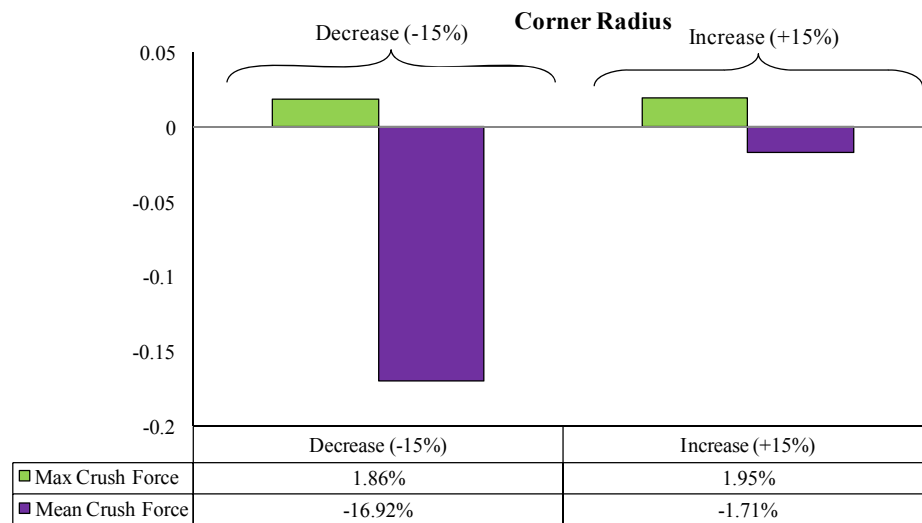
Figure 4.10   Sensitivity of responses to changes in the corner radius

The change in the geometry of the tube also affected the crush performance responses as shown in Figs. 4.11 and 4.12. The cross-sectional geometry of the tube can change by width, height, and the thickness of the tube. As the width and height of the tube change, the mean crush force is affected with the linear relationship. However, the perturbation on the width has a nonlinear relationship with the maximum force. Increasing the width drops the maximum force more than decreasing it with a nonlinear response. As it is shown in figure 4.12 both mean and maximum crush forces have a direct relation with the height of the side walls. Increasing the size of the side walls not only introduces a larger cross-sectional geometry but it is affected due to the extensive plastic deformation due to the flow of material between forming tools.

67
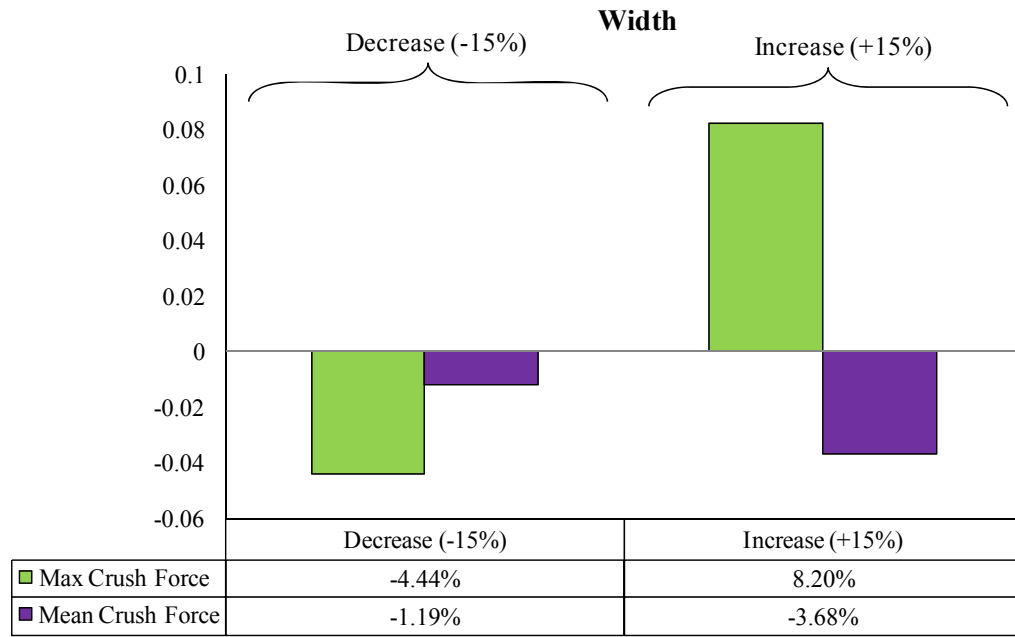
Figure 4.11   Sensitivity of responses to changes in width
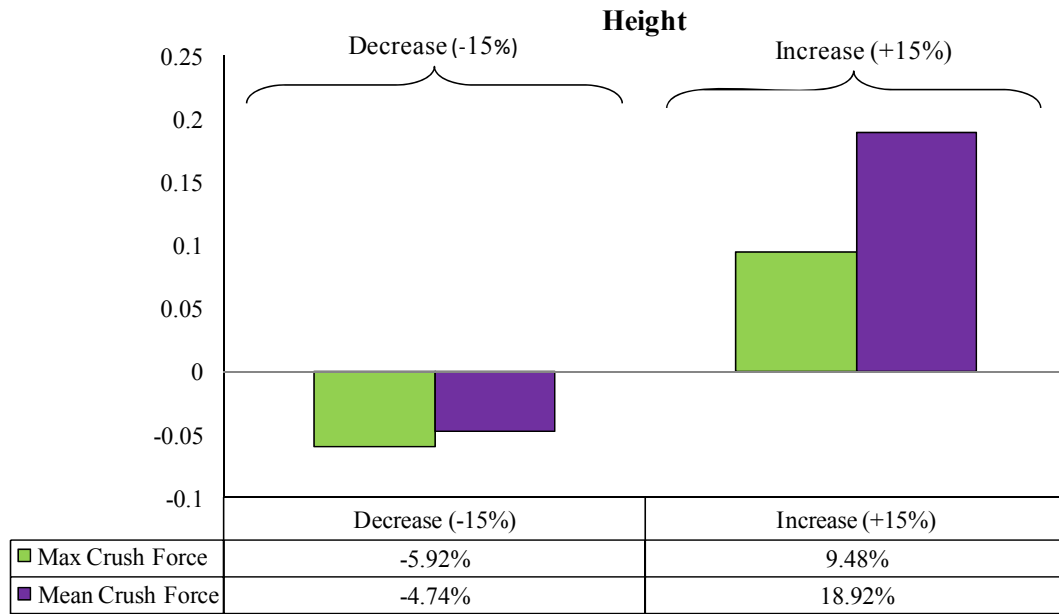
Figure 4.12   Sensitivity of responses to changes in height

Change in the sheet thickness influence the crush results directly as depicted in

Fig. 4.13. The stress distribution, plastic deformation, and flexural stiffness are highly

68

affected by thickness resulting in a significant impact on the crushing behavior. Reducing the sheet thickness is also influenced by less plastic deformation and thinning and the material behaves more closely to the expected designs. But increasing the sheet thickness introduces more plastic deformation and work hardening as well as thinning. However, change in the plastic deformation is higher than the thinning which gives a higher contribution to the crash once it is considered with the thickness increase.

Sheet Thickness

	Decrease (-15%)	Increase (+15%)
■ Max Crush Force	-14.22%	17.63%
■ Mean Crush Force	-10.75%	22.53%
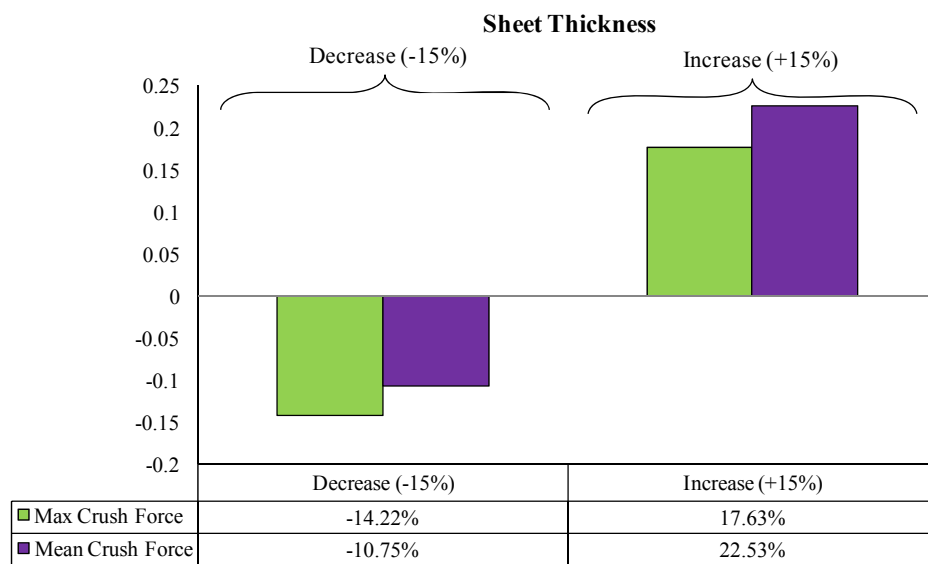
Figure 4.13   Sensitivity of responses to changes in sheet thickness

The sensitivity results are also presented differently in order to show the competition of each variable for energy absorption response in fig 4.14 and 4.15.

Both responses are shown that affected from thickness change more than the other variables which introduces the most common approach to enhance the energy absorption behavior (increasing thickness) that is always increases the mass of the component. The maximum crush force is increased due to the change in the manufacturing response based on the baseline selected. The maximum crush force is mainly influenced by the

69

plastic/elastic buckling, the stress wave behavior and the cross-sectional geometry. It is seen that the variation in the manufacturing affected responses such as work hardening and thinning affected the maximum crush force in a way that any change with respect to the baseline process parameters results into an increase in the maximum crush force. As it is shown in Fig 4.15, the mean crush force could be influenced by 7% due to the change in the manufacturing process parameters. This shows an important potential to enhance the energy absorption by adjusting the manufacturing process variables.

	Friction Coefficient	Punch Velocity	Holding Force	Thickness	Corner Radius	Height	Width
Decrease (-15%)	1.83%	1.36%	1.22%	-14.22%	1.86%	-5.92%	-4.44%
Increase (+15%)	1.88%	2.06%	1.81%	17.63%	1.95%	9.48%	8.20%
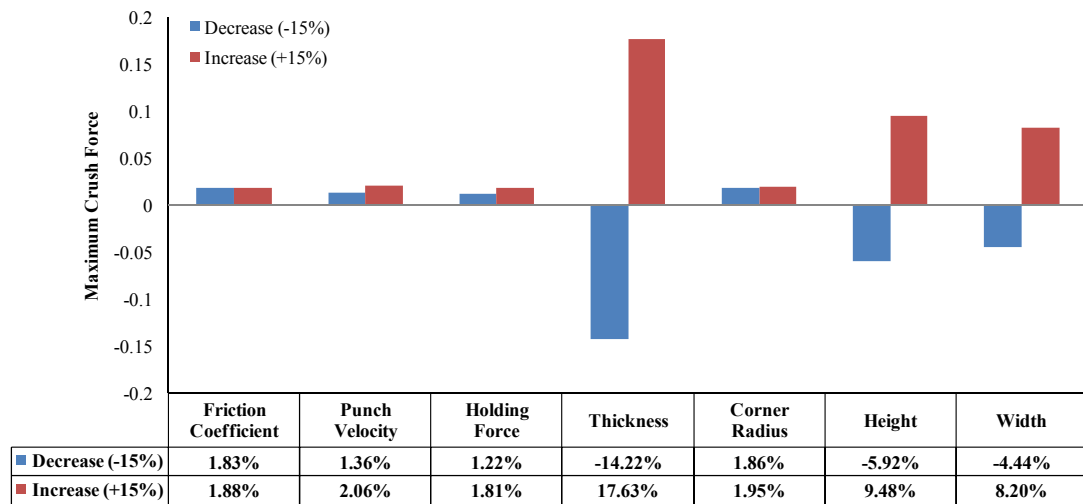
Figure 4.14   Sensitivity of maximum crush force to design variables

70

	Friction Coefficient	Punch Velocity	Holding Force	Thickness	Corner Radius	Height	Width
■ Decrease (-15%)	1.03%	-1.37%	0.91%	-10.75%	-16.92%	-4.74%	-1.19%
■ Increase (+15%)	4.45%	6.51%	4.71%	22.53%	-1.71%	18.92%	-3.68%
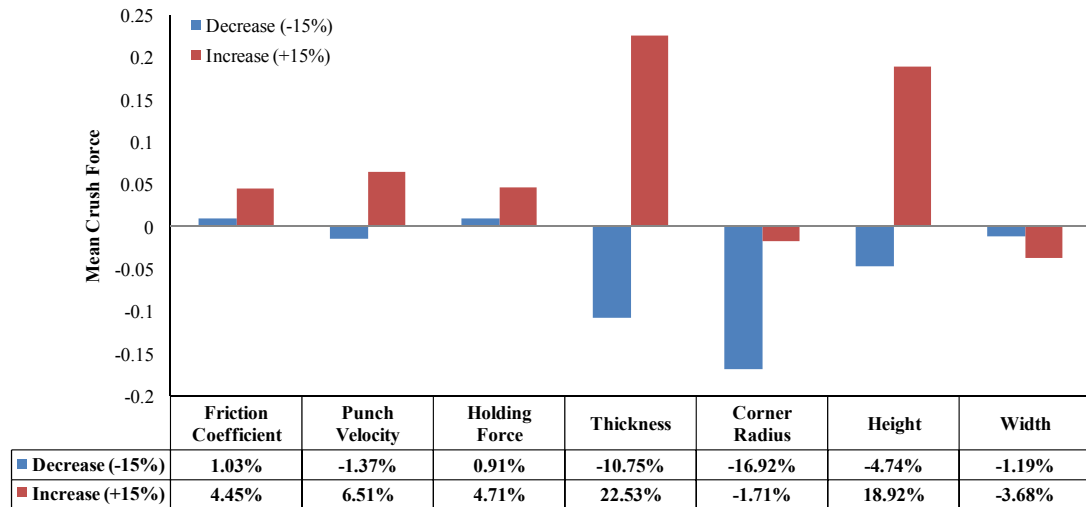
Figure 4.15   Sensitivity of mean crush force to design variables

4.2   Internal State Variable Material Model

In order to predict structural responses and performance in the virtual design optimization methodology, it is essential to link external loads (like force and displacement) to the structural internal material responses, such as stress and strain. The relationship between external stimuli and material internal responses are termed as constitutive equations of the material. They are essentially set of mathematical or phenomenological equations. The phenomenological equations are established based on the physical behavior observed in dislocation plasticity in lower length scales such that the continuum model can also link to the material microstructure. In the present study, the plastic behavior is represented through isotropic and kinematic hardening to model the post yield behavior as well as static and dynamic recovery that can model the saturation of stress-strain responses. The present internal state variable model is also capable of considering the adiabatic heating due to the plastic deformation as shown in chapter II. Similar boundary value problem that is discussed in the previous section is studied here using the internal state variable material model. Figure 4.16 compares the coupled

71

process-performance and separate simulation. The process simulation includes a hot forming simulation. The coupled simulation has a more stable response compare to the separate simulation responses. The maximum crush force decreases drastically due to the inclusion of the manufacturing state variables in the material behavior. Deformation shape in the coupled simulation is more confined in the coupled simulation whereas the separate simulation shows a larger folding size such that it presents a global response.
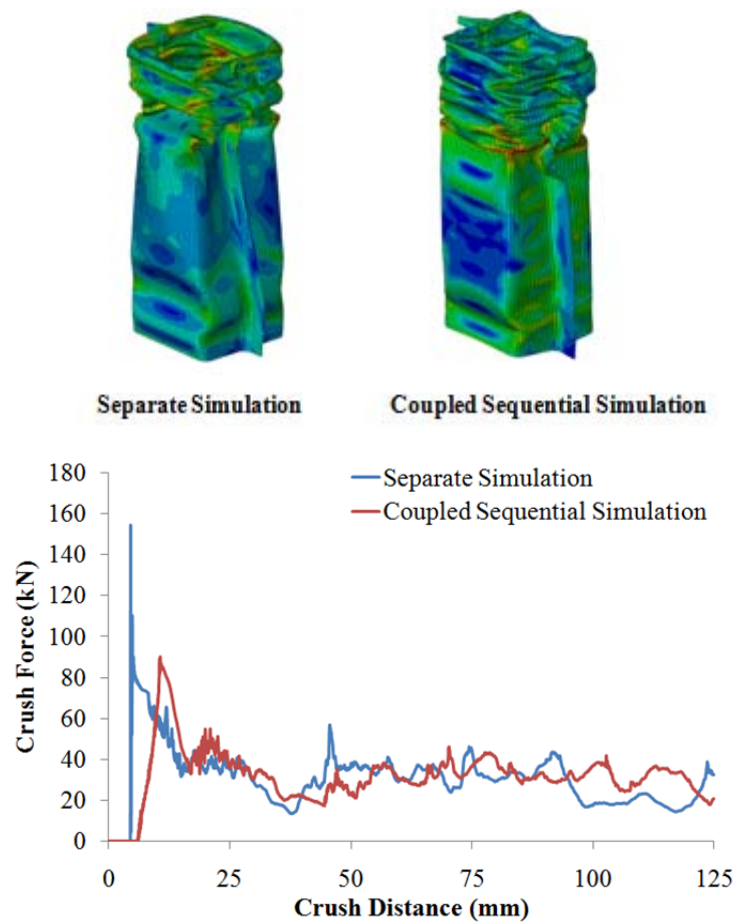
Figure 4.16   Comparison between crushing behavior of two double-hat tubes by including and excluding the manufacturing process effects using ISV model in isothermal condition (deformation is shown with the scale factor of 0.6).

72

4.2.1   Effect of adiabatic heating

Experimental studies have shown that the very large amount of plastic dissipates due to adiabatic heating. The ISV model used in this study is capable of considering the adiabatic heating due to plastic deformation based on equation 2.28 in chapter II. This temperature changes affects the constitutive relation that are considered to be temperature dependent. The increase in temperature softens the material behavior similar to what is observed in the experimental studies on the coupons at elevated temperature. In this section the effect of adiabatic heating on the crush behavior in separate and coupled simulation is discussed. The boundary value problem used is similar to the previous sections.
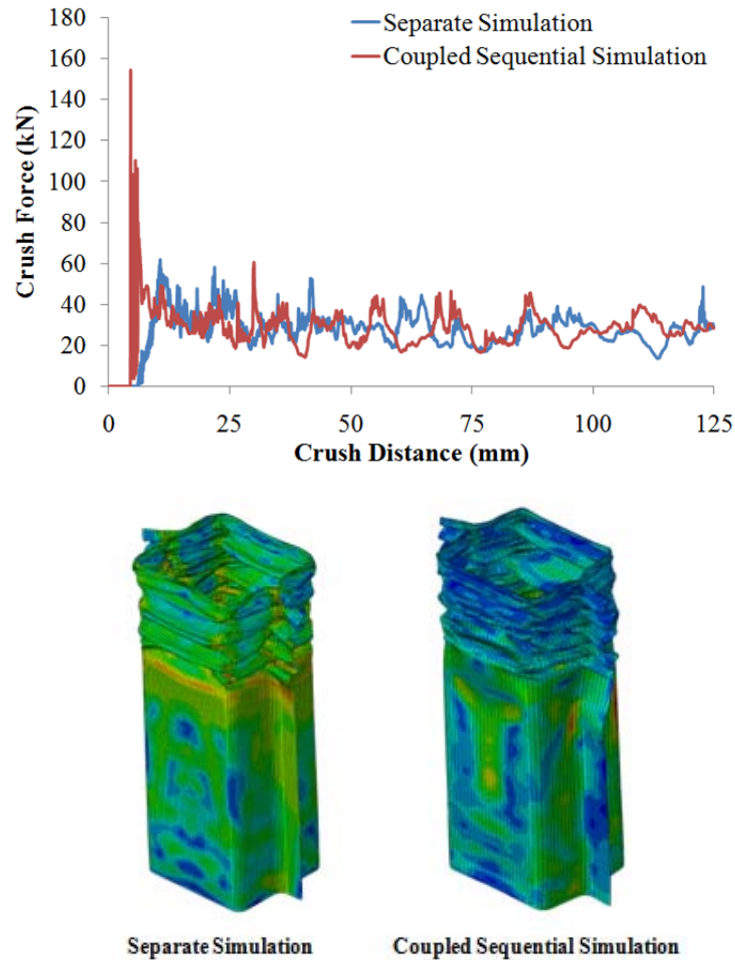
Figure 4.17   Comparison between crushing behavior of two double-hat tubes by including and excluding the manufacturing process effects using ISV model including the adiabatic heating due to plastic deformation (deformation is shown with the scale factor of 0.6).

4.2.2   Effect of manufacturing process and geometric attributes on crush using ISV model

Similar to what is discussed in the classical plasticity model, a sensitivity analysis is performed. The upper and lower bounds for the selected seven design variables are shown in Table 4.2. An FE simulation is performed by perturbing a single design variable by ±15% from its average value while keeping the other design variables fixed at their corresponding average (baseline) values shown in the first row of Table 4.2 in bold.

74

Table 4.2   The values assigned to design variables for sensitivity analysis

Sensitivity	Width (mm)	Height (mm)	Corner Radius (mm)	Thickness (mm)	Holding Force (kN)	Punch Velocity (m/s)	Friction Coefficient
Friction Coefficient ±15%	**55**	**27.5**	**5**	**1.75**	**30**	**6**	**0.055**
	55	27.5	5	1.75	30	6	0.04675
	55	27.5	5	1.75	30	6	0.06325
Punch Velocity ±15%	55	27.5	5	1.75	30	6	0.055
	55	27.5	5	1.75	30	4.5	0.055
	55	27.5	5	1.75	30	6.9	0. 055
Holding Force ±15%	55	27.5	5	1.75	30	6	0. 055
	55	27.5	5	1.75	22.5	6	0. 055
	55	27.5	5	1.75	34.5	6	0. 055
Thickness ±15%	55	27.5	5	1.75	30	6	0. 055
	55	27.5	5	1.3125	30	6	0. 055
	55	27.5	5	2.0125	30	6	0. 055
Corner Radius ±15%	55	27.5	5	1.75	30	6	0. 055
	55	27.5	3.75	1.75	30	6	0. 055
	55	27.5	5.75	1.75	30	6	0. 055
Height ±15%	55	27.5	5	1.75	30	6	0. 055
	55	20.625	5	1.75	30	6	0. 055
	55	31.625	5	1.75	30	6	0. 055
Width ±15%	55	27.5	5	1.75	30	6	0. 055
	41.25	27.5	5	1.75	30	6	0. 055
	63.25	27.5	5	1.75	30	6	0. 055
Upper Bound	70	35	7.5	2.5	50	10	0.10
Lower Bound	40	20	2.5	1	100	2	0.01

The sensitivity values are normalized for both mean crush force and maximum crush force responses and shown separately based on the variable considered to be changed in each figure. Each bar chart is divided into two groups, the responses shown on the left side are derived as a result of a -15% perturbation in a design variable while the responses shown on the right are derived from a +15% perturbation. It appears that the by changing the manufacturing process variables such as holding force and punch velocity affect between 1% to 15% due to the perturbation imposed in the process parameters. In this study, performance of the crush tube as measured by the maximum and mean values of the crush force. Fig 4.18 shows the effect of changes in friction coefficient on the energy absorption characteristics. Changing the friction coefficient during manufacturing process has a nonlinear effect on the mean and maximum crush forces.

75
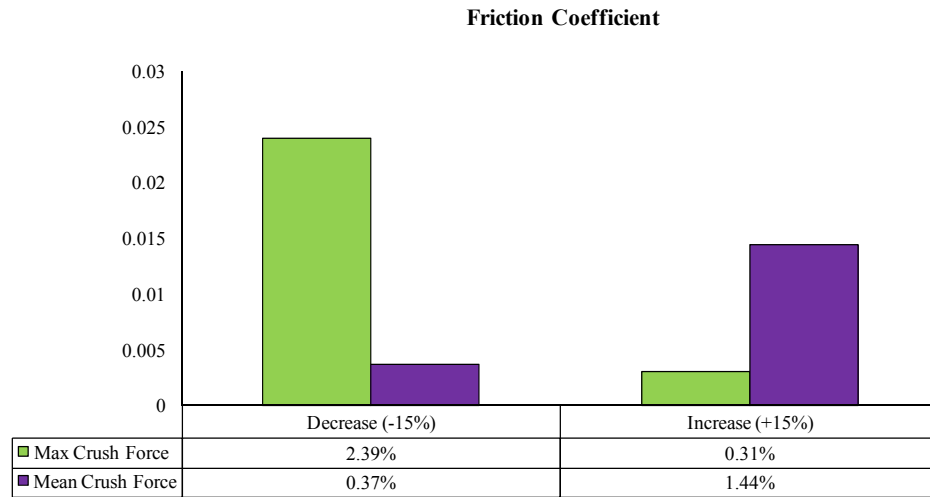
Figure 4.18   Sensitivity of responses to changes in the friction coefficient

Change in the holding force does not have a strong and reverse influence on the mean crush force mainly due to the work hardening and thinning as shown in Fig. 4.19.
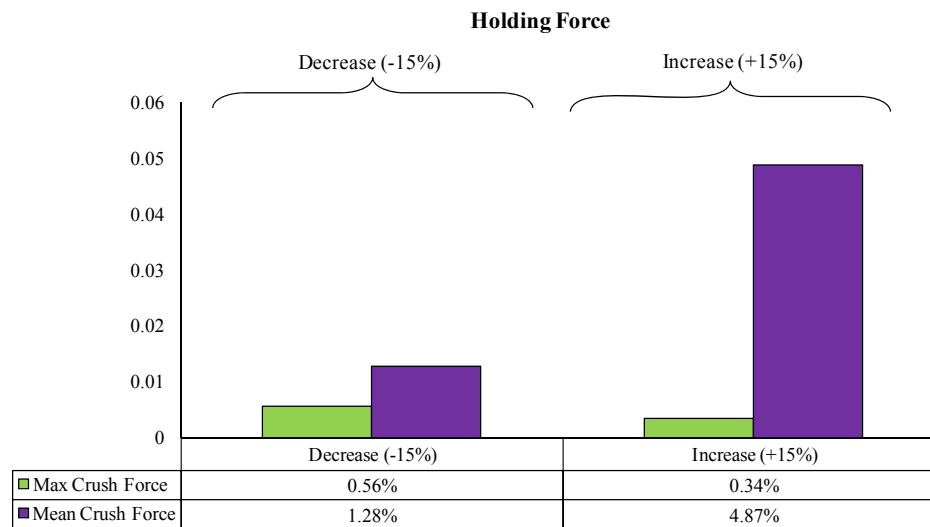
Figure 4.19   Sensitivity of responses to changes in the holding force

Punch velocity can affect the result of energy absorption because of the strain rate dependency of the material. It can be seen in Fig. 4.20 The mean crush force has a

76

inverse relationship with the change in the punch velocity whereas the maximum crush force is also increased due to the increasing in the yield point resulted from the equilibrium state of material that affected due to manufacturing process.
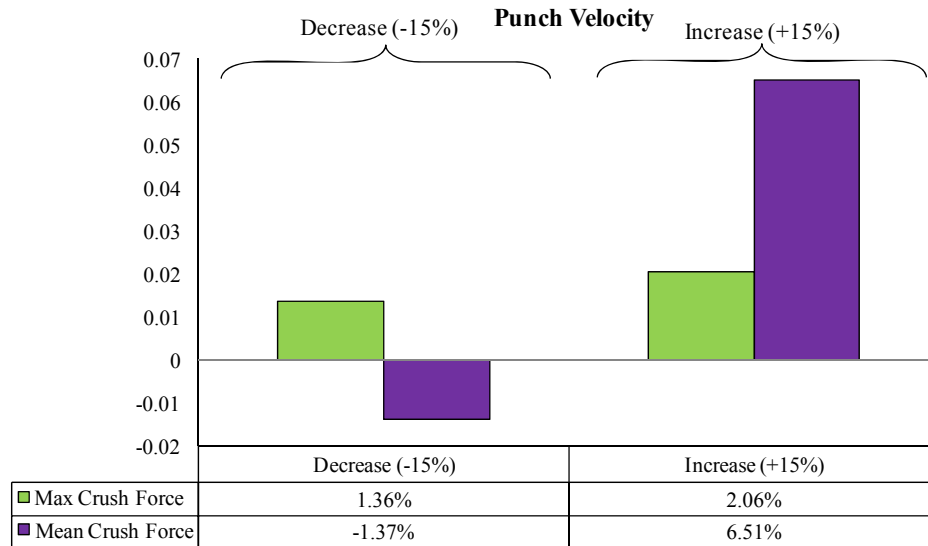
Figure 4.20   Sensitivity of responses to changes in the punch velocity

Change in the workpiece temperature influences the crush behavior considerably as illustrated in Fig. 4.21. The increase in the workpiece temperature causes 20% of increase in the maximum force .
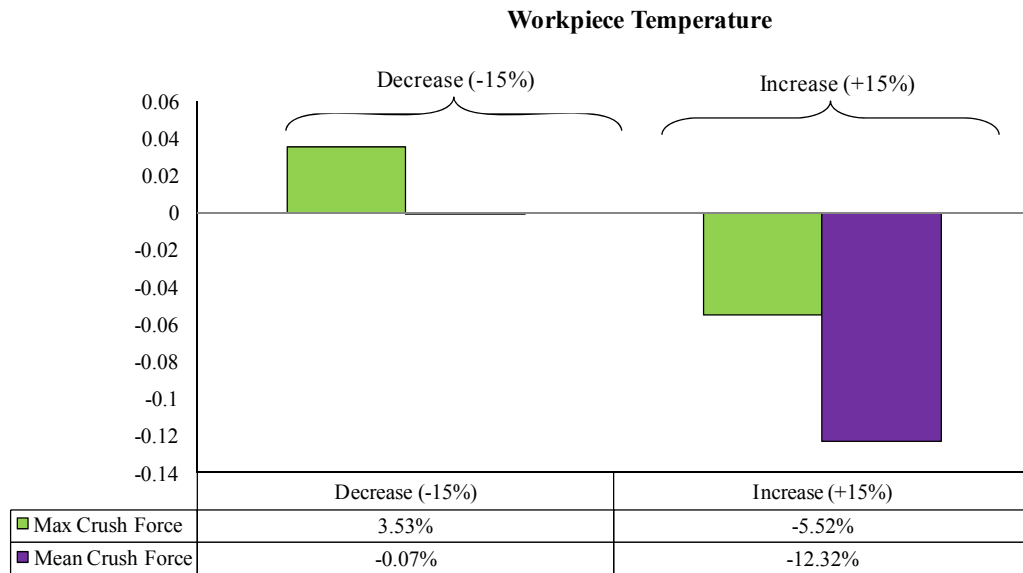
Figure 4.21   Sensitivity of responses to changes in the workpiece temperature
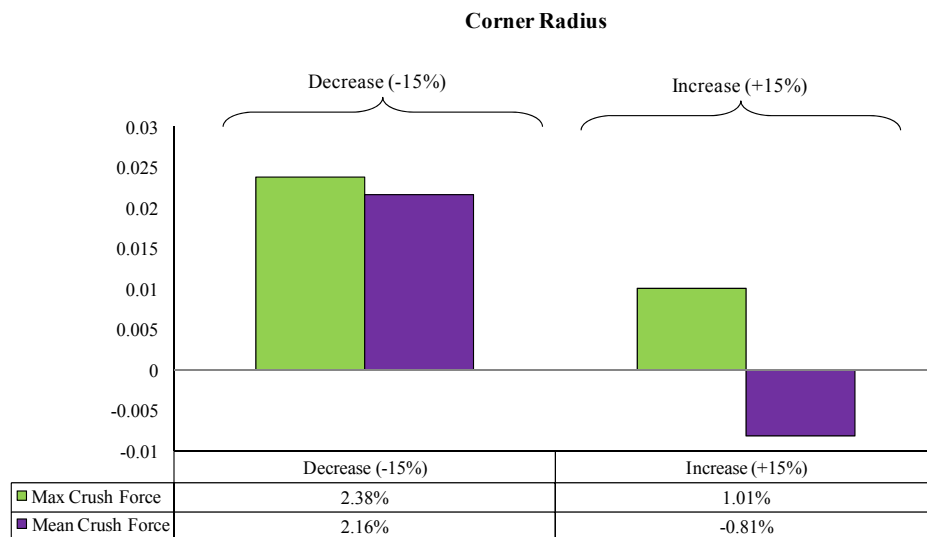
Figure 4.22   Sensitivity of responses to changes in the corner radius

The change in the geometry of the tube also affected the crush performance responses as shown in Figs. 4.22 to 4.26. The cross-sectional geometry of the tube can change by width, height, and the thickness of the tube. As the width and height of the tube change, the mean crush force is affected with the linear relationship. However, the

78

perturbation on the width has a nonlinear relationship with the maximum force. Increasing the width drops the maximum force more than decreasing it with a nonlinear response. As it is shown in figure 4.12 both mean and maximum crush forces have a direct relation with the height of the side walls. Increasing the size of the side walls not only introduces a larger cross-sectional geometry but it is affected due to the extensive plastic deformation due to the flow of material between forming tools.

	Decrease (-15%)	Increase (+15%)
Max Crush Force	-6.71%	11.71%
Mean Crush Force	-1.78%	8.65%

Figure 4.23   Sensitivity of responses to changes in width

Figure 4.24   Sensitivity of responses to changes in height

Change in the sheet thickness influence the crush results directly as depicted in Fig. 4.25. The stress distribution, plastic deformation, and flexural stiffness are highly affected by thickness resulting in a significant impact on the crushing behavior. Reducing the sheet thickness is also influenced by less plastic deformation and thinning and the material behaves more closely to the expected designs. But increasing the sheet thickness introduces more plastic deformation and work hardening as well as thinning. However, change in the plastic deformation is higher than the thinning which gives a higher contribution to the crash once it is considered with the thickness increase.

80

Sheet Thickness

	Decrease (-15%)	Increase (+15%)
☐ Max Crush Force	-8.04%	34.19%
☐ Mean Crush Force	-18.35%	26.02%
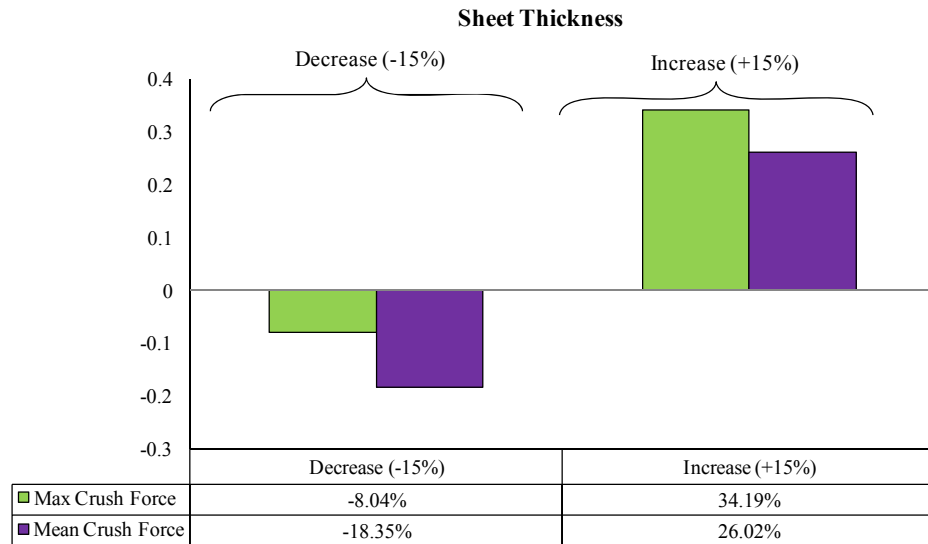
Figure 4.25   Sensitivity of responses to changes in sheet thickness

The sensitivity results are also presented differently in order to show the competition of each variable for energy absorption response in fig 4.26 and 4.27.

Both responses are shown that affected from thickness change more than the other variables which introduce the most common approach to enhance the energy absorption behavior (increasing thickness) that is always increases the mass of the component. The maximum crush force is shown to me more sensitive to punch velocity as a manufacturing process. However, the mean crush force is more influenced by the manufacturing process parameters. It is seen punch velocity and holder force are considered to be the most influential factors in the performance analysis and design.

81

	Friction Coefficient	Punch Velocity	Holding Force	Thickness	Corner Radius	Height	Width
■ Decrease (-15%)	2.39%	-0.05%	0.56%	-8.04%	2.38%	-2.50%	-6.71%
■ Increase (+15%)	0.31%	15.09%	0.34%	34.19%	1.01%	6.24%	11.71%
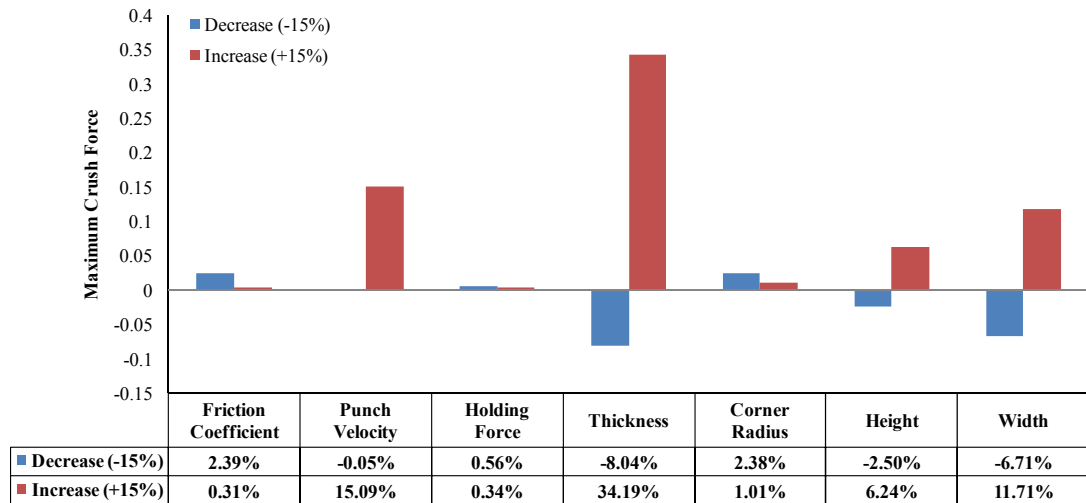
Figure 4.26   Sensitivity of maximum crush force to design variables

	Friction Coefficient	Punch Velocity	Holding Force	Thickness	Corner Radius	Height	Width
■ Decrease (-15%)	0.37%	-3.64%	1.28%	-18.35%	2.16%	-6.00%	-1.78%
■ Increase (+15%)	1.44%	4.87%	4.87%	26.02%	-0.81%	8.12%	8.65%
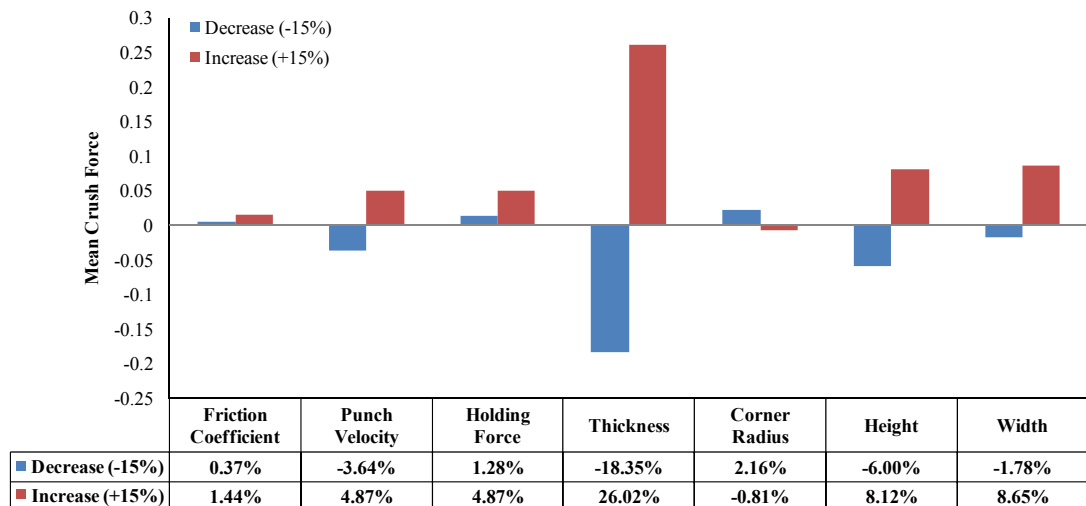
Figure 4.27   Sensitivity of mean crush force to design variables

4.3   Effect of Initial Texture on the Crushing Behavior

In thin-walled automotive structural components such as side rails, crash energy absorption is accommodated by plastic deformation which depends on both material properties and geometric configuration. Besides their ease of manufacturing through the extrusion process, prismatic tube models with different cross-sectional configurations are

82

very suitable for the study of deep plastic collapse or the general mode of deformation under axial crush load, and as such, have received considerable attention for many years.

The main energy absorption mechanism in multi-corner (e.g., square) metallic tubes is the extensive plastic deformation in localized regions as observed in both laboratory experiments and finite element (FE) simulations.

Plastic deformation occurs due to the presence of dislocations that cause slip and/or twin mechanism(s) in atomistic scale depending on the atomistic arrangement and crystalline structures (e.g., HCP, FCC and BCC) of the material. A polycrystalline material consists of a combination of single crystals known as grains oriented in specific directions. The major source of plastic deformation inside crystals is the presence and evolution of statically stored dislocations inside the grains and the geometrically necessary dislocations in the grain boundaries (Bammann 2001, Regueiro et al 2002). As the material undergoes plastic deformation, the grains rotate due to the presence of geometrically necessary dislocations. Therefore, plastic deformation is a complex multiscale phenomenon from both time and length scale standpoints (Roters et al. 2010). The main purpose of the work presented in this paper is to enhance the prediction capability of computational tools for use in both design optimization and detail analysis of metallic structures under large deformation.

Classical plasticity models are founded based on semi-empirical investigations without considering the actual physical mechanisms responsible for the material response. The main drawback of these models is that they are not physically motivated and they are constructed based on experimental observation in the experiment based on the stress-strain responses. Physically motivated internal state variable models try to incorporate the physics at lower length scales through some state variables and their

83

evolution equations. The formulations of these models are presented such that these state variables contribute to the free energy of the material within a consistent thermodynamic framework. The corresponding set of constitutive equations is typically motivated from dislocation mechanics, texture and damage evolution as well as adiabatic heating, and as such, this modeling methodology can be considered as hierarchical multi-scale models (Horstemeyer 2001). However, this modeling approach can be very challenging due to the computational complexity related to the solution of differential equations, difficulty related to bridging between different length scales within local or nonlocal continuum mechanics along with the need for the large number of experiments or subscale simulation to calibrate the model parameters and the determination of their physical bounds. Another technique which is considered as concurrent approach is to connect analysis at different length scales to continuum level using finite element analysis and solve them simultaneously. For instance, atomistic simulation or molecular dynamics is coupled to continuum model in the finite element simulation to study the crack propagation. The main challenge in this modeling strategy is to bridge different length scales by considering the actual hierarchy in the length scales. Direct coupling of continuum model FE to atomistic scale implies that two length scales of the order of 1 mm is connected to 1e-9. This requires a proper statistical methodology to account for the special treatments of the model in both length scales. One other methodology is to connect macroscale model to atomistic via multiple level of hierarchy based on the physical microstructure of material. The hierarchical structure of dislocation plasticity entails five levels related to length scales including macro-scale plasticity in 1e-2m, polycrystal plasticity in 1e-4m, dislocation pattern in 1e-6m, discrete dislocations in 1e-7m and atomistic scale in 1e-9m. The present study can be considered as a concurrent

84

multi-scale simulation which tries to use the meso-scale information to continuum level (macro-scale to polycrystalline plasticity). Therefore, the effect of lower length scales (dislocation patterns, discrete dislocation and atomistic level) is not modeled and its effects are modeled presented through a phenomenological model. Hence, the level of detail in the phenomenological model determines the physical information from lower length scale. The main contribution of this type of simulation is that an explicit representation of microstructure can be captured and during the plastic deformation. Moreover, the present concurrent multi-scale simulation can help to pass the microstructure generated from different load path in the manufacturing process and consider them as a history variable to initialize the simulation in the performance analysis.

Recently, consideration of history effects and microstructural influences on the response of structural components has become an active research area. Dipaolo et al. (2004, 2006) conducted a series of controlled experiments focused on the symmetric quasi-static axial crush response of welded stainless steel square tubes. They first investigated different control methods in the form of tube end constraints and collapse initiators (triggers) to control the so-called configuration response (combination of collapse geometry and the shape of the load-displacement curve). This was then followed by the examination of the effects of alloy composition and microstructure on the configuration response. Their results showed that the combination of greater carbon content and smaller grain size enhanced both the peak crush load as well as energy absorption for the secondary fold formation. Study on the microstructural evolution during crush response and its effect on the energy absorption has not been under attention previously. On the other hand, experimental evidence to verify and confirm the

85

importance of them is also short. The impact energy of metallic crush tubes is dissipated through plastic deformation deals with microstructural effects including evolution of dislocation density and resulting slip and twin between atoms in dislocation pattern level and atomistic level and the evolution of orientation at the meso-scale level. In the meantime, the damage can be instigated and propagated in different length scales as another mechanism of energy dissipation. It has been observed that energy mechanism in multi-corner tubes can be represented through some basic localized regions (Najafi & Rais-Rohani, 2008, 2011). It has been shown that the localized zones dissipate the plastic energy through basic deformation mechanisms seen in single-cell square cross-sections through extensional, quasi-inextentional, and loading-unloading deformations (Wierzbicki & Abramowicz 1983, 1989, Najafi 2009).

Most of the researches used plastic strain as a representation of material state to somehow consider the microstructural changes due to the manufacturing processes (Najafi & Rais-Rohani 2011). There have been some attempts to incorporate more realistic history effects using internal state variable constitutive models (Najafi et al. 2011). Incorporation of anisotropic texture in the continuum level models is a very challenging problem such that in most of continuum level material models this effect is neglected. Among others, the most traditional approach to model texture-induced anisotropy is to incorporate a distorted yield surface (Barlat et al 1993, 1994) in the material model. This approach basically considers a distorted convex shape for the yield surface but neglects the evolution of the yield surface during plastic deformation. Popov and Ortiz introduce the distorted yield surface considering an evolution equation based on some statistical information (Ortiz & Popov 1983). Defalias (2000,2001) and Regueiro et al. (2001) also considered a structure tensor and its evolution to capture the anisotropic

86

plasticity. The main drawback of aforementioned methodology is complexity of implementation, preserving the convexity of the yield surface and large amount of experimental data to calibrate models. Another approach is to use a lower-length scale models and bridge the lower-scale to a macro-scale model. In this model a material point at the continuum level is linked to a lower length scale model. In metallic materials, we consider the grain orientation and textures at the mesoscale using crystal plasticity models (Marin 2006). In modern practice of simulating problems experiencing plastic deformation, crystal plasticity models can properly capture the anisotropic behavior. This approach has been used to evaluate a number of problems such as forming, extrusion, spring back as well as deriving forming limit diagrams (Xie C. L., Nakamachi 2002, Raabe & Roter, 2004, Raabe et al 2002, 2005, Chen et al. 2007, Beaudoin et al 1993, 1994, Horstemeyer et al. 2005).

In this study, a material subroutine containing a crystal plasticity formulation at the meso-scale level is used to simulate the macro-scale crush response. The model accounts for crystal orientations and their effect on the flow rule, stress-strain response during loading, unloading, yielding and hardening behavior (Marin 2006). Crush tubes experience excessive distortions in the localized regions due to collapse loads. In this study, the conceptual influence of anisotropic texture on the crush behavior of prismatic tubes is taken into consideration. Four basic texture architectures are considered as initial texture for the aluminum tubes. It is assumed that the entire structure has the same texture architecture.

4.3.1 Basic Folding Elements and Localized Regions in the crush tubes

Since the collapse behavior under axial crush loads is heavily influenced by the deformation of corner regions, the collapse response of simple square tubes is used as reference. In general, the folding mechanism in a two-flange corner region involves extensional, quasi-extensional and quasi-inextensional modes of deformation (Wierzbicki & Abramowicz 1983, 1989). Using the description presented by Abramowicz (2003), the folding deformation can be expressed in terms of asymmetric and symmetric corner elements as shown in Fig. 4.28a and 4.28b respectively. The localized regions observed in these two mode shapes can be considered as a general deformation mechanism in any multi-corner cross sectional geometry. We performed a series of FE simulations to model the crush response of square tube models, and found the crush mode to be highly dependent on the trigger mechanism and the loading rate. By adjusting the location of the indentation trigger mechanism under quasi-static loading we were able to find both the symmetric and asymmetric corner element deformations as shown in Figure 4.28.
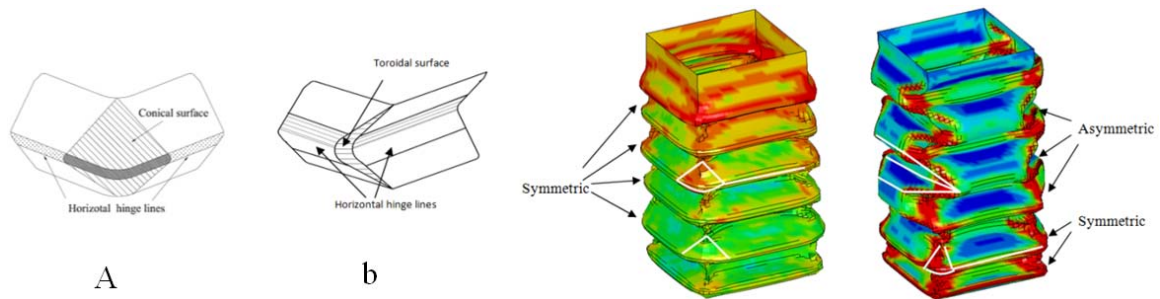
Figure 4.28   Basic folding mechanisms in multicorner tubes represented by a) pure symmetric corner deformation, b) pure asymmetric corner deformation, and c,d) combination of symmetric and asymmetric corner deformation resulting in symmetric axial collapse

As noted in Wierzbicki and Abramowicz (1989) and Abramowicz and Jones (1984), the symmetric collapse mode involving symmetric and asymmetric elements

88

includes a cylindrical surface created from the horizontal hinge lines caused by inextensional deformation, inclined hinge lines forming inextensional deformation through the conical surface, and a toroidal surface that has quasi-inextensional deformation. In the toroidal surface, two bending deformations are present (Najafi 2009). The double bending action is due to the cylindrical surface formed through the formation of inclined hinges combined with a global bending due to cylindrical formation of horizontal hinge lines. A toroidal surface is formed because of the subsequent bending on the cylindrical surface.

The symmetric extensional collapse mode involving only symmetric elements includes horizontal and inclined hinge lines along with a conical surface that has extensional deformation. Whereas in symmetric quasi-inextensional collapse mode involving only asymmetric element the major part of energy is dissipated through quasi-inextensional deformation of the toroidal surface, in the symmetric elements or extensional deformation, energy dissipation is mainly due to the extensional deformation of the conical surface.

In order to show the material behavior in the localized region, the stress-strain history of the elements located in these regions is reported in this section. For this study, two squared section tubes with 80mm edges and the length of 400mm is axially crushed between a moving flat rigid wall and fixed boundary in two ends in LS-DYNA using Belytchko-Tsai shell element and penalty contact formulation for both wall tube and self contact interactions [DYNA MANUAL]. Fig 4.29 shows the stress-strain response of a representative element in a horizontal hinge-line region. The normal stress in YY direction is plotted versus normal strain in element coordinate system. Both stress and strain are calculated in the upper surface of the shell element containing three integration

points through the shell thickness. As expected, the largest stress occurs in YY direction that is perpendicular to the horizontal hinge line. Since the values are calculated in the upper surface, the stress is mainly tensile. Similar compressive behavior can be captured by calculating the stress and strain on the lower surface. Fig 4.30 shows the stress-strain variations on the lower surface of the toroidal surface. The stress in this region is compressive. Figure 4 shows the stress and strain response of an element which is located in the "moving" inclined hinge line. The material experiences both loading and unloading in different regions. Because of this property, the material with the Baushinger (Wierzbicki & Schneider 1999) effect should be modeled using a model that has kinematic hardening or anisotropic texture behavior.
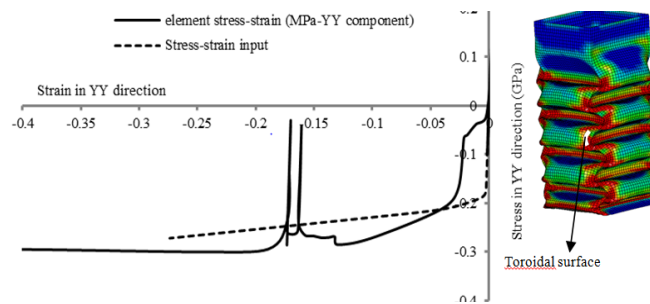
Figure 4.29   Stress-strain response of an element of the toroidal surface (Najafi 2009)
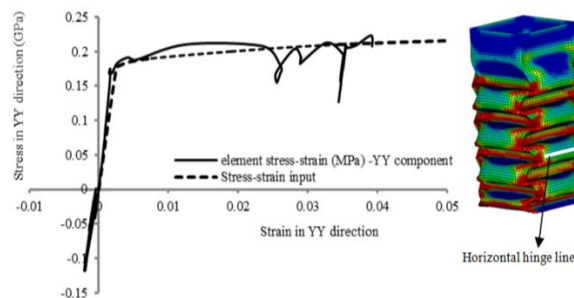
Figure 4.30   Stress-strain response of an element of the horizontal hinge line (Najafi 2009)

90
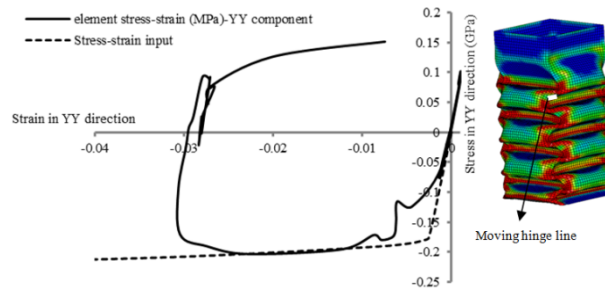
Figure 4.31   Stress-strain response of an element of the moving hinge line (Najafi 2009)

The simulations indicate that the material experiences different loading and unloading conditions during crush process which can be affected by material and microstructural behavior. Usually the material models are only calibrated based on tensile and compressive behavior in coupon level. The change in the stress-strain response affects the energy absorption prediction of the tube which is one of the typical consequences of the presence of anisotropic texture in the material. Anisotropic texture is usually detected in thin-walled structures manufactured by any kind of forming process (e.g., extrusion, stamping) due to large strains experienced during the manufacturing processes. The ability to model the anisotropic texture and damage can improve and expand the computational simulation capability to explore the energy absorbing capacity of crush tube designs. In this study, texture-induced anisotropy will be introduced in simulations through a crystal plasticity constitutive model in FE.

4.3.2   FE Modeling

Axial crushing simulation of tubes is usually done using explicit FE solvers (Najafi & Rais-Rohani 2011). It has been shown that explicit solvers are more capable of producing converged solutions than implicit solvers for highly nonlinear problems such as axial crush. In this study, the VUMAT developed by Marin (2006) is integrated within ABAQUS/EXPLICIT solver (ABAQUS manual 2010, LS-Dyna manual 2009) to

www.manaraa.com

perform crush analysis. In order to study the effect of anisotropic texture, some basic load paths are considered to generate the initial texture required for crush simulations. The three simple loading paths include uniaxial tension and compression, and simple shear. The load path calculations are performed with ABAQUS/Standard using UMAT version of the crystal plasticity model. A random crystal orientation data for the aggregate of crystals is used as an input for the material subroutine as shown in figure 4.32.
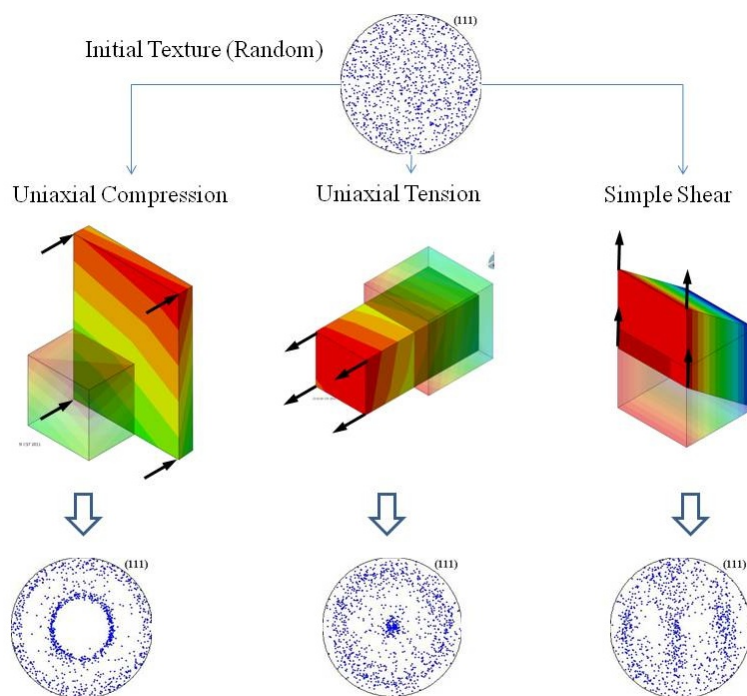
Figure 4.32 <111> pole figure of initially random distribution of 1024 crystal orientation and the resulting texture due to different load paths

The orientations data is evolving during the loading process and results in the new arrangement of grain orientation in the aggregate. Figure 4.32 shows the resulting orientation distribution of the aggregate due to 75% of uniaxial tension, compression, and simple shear. The material constants used for anisotropic elasticity, power-law kinetics, and the hardening law presented by Marin (2006) correspond to those of FCC

92

polycrystalline aluminum alloy presented in Table 4.3. The FCC crystals in the aggregate deform by crystallographic slip on well-defined {111} (111) slip systems. The total number of state variables at each integration point is the sum of stress and strain components, number of slip systems, number of kinematic hardening, number of state variables of constitutive relation, and number of shear strain rates. For an FCC crystal, there are seventy state variables at each crystal integration point. The limit on the number of dependent state variables in ABAQUS/EXPLICIT is 10000 variables. Since implicit solvers do not have such limitation, we performed the basic load path simulations using ABAQUS/Standard. Thus, we considered an FCC material aggregate containing 500 grains representing the random texture (Fig. 4.32). Because crush simulation is performed in ABAQUS/EXPLICIT, we must reduce the number of grains to allow the crystal evolution information during each time step calculation. Considering that 500 grains requires a memory allocation for 500×70 state variables, which is well beyond the limitation of the FE solvers, we reduced the number of orientation data to 40. Based on the original texture pattern, we tried to keep the patterns the same while reducing the number of orientation data. Figure 4.33 shows the pole figures for the actual and reduced data.

93

Table 4.3   Material parameters for Al7050

C_{11}	108.2 GPa
C_{12}	61.3 GPa
C_{44}	28.5 GPa
M	0.02
γ_0	1.0 s^{-1}
h_0	240.0 MPa
$\kappa_{s,0}$	205.0 MPa
$\kappa_{s,S0}$	290.0 MPa
m^1	0.0
γ_{s0}	5×10^{10} s^{-1}
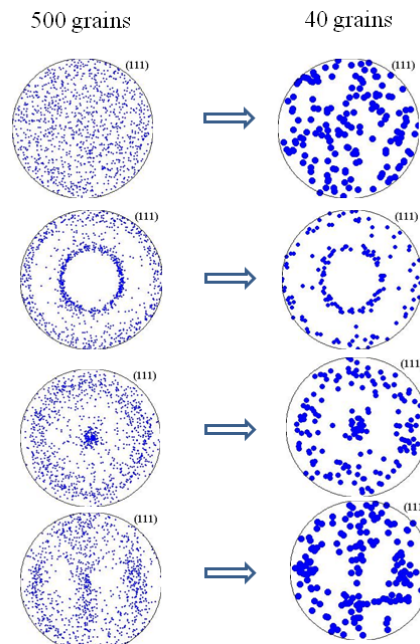
Figure 4.33   <111> pole figures of 500 crystal orientations and the reduced pole figure
information

The square tube model in figure 4.34 has a length of 80 mm and a side dimension
of 40mm. The short length is chosen to focus on the formation of a single fold. The tube
response falls into two basic folding mechanisms described in Fig.4.32. Studying these
two collapse mechanisms helps to understand the energy absorption mechanism in wide
range of multicell multicorner tubes (Najafi&Rais-Rohani 2011). The other basic folding

94

mechanism which is usually seen in experiments is captured by introducing an asymmetric trigger mechanism in two opposite walls. As shown in Fig.4.34, 4140 solid (C3D8R) elements are used for the present simulation with three elements through the wall thickness. C3D8R is a reduced integration element with viscous enhanced hourglass formulation. The contact friction coefficient between the rigid walls and tube is set at 0.1 to prevent slippage between surfaces based on the penalty formulation defined between a discrete rigid wall and deformable tube. To prevent element-element inter-penetration due to excessive deformation, a self-contact condition is defined for all the element surfaces of the tube with the same friction property. In order to increase the computational efficiency a mass scaling of 10 is used for the deformable elements. As shown in figure 4.35, the tube is located between two discrete rigid surfaces, with one wall is fixed and the other wall moves with the same displacement increment throughout the simulation (constant velocity=10 m/s).
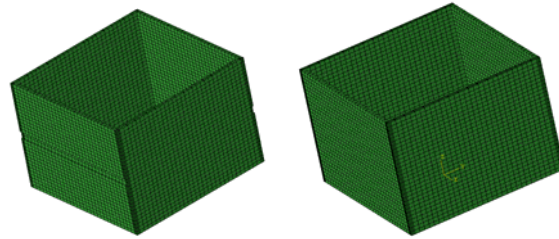
Figure 4.34   FE models with solid elements to capture asymmetric (Model A) and symmetric (Model B) corner elements.

95
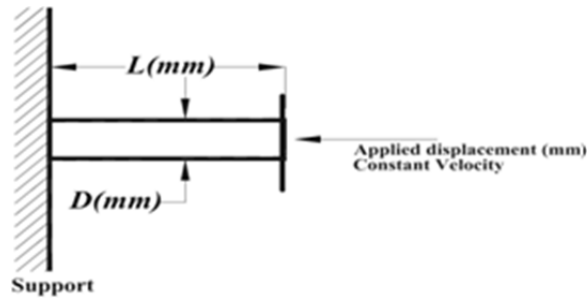
Figure 4.35   Quasi-Static loading of short tubes.

4.3.3   Results

The collapse modes of imposed by trigger mechanisms in the tube models for random texture are shown in Figure.4.36. Because there is no geometric trigger is used the deformation mode is symmetric in the corners which involves major localized regions including conical surfaces and horizontal hinge lines.
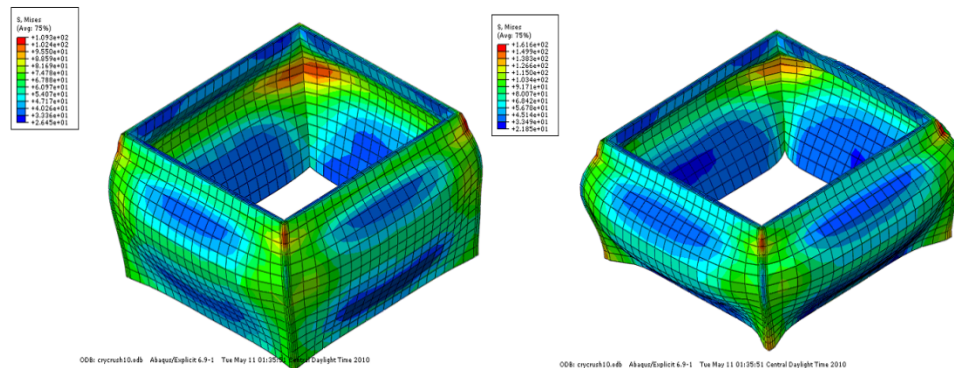
Figure 4.36   deformation process of Model (B) under quasi-static loading

For the sake of comparison the crush mode shape of the tube having this deformation mode at similar displacements are compared in figure 4.37. It is illustrated that the difference in the textural arrangement does not affect the results the deformation mode considerably since in the thin walled structure the main driver for deformation is highly depends on the boundary conditions and the overall geometry rather than material

96

behavior. However, it is shown that the texture resulted from uniaxial compression is stiffer that the other cases by looking at the folding patterns especially in Δ=28.5 mm whereas, the folding deformation is more for random and uniaxial tensile textures. Von-misses stress is also shown in the contours with the same scale that shows despite of the close similarity between deformation modes, the stress distributions in each case is different.

Uniaxial Compression

Δ=2.5 mm Δ=8.5 mm Δ=17.0 mm Δ=28.5 mm Δ=42.5 mm

Random

Δ=2.5 mm Δ=8.5 mm Δ=17.0 mm Δ=28.5 mm Δ=42.5 mm

Simple Shear

Δ=2.5 mm Δ=8.5 mm Δ=17.0 mm Δ=28.5 mm Δ=42.5 mm

Uniaxial Tension

Δ=2.5 mm Δ=8.5 mm Δ=17.0 mm Δ=28.5 mm Δ=42.5 mm
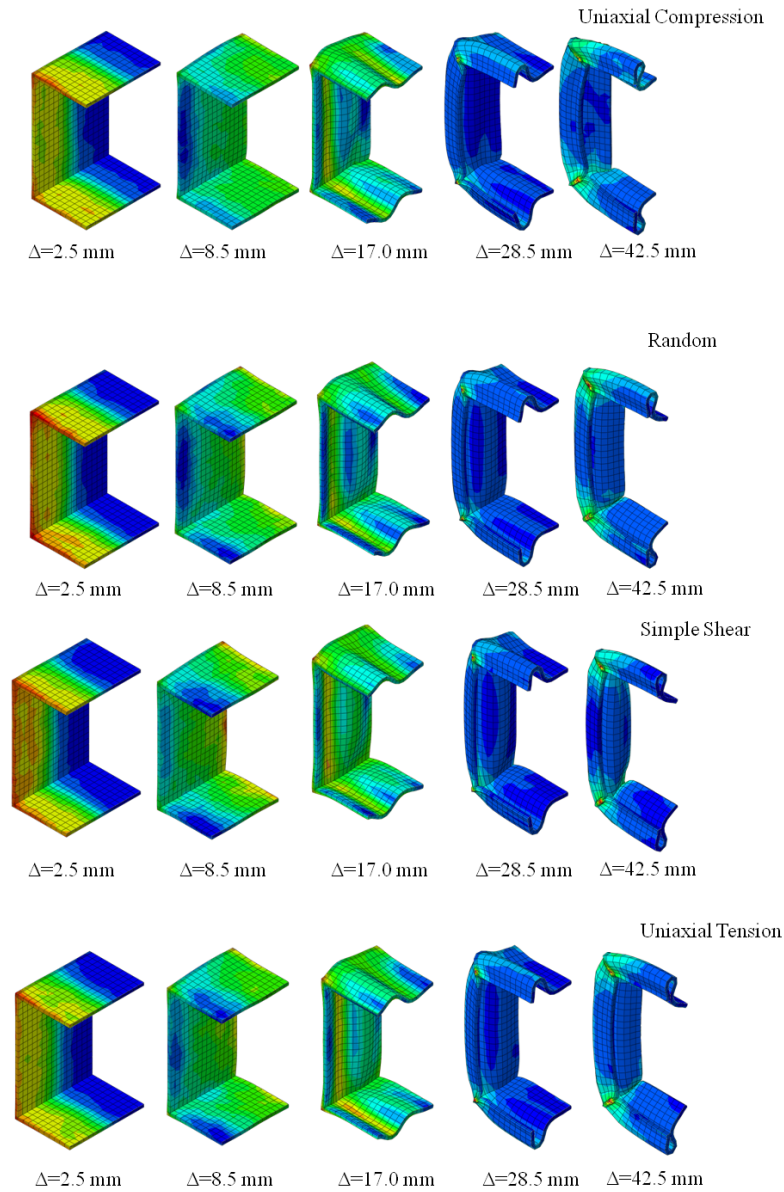
Figure 4.37   Comparison of crush mode in square tubes with different initial textures

As mentioned in figure 4.37, four initial textures are considered in this study. It is assumed that the entire structure has the same orientation distribution. The energy absorption behavior in terms of crush load versus crush distance is illustrated in figure 4.38. The crush performance can be studied in terms of the overall load-displacement behavior including the peak loads and mean crush force. It has been shown that the

98

texture helps to increase the energy absorption once compared with the random texture and texture due to simple shear. However, the peak crush force in random texture is lower than the other cases. The energy absorption behavior of simple shear case has the lowest value till the second peak but after this point the random texture is seen to have the lowest force. The uniaxial compression shows better performance in overall energy absorption behavior compared with uniaxial tension. In order to track the evolution of crystallographic orientation in the localized regions, multiple points is selected in the top and bottom of the conical surface and horizontal hinge lines. Figure 4.39 illustrates the evolution of texture with the axial deformation in the localized regions shown in this picture. It is seen that the texture evolves to create a new orientation pattern in the internal face of the tube for both conical surfaces and horizontal hinge lines. The first column is also shown that the orientation pattern becomes different at the early stage of loading. The last row shows the evolution of orientation in the sharp corner. The orientation is not evolving in this region considerably compare to the other cases. It is also seen that the crystallographic orientation is evolving more in the internal faces of the tube than the external faces.
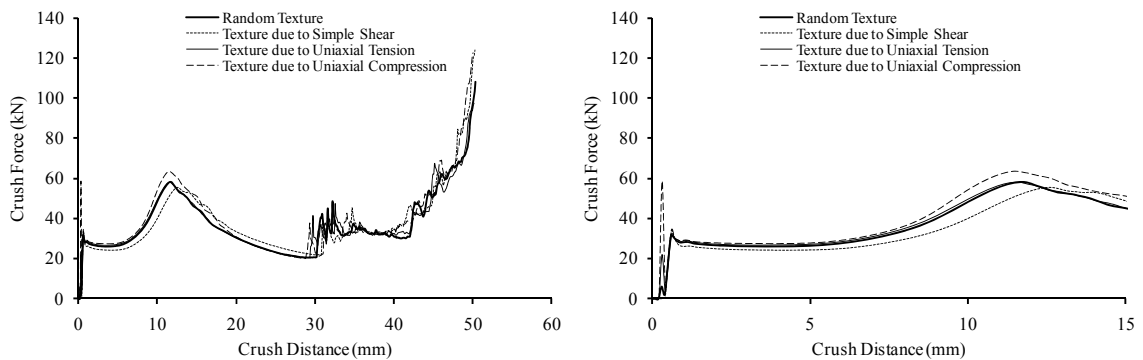
Figure 4.38   Comparison of energy absorption behavior resulted from different textures

99

Figure 4.40 depicts the evolution of crystallographic texture for the tube with uniaxial compression texture. It is seen that the overall orientation of the material changes with the axial displacement but the overall circular pattern does not change. It is also seen that the overall pattern of crystallographic orientation evolves but it comes back close to the original orientation in the second row which shows the evolution in the internal face of the tube. However, in these pole figures we do not track each material filament orientation one by one to see how the orientation evolves.

The evolution of the crystallographic texture for the tube that has a texture due to simple shear is presented in figure 4.41. It is seen that the orientations in the inner face of the tube (first row) in the corner is concentrated as the deformation is imposed to result in the folding deformation. It is also seen that the orientation close to the circular boundary is amalgamated in the central areas.
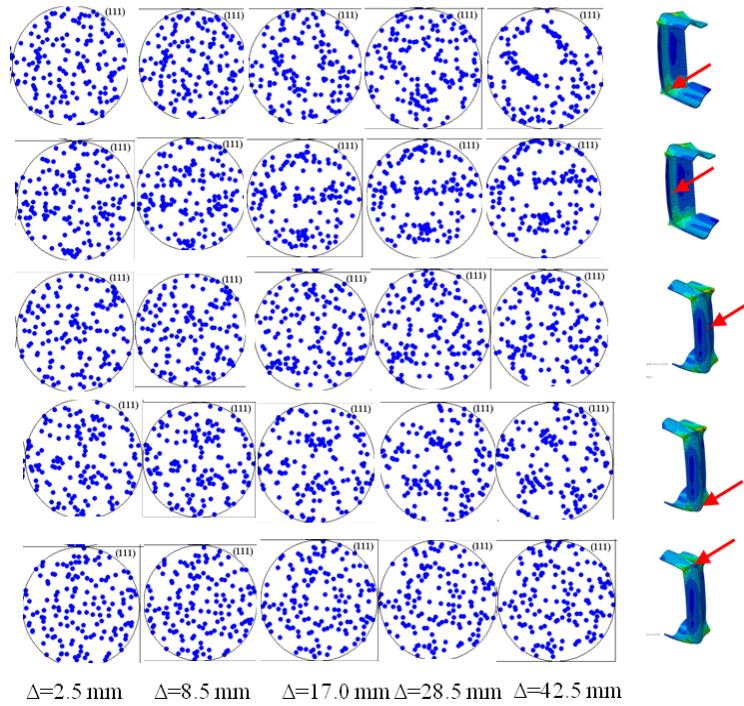
Figure 4.39   Evolution of crystallographic orientation in the localized regions for the tube with initial random texture
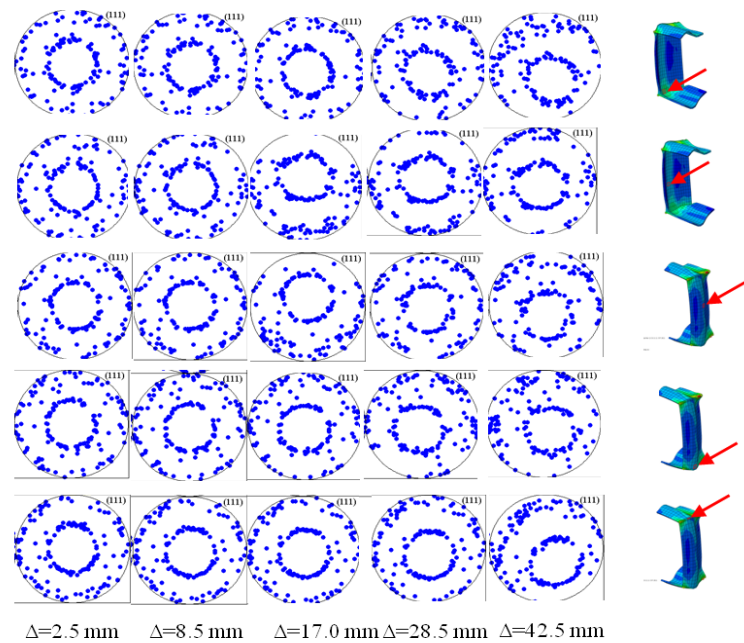
Figure 4.40   Evolution of crystallographic orientation in the localized regions for the tube with initial texture resulted from uniaxial compression

101
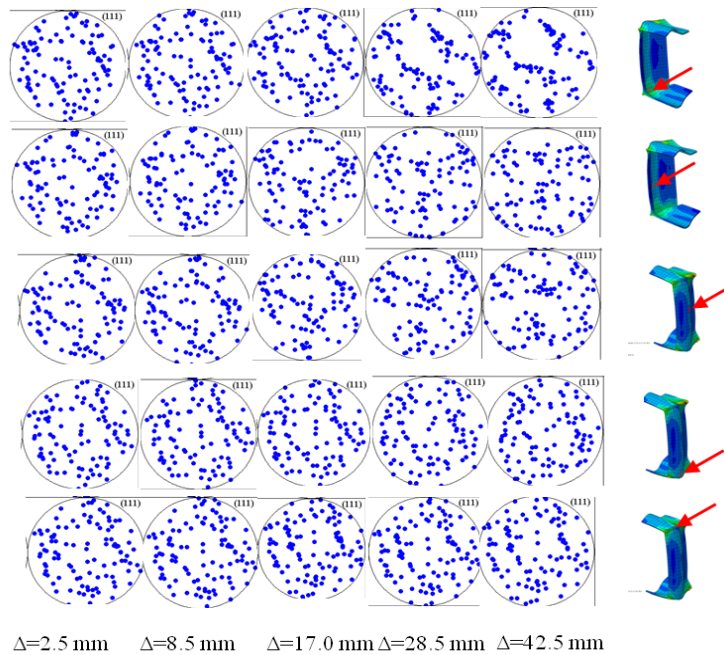
Figure 4.41   Evolution of crystallographic orientation represented in pole figures in the localized regions for the tube with initial texture resulted from simple shear

Finally, The result of orientation evolutions for the tube with initial texture resulted from uniaxial tensile is presented in figure 4.42. It is seen that in most of the localized regions the concentrated orientation scatters and form a random orientation in the localized regions. At the end, it is worth noting that the present simulation is performed with 40 grains representing a 1000 crystal aggregates. Therefore, this assumption should be considered for any generalization. Although the energy absorption behavior may be represented very closely in these cases that we considered here, present study shows that the plastic deformation is utilized based on different mechanisms of plastic deformation.

102

Δ=2.5 mm   Δ=8.5 mm   Δ=17.0 mm Δ=28.5 mm Δ=42.5 mm
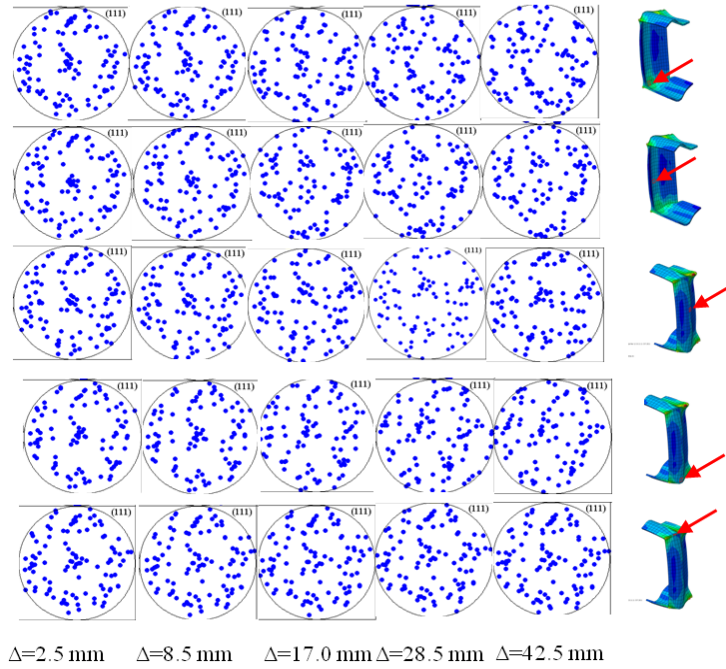
Figure 4.42   Evolution of crystallographic orientation represented in pole figures in the localized regions for the tube with initial texture resulted from uniaxial tension

103

CHAPTER V

DESIGN OPTIMIZATION

In order to concurrently optimize the process and performance responses by considering their interaction, the optimization problem can be written in different forms. The optimization can be performed by integrating all the responses into one level problem as objective functions or constraints. This approach is called all-at-once optimization which both manufacturing and performance attributes are treated in the same level. The sequential nature of the problem retained as the manufacturing effects are transferred to energy absorption simulation as shown in figure 5.1. In this approach the performance attributes are captured once manufacturing effects are transferred into performance simulation.
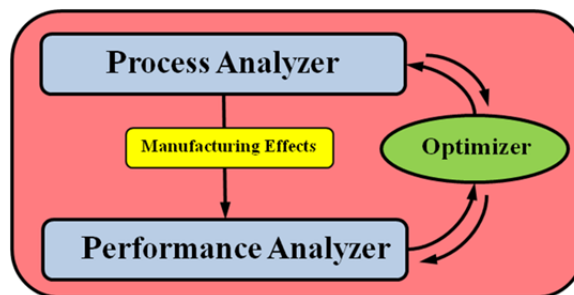
Figure 5.1   All-at-once optimization of coupled sequential process-performance
                simulation

However, this problem can be solved by decomposing problem into multiple levels as illustrated in figure 5.2. In this approach, manufacturing analyzer and performance analyzer are connected to a separate optimizer. Therefore, two separate

104

optimization formulations are developed for the crush and forming problems. The relation between the two levels is achieved through manufacturing effects. In order to find the optimal point for the whole system, optimization for each subsystem is performed until convergence achieved showing a balance between the top level and bottom level.
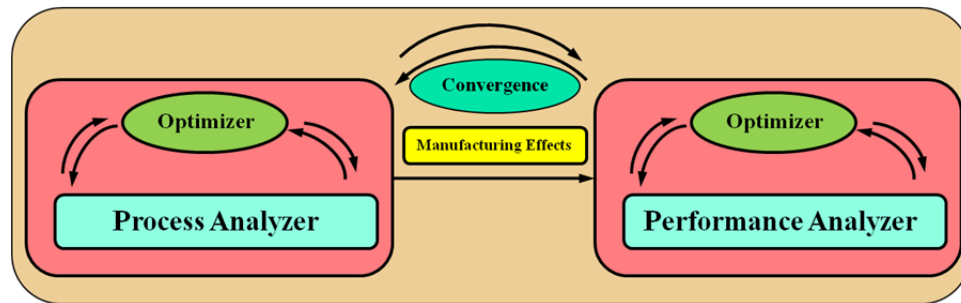
Figure 5.2   Multi-level decomposition and optimization process of coupled sequential process-performance simulation

5.1   All at Once

In the optimization problem, it is assumed that the design vector X can evaluate the objective and constraint functions based on appropriate analysis tools. For instance, in order to enhance the energy absorption component in the automotive structures, weight can be considered as the objective function subjected to some constraint such as head injury criteria, acceleration or intrusion distance. Therefore, in general the optimization process attempts to minimize (or maximize) the objective function denoted as f(x) subject to some equality h(x) or inequality g(x) constraints. In general the canonical form of the optimization problem is expressed in equation (5.1).

$$\begin{aligned} \min_{\mathbf{X}} \quad & f(\mathbf{X}) \\ \text{subject to} \quad & g(\mathbf{X}) \leq 0 \\ & h(\mathbf{X}) = 0 \end{aligned} \qquad (5.1)$$

www.manaraa.com

The solution to this problem known as the optimum design is X^*. As it has shown in figure 5.1, the responses of process and performance levels are integrated in objective functions and constraints. If there is more than one response is considered as objective, a composite function representing a combination of multiple objectives is required for single objective methodology. There exist many different approached to solve this problem addressed in the literature including Sequential Quadratic Programming (SQP), Generalized Reduced Gradient (GRG) as well as heuristic algorithms such as Simulated Annealing (SA), evolutionary Genetic Algorithm (GA), and Particle Swarm Optimization (PSO), and In all-at-once (AAO) optimization strategy. In this present formulation, a single objective is considered with some constraints that forms a formulation for the all-at-once (AAO) optimization.

5.1.1   Multi-attribute optimization

In many decision-making problems, we seek to enhance more than one objective or attribute. For example, in a coupled process-performance optimization problem, both manufacturing- and performance-level objectives need to be considered for the optimization. Hence, the objective function may be formulated to find a compromise between different objectives as they are usually conflicting. Dealing with more than one objective introduces a vectored value objective function. To find the minimum or maximum value of the objective function, a transformation scheme is required to map the vectored value vectors to a scalar measure of all the vector elements of the objective function known as master function. One common approximation to this problem is to combine the vectors through a linear combination. Provided the objective functions are normalized value a weighted some of the objective function vectors can also be used.

106

Other methodology is to deal with the multi-objective problem is to treat one of the vector elements as the problem objective function and the rest are treated as constraints. In both of these methodologies the weights or bounds should be changed to explore the possible design. The outcome of the present optimization formulation is resulted into a Pareto optimum set or Pareto frontier. Pareto frontier represents the non-dominant point which means that a set of points that cannot minimize all the members of the objective function vectors.

5.2   Multi level optimization

Design of complex systems poses many challenges in the analysis and optimization of new products. The complexity of a system stems from the large number of design variables and nonlinear responses that often require high fidelity simulations. Many complex engineering systems are more readily optimized when they are decomposed into two or more subsystems with partitioned design variables and separate objective functions and design constraints. This approach has several advantages such as reducing the problem size in each subproblem thereby simplifying the validation of models and results; it allows parallelization of the optimization process and utilization of different optimization formulations and solution techniques for each subproblem based on the nature of the problem (Krishnamachari 1996).

In the field of structural optimization, early works in multilevel decomposition and optimization of hierarchical systems can be traced to those of Kirsch *et al.* (1972) and Sobieszczanski-Sobieski (1974). Kirsch (1975) used model coordination and goal coordination methods to formulate a general multilevel decomposition whereas Sobieszczanski-Sobieski (1982) developed multilevel optimization by linear

decomposition (MOLD) with applications to two- and three-level systems (Sobieszczanski-Sobieski *et al*. 1985; 1987). Haftka (1984), Thareja and Haftka (1986), and Renaud and Gabriele (1989) explored various options to offset the numerical difficulties occasionally encountered in MOLD. As an alternative to MOLD, Vanderplaats *et al*. (1990) developed a reformulated decomposition method by including all variables and constraints at the system level and using a sequential linearization method.

More modern approaches include analytical target cascading (ATC) methodology, first introduced by Kim (2001) in its complete form for solution of optimization problems that can be decomposed into hierarchical multilevel systems. A coordination strategy is used to ensure that the separately optimized subsystems satisfy the optimality conditions at the system level (Michelena *et al.* 2003). The efficiency of ATC depends on the availability of computationally inexpensive models for system and subsystem analyses (Michelena *et al*. 1999; Kim *et al.* 2003). Therefore, high fidelity and computationally expensive models need to be replaced by low-fidelity surrogate models (metamodels). The main feature of ATC is that the target responses defined at the system level are cascaded down to subsystem level elements while the element responses are transferred up in a manner that the deviation values approach zero as the solution reaches convergence. The ATC formulation has been applied to several complex problems including ground vehicle chassis design (Kim et al 2003), aircraft design (Allison et al 2006), product development in automotive application (Kokkolaras et al 2002), product families (Kokkolaras et al 2005) and railway traction system (Moussouni et al 2008). Different coordination strategies and problem formulations have also been proposed in

108

order to facilitate the solution process (Michelena et al 1999, Tosseram et al 2006, Han & Papalambros 2010).

5.2.1   Analytical Target Cascading in Hierarchical Systems

Analytical Target Cascading (ATC) methodology (Michelena *et al*. 1999; Kim *et al.* 2003) offers an effective approach for sequential optimization of hierarchical multilevel systems. Each subsystem level in this formulation can have one or more elements. Elements at the same level may be interdependent through some shared variables defined as *linking variables*. The main premise of ATC is the use of level-by-level cascading whereby the upper-level design *targets* from a parent element are propagated down to the connecting lower-level elements or children while outputs (*capabilities*) of individual child elements are transferred upward as inputs to the higher-level element (parent). A coordination strategy is used to ensure that the separately optimized subsystems satisfy the optimality conditions at the system level. The ATC solution follows an iterative process until the selected tolerance for the difference between the capabilities and targets is achieved.

The all-at-once (AAO) formulation for a target optimization problem can be represented as

$$\begin{cases} \min_{x} & \|R(x) - T\|_2^2 \\ subject\ to & g(x) \leq 0 \\ & h(x) = 0 \\ & x_L \leq x \leq x_U \end{cases} \tag{5.2}$$

where the objective function to be minimized is represented by L2 norm squared of the deviation between the response vector *R* and the desired targets denoted by vector *T*. The feasible design space is defined by the inequality design constraints *g(x)* and equality

109

design constraints *h(x)* as well as the lower and upper bounds on the vector of design variables *x* denoted by x_L and x_U, respectively.

Applying the basic ATC formulation (Kim et al 2003) to decompose the AAO problem in Eq. (5.2) to two levels with one element each, leads to a system level optimization problem in the form

$$\begin{cases} \begin{aligned} &\min_{x^u \ = \ \{x_u^u, R_{li}^u, \varepsilon_{Ri}\}} && \|R_u^u(x_u^u) - T\|_2^2 + \sum_{i=1}^n \varepsilon_{Ri} \\ &\quad subject\ to && g(x_u^u) \le 0 \\ &&& h(x_u^u) = 0 \\ &&& \|R_{li}^u - R_{li}^l\| \le \varepsilon_{Ri} \\ &&& \vdots \\ &&& x_L^u \le x^u \le x_U^u \\ &&& where\ i = 1, \cdots, n \end{aligned} \end{cases} \tag{5.3}$$

and the subsystem level optimization problem in the form

$$\begin{cases} \begin{aligned} &\min_{x^l \ = \ \{x_i^l, y_{lj}^u\}} \|R_i^l(x_i^l) - T_i^l\|_2^2 + \sum_{i=1}^n \|R_{li}^l(x_i^l) - R_{li}^u\|_2^2 + \sum_{j=1}^m \|y_{lj}^l - y_{lj}^u\|_2^2 \\ &\quad subject\ to\ \ g_j(x_i^l) \le 0 \\ &\qquad\qquad\qquad h_j(x_i^l) = 0 \\ &\qquad\qquad x_L^l \le x^l \le x_U^l \\ &\qquad\qquad where\ i = 1, \cdots, n\ \ and\ \ j = 1, \cdots, m \end{aligned} \end{cases} \tag{5.4}$$

The aim in Eq. (5.3) is to minimize the difference between the desired system-level response and the corresponding target value $R_u^u(x_u^u) - T$ as well as the relaxation tolerances ε_{Ri} that reflect the deviation between the optimal responses from the subsystem level known as capabilities R_{li}^l and their counterpart variables R_{li}^u in the system level. Therefore, the decision variable vector in the system level problem contains the local design variables representing the system behavior x_u^u, target responses for the subsystem level $R_u^u(x_u^u)$, and deviation parameters ε_{Ri}. The system-level constraints include $g(x_u^u)$ and $h(x_u^u)$ as well as $\|R_{li}^u - R_{li}^l\| \le \varepsilon_{Ri}$, the upper x_U^u and lower

x_L^u bounds on system-level design variables x_u^u. In the subsystem-level problem, $R_i^l(x_i^l) - T_l^l$ represents the differences between the subsystem objectives and the corresponding targets along with deviation between the system-level targets for subsystem-level responses and the corresponding values found a the subsystem level $\|R_{li}^l(x_i^l) - R_{li}^u\|$. The decision variable vector at the subsystem level only consists of the local design variables. If there is more than one element (*m* elements) exists in the lower level, the linking variables that are shared between different elements in the same level of hierarchy the terms $\|y_{lj}^l - y_{lj}^u\|_2^2$ is trying to minimize the difference between linking variables.

Several approaches have been suggested in the literature to solve the decomposed problem in Eqs. (5.3) and (5.4) (Michelena 2008, Tosseram 2005). One conventional approach that has been used in the area of multidisciplinary design optimization is fixed point iteration (FPI). The advantages of FPI algorithm is that it is fairly intuitive to implement, requires no derivative information, and usually no modification of subspace analysis tools is required. However, FPI usually needs to be modified to produce a convergence reliable answer, even when one or more analysis solutions (fixed points) exist. In addition, original implementation of FPI has to be performed sequentially which may increase the computational cost. In this article, a modified FPI methodology with genetic algorithm (GA) optimizer for each element is used to perform the couple process-performance optimization.

5.3   Metamodeling

In order to reduce the complexity and computational cost of design optimization involving high fidelity simulations, reduced-order or surrogate models are often used.

Different metamodeling techniques have been developed for this purpose. To train or construct a metamodel, a set of design points is selected using a sampling approach, and a design of experiments is performed to evaluate the desired response value at each design point.

In this study, Latin hypercube sampling is used to produce a uniform distribution of training points in the design space. Fifty training points are generated for seven design variables that include four geometric attributes and three process parameters as described earlier. Table 2 lists the training points and the corresponding values of the selected design variables.

Seven responses are extracted for each set of simulations based on Eqs. (3.1) through (3.3) and (4.1). The calculated response values for each training point are listed in Table 3. It is worth noting that four out of fifty simulations as highlighted in Table 3 did not converge due to the extensive plastic deformation (necking) and contact instabilities in stamping, springback, and crush simulations. Hence, they were excluded from the training set.

Recent studies (Wang & Shan 2007, Barthelemy & Haftka 1993, Fang & Horstemeyer 2006, Parrish et al 2011) have shown that radial basis function (RBF) based metamodels are suitable for representation of highly nonlinear responses using relatively small number of training points. The formulation and approximation related to RBF metamodeling can be found in the literature. In the coupled process-performance FE simulations, it is required to perform deep drawing, springback, and crush simulations in sequence. However, once the metamodels are built, all responses can be evaluated simultaneously as each response is represented by an independent surrogate model. In

112

RBF formulation (Fang & Horstemeyer 2006, Acar & Rais-Rohani, 2008), an approximate response prediction at point x is found as

$$\hat{f}(x) = \sum_{i=1}^{n} \lambda_i \phi(\|x - x_i\|) \tag{5.5}$$

where x_i is the vector of normalized design variables at the *ith* training point, and $\|x\text{-}x_i\|$ is the Euclidian norm or distance from an arbitrary design point to the *i*th training point. The λ_i parameters are the unknown interpolation coefficients that must be calculated. Φ is the radially symmetric basis function that can take different forms. We considered both the multiquadric and thin-plate basis functions expressed as

Multiquadric: $\qquad \phi(r) = \sqrt{r^2 + c^2}$

$\qquad\qquad\qquad\qquad\qquad\qquad\qquad\qquad\qquad\qquad\qquad\qquad (5.6)$

Thin-Plate: $\qquad\quad \phi(r) = r^2\ln(c \times r)$

where c is a tuning parameter that can vary in the range of $0 < c \leq 1$ depending on the selected response. Five random test points are generated based on LHS and the accuracy of the prediction is examined by comparing the FE simulation responses with those approximated by the RBF metamodels. The results show that for rupture and springback responses, the thin-plate RBF is superior, whereas for the remaining responses, multiquadric RBF is better.

CHAPTER VI

APPLICATIONS

6.1 Parametric Model for coupled process-performance simulation

An automated parametric model is developed for coupled forming-crush simulation. The double-hat tube model has a symmetric cross-section. All the runs are controlled through a global shell script that creates, submits, and post-processes the models. The script requires a model input file for deep drawing, springback, and crush analyses as FE input decks and a FORTRAN code to generate the parametric values needed for a set of design points represented by a tabulated text file. Another FORTRAN code is developed to insert the parameter values inside the FE input decks. Once the input decks are created, they are copied to each folder for the deep drawing, springback, and crush simulations to be performed sequentially. When each simulation is finished, a user defined FORTRAN subroutine is used to extract the responses as will be discussed in the next section.

In this study, both single-hat sections are considered to have the same geometric attributes as well as the same manufacturing process parameters, although the parametric model can be used to account for non-symmetric cross-sections as well. The mesh density is held constant for the double-hat tube such that in longitudinal and cross-sectional directions, 210 and 125 elements are defined, respectively. This mesh density was found to be an optimum mesh density for the three simulations (i.e., deep drawing, springback, and crush).

114

The overall geometry is produced in the deep drawing stage and remains the same for the springback and crush simulations. The blank length is always equal to 250 mm, whereas the blank width is selected to be twice as large as a single hat section's perimeter; therefore, the widths of the blank sheets vary with the actual assigned tube width. This ratio can be considered as a manufacturing process variable in these simulations as well, but it is held fixed in this study.

Because of the fact that after the springback analysis some material is left as scrap, the single hat section is trimmed after springback (Fig. 4.3). The trimming process is performed by simply deactivating/excluding the elements on each side of the tube from the crush simulation so that the final shape of the end product will be analyzed in crush simulation. Because there is no cutting involved in this process, no additional residual stresses are introduced due to trimming of the hat sections. The two single hat sections will be assembled at the beginning of the crush simulation using tie contact formulation. In this study, both single hats are joined together perfectly as shown in Fig. 4.4 as the distance between the single hats is always within a tolerance that is equal to the shell thickness.

Geometric attributes are tube cross-sectional dimensions (i.e., *width*, *height*, *corner radius,* and *blank thickness*) and manufacturing process parameters are *holding force*, *punch velocity* and work piece-die set *friction coefficients*. The friction coefficients for holders, dies, and punch are assumed to be equal but can be treated as different design variables. "*Width*" translated into the punch width, "*corner radius*" is translated into the die and holders' corner radius, "*thickness*" is assigned directly to the shell elements that define the blank and "*height*" is captured by controlling the punch travel distance in the direction normal to the blank surface; this parameter determines the simulation

115

termination time as well as the prescribed *punch velocity*. *Holding force* defined as a manufacturing process parameter is the amount of maximum incremental force in the first step of deep drawing. The rate of holding force application is kept constant in all the simulations. *Punch velocity* is assumed to be constant in the direction perpendicular to the sheet metal; this parameter along with the height determine the deep drawing simulation termination time. Friction coefficients are assigned to the contact tangential definition. Both kinematic and penalty tangential contact formulations produced the same response in the deep drawing simulation.

6.2 Multiobjective optimization of coupled simulation using classical plasticity model

In order to reduce the complexity and computational cost of design optimization involving high fidelity simulations, reduced-order or surrogate models are often used. Different metamodeling techniques have been developed for this purpose. To train or construct a metamodel, a set of design points is selected using a sampling approach, and a design of experiments is performed to evaluate the desired response value at each design point.

In this study, Latin hypercube sampling is used to produce a uniform distribution of training points in the design space. Fifty training points are generated for seven design variables that include four geometric attributes and three process parameters as described earlier. Table 6.1 lists the training points and the corresponding values of the selected design variables.

The calculated response values for each training point are listed in Table 6.2. It is worth noting that four out of fifty simulations as highlighted in Table 6.2 did not converge due to the extensive plastic deformation (necking) and contact instabilities in

116

stamping, springback, and crush simulations. Hence, they were excluded from the

training set.

Table 6.1   Training points based on Latin hypercube sampling method

DOE Points	Width (mm)	Height (mm)	Corner Radius (mm)	Thickness (mm)	Holding Force (KN)	Punch Velocity (m/s)	Friction Coefficient	DOE Points	Width (mm)	Height (mm)	Corner Radius (mm)	Thickness (mm)	Holding Force (KN)	Punch Velocity (m/s)	Friction Coefficient
Max	70.00	35.00	7.50	2.50	50.00	10.00	0.35	Max	70.00	35.00	7.50	2.50	50.00	10.00	0.35
Min	40.00	20.00	2.50	1.00	10.00	2.00	0.10	Min	40.00	20.00	2.50	1.00	10.00	2.00	0.10
1	59.94	27.22	4.86	1.05	34.30	5.70	0.15	26	53.16	31.25	4.90	1.16	10.78	3.56	0.34
2	41.37	34.45	4.30	1.54	44.85	9.92	0.23	27	69.43	21.79	5.69	2.38	15.92	7.04	0.30
3	53.31	25.36	6.20	2.49	32.63	6.58	0.21	28	63.85	25.57	5.98	1.58	33.52	2.19	0.29
4	56.34	27.60	4.76	1.50	27.98	8.26	0.27	29	61.23	33.46	6.64	1.09	12.82	7.80	0.10
5	62.13	33.79	2.90	1.28	31.88	7.56	0.14	30	48.28	22.42	6.87	2.45	35.12	6.72	0.25
6	45.77	24.46	7.35	1.88	47.78	3.09	0.27	31	41.06	31.62	3.19	2.01	31.02	8.42	0.20
7	56.18	31.94	5.21	1.98	28.70	7.33	0.15	32	47.35	21.83	2.88	1.73	15.27	3.13	0.29
8	43.60	23.41	5.17	2.30	22.40	5.48	0.13	33	57.31	30.53	4.30	1.84	20.72	7.69	0.26
9	62.80	26.34	4.47	2.37	48.81	2.93	0.22	34	44.91	29.37	5.87	1.56	23.26	8.03	0.17
10	54.30	32.94	3.31	1.08	49.91	7.24	0.18	35	64.54	30.83	4.68	1.46	17.90	9.21	0.26
11	48.91	29.75	6.72	2.10	43.67	6.11	0.35	36	65.21	34.40	6.93	1.00	39.32	5.60	0.32
12	44.49	26.97	3.96	2.27	40.05	2.48	0.25	37	51.01	23.91	2.80	1.41	26.36	3.30	0.11
13	43.95	28.92	5.31	1.79	36.06	6.28	0.22	38	54.83	20.58	7.49	1.62	11.50	4.37	0.14
14	66.64	20.91	5.46	1.15	38.78	4.61	0.19	39	40.08	32.21	6.27	2.32	37.14	5.02	0.31
15	47.04	24.50	7.25	1.21	25.59	8.88	0.23	40	50.78	26.75	6.08	1.76	42.57	5.98	0.12
16	68.44	20.87	4.06	1.43	23.63	2.12	0.31	41	55.14	22.11	3.03	1.94	18.26	5.27	0.16
17	51.65	32.50	3.85	2.15	20.18	3.66	0.16	42	49.06	21.33	2.53	1.68	41.64	6.89	0.20
18	69.33	20.22	4.13	1.69	43.00	9.04	0.12	43	60.63	22.92	5.72	2.22	21.60	9.78	0.33
19	52.55	28.04	5.59	2.18	46.71	3.84	0.30	44	65.97	23.86	2.64	2.13	12.35	4.12	0.28
20	42.38	23.07	4.53	1.33	46.98	4.83	0.28	45	58.32	34.95	6.44	1.31	30.74	4.01	0.11
21	59.10	28.29	3.59	2.08	16.59	5.10	0.21	46	49.74	25.92	3.45	1.23	45.73	9.41	0.19
22	57.69	29.25	6.35	1.38	13.57	8.63	0.33	47	67.60	28.57	3.61	2.04	40.93	9.53	0.17
23	64.70	30.45	3.77	2.23	19.46	6.46	0.24	48	42.88	32.78	7.06	1.66	24.41	4.43	0.18
24	46.42	26.03	7.14	1.83	29.26	8.79	0.34	49	59.75	24.97	3.26	1.27	37.40	2.63	0.13
25	63.29	33.82	5.08	2.43	14.63	2.78	0.24	50	68.10	30.02	6.54	1.90	27.08	8.09	0.32

Table 6.2   Results from coupled sequential process-performance simulations at the training points using classical plasticity model

DOE Points	Rupture	Thinning	Springback	Max Crush Force (kN)	Mean Crush Force (kN)	Mass (kg)	DOE Points	Rupture	Thinning	Springback	Max Crush Force (kN)	Mean Crush Force (kN)	Mass (kg)
1	407.61	27.948	2.88	76.72	18.42	0.11	26	681.7	57.925	1.31	86.41	26.16	0.121
2	3725.3	315.37	1.91	112.26	38.24	0.15	27	1886.1	121.56	0.41	175.46	71.53	0.243
3	1753.9	109.63	1.17	180.83	78.35	0.23	28	558.03	31.792	1.39	118.99	43.29	0.163
4	1293	117.44	0.76	111.14	32.86	0.15	29	222.61	10.878	3.40	89.89	27.71	0.127
5	N/A	N/A	N/A	N/A	N/A	0.15	30	1467.3	75.93	1.66	167.05	79.20	0.208
6	636.12	25.873	1.74	120.23	57.16	0.16	31	5678	498.94	0.37	142.48	51.05	0.189
7	1714.4	138.89	0.28	158.71	53.83	0.21	32	2830.3	232.05	0.27	103.73	42.08	0.141
8	1671.3	94.421	0.43	146.20	67.15	0.19	33	2272.6	205.34	1.01	145.16	47.63	0.196
9	2194.4	168.14	0.64	179.59	76.69	0.25	34	773.27	55.835	0.25	109.81	36.31	0.147
10	N/A	N/A	N/A	N/A	N/A	0.12	35	2376.7	210.7	1.09	120.34	36.06	0.165
11	1433.8	103.78	1.47	153.90	58.60	0.21	36	391.38	39.249	1.69	85.31	23.02	0.121
12	2920.9	230.19	0.72	156.66	62.18	0.20	37	1566.4	132.14	0.53	91.46	27.05	0.124
13	1502.1	115.16	1.32	123.33	50.54	0.16	38	267.34	2.8886	2.54	102.29	41.07	0.141
14	350.76	18.067	1.42	80.04	23.55	0.11	39	2009.6	153.73	1.95	171.82	76.34	0.22
15	357.43	20.295	1.32	77.83	26.14	0.11	40	609.89	29.143	0.17	122.28	44.80	0.165
16	942.04	66.742	0.33	102.63	35.98	0.14	41	2948.9	242.88	0.35	126.87	48.21	0.173
17	2355.7	203.79	0.64	168.16	59.96	0.22	42	3822.2	322.59	0.21	100.78	36.28	0.138
18	1475.9	113.23	0.67	120.53	41.73	0.17	43	2003.8	156.98	0.80	157.44	62.25	0.214
19	1699.4	119.62	1.12	159.61	64.80	0.21	44	N/A	N/A	N/A	N/A	N/A	0.217
20	1061.3	80.62	0.94	78.69	25.74	0.11	45	263.18	11.24	3.39	111.00	38.53	0.152
21	2841.1	246.63	0.95	158.65	53.05	0.21	46	2253.7	216.62	1.52	83.55	24.36	0.112
22	762.25	60.396	1.00	106.35	33.64	0.14	47	3870.9	336.04	0.32	167.57	60.88	0.227
23	3974.8	339.85	0.73	184.79	65.03	0.25	48	476.03	22.666	1.95	121.89	50.46	0.163
24	938.96	63.344	1.24	121.97	46.42	0.16	49	936.71	71.315	1.92	89.43	25.48	0.124
25	N/A	N/A	N/A	N/A	N/A	0.287	50	1187.1	94.306	0.82	159.65	52.38	0.219

6.2.1   Multi-objective optimization

When faced with competing objective functions, the optimization problem

becomes one of finding the non-dominated design points that form the Pareto frontier.

117

In this paper, we utilized multi-objective genetic algorithms (MOGA) as implemented in MATLAB to identify the Pareto optimal set. The MOGA procedure is as follows:

1. Design variables expressed in real number are converted to bit strings.

2. A random initial population is generated.

3. Using a fitness function, members of the population are examined by

   o assigning a rank to each solution based on non-dominated front (Fonseca & Fleming 1993).

   o assigning a fitness value based on Pareto ranking.

   o calculating the niche count of each solution.

   o calculating the shared fitness value of each solution.

   o normalizing the fitness values by using share fitness values.

4. Using a stochastic method to select parents for future generation.

5. Performing crossover and mutation operations.

6. Establishing a new population.

7. Evaluating the population attributes.

8. Continuing steps 3 to 7 to evaluate all the objectives.

9. Selecting half of the individuals that have the higher rank than the rest.

10. Continuing the solution process until a stopping criterion is satisfied based on the average change in the spread of Pareto solution being less than the tolerance specified.

In order to enhance the energy absorption behavior of the crush tube while improving the manufacturing responses, seven design variables are selected, including tube height, width, thickness, corner radius, holding force, punch velocity, and friction

118

coefficient. The multi-objective optimization problem for the coupled process-performance problem is defined as finding the optimum values of design variables that would minimize rupture, thinning, springback, mass, and maximum crush force, and maximize the mean crush force subject to design variable side constraints. Therefore, the multi-objective optimization problem is expressed as

$$\min_{x = x_1, \ldots, x_7} \{R(x), T(x), S(x), -P_m(x), P_{max}(x), M(x_1, \ldots, x_4)\}$$
$$s.t. \, 40 \leq x_1 \leq 70$$
$$20 \leq x_2 \leq 35$$
$$2.5 \leq x_3 \leq 7.5 \qquad\qquad (6.1)$$
$$1.0 \leq x_4 \leq 2.5$$
$$10 \leq x_5 \leq 50$$
$$2 \leq x_6 \leq 10$$
$$0.01 \leq x_7 \leq 0.1$$

where variables x_1 to x_7 are width, height, corner radius, thickness, holding force, punch velocity, and friction coefficient, respectively. *R(x)* is rupture, *T(x)* is thinning, *S(x)* is springback, *P$_m$(x)* is the mean crush force, *P$_{max}$(x)* is the maximum crush force, and *M(x)* is mass. To have a minimization problem for all the objectives, the mean crush force is multiplied by negative one.

The optimization problem is solved using the MOGA toolbox in MATLAB (2008) with an initial population of 105 individuals. The initial population is created by a generation of random numbers in MATLAB within the bounds of the design variables. The tournament selection algorithm is used here (Konak et al 2006). The crossover fraction is selected as 80% using intermediate crossover function and the function tolerance to stop the optimization procedure is selected as 1e-4. Stopping criterion is applied at generation number 1400 if the optimizer could not find the optimum point. The optimization problem formulated in Eq. (6.1) converged to the Pareto optimum set after 221 GA iterations.

119

The list of twenty-two design points forming the Pareto frontier is shown in Table 6.3. As expected from the Pareto optimal set, no design point can be found where all the objective functions simultaneously reach their respective optimum values. However, by sorting the responses in an ascending order for each response, the best design with respect to each response can be identified. Table 6.4 provides the sorted responses based on the desired response values. Each column represents the ranked Pareto ID's shown in Table 6.3. For example, the minimum rupture and thinning are reported by Pareto ID point 13 that has the vector of design variables: 56.26, 29.65, 6.13, 1.65, 19.73, 4.30, and 0.15, whereas the optimum point for springback, maximum crush force, mean crush force, and mass are 6, 1, 2, and 3, respectively.

Table 6.3   Non-dominated optimal points on Pareto frontier for classical plasticity model

Pareto point ID	Width (mm)	Height (mm)	Corner Radius (mm)	Thickness (mm)	Holding Force (kN)	Punch Velocity (m/s)	Friction Coefficient	Rupture	Thinning	Springback	Max Crush Force (kN)	Mean Crush Force (kN)	Mass (kg)
1	41.49	21.88	4.26	1.02	30.38	3.95	0.23	840.76	80.54	1.16	56.39	17.94	0.08
2	70.00	34.98	4.99	2.50	43.00	4.77	0.24	3320.39	238.40	0.35	216.98	87.99	0.30
3	40.53	21.79	4.60	1.03	30.75	3.87	0.23	683.19	65.66	1.24	56.40	19.15	0.08
4	69.69	34.70	4.28	2.50	27.61	5.79	0.24	4179.67	298.90	0.23	219.28	84.26	0.30
5	58.96	34.63	5.58	2.20	23.01	4.34	0.15	1626.14	135.32	1.23	183.86	68.70	0.25
6	40.84	20.36	2.90	2.30	13.79	3.01	0.18	3697.10	255.86	0.01	136.36	64.98	0.18
7	69.97	34.90	4.94	2.50	35.64	5.98	0.27	3657.54	261.49	0.25	219.11	85.51	0.30
8	51.87	26.05	4.73	1.03	26.06	4.33	0.13	175.10	20.46	2.33	68.21	16.47	0.10
9	61.43	34.81	3.88	2.44	31.26	5.18	0.27	4163.41	309.81	0.45	208.04	78.95	0.28
10	48.76	23.83	2.96	1.01	30.44	4.48	0.29	1635.14	150.50	0.93	61.96	13.76	0.09
11	52.58	34.11	4.35	1.93	17.88	5.22	0.18	2102.08	191.86	0.96	155.23	52.94	0.21
12	65.51	30.09	4.00	2.27	35.54	4.92	0.26	3213.49	249.72	0.75	189.47	71.33	0.26
13	56.26	29.65	6.13	1.65	19.73	4.30	0.15	136.49	5.14	1.87	124.09	41.20	0.17
14	48.95	24.14	5.53	2.23	15.16	3.83	0.13	1059.52	78.70	1.03	146.50	62.86	0.19
15	41.71	26.21	4.29	1.40	31.41	4.46	0.23	1288.99	114.38	1.34	86.79	31.41	0.12
16	53.25	29.43	2.66	1.56	25.60	3.73	0.15	2262.46	199.96	1.12	115.61	33.08	0.16
17	56.47	21.49	5.52	2.24	18.10	3.36	0.21	1239.32	85.16	1.45	150.18	65.50	0.20
18	48.09	23.98	5.63	2.07	17.71	4.15	0.18	890.61	61.56	1.33	135.39	58.68	0.18
19	55.37	25.67	4.44	1.05	29.84	5.09	0.23	517.60	48.56	1.89	69.99	16.65	0.10
20	48.20	34.46	3.59	2.47	33.52	4.82	0.23	4478.39	336.93	0.46	195.31	75.90	0.26
21	45.50	30.14	3.40	1.80	29.26	4.53	0.13	2569.69	221.73	0.55	129.77	43.83	0.17
22	52.58	34.11	4.38	1.81	17.88	5.22	0.18	1854.37	173.64	1.14	144.93	48.12	0.20

120

Table 6.4   Sorted listing of design points on the Pareto frontier based on Pareto ID
numbers specified in Table 6.3 for each response.

Rupture	Thinning	Springback	Max Crush Force	Mean Crush Force	Mass
13	13	6	1	2	3
8	8	4	3	7	1
19	19	7	10	4	10
3	18	2	8	9	8
1	3	9	19	20	19
18	14	20	15	12	15
14	1	21	16	5	16
17	17	12	13	17	13
15	15	10	21	6	21
5	5	11	18	14	6
10	10	14	6	18	18
22	22	16	22	11	14
11	11	22	14	22	22
16	16	1	17	21	17
21	21	5	11	13	11
12	2	3	5	16	5
2	12	18	12	15	20
7	6	15	20	3	12
6	7	17	9	1	9
9	4	13	2	19	2
4	9	19	7	8	4
20	20	8	4	10	7

It can be seen that the sorted points for the rupture and thinning responses appear
to be in agreement in most of the cases meaning that the optimal point for rupture is
approximately the optimum point for thinning. The same pattern is observed for
maximum crush force and tube mass as they increase/decrease simultaneously.
Conversely, the springback response is in strong conflict with thinning and rupture as the
order of optimum points is inverted. A similar situation is also observed between the
mean crush force with mass and the maximum crush force considering the fact that the
mean crush force is maximized whereas mass and maximum crush force are minimized.
Hence, a hypercube of Pareto optimum set with six dimensions (for six objectives) can be
reduced to a two-dimensional plot as shown in Fig. 6.1 with one axis representing the
process objectives and the other the performance objectives. For the performance
objectives, the mean crush force is normalized and for the process parameters, thinning

121

response is normalized by their respective maximum values. The Pareto frontiers in the performance and process space are shown separately in Figs. 6.2 and 6.3, respectively.
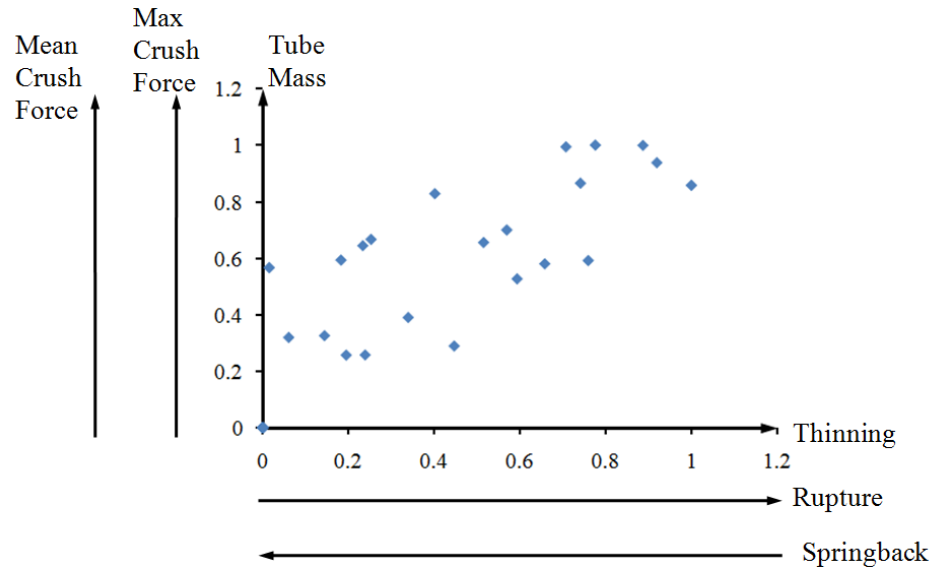
Figure 6.1   Pareto frontier representing the response values in the optimum set
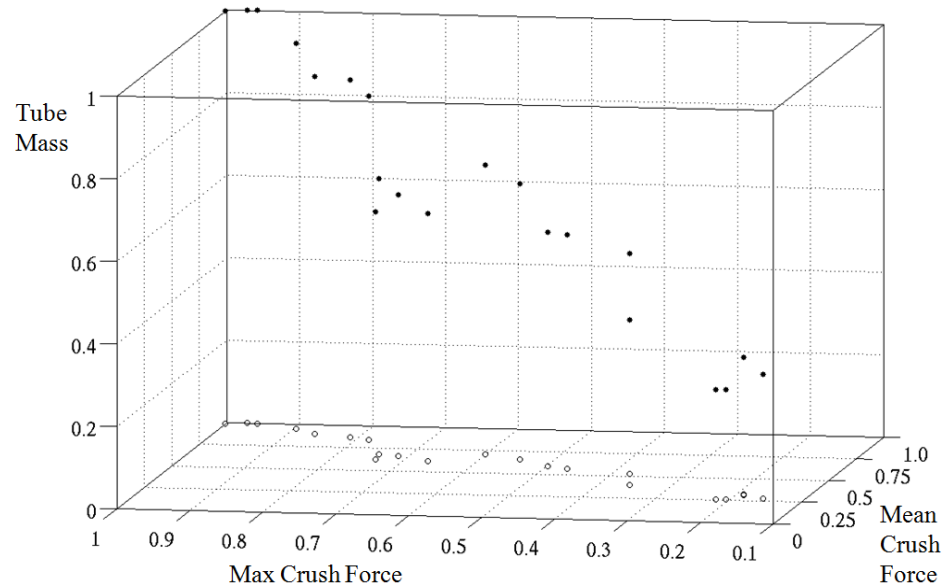
Figure 6.2   Pareto frontier in the performance space (the hollow circles are the projection of the solid circles in the plane)

122
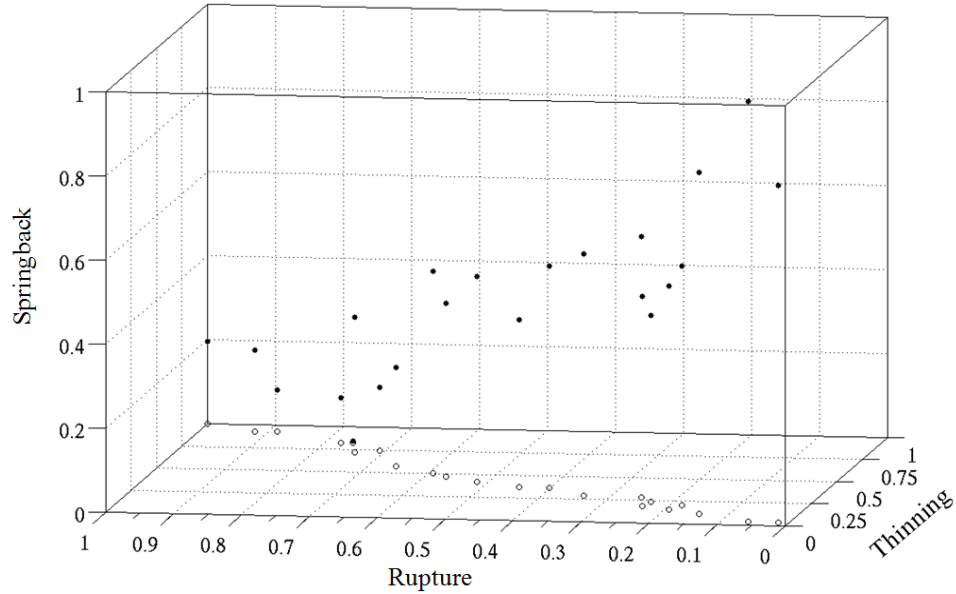
Figure 6.3   Pareto frontier in the process space(the hollow circles are the projection of the solid circles in the plane)

6.3   Multiobjective optimization of coupled simulation using ISV model

The same framework is used to incorporate ISV material model in process-performance simulations. In order to enhance the energy absorption behavior of the crush tube while improving the manufacturing responses, seven design variables are selected, including tube height, width, thickness, corner radius, holding force, punch velocity, and friction coefficient. For the design optimization, the same metamodelling formulation RBF is utilized based on the training points and responses provided in tables 6.4 and 6.5.

123

Table 6.5   Training points based on Latin hypercube sampling method

DOE Points	Width (mm)	Height (mm)	Corner Radius (mm)	Thickness (mm)	Holder Force (KN)	Punch Velocity (m/s)	Friction Coefficient	DOE Points	Width (mm)	Height (mm)	Corner Radius (mm)	Thickness (mm)	Holder Force (KN)	Punch Velocity (m/s)	Friction Coefficient
Max	70.00	35.00	7.50	2.50	50.00	10.00	0.10	Max	70.00	35.00	7.50	2.50	50.00	10.00	0.10
Min	40.00	20.00	2.50	1.00	10.00	2.00	0.01	Min	40.00	20.00	2.50	1.00	10.00	2.00	0.01
1	59.94	27.22	4.86	1.05	34.30	5.70	0.026	26	53.16	31.25	4.90	1.16	10.78	3.56	0.10
2	41.37	34.45	4.30	1.54	44.85	9.92	0.056	27	69.43	21.79	5.69	2.38	15.92	7.04	0.08
3	53.31	25.36	6.20	2.49	32.63	6.58	0.051	28	63.85	25.57	5.98	1.58	33.52	2.19	0.08
4	56.34	27.60	4.76	1.50	27.98	8.26	0.071	29	61.23	33.46	6.64	1.09	12.82	7.80	0.01
5	62.13	33.79	2.90	1.28	31.88	7.56	0.026	30	48.28	22.42	6.87	2.45	35.12	6.72	0.07
6	45.77	24.46	7.35	1.88	47.78	3.09	0.070	31	41.06	31.62	3.19	2.01	31.02	8.42	0.05
7	56.18	31.94	5.21	1.98	28.70	7.33	0.029	32	47.35	21.83	2.88	1.73	15.27	3.13	0.08
8	43.60	23.41	5.17	2.30	22.40	5.48	0.022	33	57.31	30.53	4.30	1.84	20.72	7.69	0.07
9	62.80	26.34	4.47	2.37	48.81	2.93	0.051	34	44.91	29.37	5.87	1.56	23.26	8.03	0.04
10	54.30	32.94	3.31	1.08	49.91	7.24	0.037	35	64.54	30.83	4.68	1.46	17.90	9.21	0.07
11	48.91	29.75	6.72	2.10	43.67	6.11	0.099	36	65.21	34.40	6.93	1.00	39.32	5.60	0.09
12	44.49	26.97	3.96	2.27	40.05	2.48	0.062	37	51.01	23.91	2.80	1.41	26.36	3.30	0.01
13	43.95	28.92	5.31	1.79	36.06	6.28	0.054	38	54.83	20.58	7.49	1.62	11.50	4.37	0.02
14	66.64	20.91	5.46	1.15	38.78	4.61	0.042	39	40.08	32.21	6.27	2.32	37.14	5.02	0.09
15	47.04	24.50	7.25	1.21	25.59	8.88	0.058	40	50.78	26.75	6.08	1.76	42.57	5.98	0.02
16	68.44	20.87	4.06	1.43	23.63	2.12	0.087	41	55.14	22.11	3.03	1.94	18.26	5.27	0.03
17	51.65	32.50	3.85	2.15	20.18	3.66	0.033	42	49.06	21.33	2.53	1.68	41.64	6.89	0.04
18	69.33	20.22	4.13	1.69	43.00	9.04	0.018	43	60.63	22.92	5.72	2.22	21.60	9.78	0.09
19	52.55	28.04	5.59	2.18	46.71	3.84	0.083	44	65.97	23.86	2.64	2.13	12.35	4.12	0.08
20	42.38	23.07	4.53	1.33	46.98	4.83	0.074	45	58.32	34.95	6.44	1.31	30.74	4.01	0.01
21	59.10	28.29	3.59	2.08	16.59	5.10	0.048	46	49.74	25.92	3.45	1.23	45.73	9.41	0.04
22	57.69	29.25	6.35	1.38	13.57	8.63	0.094	47	67.60	28.57	3.61	2.04	40.93	9.53	0.03
23	64.70	30.45	3.77	2.23	19.46	6.46	0.059	48	42.88	32.78	7.06	1.66	24.41	4.43	0.04
24	46.42	26.03	7.14	1.83	29.26	8.79	0.095	49	59.75	24.97	3.26	1.27	37.40	2.63	0.02
25	63.29	33.82	5.08	2.43	14.63	2.78	0.061	50	68.10	30.02	6.54	1.90	27.08	8.09	0.09

Table 6.6   Results from coupled sequential process-performance simulations at the training points using ISV material model

DOE Points	Rupture	Thinning	Springback	Max Crush Force (kN)	Mean Crush Force (kN)	Mass (kg)	DOE Points	Rupture	Thinning (%)	Springback	Max Crush Force (kN)	Mean Crush Force (kN)	Mass (kg)
1	4190.2	130.26	0.17	49.65	27.26	0.11	26	1285.9	36.725	0.18	54.56	32.60	0.121
2	21024	619.77	0.10	81.31	50.90	0.15	27	5751.9	145.94	0.10	143.19	83.75	0.243
3	6469.6	182.1	0.19	153.11	86.27	0.23	28	501.1	7.2843	0.23	106.38	47.28	0.163
4	11007	314.29	0.09	88.11	47.45	0.15	29	0	68.543	0.17	48.65	25.70	0.127
5	12447	381.66	0.12	73.75	40.67	0.15	30	5945.5	165.94	0.13	116.71	77.63	0.208
6	1010.6	19.299	0.36	77.29	51.38	0.16	31	19513	580.65	0.11	113.42	69.88	0.189
7	9296.8	276.48	0.12	112.88	73.71	0.21	32	3024.6	77.455	0.15	74.68	43.50	0.141
8	4963.9	137.06	0.50	96.31	67.96	0.19	33	11539	348.33	0.13	109.71	66.19	0.196
9	2335.7	57.708	0.11	129.58	84.25	0.25	34	10633	307.9	0.08	77.94	47.38	0.147
10	115240	347.12	0.16	54.81	30.35	0.12	35	12588	359.58	0.09	104.31	49.60	0.165
11	6343.9	186.3	0.25	106.01	72.04	0.21	36	4717.4	137.79	0.20	56.70	30.42	0.121
12	2481.4	55.114	0.16	106.87	69.77	0.20	37	2268.3	68.543	0.17	64.73	36.17	0.124
13	7173	219.91	0.29	81.65	55.93	0.16	38	1096.4	24.487	0.37	68.35	43.17	0.141
14	0	254.04	0.09	54.90	28.26	0.11	39	4566.1	135.14	N/A	N/A	N/A	N/A
15	9389.5	254.04	0.09	63.63	33.16	0.11	40	4681.3	141.24	0.39	82.84	54.80	0.165
16	800.35	16.072	0.23	70.04	36.71	0.14	41	6379.6	180.08	0.24	96.68	57.38	0.173
17	3219.1	92.356	0.46	121.15	72.62	0.22	42	11381	336.38	0.09	79.70	46.74	0.138
18	8380.3	209.05	0.15	102.24	51.78	0.17	43	10847	282.83	0.12	135.38	80.80	0.214
19	2583.7	68.184	0.49	124.70	72.38	0.21	44	5726.3	158.88	0.138	120.166	74.09315	0.21
20	3822.3	118.41	0.52	50.47	32.60	0.11	45	1188.6	34.197	0.231	72.6339	41.77252	0.15
21	6332.2	186.73	0.17	118.34	71.29	0.21	46	15089	430.03	0.112	68.9498	34.12096	0.11
22	10480	291.07	0.09	86.79	44.31	0.14	47	14251	398.29	0.091	148.171	78.62051	0.22
23	9507.8	282.51	0.22	144.27	88.62	0.25	48	1799.1	51.64	0.25	77.3871	52.70962	0.16
24	10739	300.07	N/A	N/A	N/A	N/A	49	1186.8	28.837	0.254	62.414	30.4286	0.12
25	1891.9	45.138	0.332	151.1	94.61	0.28	50	8729.5	236.36	0.092	134.435	73.96586	0.219

The multi-objective optimization problem for the coupled process-performance problem is defined as finding the optimum values of design variables that would minimize rupture, thinning, springback, mass, and maximum crush force, and maximize the mean crush force subject to design variable side constraints. Seven design variables are selected, including tube height, width, thickness, corner radius, holding force, punch velocity, and friction coefficient. The multi-objective optimization problem for the coupled process-performance problem is defined as finding the optimum values of design

124

variables that would minimize rupture, thinning, springback, mass, and maximum crush force, and maximize the mean crush force subject to design variable side constraints. Therefore, the multi-objective optimization problem is expressed as

$$\min_{x \, = \, x_1, \dots, x_7} \{R(x), T(x), S(x), -P_{max}(x), P_{max}(x), M(x_1, \dots, x_4)\}$$
$$s.t. \, 40 \leq x_1 \leq 70$$
$$20 \leq x_2 \leq 35$$
$$2.5 \leq x_3 \leq 7.5 \qquad\qquad (6.2)$$
$$1.0 \leq x_4 \leq 2.5$$
$$10 \leq x_5 \leq 50$$
$$2 \leq x_6 \leq 10$$
$$0.01 \leq x_7 \leq 0.1$$

where variables x_1 to x_7 are width, height, corner radius, thickness, holding force, punch velocity, and friction coefficient, respectively. $R(x)$ is rupture, $T(x)$ is thinning, $S(x)$ is springback, $P_m(x)$ is the mean crush force, $P_{max}(x)$ is the maximum crush force, and $M(x)$ is mass. To have a minimization problem for all the objectives, the mean crush force is multiplied by negative one.

The optimization problem is solved using the MOGA toolbox in MATLAB (2008) with an initial population of 105 individuals. The initial population is created by a generation of random numbers in MATLAB within the bounds of the design variables. The tournament selection algorithm is used here (Konak et al 2006). The crossover fraction is selected as 80% using intermediate crossover function and the function tolerance to stop the optimization procedure is selected as 1e-4. Stopping criterion is applied at generation number 1400 if the optimizer could not find the optimum point. The optimization problem formulated in Eq. (6.2) converged to the Pareto optimum set after 323 GA iterations. The Pareto frontier related to this multi-objective optimization are listed in table 6.7.

125

Table 6.7   Non-dominated optimal points on Pareto frontier for ISV material model

Pareto point ID	Width (mm)	Height (mm)	Corner Radius (mm)	Thickness (mm)	Holding Force (kN)	Punch Velocity (m/s)	Friction Coefficient	Rupture	Thinning	Springback	Max Crush Force (kN)	Mean Crush Force (kN)	Mass (kg)
1	41.49	21.88	4.26	1.02	30.38	3.95	0.23	840.76	80.54	1.16	56.39	17.94	0.08
2	70.00	34.98	4.99	2.50	43.00	4.77	0.24	3320.39	238.40	0.35	216.98	87.99	0.30
3	40.53	21.79	4.60	1.03	30.75	3.87	0.23	683.19	65.66	1.24	56.40	19.15	0.08
4	69.69	34.70	4.28	2.50	27.61	5.79	0.24	4179.67	298.90	0.23	219.28	84.26	0.30
5	58.96	34.63	5.58	2.20	23.01	4.34	0.15	1626.14	135.32	1.23	183.86	68.70	0.25
6	40.84	20.36	2.90	2.30	13.79	3.01	0.18	3697.10	255.86	0.01	136.36	64.98	0.18
7	69.97	34.90	4.94	2.50	35.64	5.98	0.27	3657.54	261.49	0.25	219.11	85.51	0.30
8	51.87	26.05	4.73	1.03	26.06	4.33	0.13	175.10	20.46	2.33	68.21	16.47	0.10
9	61.43	34.81	3.88	2.44	31.26	5.18	0.27	4163.41	309.81	0.45	208.04	78.95	0.28
10	48.76	23.83	2.96	1.01	30.44	4.48	0.29	1635.14	150.50	0.93	61.96	13.76	0.09
11	52.58	34.11	4.35	1.93	17.88	5.22	0.18	2102.08	191.86	0.96	155.23	52.94	0.21
12	65.51	30.09	4.00	2.27	35.54	4.92	0.26	3213.49	249.72	0.75	189.47	71.33	0.26
13	56.26	29.65	6.13	1.65	19.73	4.30	0.15	136.49	5.14	1.87	124.09	41.20	0.17
14	48.95	24.14	5.53	2.23	15.16	3.83	0.13	1059.52	78.70	1.03	146.50	62.86	0.19
15	41.71	26.21	4.29	1.40	31.41	4.46	0.23	1288.99	114.38	1.34	86.79	31.41	0.12
16	53.25	29.43	2.66	1.56	25.60	3.73	0.15	2262.46	199.96	1.12	115.61	33.08	0.16
17	56.47	21.49	5.52	2.24	18.10	3.36	0.21	1239.32	85.16	1.45	150.18	65.50	0.20
18	48.09	23.98	5.63	2.07	17.71	4.15	0.18	890.61	61.56	1.33	135.39	58.68	0.18
19	55.37	25.67	4.44	1.05	29.84	5.09	0.23	517.60	48.56	1.89	69.99	16.65	0.10
20	48.20	34.46	3.59	2.47	33.52	4.82	0.23	4478.39	336.93	0.46	195.31	75.90	0.26
21	45.50	30.14	3.40	1.80	29.26	4.53	0.13	2569.69	221.73	0.55	129.77	43.83	0.17
22	52.58	34.11	4.38	1.81	17.88	5.22	0.18	1854.37	173.64	1.14	144.93	48.12	0.20

The Pareto points are plotted in sorted order based on the rupture and mean crush force responses in figure 6.4. As it is illustrated , there is a nonlinear relationship between thinning and rupture once using ISV model which is mainly due to the nonlinear behavior of material at elevated temperature. Similarly, there is an inverse relationship between spring back and rupture responses. But the responses in the crash simulation using ISV model is similar to the classical plasticity model. Inverse relationship between mass and mean crush force and direct relationship between mass and maximum force is observed.

126
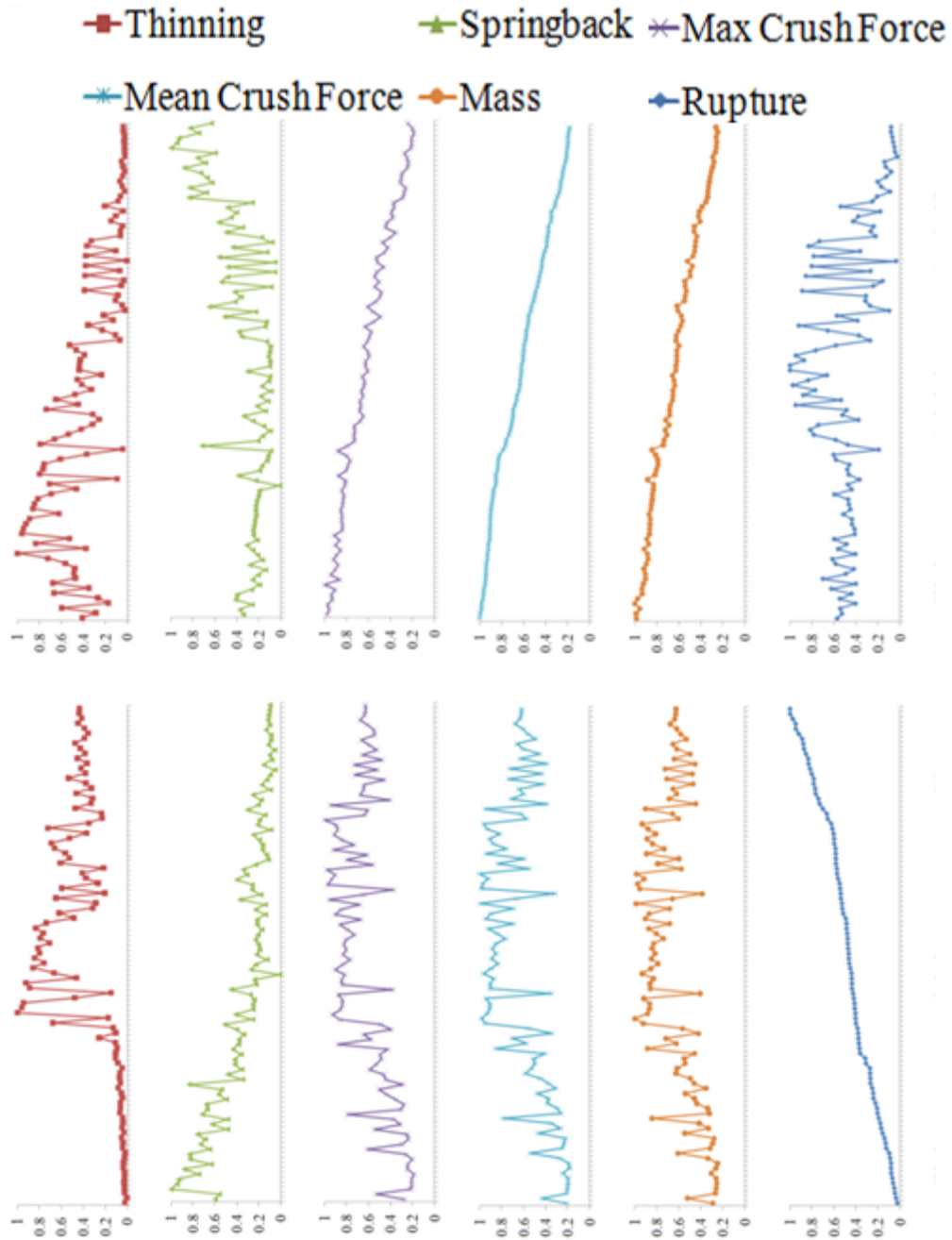
Figure 6.4   Pareto frontier obtained from multiobjective optimization based on BCJ model

6.4   Multilevel optimization using ATC

In this section, the coupled sequential process-performance simulation is decomposed into a hierarchical system containing two levels. Performance attributes such

127

as energy absorption are addressed in the top (system) level whereas manufacturing process design problem appears in the bottom (subsystem) level in this two-level hierarchy. ATC approach is used in formulation of the decomposed problem. The key consideration is the inclusion of manufacturing-induced changes in the material/component as an integral part of performance analysis and design. The approach is demonstrated in process-performance analysis and optimization of a double-hat stamped tube by considering the manufacturing process parameters and geometric attributes of the component as design variables. The responses used as coupling variables are driven based on a fully coupled process-performance finite element analysis (FEA). To enhance the computational efficacy, the actual FE simulations in each level are replaced with surrogate models using radial basis functions. The heuristic optimization strategy of genetic algorithms (GA) is used to solve the optimization problem in each level while maintaining consistency between the system and subsystem level problems in the ATC framework.

For the multilevel design problem, similar model used for AAO is used here. In order to perform mathematical optimization to include manufacturing process effects in energy absorption behavior (performance), in lieu of fully coupled forming-spring back-crush simulation, a decomposition strategy is used to partition the problem into two disciplines including processing and energy absorption. In order to adapt the coupled simulation to ATC framework, decomposition or partitioning is required. A sequential partitioning is used to decompose the process-performance problem to a bi-level hierarchy with each level representing the important aspects of the performance and process disciplines.

128

Forming simulation is composed of two simulations including deep drawing simulation in ABAQUS/EXPLICIT followed by a springback simulation in ABAQUS/STANDARD, whereas the crush simulation is performed in ABAQUS/EXPLICIT. In contrast with fully coupled sequential simulation where the entire history variables are directly transferred from process-simulation to performance simulation, in the ATC decomposition approach, we are looking to find the major history variables that have the most influence on the crush simulation based on the classical plasticity models used.

By the inclusion of different factors and combinations of the history variables, we determined that the main parameters that affect the crush behavior are the equivalent plastic strain and the deviation captured through the springback. Due to the extensive plastic deformation in the folding process observed during crush, the residual stresses do not affect the crush behavior, and due to the optimization requirements, a very small tolerance is set for thinning in the manufactured product.

In order to quantify the process responses in a scalar format, springback is defined as a deviation angle from the punch shape representing the desired shape for the tube. Investigation shows that the equivalent plastic strain (PEEQ) distribution in the workpiece after deep drawing appears in three uniform regions as shown in figure 6.5.

Region 1 does not show any PEEQ due to the absence of any plastic deformation in the flat part of the punch head. Region 2 shows approximately uniform distribution of PEEQ in the round corner regions of the tube that are permanently deformed to form the tube corners, whereas Region 3 shows approximately uniform distribution of PEEQ in the side-wall portion of the tube. Regions 2 and 3 will take nonzero values with PEEQ in Region 3 being always greater than that in Region 2. Therefore, the process-level

129

responses are defined as PEEQ in Region 2 and a positive scale factor that will be multiplied by Region 2's PEEQ to represent PEEQ in Region 3. Hence, the process simulation capabilities identified as springback angle, PEEQ for Region 2 and PEEQ scale factor for Region 3 are transferred to the top level as capabilities from the bottom level. As will be shown in more detail later, the corresponding target values will be treated as decision variables in the top-level problem.
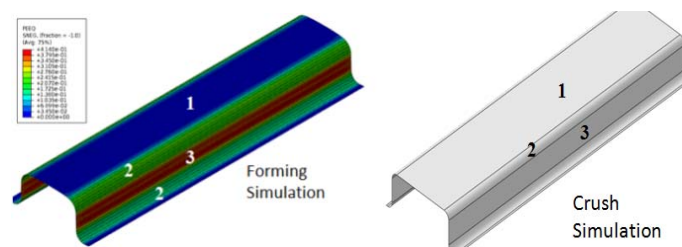
Figure 6.5   Equivalent plastic strain in forming process transferred to crush simulation

The PEEQ values in the top level will offset the initial yield point of the stress-strain curve and replace the actual stress-strain curve used in the forming simulation for the crush simulation. Therefore, the stress-strain curves used in crush simulation are different in Region 2 and 3 while Region 1 uses the same stress-strain curve that is used in the forming simulation. The process-performance problem is decomposed into two elements including forming simulation at the bottom and crush simulation at the top as shown in figure 6.6. Each element tries to capture the global optimum point till the ATC iteration reaches a converged solution where the demands and capabilities are brought together within a desired tolerance. The mathematical formulation of the ATC approach will be presented later in more detail in the next sections.

www.manaraa.com
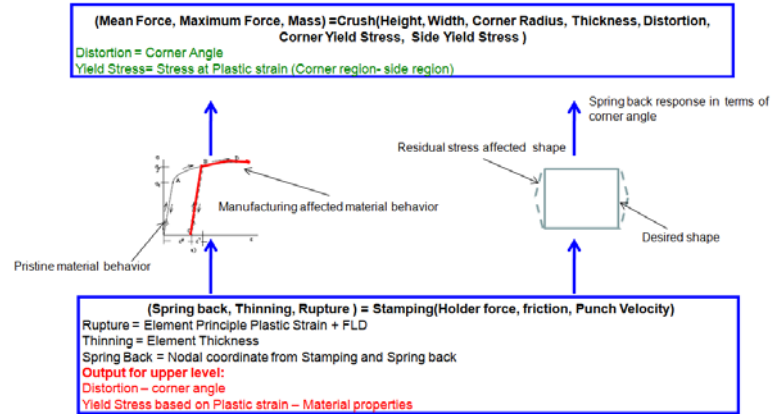
Figure 6.6   Flowchart of Bi-Level Bottom-Up Decomposition for Integrated Process-
             Performance Simulation

6.4.1   FE Simulation of crushing process

Other than geometric attribute used to define the tube cross-section, the

springback deviation angle is considered in the FE model. The material model assigned in

each region is defined based on the updated stress-strain behavior manipulated based on

the average equivalent plastic strain observed at the end of stamping process. The two

double hat sections are modeled using single under integrated shell elements having five

integration points through the thickness assembled on two edges of the hat sections as

shown in figure 6.7.

131
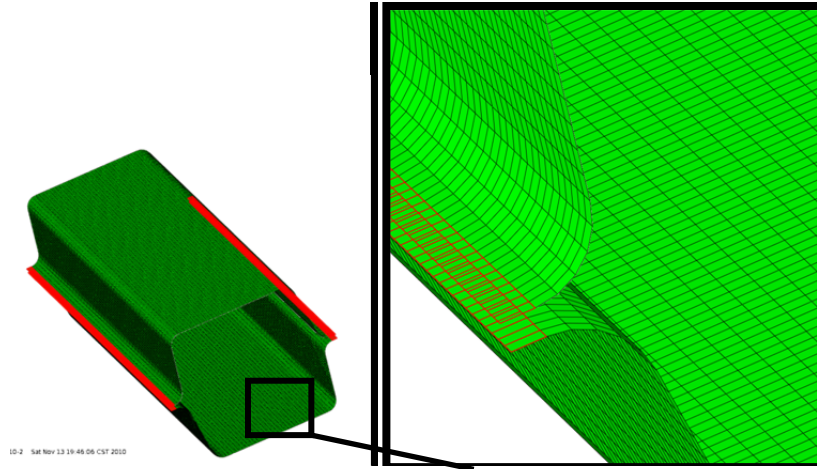
Figure 6.7   Assembling two single hat sections

Tubes are connected through the highlighted edges shown in figure 6.6 using tie contact formulation. Tie contact is constrained the surfaces of the master and slave surfaces similar to multiple constraint points as long as the clearance between two surfaces are below the tolerance defined as an input variable equal to the blank thickness. If the surfaces are out of prescribed tolerance, it becomes a contact interaction. Utilizing a proper contact formulation to perform the crush simulation is critical owing to the geometry of the double hat, expected folding pattern and the tie contact between two single hat sections. Six contact interaction sets between elements are defined in the crush simulation including interactions between lower single hat and rigid wall, upper single hat and rigid plate, interaction between upper and lower single hat sections, tie contact between the assembly edge of upper and lower surfaces, and self contact interaction for upper and lower hat separately to prevent interpenetration of each single hat. For all of the aforementioned contact interaction sets penalty function formulation is used. Despite of computational cost, using penalty function provides a proper flexibility for the explicit code to find the stable time step affected by severity of the contacts. Moreover, maximum ratio of thickness to element length is used to overcome the difficulty of the fine mesh

132

density that results to have relatively thick shell elements. This option is used to enhance the effect of contact thickness and consequently to reduce the mesh distortion.

Crush simulation is done by fixing the tube in one end and applying load through a rigid wall defined with prescribed displacement in the other end. The rigid wall is defined to move with constant velocity to simulate constant loading rate as shown in figure 6.7.
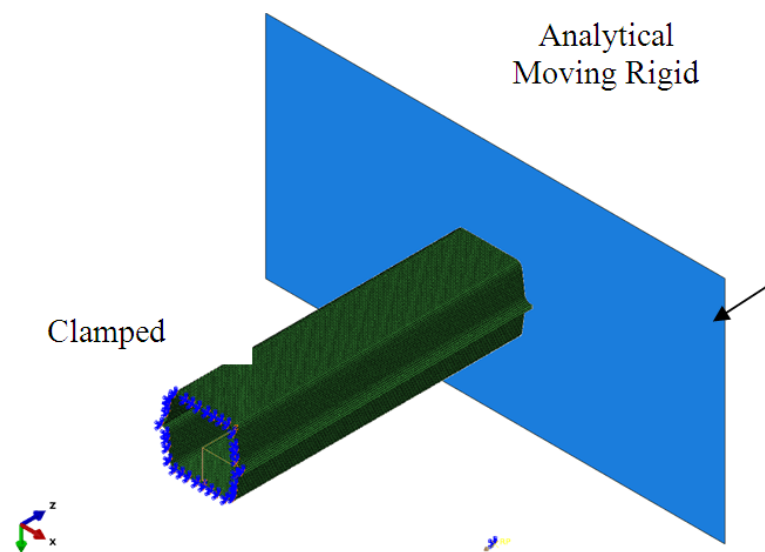
Figure 6.8   Description boundary conditions and loading for crush

The material behavior in the crush tube is also divided into three distinct regions as side, corner and unaffected sections. The plastic strain resulted from forming process changes the yield point in the stress-strain behavior and resulted in different properties.

The material model used in this study is piece-wise linear isotropic hardening. The constant for the linear kinematic hardening is calculated based on the slope of a line connecting two adjacent points in stress-strain curve. Model uses von Misses yield surface and the 1D stress-strain input is considered as equivalent von-Misses stress versus effective plastic strain. Coupling scheme is utilized by transferring residual stresses and

133

equivalent plastic strains as the material state variables. The yield surface expands due to the isotropic hardening assumption in the model and therefore the instantaneous yield point varies during loading process. The yield point at the end of the forming simulation is captured by finding the plastic strain. In this study, a magnesium AZ31 sheet material data at room temperature is used for all the simulations. In order to account for the rate dependency, the stress-strain curves are provided in two different rates such that the other rates can be interpolated based on the assigned curves. The elastic modulus, Poisson ratio and density are 45GP, 0.33 and 1.738 kg/m3 respectively. The material behavior in terms of true stress versus true strain is plotted in figure 6.9.
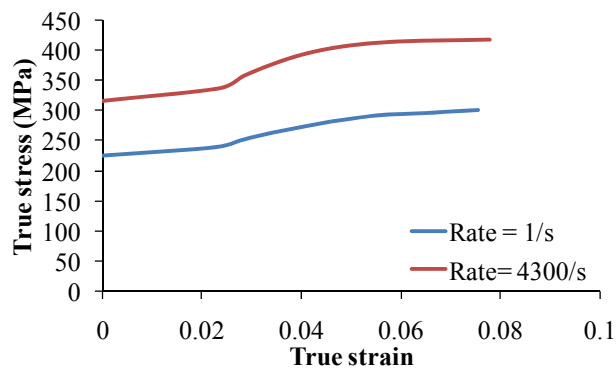
Figure 6.9   Magnesium AZ 31 stress-strain behavior in two different strain rates

6.4.1.1   Parametric Model

An automated parametric model is developed for coupled forming-crush simulation. A double hat tube is considered which has symmetry in cross section. All the runs are controlled through a global shell script that creates, submits and post-processes the models. The script requires a model input file for stamping, springback and crush analyses as the FE input decks and. A FORTRAN code is developed to insert the design variable parameters inside the FE input decks from the predefined design of experiment

134

(DOE) table. Once the input decks are created, they will be copied to each folder such that stamping and springback simulations performed sequentially for a set of design variables offered by the DOE table rows.

In this study, both of single hat tubes are considered to have same geometric attributes as well as same manufacturing processes parameters but the parametric model can account for non-symmetric cross section parameters as well. The mesh density is held constant for double hat tubes such that in longitudinal and cross-sectional directions 210 and 125 elements are defined. This mesh density is derived as an optimum mesh density for all the three simulations. The tube geometry will be produced in deep drawing stage and will be remained same for the spring back simulations. The blank length is always equal to 250mm where as the blank width is selected to be twice higher than upper or lower single hat section perimeters therefore, the width of the blanks sheet varies based on the tube width. This ratio can be considered as a manufacturing process variable. However, in the present study, this ratio is constant. The design variables include the geometric attributes that are intended to be optimized in the performance level and manufacturing process parameters in the stamping simulations. However, in the process simulation both geometric and manufacturing parameters are considered as model parameters to capture the updated geometry from the performance level. Geometric attributes includes tube cross sectional dimensions including tube *width*, *height*, *corner radius* and *blank thickness* and manufacturing process parameters are *holder force*, *punch velocity* and *friction coefficients* between the work piece and tools. The friction coefficients for holders, dies and punch are assumed to be identical in this study but can be treated as different design variables. "*Width*" translated into the punch width, "*corner radius*" is translated into the die and holders' corner radius, "*thickness*" is assigned

135

directly to the shell elements defined on the blank and the "*height*" is captured by controlling the punch travel in the direction normal to the blank surface this parameter determines the simulation *termination time* as well as the prescribed *punch velocity*. *Holder force* defined as a manufacturing process parameter is the amount of holding force in the deep drawing simulation. The rate of holding force application is kept constant in all the simulations. *Punch velocity* is assigned as a constant velocity in the direction parallel to sheet metal normal this parameter along with height are determining the deep drawing simulation termination time. Friction coefficients are assigned to the contact tangential definition. In this study, both kinematic and penalty tangential contact formulations illustrate the same response for deep drawing simulation.

A parametric model is developed in PYTHON to model the crush simulation based on five geometric attributes including *width*, *height*, *corner radius, blank thickness* and *springback angle* in ABAQUS-CAE keeping the same mesh density mentioned in process simulation for the crush simulation. After generating the input file for crush simulation three material cards associated with each region is appended automatically through a FORTRAN code to include the effect of plastic strain (PEEQ) resulted from manufacturing process (figure 6.5). Each PEEQ value updates the yield point and consequently the stress-strain curve for crush simulation. Therefore, the crush simulation has two design variables or solution parameters known as PEEQ's in region 2 and 3 shown in figure 6.5.

6.4.1.1.1   Parametric study

The sensitivity analysis is performed to investigate the sensitivity of responses due to variation in the design variables in each level. FE simulation is performed using

136

the average points of the selected rage for each design variables and the responses

associated with this simulation considered as the base line responses. Then, each design

variable is perturbed by ±15% while keeping the rest of design variable constants. Table

6.8 lists the range defined for each design variable as well as the table of design variable

used for the sensitivity analysis in the manufacturing process level.

Table 6.8   The value assigned in each FE simulation for sensitivity study and the actual
            range of variables

Sensitivity	Holding Force (kN)	Punch Velocity (m/s)	Friction Coefficient
Friction Coefficient ±15%	30	6	0.225
	30	6	0.16875
	30	6	0.25875
Punch Velocity ±15%	30	6	0.225
	30	4.5	0.225
	30	6.9	0.225
Holding Force ±15%	30	6	0.225
	22.5	6	0.225
	34.5	6	0.225
Upper Bound	50	10	0.35
Lower Bound	10	2	0.1

Figure 6.10 to 6.12 show the result of the sensitivity study. Effect of varying each

manufacturing design variable by ±15% normalized and shown in each figure separately.

Bar chart is divided into two groups on the left illustrating the response that are deviated

as a result of -15% deviation of design variable and on right representing the responses

derived as a result of +15% deviation of design variable. As it is clearly shown the spring

back is very sensitive to the manufacturing parameters. The thinning is very sensitive to

the punch velocity mainly due to the rate sensitivity of the material. Rupture can highly

be affected by the tool-blank friction coefficient. Figure 6.10 to 6.12 also shows the

sensitivity of the manufacturing variables to the PEEQ in region 2 and 3 identified as

CPS (Corner equivalent plastic strain) and SPS (Side-wall equivalent plastic strain).

137

Holder Force

	Decrease (-15%)	Increase (+15%)
■ SPS	8.05%	5.01%
■ CPS	-0.33%	-3.63%
■ Rupture	1.00%	-1.15%
■ Thining	1.67%	0.54%
■ Spring Back (Tet)	-10.91%	16.92%
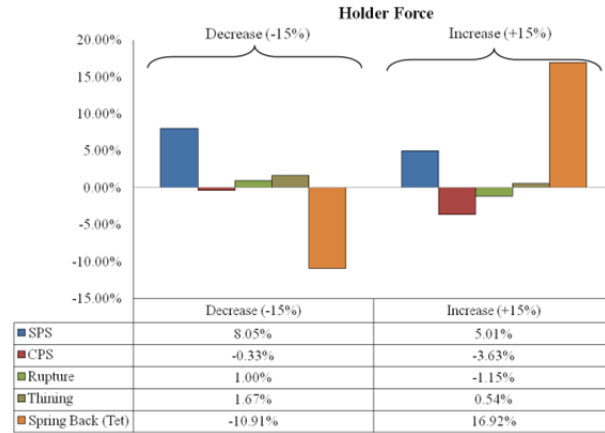
Figure 6.10   Sensitivity of the holder force on the responses measured in stamping process simulation

Punch Velocity

	Decrease (-15%)	Increase (+15%)
■ SPS	6.64%	4.27%
■ CPS	-1.86%	-5.16%
■ Rupture	4.14%	-3.86%
■ Thining	7.31%	-5.80%
■ Spring Back (Tet)	-28.02%	16.20%
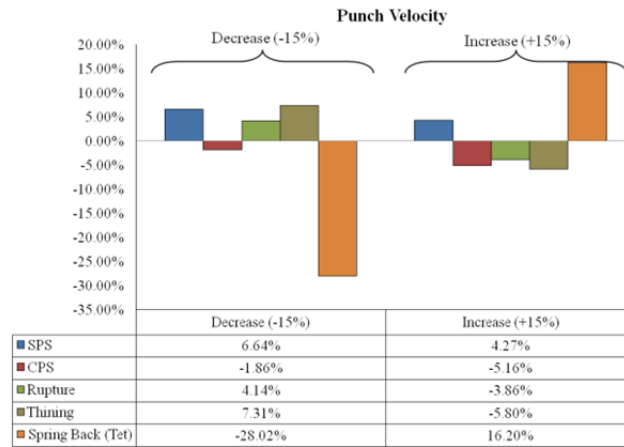
Figure 6.11   Sensitivity of the punch velocity on the responses measured in stamping process simulation

138

Friction Coefficient

	Decrease (-15%)	Increase (+15%)
■ SPS	3.07%	7.55%
■ CPS	-5.74%	-0.70%
■ Rupture	4.69%	-4.25%
■ Thining	7.95%	-5.06%
■ Spring Back (Tet)	-34.61%	51.94%
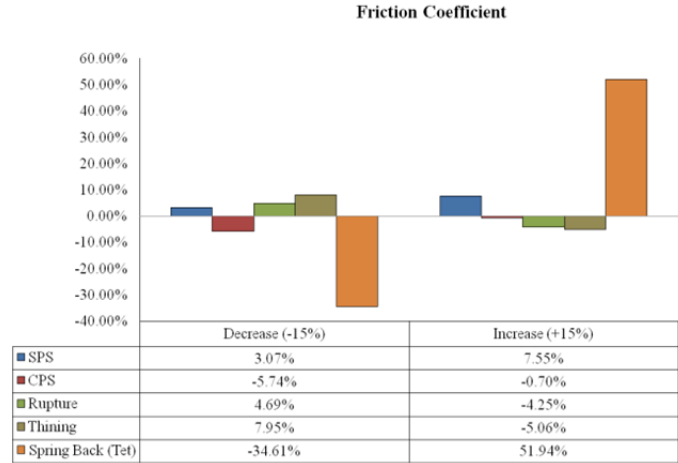
Figure 6.12   Sensitivity of the friction coefficient on the responses measured in stamping process simulation

Traditionally, the energy absorption is designed based on the geometric attributes. However, in this study, the influence of the springback and the equivalent plastic strain is also considered as design variables such that in the ATC iteration the difference between calculated PEEQ in the manufacturing level has proper consistency with the one desirable for energy absorption (performance). Similarly, a sensitivity analysis is performed at this level to identify the effect of the responses in the lower level on the crush behavior. The range defined for each design variable (response of lower level) as well as the table of design variable used for the sensitivity analysis in crush analysis level is resented in table 6.9.

139

Table 6.9   The value assigned in each FE simulation for sensitivity study and the actual range of variables

Sensitivity	Height (mm)	Width (mm)	Corner Radius (mm)	Blank Thickness (mm)	Springback Angle (Deg)	Corner PEEQ	Side Wall PEEQ
Side Wall PEEQ ±15%	27.5	55	5	1.75	4.5	0.425	0.85
	27.5	55	5	1.75	4.5	0.425	0.7225
	27.5	55	5	1.75	4.5	0.425	0.9775
Corner PEEQ ±15%	27.5	55	5	1.75	4.5	0.425	0.85
	27.5	55	5	1.75	4.5	0.36125	0.7225
	27.5	55	5	1.75	4.5	0.48875	0.9775
Springback Angle ±15%	27.5	55	5	1.75	4.5	0.425	0.85
	27.5	55	5	1.75	3.825	0.425	0.85
	27.5	55	5	1.75	5.175	0.425	0.85
Maximum	35	70	7.5	2.5	9	0.8	1.98
Minimum	20	40	2.5	1	0	0.05	0.088

The results of the sensitivity analysis on the performance responses are presented in figures 6.13 to 6.15. Since no geometric attribute is changed, the mass of the tube will not change in this analysis. Mean crush force and maximum force are known to be the responses in the performance level. Similar to the previous sensitive study, Bar chart is divided into two groups on the left illustrating the response that are deviated as a result of -15% deviation of the capacities in the design variable vector and on right representing the responses derived as a result of +15% deviation of the same variables. It is shown that the distortion angle and side wall (region 2) PEEQ has a nonlinear effect on the mean crush force and inverse effect on the maximum force. The same effect is observed for the corner (region 3) PEEQ for the mean force and direct relation with the maximum force.
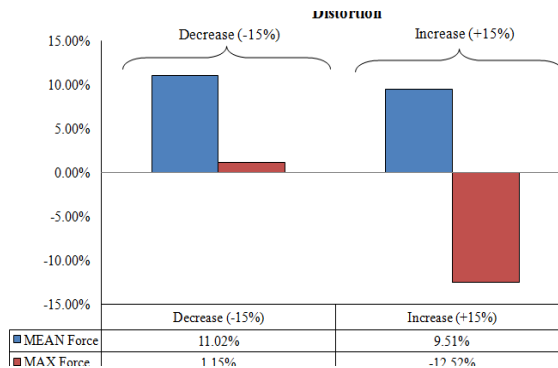
Figure 6.13   Sensitivity analysis on corner radios and its contribution to responses
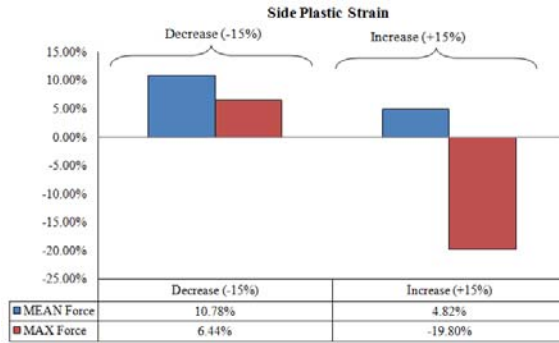
Figure 6.14   Sensitivity analysis on blank height and its contribution to responses
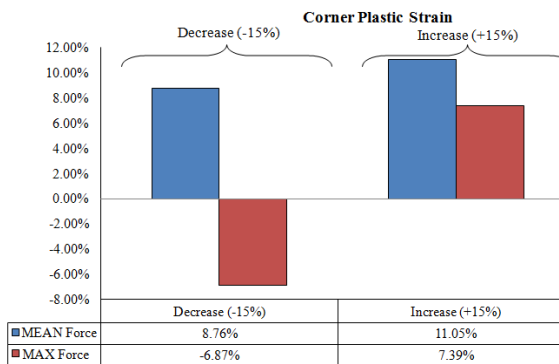
Figure 6.15   Sensitivity analysis on the blank thickness and its contribution to responses

6.4.1.1.2   Multi-level Process-Performance optimization based on ATC

In order to reduce the computational cost during design optimization based on ATC, surrogate models known as metamodels are used. In order to train or construct the metamodels a set of sample inputs and outputs are required for each level. These samples could be produced by the design of experiment (DOE) methods. The sampling method tries to give a proper distribution throughout the range specified. In this article, Latin hypercube sampling is used to produce a uniform distribution in the design space. The presented training points are captured through Latin hypercube sampling in MATLAB. Fifty points are generated for each level of hierarchy. The process level contains seven

141

variables including four geometric attributes and three process parameters as described in the previous sections. Table 6.10 is listed out the training points used for the process (bottom level).

Table 6.10   Design of experiment points based for the bottom level (manufacturing process) problem

DOE points	Height (mm)	Width (mm)	Corner Radius (mm)	Blank Thickness (mm)	Springback Angle (Deg)	Corner PEEQ	Side Wall PEEQ	DOE points	Height (mm)	Width (mm)	Corner Radius (mm)	Blank Thickness (mm)	Springback Angle (Deg)	Corner PEEQ	Side Wall PEEQ
1	27.45	54.99	4.98	1.75	4.49	0.42	0.84	26	33.03	41.48	6.61	2.47	6.90	0.77	1.81
2	20.42	69.54	3.20	2.47	0.92	0.06	0.14	27	34.51	62.59	2.91	1.27	8.07	0.65	0.98
3	21.19	40.74	6.91	2.41	0.22	0.79	1.83	28	30.46	64.34	3.09	2.41	0.09	0.09	0.16
4	34.82	43.98	7.21	2.33	0.36	0.08	0.13	29	33.87	40.21	2.69	2.06	8.16	0.07	0.15
5	33.99	66.42	6.14	2.48	8.40	0.79	1.20	30	20.17	67.68	7.06	1.56	8.04	0.74	1.24
6	21.77	40.27	6.16	2.43	8.94	0.77	1.21	31	22.85	44.14	7.14	1.04	0.05	0.08	0.17
7	34.93	50.98	2.64	1.02	0.12	0.12	0.20	32	20.56	67.51	4.96	2.50	2.32	0.79	1.22
8	20.25	65.71	3.24	2.27	8.31	0.06	0.10	33	20.44	64.87	3.38	1.11	8.99	0.22	0.49
9	33.40	69.29	4.71	1.01	0.27	0.78	1.28	34	21.19	40.04	3.27	2.38	5.62	0.41	1.02
10	34.33	44.06	2.57	2.30	3.22	0.79	1.20	35	33.73	69.55	3.46	2.26	7.56	0.16	0.36
11	34.84	45.69	5.80	1.11	0.86	0.79	1.98	36	20.74	41.75	2.75	1.91	1.19	0.71	1.12
12	21.41	67.75	2.84	2.46	8.37	0.78	1.68	37	20.06	67.38	6.30	1.41	0.68	0.20	0.32
13	27.02	41.16	7.35	1.14	0.14	0.75	1.22	38	34.92	49.81	7.35	2.09	8.61	0.17	0.26
14	21.91	43.02	6.84	1.07	8.43	0.63	1.57	39	26.10	55.90	2.59	1.04	0.68	0.79	1.74
15	28.96	69.99	7.49	1.45	1.06	0.07	0.17	40	29.58	68.53	7.45	2.37	1.61	0.73	1.52
16	22.34	48.07	2.61	1.15	0.04	0.17	0.42	41	32.29	40.75	4.83	1.82	0.07	0.15	0.38
17	20.05	64.43	2.64	1.12	5.13	0.73	1.11	42	22.23	55.63	7.17	1.17	8.40	0.11	0.19
18	31.90	47.14	7.08	2.20	8.92	0.08	0.20	43	24.00	59.32	7.34	1.14	0.40	0.65	1.50
19	22.28	41.54	3.38	1.02	5.88	0.06	0.09	44	33.25	64.73	2.84	1.05	3.47	0.25	0.60
20	21.03	68.94	7.18	2.19	8.32	0.14	0.32	45	20.99	46.65	7.49	2.41	0.89	0.13	0.31
21	30.03	46.18	2.58	1.47	8.74	0.78	1.95	46	34.86	62.34	6.56	1.50	2.39	0.21	0.31
22	33.18	68.93	3.01	1.99	0.25	0.66	1.62	47	27.27	67.48	6.73	1.70	8.22	0.71	1.71
23	34.27	69.19	6.99	1.01	8.57	0.30	0.59	48	30.00	42.67	2.78	2.43	0.70	0.62	1.43
24	34.18	40.84	6.36	1.28	8.14	0.70	1.14	49	25.12	69.44	2.86	1.23	4.96	0.14	0.23
25	20.53	44.39	5.11	2.49	2.27	0.12	0.19	50	34.24	44.08	6.81	1.11	5.22	0.23	0.49

Each row represents a set of parameters for coupled process-springback (deep drawing-springback) simulations in table 6.10. Six responses are extracted for each set of simulations including rupture and springback based on the equations expressed in previous section (3.1,3.2). The values associated with each response in listed in table 6.11. It is worth noting that four out of fifty simulations which are highlighted in table 6.10 are not successfully ran due to the computational convergence resulted from extensive plastic deformation and contact instabilities in stamping, spring back and crush simulations.

142

Table 6.11   Bottom level responses including local responses and manufacturing effects

DOE points	Side Wall PEEQ	Corner PEEQ	Rupture	Thinning	Springback Angle (Deg)	DOE points	Side Wall PEEQ	Corner PEEQ	Rupture	Thinning	Springback Angle (Deg)
1	0.44	0.24	1527.00	116.53	1.64	24	0.99	0.596	3895.90	419.28	1.39
2	0.38	0.24	1727.30	97.83	3.36	25	2.50	0.68	23988.00	706.98	0.80
3	0.44	0.20	482.20	8.60	3.66	26	0.30	0.162	658.70	47.57	3.17
4	0.54	0.29	1706.90	172.77	1.58	27	0.20	0.09024	158.14	2.26	8.74
5	0.48	0.31	2037.10	124.34	1.52	28	0.60	0.36	3066.40	252.29	1.07
6	0.95	0.52	3363.30	297.59	0.22	29	0.44	0.24	1629.70	160.10	0.43
7	0.17	0.30	504.51	41.18	1.31	30	2.20	0.55	21297.00	840.96	0.52
8	0.58	1.20	8601.50	637.71	1.56	31	2.90	0.8	30216.00	870.47	0.04
9	0.24	0.19	587.51	48.69	3.65	32	0.94	0.427	4191.10	345.38	0.40
10	0.20	0.09	240.29	8.72	6.10	33	0.30	0.1054	282.53	8.26	3.18
11	0.20	0.09	432.20	27.44	3.98	34	0.42	0.191	460.17	12.88	4.82
12	0.25	0.15	316.05	16.81	4.25	35	0.84	0.366	4356.10	397.43	2.06
13	0.59	0.26	1602.40	149.27	2.28	36	0.39	0.21	1520.40	113.71	1.77
14	0.40	0.18	949.01	43.96	1.63	37	0.47	0.21	1154.10	72.34	1.14
15	0.41	0.22	618.52	39.40	1.42	38	0.23	0.104	268.74	10.24	2.80
16	0.38	0.21	1257.20	88.95	3.79	39	0.19	0.15	403.01	28.07	4.74
17	2.60	0.72	29561.00	787.96	0.32	40	0.56	0.25	1464.00	145.38	2.92
18	2.80	0.75	35001.00	856.95	0.74	41	0.45	0.16	853.49	29.86	5.36
19	0.20	0.11	227.10	16.10	2.52	42	0.31	0.11	268.83	8.72	3.01
20	0.25	0.14	421.70	24.11	3.37	43	0.34	0.123	1095.60	96.79	0.89
21	0.68	0.37	1482.80	70.74	1.50	44	2.50	0.69	22759.00	895.78	0.95
22	0.06	0.38	2618.90	182.12	1.36	45	0.22	0.098	224.50	9.01	4.38
23	0.63	0.34	2106.00	202.41	1.76						

The same procedure is applied for the performance (top) level problem. A set of training point is introduced via LHS to generate the DOE table. the design variables in this level are five geometric attributes and two material history state variables as known as PEEQ in the side-wall and corner part of the tube. Table 6.12 shows the values of the DOE points.

143

Table 6.12   Responses of FE simulation in the top level for the DOE in table 6.11.

DOE points	Mean Crush Force (kN)	Max Crush Force (kN)	Mass (kg)	DOE points	Mean Crush Force (kN)	Max Crush Force (kN)	Mass (kg)
1	47.27	130.47	0.17	26	94.75	194.94	0.24
2	83.14	194.53	0.25	27	33.96	132.48	0.15
3	81.87	146.53	0.18	28	80.21	221.31	0.27
4	71.15	198.60	0.24	29	66.54	159.05	0.20
5	99.13	243.06	0.30	30	44.69	133.18	0.15
6	77.46	167.94	0.18	31	21.84	64.37	0.08
7	19.10	82.01	0.11	32	83.09	192.27	0.25
8	75.47	165.15	0.22	33	23.82	89.58	0.11
9	20.58	88.77	0.12	34	77.89	138.67	0.18
10	71.20	183.64	0.23	35	85.51	220.26	0.28
11	22.91	89.50	0.12	36	47.23	111.57	0.14
12	85.80	203.55	0.24	37	36.04	106.51	0.14
13	26.68	75.76	0.10	38	72.50	193.15	0.23
14	23.68	75.28	0.08	39	18.94	81.87	0.10
15	37.56	139.56	0.17	40	85.53	230.29	0.27
16	19.80	71.35	0.10	41	46.85	132.19	0.17
17	22.55	76.20	0.11	42	28.14	93.41	0.11
18	76.43	184.14	0.22	43	24.30	81.92	0.11
19	17.10	61.20	0.08	44	22.54	99.95	0.12
20	72.62	178.43	0.22	45	80.98	159.06	0.19
21	39.28	124.49	0.14	46	40.28	134.65	0.18
22	57.97	195.96	0.24	47	55.44	146.41	0.19
23	25.08	96.92	0.13	48	70.13	168.04	0.22
24	30.82	114.74	0.13	49	26.25	98.37	0.13
25	81.53	158.99	0.19	50	24.44	90.47	0.11

The PYTHON script as well as material manipulator will generate input deck in ABAQUS/EXPLICIT to extract responses for the crush simulation. The responses of crush simulation in terms of mean crush force from equation 4.1, maximum force and the tube weight are shown in table 6.13 as the response values associated with performance level problem.

Table 6.13   Design of experiment points for bottom level FE simulation based on Latin hypercube sampling (LHS) method

DOE points	Width (mm)	Height (mm)	Corner Radius (mm)	Blank Thickness (mm)	Holder force (kN)	Punch Velocity (m/s)	Friction Coefficient	DOE points	Width (mm)	Height (mm)	Corner Radius (mm)	Blank Thickness (mm)	Holder force (kN)	Punch Velocity (m/s)	Friction Coefficient
1	54.91	27.49	4.98	1.75	29.95	5.97	0.22	24	60.91	32.17	3.09	2.41	10.38	2.48	0.15
2	42.38	20.37	6.91	2.41	10.98	9.94	0.30	25	67.75	20.11	2.69	2.06	46.25	2.20	0.25
3	69.64	21.99	7.21	2.33	11.59	2.32	0.13	26	40.34	33.84	7.06	1.56	45.75	9.35	0.14
4	67.98	33.21	6.14	2.48	47.32	9.84	0.11	27	45.70	22.07	7.14	1.04	10.23	2.34	0.25
5	43.55	20.13	6.16	2.43	49.74	9.64	0.12	28	41.13	33.75	4.96	2.50	20.32	9.87	0.11
6	40.50	32.86	3.24	2.27	46.93	2.14	0.11	29	40.87	32.44	3.38	1.11	49.96	3.83	0.28
7	66.81	34.65	4.71	1.01	11.19	9.80	0.13	30	40.02	20.02	2.38	2.26	34.96	5.83	0.35
8	68.66	22.03	2.57	2.30	24.30	9.90	0.10	31	67.46	34.78	3.46	2.26	43.58	3.12	0.31
9	69.69	22.84	5.80	1.11	13.84	9.93	0.35	32	41.47	20.87	2.75	1.91	15.28	9.01	0.12
10	54.04	20.58	7.35	1.14	10.60	9.52	0.13	33	40.12	33.69	6.30	1.41	13.00	3.59	0.13
11	43.82	21.51	6.84	1.07	47.47	8.16	0.35	34	69.84	24.90	7.35	2.09	48.27	3.24	0.11
12	57.93	34.99	7.49	1.45	14.69	2.20	0.35	35	52.20	27.95	2.59	1.04	13.03	9.88	0.28
13	44.67	24.03	2.61	1.15	10.17	3.25	0.35	36	59.17	34.27	7.45	2.37	17.16	9.27	0.24
14	63.79	23.57	7.08	2.20	49.62	2.31	0.35	37	64.57	20.37	4.83	1.82	10.31	3.11	0.34
15	44.56	20.77	3.38	1.02	36.12	2.07	0.12	38	44.46	27.82	7.17	1.17	47.35	2.63	0.17
16	42.06	34.47	7.18	2.19	46.98	2.94	0.31	39	29.66	29.66	7.34	1.14	11.80	8.40	0.30
17	60.06	23.09	2.58	1.47	48.83	9.82	0.35	40	66.50	32.37	2.84	1.05	25.44	4.16	0.32
18	66.35	34.46	3.01	1.99	11.13	8.53	0.34	41	41.98	23.33	7.49	2.41	13.95	2.88	0.30
19	68.54	34.59	6.99	1.01	48.10	4.72	0.21	42	69.71	31.17	6.56	1.50	20.64	3.66	0.10
20	68.35	20.42	6.36	1.28	46.19	8.95	0.13	43	54.54	33.74	6.73	1.70	46.53	9.03	0.33
21	41.06	22.20	5.11	2.49	20.11	2.77	0.11	44	59.99	21.34	2.78	2.43	13.10	8.12	0.30
22	66.06	20.74	6.61	2.47	40.67	9.73	0.31	45	68.48	22.04	6.81	1.11	33.22	3.92	0.26
23	69.01	31.30	2.91	1.27	45.89	8.36	0.10								

144

6.4.1.1.3   Metamodeling

The Metamodeling process here is done through radial basis function. Two main strategies are used to verify the metamodels and tune up the models. The models were tuned by selecting the parameter or combination of parameters that produced the least error for each response for each material. Cross-validation generalized mean square error (GMSE) was used as the error metric. The cross-validation approach is used when the number of design points is limited as in crash simulations. A metamodel is created using all except one design point and the predicted response is compared to the actual response at that design point to measure error. This process is repeated for all design points and the average is used as the overall error of the metamodel. At the end, five test points are also simulated and compared with the predicted values of metamodels. It is shown that the average error is less than 15% for all the responses.

6.4.1.1.4   ATC optimization

The bi-level hierarchical optimization problem in the ATC framework is formulated based on the desired responses in the process (bottom) and performance (top) levels. The problem is formulated as a bottom-top coordination problem such that optimization begins in the bottom level and the responses are mapped to the top level.

The system (top) level problem will consider the geometrical optimization and the material history information from manufacturing process to enhance the energy absorption and weight efficiency of the double-hat tube. The top-level optimization problem is formulated as

145

$$\begin{cases} \min_{x^u = \{x^u_{uj}, R^u_{li}, \varepsilon_{Ri}\}} \left(P_{max}\left(x^u_{uj}, R^u_{li}\right) - P_m\left(x^u_{uj}, R^u_{li}\right) - 0\right)^2 + \left(M(x^u_{ui}) - 0\right)^2 + w\sum_{i=1}^3 \varepsilon_{Ri} \\ \quad subject\ to \qquad \left(R^u_{li} - R^l_{li}\right)^2 \le \varepsilon_{Ri} \\ \qquad\qquad\qquad 40 \le x^u_{u1} \le 70 \\ \qquad\qquad\qquad 20 \le x^u_{u2} \le 35 \\ \qquad\qquad\qquad 2.5 \le x^u_{u3} \le 7.5 \\ \qquad\qquad\qquad 1.0 \le x^u_{u4} \le 2.5 \\ \qquad\qquad\qquad 0.0 \le R^u_{l1} \le 10.0 \\ \qquad\qquad\qquad 0.05 \le R^u_{l2} \le 1.8 \\ \qquad\qquad\qquad 0.06 \le R^u_{l3} \le 1.8 \\ \qquad\qquad\qquad 0.0 \le \varepsilon_{R1} \le 1.0 \\ \qquad\qquad\qquad 0.0 \le \varepsilon_{R2} \le 1.0 \\ \qquad\qquad\qquad 0.0 \le \varepsilon_{R3} \le 1.0 \\ \qquad\qquad\qquad where\ i = 1,\cdots,3\ and\ j = 1,\cdots,4 \end{cases} \qquad (6.5)$$

where $P_{max}\left(x^u_{uj}, R^u_{li}\right)$, $P_m\left(x^u_{uj}, R^u_{li}\right)$ and $M(x^u_{ui})$ are the maximum crush force, mean crush force, and mass of the tube, respectively, in the performance level. The forces depend on the geometric attributes or local design variables identified as width, height, corner radius, and blank thickness corresponding to index j going from 1 to 4, respectively, as well as the calculated capabilities for distortion angle, corner PEEQ, and side PEEQ for values of index i going from 1 to 3, respectively, in the process level.

The aim of the optimization problem in the top level is to minimize the difference between the maximum crush force and the mean crush force since it is desired to increase the mean crush force and at the same time reduce the maximum force to the same level of mean crush force to reduce the force variation appears at the beginning of the crush with the steady state mean force. Therefore, the target is assigned to be zero. The vector of design variables includes the geometric attributes , the response capabilities , and the relaxation tolerances for the auxiliary constraints defined as . The values are the targets that are transferred from the process level. The auxiliary constraint is defined here as three separate inequalities in order to impose an even relaxation tolerance on all of them. Side constraints are imposed on all members of the design variable vector as shown in

146

equation (11). The top-level problem in this formulation is mainly limited to identify the best geometry for energy absorption and weight efficiency. The weight factor w in the objective function imposes a penalty for non-zero relaxation tolerances while helping to enhance the computational convergence of ATC. This factor is selected and scaled through the iterations of ATC to magnify the contribution of relaxation parameters in the objective function for deviations greater than zero.

In the process-level optimization problem, we are focusing on the manufacturing quality of the component. Three manufacturing process design variables (i.e., holder force, friction coefficient, and punch velocity) are defined to control the manufacturing quality as measured by two local responses: rupture and thinning. The process-level optimization problem is formulated as

$$\begin{cases} \begin{array}{cc} \min \\ x^l = \{x_{lk}^l\} \end{array} & \left(Rup(x_{lk}^l) - 0\right)^2 \;+\; \left(Thn(x_{lk}^l) - 0\right)^2 \;+\; \sum_{i=1}^{3}\left(R_{li}^l(x_{lk}^l) - R_{li}^u\right)_2^2 \\ \\ \quad subject\ to & \begin{array}{l} 10 \le x_{l1}^l \le 50 \\ 2 \le x_{l2}^l \le 10 \\ 0.1 \le x_{l3}^l \le 0.35 \\ where\ i = 1,\cdots,3\ \ and\ \ k = 1,\cdots,3 \end{array} \end{cases} \tag{6.6}$$

where $Rup(x_{lk}^l)$ represents the rupture and $Thn(x_{lk}^l)$ the thinning metric as defined in Eqs. (4) and (5), respectively. Besides minimizing the local-level objectives, the ATC formulation also seeks to minimize the difference between the targets cascaded down from the top level and the capabilities calculated in the process level. The responses are known as the springback deviation angle $R_{li}^l(x_l^l)$, PEEQ in the corner regions $R_{l2}^l(x_{lk}^l)$, and PEEQ in the side walls $R_{l3}^l(x_{lk}^l)$. As mentioned earlier, metamodels are created to calculate the rupture, thinning, and responses in vector. The springback value in this formulation is treated as a parameter that will also be determined based on the top-level

147

demand. Therefore, instead of minimizing the springback angle in the bottom level, it is balanced based on the demands of the performance analysis. In the process-level problem, the local design variables represent the process control parameters holding force, friction coefficient, and punch velocity, respectively.

Figure 12 illustrates the design optimization problem in each level. The ATC optimization of the two-level problem requires an iterative solution process until an optimum design point is found where the relaxation tolerances's in the top level becomes very small. In this case, the solution process started from the bottom-level problem by specifying an initial guess for the top-level demands or targets. All the responses are normalized based on the maximum value reported in the DOE Tables 5 and 3. Using GA, the optimum manufacturing process parameters and the corresponding responses are found. With manufacturing responses transferred to the top level, GA is used to find the optimum geometry and target response values. This bottom-top solution iteration process is continued until convergence is reached.

Our study showed that the relaxation tolerance bounds in the system level should be selected with caution. During the early iteration of ATC, the optimization problem may report no feasible solution if a tight range is assigned to these variables.
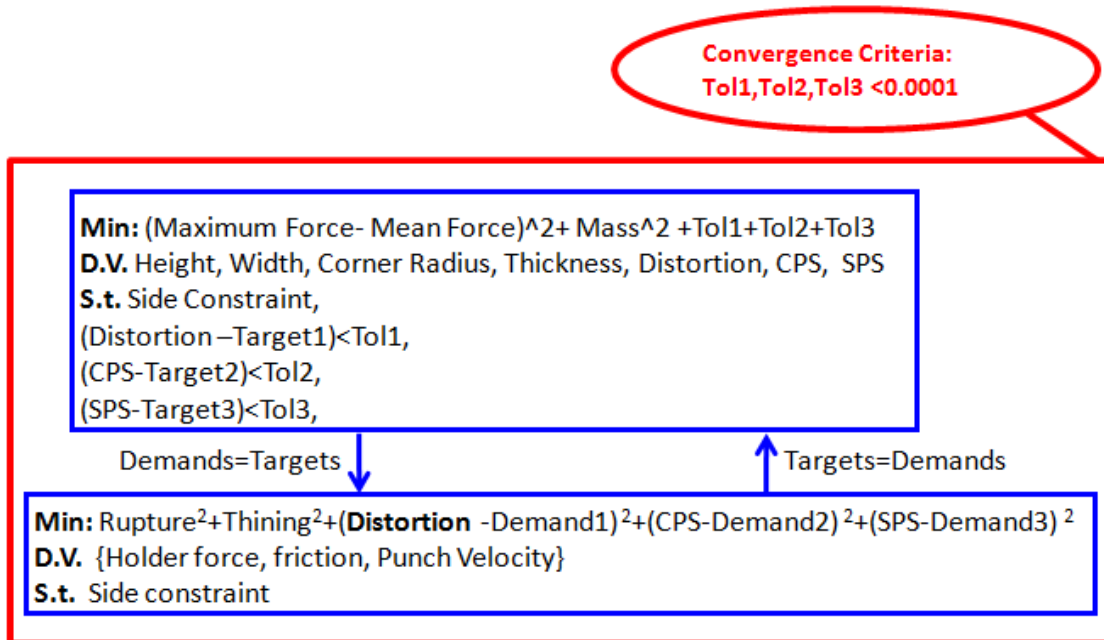
Figure 6.16   flowchart of ATC approach for coupled process-performance optimization

Since the GA optimization method is a population based approach, it is well suited to capture the global optimum point. The Population size for both the top- and bottom-level problems consists of twenty individuals. The initial population is selected from the feasible design domain within the specified bounds of design variables that satisfy the constraints defined in the optimization problem. The individuals in the population are identified by specific chromosomes in a binary format.

The scaling function used to rank the objective function is defined based on ranking the individuals. Once the individuals are ranked, a score will be assigned to each individual based on $\sqrt{r}$ value, where r is the rank associated with each individual in the population. The square root yields nearly equal scores for poorly ranked individuals. Therefore, the selection procedure for the parents of the next generation uses this fitness scaling procedure such that selection function assigns a higher probability of selection to individuals with higher fitness scaled values. It is worth noting that if the scaled value

149

between two individuals has high gradients, the individuals with the highest scaled value reproduce too quickly and dominate the population pool. Consequently, GA may be trapped in a local region of the design domain and fail to search any other region for global optimum.

Stochastic uniform selection is used to find the parents for the next generation. In order to produce the next generation, the two best (elite) individuals in the current population are retained while crossover and mutation operations are performed to generate the remaining eighteen individuals in the population (i.e., 14 by crossover and 4 by mutation). The crossover operation is performed using scattered function where a random binary vector is generated such that value 1 and 0 specify which member of the parents should be considered to create the child. The motivation behind the mutation is to preserve diversity in the population and enable broader search through small random change in the individuals utilizing Gaussian distribution to create mutation children. The migration takes place every twenty generations with fraction of the number of individuals specified as 20% in the forward direction.

The nonlinear constrained optimization problem in each level is expressed as a Lagrange function by combining the nonlinear constraints and objective function using a penalty parameter. The approximate subproblem is minimized using GA by considering an initial value of 10 for the penalty parameter. The Lagrangian estimates are updated once the subproblem is minimized with a feasible solution. Otherwise, the penalty parameter is increased by a factor of 10. The optimization process is terminated once one of the criteria including the number of generations reaching the maximum of 100 or objective function change in two consecutive solutions reaching the tolerance of 1e-6 is

150

met. The feasibility of the solution is checked based on the nonlinear constraint tolerance of 1e-6.

6.4.1.1.5　Optimization results

The optimal points of the ATC formulation in some selected iterations are presented in Tables 6.14 and 6.15 for the top and bottom level problems, respectively. The results in each table are for ten different iteration points including the final solution shown in the last row of each table. The optimum geometry in Table 6.14 represents approximately a rectangular cross-section with a medium corner radius and minimum blank thickness values. While for height the optimum value is its lower bound, the optimum width is closer to the upper bound value. The springback allowed for this design is 3.36 meaning that the corner angle is 93.36 degree instead of 90 degree, which satisfies the design constraints by allowing the cross section to deviate from a perfect rectangular cross-section.

Table 6.14　Sample solutions for the performance (top) level problem in different iterations using initial w=1.5

ATC Iteration number	Height (mm)	Width (mm)	Corner Radius (mm)	Blank Thickness (mm)	Spring Back Angle (Deg)	Corner PEEQ	Side Wall PEEQ	Spring back Tolerance	Corner PEEQ Tolerance	Side Wall PEEQ Tolerance
1	26.06	40.35	7.17	1.01	2.55	0.154	1.05	0.1546	0.0432	0.0530
10	30.02	65.47	4.53	1.03	3.62	0.057	0.43	0.0004	0.0045	0.0218
20	26.52	43.82	5.75	1.02	3.82	0.10	0.45	0.0135	0.0046	0.0079
40	26.67	63.11	6.00	1.02	3.40	0.10	0.42	0.0344	0.0042	0.0030
60	20.00	57.99	7.45	1.19	2.64	0.06	0.40	0.0011	0.0050	0.0015
79	20.17	44.14	7.50	1.00	2.90	0.11	0.51	0.0001	0.0152	0.0600
90	28.39	45.94	5.05	1.00	3.71	0.07	0.67	0.1271	0.0030	0.0387
102	21.23	60.80	4.15	1.21	3.62	0.08	0.59	0.0265	0.0082	0.0818
103	22.37	50.19	7.41	1.05	2.78	0.19	0.50	0.0009	0.0010	0.0155
104	20.00	64.76	5.45	1.00	3.36	0.08	0.33	0.0000	0.0000	0.0001

Results in Table 6.15 show that it is desirable to have high punch velocity, low friction and medium range holder force to have the best quality for the manufacturing and the demands of the top level.

Table 6.15   Sample solutions for the process (bottom) level problem in different iterations using initial w=1.5

Iteration number	Holder force (kN)	Punch Velocity (m/s)	Friction Coefficient
1	10.00	8.54	0.35
10	42.62	2.57	0.33
20	47.66	4.05	0.25
40	29.93	3.61	0.21
60	43.37	4.12	0.20
79	13.30	2.25	0.24
90	42.83	2.00	0.10
102	27.73	3.79	0.21
103	25.75	2.22	0.25
104	48.54	9.92	0.10

The solution details of the selected iterations are shown in Table 6.16. The weight factor *w* starts with an initial value of 1.1 and grows in each iteration before reaching its final value of 104 in the last iteration. Both top- and bottom-level optimizations presented a feasible minimum solution throughout the optimization process. The number of function evaluations for the top problem varies for each iteration whereas it remains constant for the bottom level. The number of generations in the top level problem varies from 4 to 22, whereas this number for the bottom level problem stays constant at 51. The objective function variations in Table 9 indicate that greater oscillation occurs in the solution of the top-level problem than the bottom. This is primarily due to the fluctuations observed in the crush force response. It is also worth noting that although the number of function calls in each level is rather high, the computational cost remains reasonably low due to the use of analytical surrogate models in lieu of high fidelity

152

response simulations. the 20 populations are evaluated within less than 0.01 second of CPU time while using parallel evaluation procedure where as the time required to perform the simulation for each design point are approximately 35, 5, 180 minutes.

Table 6.16 The list of computational variables and outputs at each iteration for the performance (top) level and process (bottom) level using initial w=1.1

Iteration number	Weight Factor	Average of Relaxation Tolerances	Toplevel ExitFlage	Toplevel Objective function	Toplevel Function count	Toplevel GA Generation	Bottom level ExitFlage	Bottom level Objective function	Bottom level Function count	Bottom level GA Generation
1	1.1	0.0836	1	1.7456	4740	4	1	1.4034	1040	51
10	11.0	0.0089	1	1.6456	7200	5	1	0.0080	1040	51
20	22.0	0.0087	1	1.5331	5020	4	1	0.0102	1040	51
40	44.0	0.0139	1	19.2419	4680	4	1	0.0263	1040	51
60	66.0	0.0025	1	10.8404	4780	4	1	0.0202	1040	51
79	86.9	0.0251	1	47.8914	22980	21	1	0.0397	1040	51
90	99.0	0.0563	1	21.2717	4288	4	1	0.0308	1040	51
102	112.2	0.0388	1	8.7915	4640	4	1	0.0098	1040	51
103	113.3	0.0058	1	2.9293	5160	4	1	0.0435	1040	51
104	114.4	0.0000	1	0.1884	24940	22	1	0.0229	1040	51

The result obtained from multi-level optimization is compared with some of the points in the Pareto frontier of multi-objective AAO optimization in fig. 6.17. In this figure, lower bound and upper bound of mean and max crush forces in the Pareto front are plotted to shown the range of optimal solutions for AAO. Additionally, the response in the Pareto frontier which are equal or close to the ATC responses in the mean crush force and maximum force are shown for comparison. It has been shown that the similar mean and max crush force is obtained from ATC formulation.

153
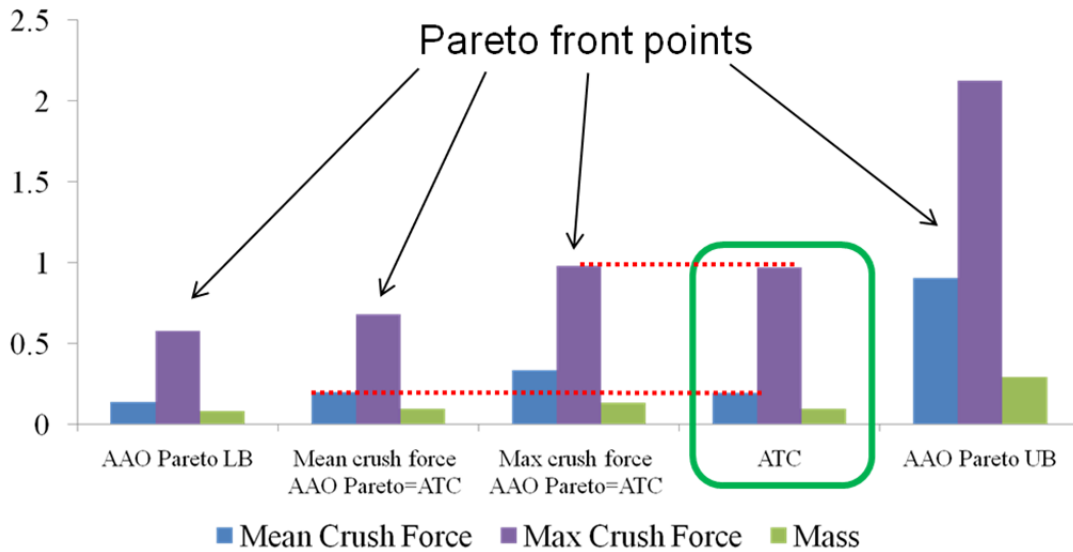
Figure 6.17   Comparison between the AAO and ATC

Figure 6.18 shows the optimum values of the geometric attributes obtained from ATC and its equivalent in the Pareto front result of AAO. It is seen that the ATC optimization provides lower value for the side walls. This shows that the ATC considers the effect of plastic deformation and thinning in the manufacturing process by reducing the punch travel in the forming process.

154
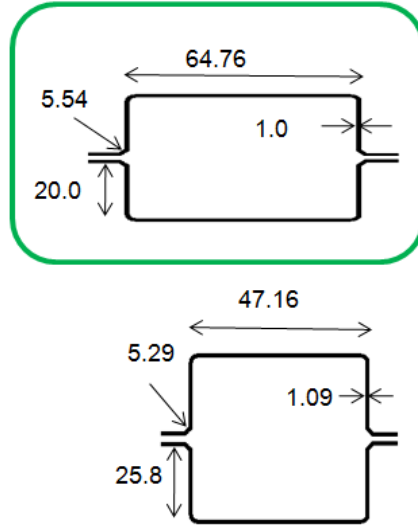
Figure 6.18   Comparison between the optimal cross-sectional geometry from ATC
(green border) and AAO

CHAPTER VII

COMPUTATIONAL FRAMEWORK

Due to the size and number of simulation in this research a computational framework is required to effectively use the computational resources. Moreover, the different tools are used in this framework that is going to be explained in this chapter. As it has been discussed in chapter V, the metamodelling strategy is used to produce the surrogates for optimization problems. This approach saves the time and computational resources and provides opportunity to parallel function evaluations. The all-at-once approach and analytical target cascading approach are used for optimization problem that each of which has different computational and computational architecture to perform coupled process-performance simulations.

7.1   All-at-once computational strategy

The all-at-once or full coupled simulation is one of the approaches used for coupled process-performance optimization. Since the coupling variables are transferred based on one-to-one transformation of information in the integration points and nodal coordinates, the simulations should be performed in sequence to build up the metamodels. Therefore, a set of design of experiment is considered as input set of data to the computational tools and a set of response vectors is required as output vector. Figure 7.1 illustrates the overview of the computational/computation framework.

156
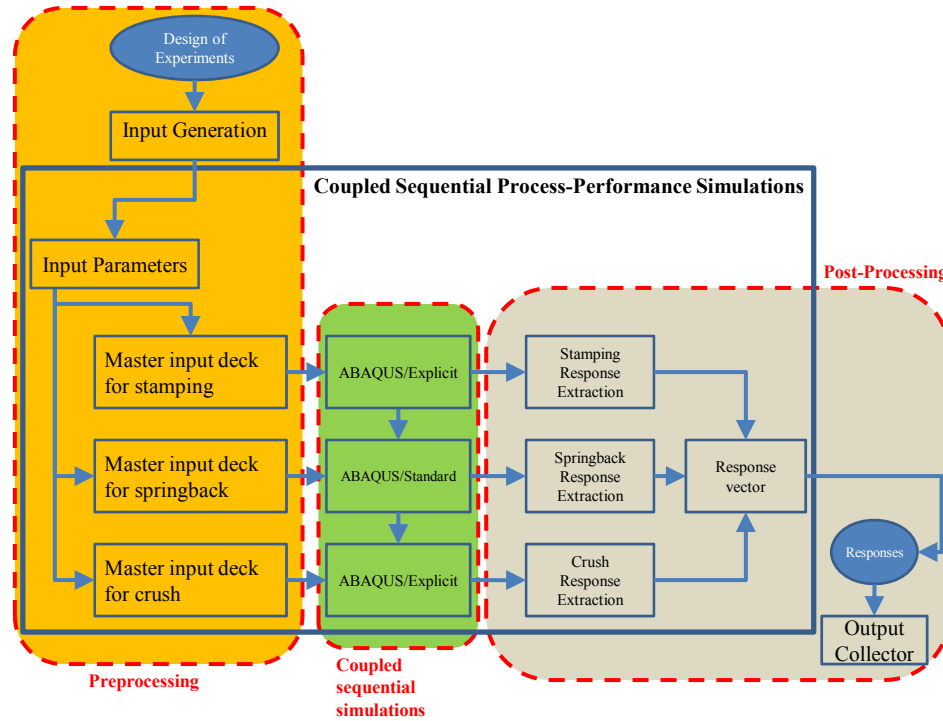
Figure 7.1   Overview of computational/computation framework

The framework is divided into three major sections called preprocessing, simulation and post processing. In preprocessing the models related to each simulation is generated using the DOE table and master input deck. Solution runs the simulations sequentially and post processing stores the result related to each simulation in terms of the responses defined.

7.1.1   Preprocessing

Based on the DOE table provided from the Latin Hypercube Sampling (LHS) design of experiment function in MATLAB, different set of design points are produced for the coupled simulations and saved in a text format called doe.txt. Therefore, it is required to have a code that takes each row of DOE matrix and creates a PARAM_INP.txt file for each simulation. This is done using a FORTRAN code called GEN_INP.f that produces the PARAM_INP.txt file and updates the DOE table by

157

eliminating the design variables row used to build the PARAM_INP.txt. The updated

DOE file called doe.out which is renamed to doe.txt through shell script and used for the

rest of DOE table. Each coupled simulations is designed to be performed in a directory by

copying the associated PARAM_INP.txt (Appendix A)as well as the input decks. This is

done through a shell script called main.sh which basically calls the GEN_INP.f

(Appendix A)to create PARAM_INP.txt and doe.out and then copies PARAM_INP.txt

and input decks to a folder starts with letters MXMN and follows by a number associated

with each row of DOE table. doe.out is renamed to doe.txt that does not have the row of

input variables used to build PARAM_INP.txt. Therefore, once the GEN_INP.f creates

the last doe point the doe.txt is an empty file. A summary of this process is illustrated in

figure 7.2.
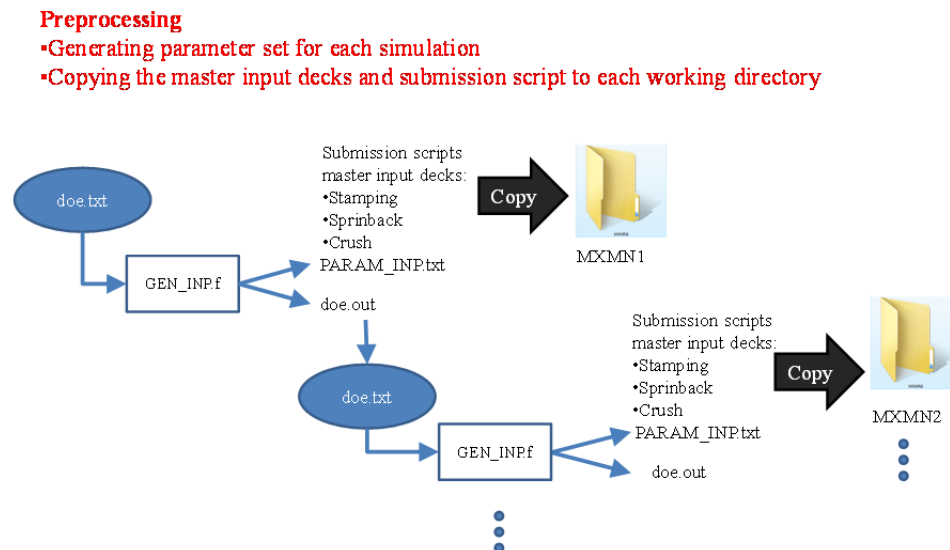
Figure 7.2   File organization and coordination for simulation based on the DOE table

7.1.2 Coupled sequential simulations

Once the input decks are created in each folder, the coupled simulation is started by starting the stamping simulations. As mentioned earlier, two material models including a classical plasticity model and internal state variable model are utilized to perform these simulations. For both material models, we used ABAQUS/Explicit for forming and crush simulations and ABAQUS/Standard for springback simulation. The coupled simulations are performed as illustrated in figure 7.3 for one case.
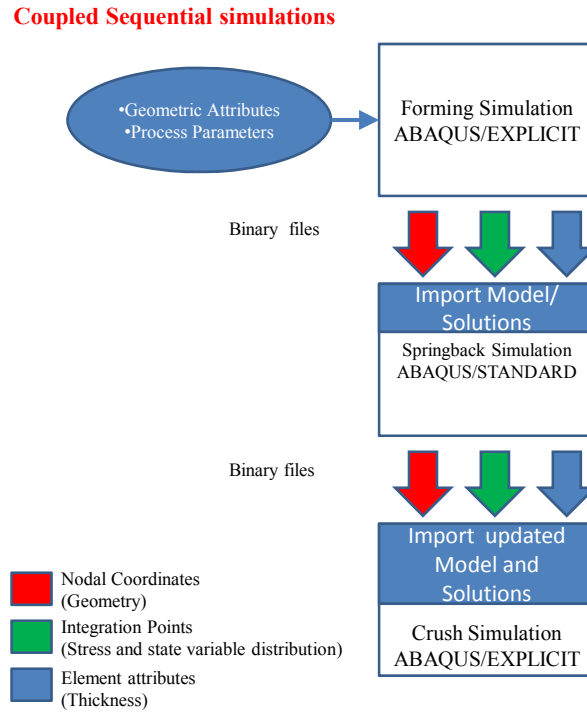
Figure 7.3   Coupled sequential process-performance simulation

In order to perform the simulation in each box a parametric model is developed as it has been explained in chapter 6 for stamping, springback and crush known as STMP.inp, SPBK.inp and CRSH.inp (Appendix B). The design variables are defined in a PARAM_INP.txt (Appendix A) file which basically lists the values of design variables

159

desired for the specific Simulations. as shown in figure 7.4. The VUMAT and UMAT is required if the ISV model is going to be used in this framework.
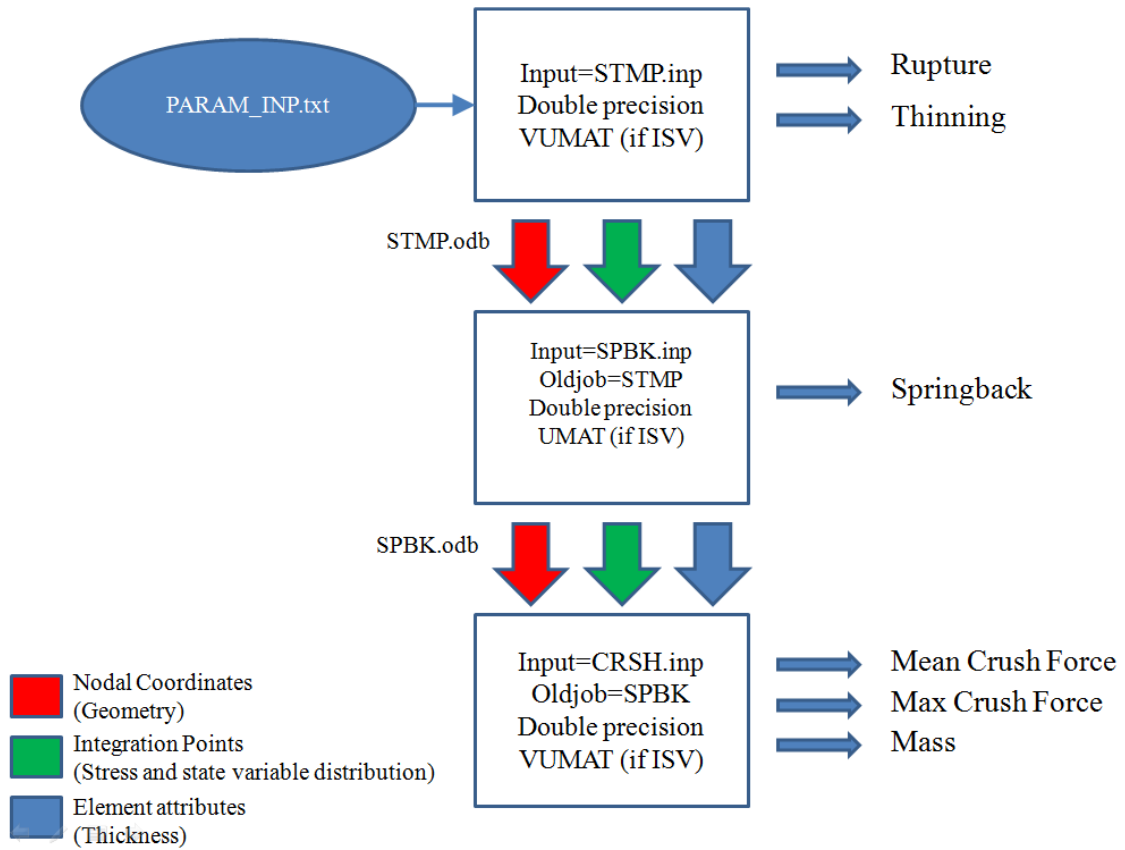
Figure 7.4   Files required to perform coupled process-performance simulation

This process can be performed in parallel format as each simulation is independent from one another. Once the stamping simulation is performed, springback simulation starts and then it will be followed by the crush simulation. This procedure is also performed within a shell script for each simulation known as mainSTMP.sh, mainSPBK.sh and mainCRSH.sh. The main purpose of these files are submit the finite element simulations whether in the local machine or through a pbs script in the cluster. The number of CPU's can also be specified in these simulations. It turnout that the

160

number of CPU for the explicit simulation does not contribute to the solution time and therefore only one CPU is used for Explicit simulations where as for Implicit simulation 4 to 12 CPU's are used. The solution time for stamping simulation jobs are around 40 min, for springback was 5 to 10 min and for the crush simulation took 2 to 3 hours of CPU time.

7.1.3   Post-processing of the FE simulations

In general, the post-processing of the results are performed using GUI software known as ABAQUS CAE. Since the number of simulation needed to be recorded is high. It is tedious to open up the GUI one by one and manipulate and store the required responses. For that, different subroutines are used to capture and report responses. As it has shown in figure 7.4, the outputs for the stamping simulations are rupture and thinning. The overall post-processing procedure is illustrated in figure 7.5.
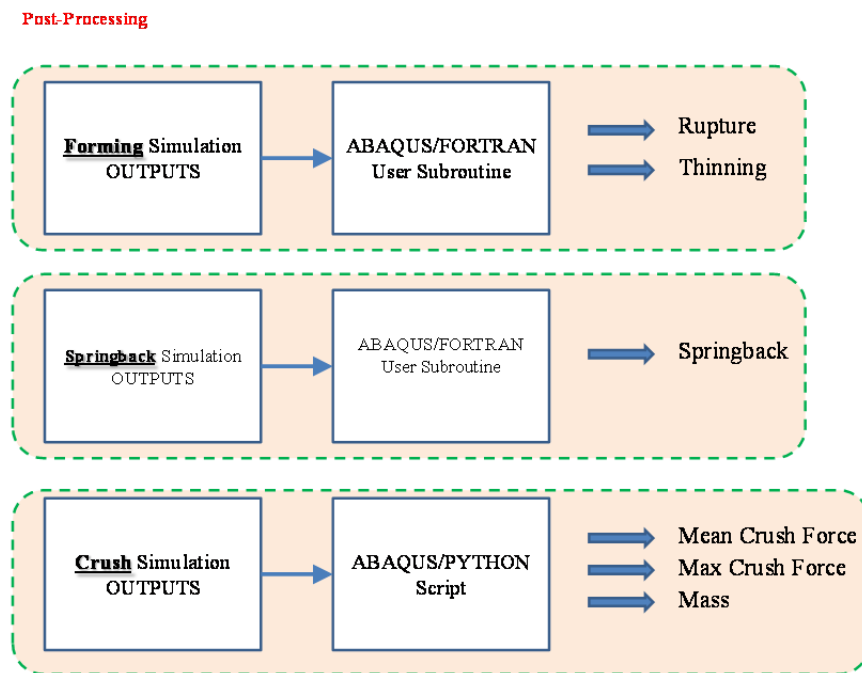
Figure 7.5   Post-processing of coupled sequential simulations

161

An ABAQUS user subroutine is developed to decode the desired responses for rupture and thinning from *.fil files. *.fil file is a binary formatted file which stores in a sequential file. Each record has the following format; the first location is assigned for the record length and the second is for record type key. The information related to each key is defined sequentially from 3 to the number of attributes. The attributes can store a single variable, a tensorial variable or an array of state variables used for the computations. The Fortran subroutine is developed to search for the particular record key (for example 22 for the plastic strain tensors and 5 for the state variable in each integration points). The stamping postprocessing is done using stmpaao.f file which is complied through the Intel Fortran Complier interconnected to ABAQUS solver. In this file, the information related to the plastic strain for each element is extracted and then the principle plastic strains are calculated then the value is checked against the forming limit diagram based on equation 3.1 in chapter 3. Then the result of thinning is extracted based on the equation 3.2.

A shell script is written to extract the information in each folder for the stamping simulation and record it as the STMP.txt file. Then each STMP.txt file is renamed to fort.[the folder index] and copied to the root directory. Once the postprocessing is done through the AssemSTMP.sh, fort.* files can be seen in the root directory that are the equal to the number of stamping simulation that are performed. In order to automatically assemble the information in each fort.* a Fortran code is written to assemble the result of stamping simulation named Assembeler.f that has the output file called STMP.TXT.

Forming Post-Processing and Response Collection
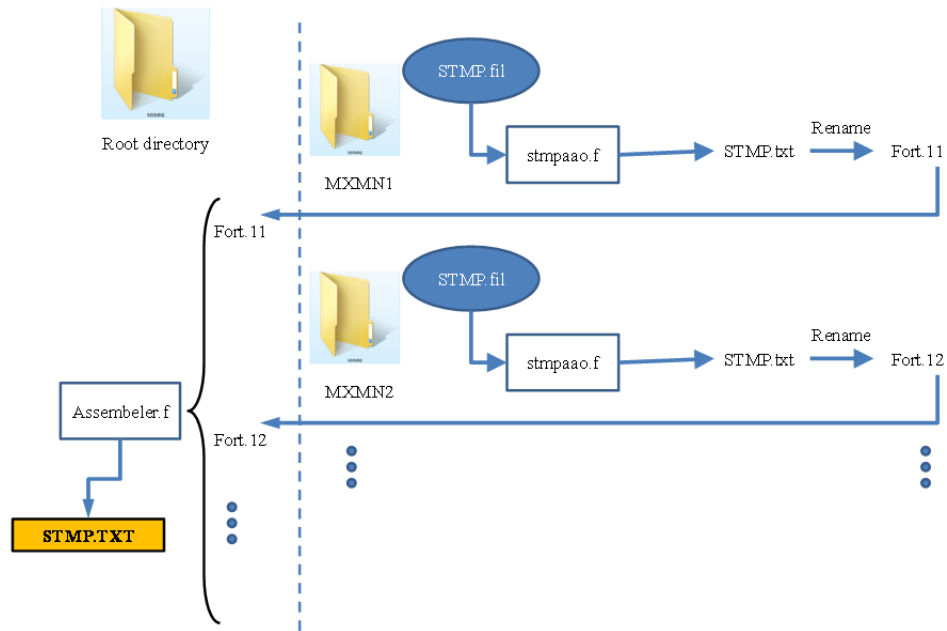
Figure 7.6   Response collection in stamping simulation

In order to extract the responses from the springback simulations, it is required to compare the nodal coordinate locations of the points at the end of stamping simulation and the springback simulation based on the equation 3.3. Therefore, two subroutine as stmpaao2.f and spbkaao.f are required to extract the springback simulation results. The same strategy is used in the shell script for extracting the springback results using AssemSPBK.sh as shown figure 7.7.

Figure 7.7   Response collection in springback simulations

In order to calculate the mean crush force and extract the maximum force it is required to access the CRSH.obd file. Moreover, because of the high level of noise in the contact force in the explicit solver it is required to use some type of filtering. This procedure is performed using a Python script in the ABAQUS/CAE. The CRSH.py file basically opens the CRSH.odb file in the ABAQUS/CAE, then extract the crush force versus time for both single hat tubes and adds them up and filters them using SAE filter with the resolution of 60Hz. The outcome of this solution is reported in a file called CRSH.rpt. in order to reduce the number of results every 200 points is selected periodically to represent the crush force curve. It is worth noting that this will not affect the behavior of the crush force curve. The final file containing the crush force versus time is again replaced in CRSH.rpt. each CRSH.rpt file in the folder is renamed to fort.10+{number of design variable} and copied to the root directory. Then the mean

164

crush force is calculated based on equation 4.1 using trapezoidal numerical integration scheme. The maximum force is also extracted in this code named AssembelerCRSH.f. This file assembles the result related to each design points.
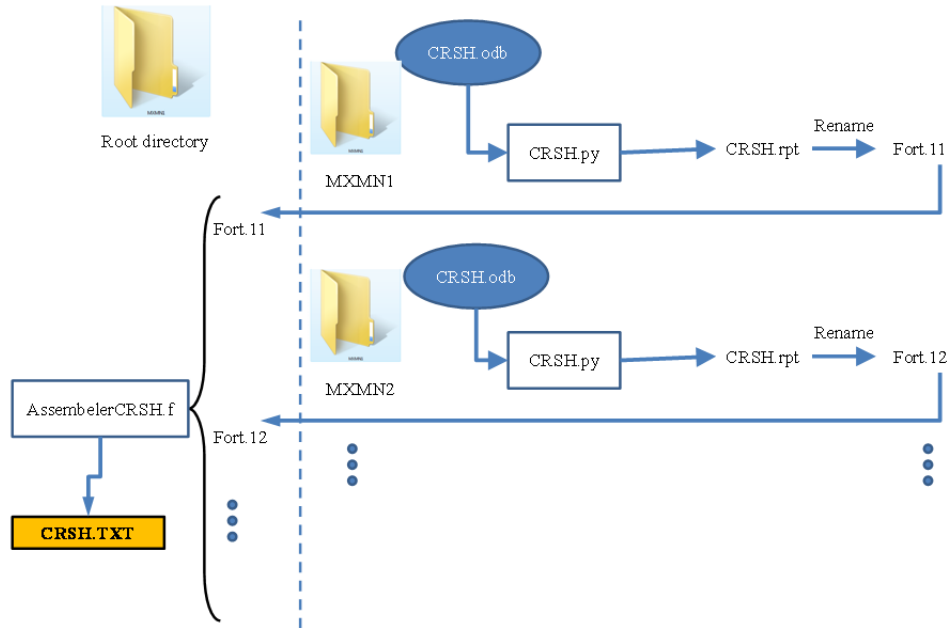
Figure 7.8   Response collection in crush simulations

The three files STMP.TXT, SPBK.TXT and CRSH.TXT contain all the information related to the responses of coupled process-performance simulations. Having these information along with the design variables in the DOE table give a set of training points for metamodelling. The metamodelling uses the radial basis functions (RBF) formulation. This is done within MATLAB *.m file developed for this purpose. After calibrating and finding the best formulation and constants, the optimizer can use these analytical functions to evaluate the responses during the function calls.

165

7.1.4   Multi-objective genetic algorithm optimization

Multiobjective GA is used for optimization. This includes a vector of objective functions based on the responses calculated in each simulation. This part is coded in MATLAB. Considering the parallel function evaluations by vectorizing the response functions in this framework decreased the optimization procedure drastically.

7.2   Analytical target cascading simulations

The multi-level decomposition used in the ATC formulation required to provide a similar computational technology. In this approach the process of metamodelling is divided into two levels including the bottom level and top level optimization problem as it is going to be discussed in the following sections.

7.2.1   Bottom level simulations

The bottom level is designed similar to what is discussed about the stamping and springback simulations. Based on equation 6.6, the number of design variables in this level is three manufacturing process parameters. But because of the coupling the geometric attributes is also considered as variable. The geometric variables will not be changed throughout the optimization process performed in the lower level but it will change through the convergence iteration between the top and bottom level. All the steps related to the preprocessing remains similar with what has been discussed in section 7.1.1. However, the post processing is changed. Based on the decomposition and optimization formulation, the local objective function should be achieved by minimizing the rupture and thinning. In order to extract the responses required to send up to the top level, two different codes are used to extract the springback angle and the equivalent plastic strain in the side walls and the corners. A modified version of spbkaao.f is

166

developed to extract the results based on the deviation of corner angle. The equivalent plastic strain is also calculated based on the average amount of PEEQ in two regions including the side walls and corners.

7.2.2   Top level simulations

Since this solution strategy is more similar to the separate simulation strategy, a Python MCRUSH1.py script is developed to create the finite element model for crush simulation. This MCRUSH1.py contains three material cards each assigned for the corner, side and the width of the tube. The variables used in this crush simulation contain five geometric attributes including tube width, height, thickness, corner radius and springback angle. The five variables do not have any value in MCRUSH1.py and it will be inserted later. These five variables are taken from first line in doe.txt and printed to PARAM_INP.txt file using GEN_INP.f. The average equivalent plastic strain in side walls and corners for each simulation, are taken from the first line in doeMAT.txt and printed into PEEQ.txt through GEN_MAT.f.

Both GEN_INP.f and GEN_MAT.f write an output named doe.out and doeMAT .out that the first line used to create PARAM_INP.txt and PEEQ.txt are omitted. A shell script controls the executions of GEN_INP.f and GEN_MAT.f to create doe.out and PARAM_INP.txt as well as doeMAT.out and PEEQ.txt. after the execution of each Fortran codes, the script renames the doe.out to doe.txt and doeMAT.out to doeMAT.txt to be prepared for the next execution. Then the PEEQ.txt, PARAM_INP.txt, and MCRUSH1.py along with three Fortran codes including CRSH_PY_GEN.f, CRSH_INP_GEN.f and Mat_Man.f are copied to the working directory. The script locates each working directory and then generates a python script containing geometric

167

variable by writing the information from PARAM_INP.txt in to MCRUSH1.py using CRSH_PY_GEN.f that outputs a new script called MCRSH.py. MCRSH.py is executed in ABAQUS/PYTHON to create an ABAQUS/EXPLICIT input deck called Job-1.inp. Since the specific contact formulation cannot be defined through ABAQUS/CAE or ABAQUS/PYTHON, this is done using CRSH_INP_GEN.f that takes Job-1.inp and modifies this file for contact formulation and includes material data through Man_Mat.f for material definition and outputs CRSH.inp. Then CRSH.inp is submitted for run in ABAQUS/EXPLICIT. The detail procedure of performing simulations for the top level is provided in figure7.9 And 7.10.
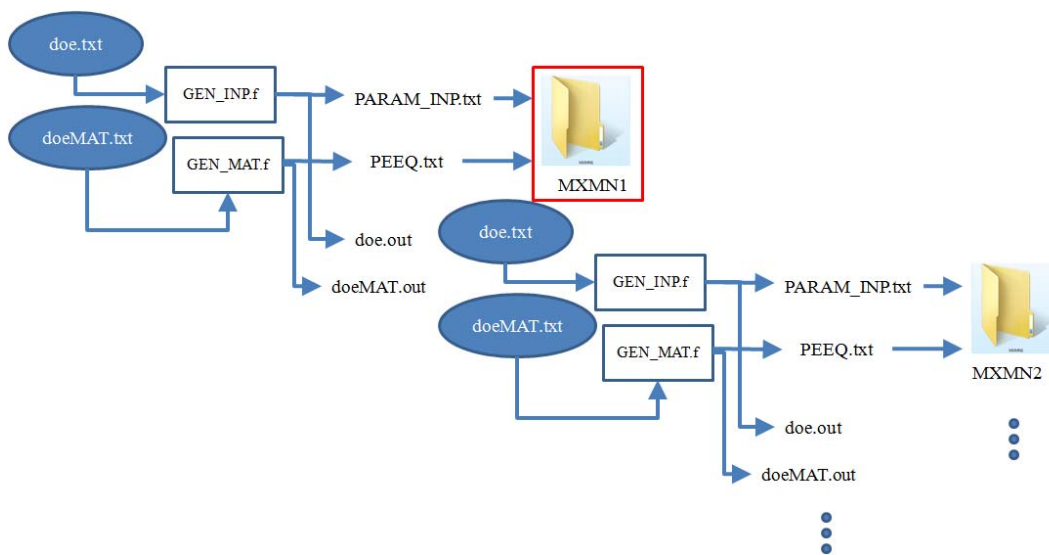
Figure 7.9   File organization and coordination for ATC optimization
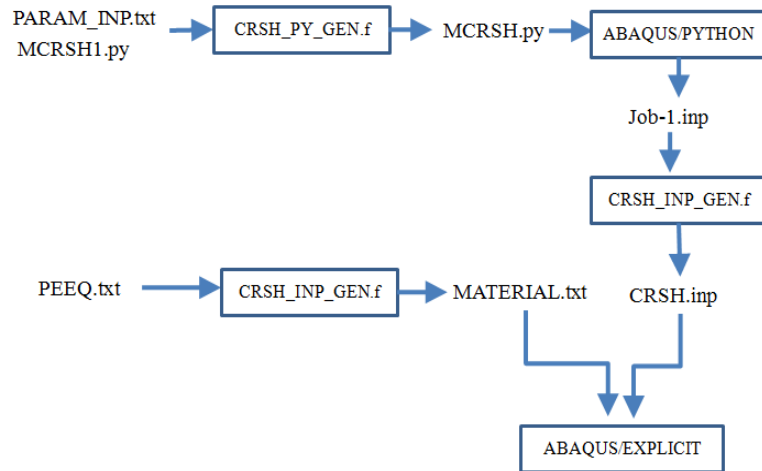
Figure 7.10   Top level file organization and input deck generation

In order to extract the responses in the top level same framework that is shown in figure 7.8 is used Once the responses are identified, surrogate models can be established in MATLAB related to the top level problem.

7.2.3   Genetic algorithm optimization

Analytical target cascading (ATC) is used to solve the decomposed problem. This includes two optimization problems performed in the top and bottom level and the iteration between top and bottom to exchange and match the responses and targets. This part is coded in MATLAB. Each level performs the optimization based on the genetic algorithms. GA requires performing numerous function evaluations to find the optimal points. Considering the parallel function evaluations by vectorizing the response functions in this framework decreased the optimization procedure from 48 hours to 3 hours.

169

CHAPTER VIII

CONCLUDING REMARKS AND FUTURE WORK

This dissertation introduced a computationally integrated framework for performing coupled sequential process-performance simulation and multi-attribute/multi-level optimization. Multiple methodologies are investigated to study the influence of manufacturing effects on the energy absorption. The multiscale nature of the dislocation plasticity in the metallic material implies that the microstructural feature evolves during the manufacturing process and causes a new microstructure at the component level. This can be captured using a hierarchical multi-scale framework using a polycrystalline crystal plasticity model. In this model, although the lower length scale effects are phenomenological but the grain orientations are explicitly considered in their model through a mean field hypothesis to model the grain interactions. Manufacturing effects are considered as the orientation change resulted from some basic load path is used to study two basic crush mode shapes. It is shown that the orientation can change the energy absorption behavior in terms of mean crush force and maximum force. It is also shown that the localized region that undergo loading and unloading deformation will be affected more by changing the initial texture. Another way is to use continuum plasticity models to consider manufacturing effects. Therefore, processing simulation is coupled to performance simulation by transferring the manufacturing effects in terms of geometric attributes and material internal state. The geometric attributes are identified in terms of deviation of the as built geometry from the desired geometry or springback. However, the

170

selection of manufacturing affected material state plays an important role in coupling between process simulation and product performance. In the present study, two classes of constitutive equations including classical plasticity and physically based internal state variable model are utilized to account for the manufacturing effects in the energy absorption. Crush response of a thin-walled tube produced using sheet-stamping process (cold forming and hot forming) is used to illustrate the approach. Sheet forming simulation is performed with a combination of two simulations in ABAQUS/EXPLICIT to model the deep drawing process followed by springback analysis in ABAQUS/STANDARD. The effect of manufacturing process parameters, geometric attributes and workpiece temperature is studied in cold forming and hot forming simulations to study the manufacturing quality attributes such as rupture, thinning and springback. It has been shown that the springback response is highly nonlinear by varying the manufacturing process variables and geometric attributes. It is also shown that the manufacturing process parameters must be adjusted due to any change in the geometrical designs.

The procedure of coupled process-performance simulation is demonstrated by performing coupled deep drawing, springback, and crush simulations of a thin-walled double-hat tube. Similar to the stamping simulations ABAQUS/EXPLICIT and ABAQUS/STANDARD were used for sheet forming process simulation with process-induced responses such as residual stresses and effective plastic strains retained and used as the initial conditions for the subsequent crush simulation using ABAQUS/EXPLICIT.

Coupled simulation results are compared with the separate simulation for both classical plasticity and internal state variable model. The BCJ-ISV model is used to perform the crushing simulation considering adiabatic heat generated due to plastic

171

dissipation as well as isothermal conditions. In all of the approaches studied in the coupled process performance simulation, it is shown that including the manufacturing responses affect the crushing response and provide a new paradigm to design a manufacturing process considering the performance attributes.

For the example problem discussed in this dissertation, sensitivity analysis was performed to determine the effect of selected process and product design variables on performance responses. It is shown that the punch velocity variations affected the crushing behavior by using both classical plasticity and ISV material models. Another important observation in the sensitivity analysis is that the manufacturing effects are more influential in the cases that adiabatic heating are ignored (isothermal condition). The heat generated in the localized region reduces the hardening and increase the saturation therefore the material behaves as a perfectly plastic material that has the lowest sensitivity to history effects. However, this requires experimental observation to draw a firm conclusion.

Two main approaches are used to perform design optimization on the coupled process-performance simulation. One based on the one-to-one mapping of the initial states and stresses from forming to crush and formulate the optimization problem as a multi-objective optimization considering manufacturing responses and performance criteria. Since both manufacturing process responses as well as crush responses are involved in a single optimization problem, it is called all-at-once approach. A multi-attribute optimization problem was formulated and solved using multi-objective genetic algorithms. The resulting Pareto optimum solutions were obtained and compared in terms of process and performance objectives. This study showed the importance of retaining material history effects through coupled sequential process-performance simulation and

172

its application in multi-attribute process-performance optimization problem. The Pareto set obtained from this optimization shows that a trade-off between the process parameters and geometric attributes should be considered to obtain desired response.

In the other approach, the problem is decomposed into a bi-level motivated from the decomposition strategy of analytical target cascading in hierarchical systems. The sequence of the simulation provides a natural hierarchy. In order to consider manufacturing responses in crush analysis, the history information are transferred from manufacturing process design and analysis to crush analysis and design. In order to reduce the computational time radial basis function methodology is used to generate surrogate models. The global optimum point at each ATC iterations, an augmented Lagrangian genetic algorithm optimization is used. Our study evaluated a bottom up coordination strategy to solve this problem. The present partitioning strategy is performed based on the bottom up coordination strategy using fixed point iteration (FPI) technique. Due to the nature of FPI and the sequential partitioning, the optimization process is needed to be performed sequentially. it is shown that the number of design variable is increased in the top level compare to the original problem due to introducing the targets/demands and relaxation tolerances. However, the complexity of the problem is decreased because of separating the process discipline from the performance discipline. The range of relaxation tolerance should be carefully assigned as it may result into non-optimum point due to reaching stopping criteria or not finding any feasible solution. We proposed our process-performance optimization using a classical plasticity model that can pass only one history variable as equivalent plastic strain in the material level. The coupling strength between process and performance level can be enhance by using high

173

fidelity material model that account for different aspects of dislocation plasticity as well as micro structures and defects.

For both of design optimization methodologies metamodels based on radial basis functions were utilized to generate surrogate models to approximate response values during the optimization process in lieu of high fidelity simulations. However, calibration of the metamodels is found to be very tricky due to the severe nonlinearity of the responses within a relatively large range of variations. In order to automatically coordinate the information between different simulations, a consistent general computational framework is proposed to automate the coupled process-performance simulations. The computational framework can be used for the purpose of autonomic computing.

The following items are proposed as the future work in this area:

The coupling between process and performance levels is highly dependent upon the material model used. Incorporating the high fidelity material models or physically based models facilitate the coupling of process to performance. One of the main coupling variables which is usually ignored in the material models is the effect of anisotropic texture and grain orientations. The model should be capable of modeling the texture evolutions. Incorporating this microstructural features improves the computational accuracy in all the stage of simulation especially for springback predictions. Moreover, this capability will also help to introduce the microstructural design into the process-performance simulation and optimization.

In this research, the adiabatic heating is considered in the crush simulation in the BCJ-ISV models which causes the temperature rise in the material. However, there is no thermal analysis performed to study the heat conduction due to the temperature gradient

appeared in the material. Coupled thermo-mechanical analysis should be performed to accurately study the deformation mechanism in the large deformation in the folding process.

Incorporating the continuum damage models into ISV material models improves the coupled process-performance simulation results. The FLD diagram is not required to capture the rupture responses. Instead, the rupture can be defined through damage parameter as an internal state variable. Additionally, the internal state variable can be considered as a manufacturing effect for coupled simulation. Therefore, the damage effects appear in the manufacturing responses can be tracked in springback and crush simulation. However, our study shows that the incorporating the damage behavior in the continuum shell element is also a challenging problem and requires in depth investigation.

In this study friction coefficient is considered as manufacturing design variable representing both the friction properties between forming tools and blank and drawbeads. However, drawbeads are ignored in the finite element model including the drawbead geometry and arrangement can help to tailor a suitable thickness and microstructure distribution.

Sustainable manufacturing can be included in the design problem through proper cost function representing the relation between manufacturing process parameters and the fuel efficiency of the forming facilities. If the Thinning, Rupture, Springback values are outside the allowable limits, then the manufactured part will be rejected and that will increase the cost. Similarly, the weight will increase the cost. Larger Punch Velocity and Holder force may require larger energy consumption, and that can increase the cost. In any case, proper cost functions need to be formulated.

175

In the multi-level decomposition in this study is applied for the classical plasticity model which contain a piecewise linear isotropic hardening. This material model provides the equivalent plastic strain as the only material state variable represented as a scalar variable. As the material model becomes more complicated, it is required to include other state variables which may be in tonsorial form. Therefore, decomposition strategy should be modified to efficiently address the complexity of the coupling variables.

The sequential nature of the coupled process-performance optimization is a hurdle to parallel computing. Defining a proper coordination strategy in the multi-level framework can improve the computational efficiency of the coupled problem especially once it is integrated with finite element software.

By including the uncertainty of the manufacturing process and material constants in the models, more reliable responses in the manufacturing level and crush level can be obtained. The responses will be represented through some statistical distributions by propagating the uncertainty from material and manufacturing process level to performance level.

Decomposition of the present problem was involved with a mean field approximation for the coupling variables in material state. The coupling variables which defined as equivalent plastic strain in the side walls and corner regions is approximated with one scalar value. Considering the uncertainty of these coupling variable can also help to obtain a more robust answer to optimization problem.

176

REFERENCES

ABAQUS/EXPLICIT version 6.10, user's manual., 2010, Hibbit, Karlsson and Sorensen Inc., Rhode Island, USA

ABAQUS/Explicit version 6.10, user's manual., 2010, Hibbit, Karlsson and Sorensen Inc., Rhode Island, USA

ABAQUS/STANDARD version 6.10, user's manual., 2010, Hibbit, Karlsson and Sorensen Inc., Rhode Island, USA

ABAQUS/Standard version 6.10, user's manual., 2010, Hibbit, Karlsson and Sorensen Inc., Rhode Island, USA

Abramowicz, W., and Jones, N., Dynamic Axial Crushing of Square Tubes, International Journal of Impact Engineering, 1984, Vol. 2, No. 2, pp. 179-208.

Abramowicz, W., and Wierzbicki, T., Axial Crushing of Multicorner Sheet Metal Columns, Journal of Applied Mechanics, Vol.56, 1989, pp. 113–120.

Abramowicz, W., Thin-Walled Structures As Impact Energy Absorbers, Thin-Walled Structures, 2003, Volume 41, Issues 2-3, February 2003, pp. 91-107.

Abramowicz, W., Thin-walled structures as impact energy absorbers, Thin-Walled Structures, Vol. 41, No. 2-3, pp. 91-107, 2003.

Acar, E., Rais-Rohani, M., Ensemble of metamodels with optimized weight factors, Structural and Multidisciplinary Optimization, Vol. 37, No. 3 pp. 279-294, 2008.

Acar, E., Rais-Rohani, M., Najafi, A., Marin, E., Bammann, D., Concurrent Design of Product-Material Systems using Multilevel Optimization, 50th AIAA/ASME/ASCE/AHS/ASC Structures, Structural Dynamics, and Materials Conference, Palm Springs, CA, May 2009

Allison, J.T., Roth, B., Kokkolaras, M., Kroo, I. and Papalambros P. Y., Aircraft Family Design Using Decomposition-Based Methods. In the Proceedings of the 11th AIAA/ISSMO Multidisciplinary Analysis and Optimization Conference, Portsmouth, Virginia, Sept. 6-8 2006.

177

Allison, J.T., Walsh, D., Kokkolaras, M., Papalambros, P. Y. and Cartmell. M., Analytical Target Cascading in Aircraft Design. In the Proceedings of the 44th AIAA Aerospace Sciences Meeting and Exhibit AIAA-2006-1326. AIAA, January 9-12 2006.

Aretz H., A simple isotropic-distortional hardening model and its application in elastic–plastic analysis of localized necking in orthotropic sheet metals, International Journal of Plasticity 24, 2008, pp. 1457–1480

Bammann, D. J., A model of crystal plasticity containing a natural length scale, Materials Science and Engineering A309–310, 2001, pp.406–410

Barlat, F., Chung, K., Anisotropic potentials for plastically deforming metals, Modeling and Simulation in Materials Science and. Engineering 1, 1993, pp.403-416.

Barlat, F., Chung, K., Richmond, O., Anisotropic Plastic Potentials for Polycrystals and Application to the Design of Optimum Blank Shapes in Sheet Forming, Metallurgical and Materials Transaction A, Vol. 25A, June 1994, pp.1209-1216

Barthelemy, J-F.M., Haftka, R. T., Approximation concepts for optimum structural design — a review, STRUCTURAL AND MULTIDISCIPLINARY OPTIMIZATION, Vol. 5, No. 3, pp. 129-144, 1993

Bathe, K.J., Chaudhary, A., A Solution Method for Planar and Axisymmetric Contact Problems. International Journal for Numerical Methods in Engineering, Vol. 21, pp. 65-88, 1985.

Bayram, Y.B., Nied, H.F., Enriched Finite Element-Penalty Function Method for Modeling Interface Cracks with Contact, Engineering Fracture Mechanics, Vol. 65, pp. 541-557, 2000.

Beaudoin, A. J., Dawson P. R., Mathur KK, Kocks UF, Korzekwa DA. Application of polycrystal plasticity to sheet forming., Computer Methods in Applied Mechanics and Engineering 1994, 117, pp.49–70.

Beaudoin, A., J., Mathur, K. K., Dawson PR, Johnson GC. Three dimensional deformation process simulation with explicit use of polycrystal plasticity models. International Journal of Plasticity, 1993, Vol 9, 833–60.

Bishop, J.F.W. , Hill, R., A theoretical derivation of the plastic properties of a polycrystalline face centered metal, Philosophical Magazine, Vol 42, 1951, pp. 1298–1307.

Bishop, J.F.W. , Hill, R., A theory of the plastic distortion of a polycrystalline aggregate under combined stresses, Philosophical Magazine, Vol 42, 1951, pp. 414–427.

Bottcher, C.S., Frik, S., Consideration of Manufacturing Effects to Improve Crash Simulation Accuracy, 4th European LS-Dyna Users Conference, 2003.

178

Chaudhary, A., Bathe, K.J,. A Solution Method for Static and Dynamic Analysis of Three-Dimensional Contact Problems with Friction. Computers & Structures, Vol. 24, pp. 855-873, 1986.

Chen, W. Wierzbicki, T., Relative merits of single-cell, multi-cell and foam-filled thin-walled structures in energy absorption, Thin-Walled Structures, Vol. 39, No. 4, pp. 287-306, 2001

Chen, W., Wierzbicki, T. Relative Merits of Single-Cell, Multi-Cell and Foam-Filled Thin-Walled Structures in Energy Absorption. Thin-Walled Structures 39, no. 4, 2001, pp. 287-306.

Chen, Y. P., Lee, W. B., To, S., Influence of initial texture on formability of aluminum sheet metal by crystal plasticity FE simulation. Journal of Material Processing and Technology, 2007, Vol 192–193, 397–403.

Cheng, J.H., Kikuchi N., An Analysis of Metal Forming Processes Using Large Deformation Elastic-plastic Formulations, Computer Methods in Applied Mechanics and Engineering, Vol. 49, pp.71-108, 1985.

Chung, W.J., Cho, J.W., Belytschko, T., On the dynamic effects of explicit FEM in sheet metal forming analysis. Engineering Computations, Vol. 15, pp. 750–776, 1998.

Dafalias, Y. F., Orientational Distribution Function in Non-Affine Rotations, Journal of the Mechanics and Physics of Solids, 2001, Vol. 49, pp. 2493-2516.

Dafalias, Y. F., Orientational Evolution of Plastic Orthotropy in Sheet Metals Journal of the Mechanics and Physics of Solids, 2000, Vol. 48, pp. 2231-2255.

Dagson, N., Influence of the Forming Process on the Crash Response of a Roof Rail Component, Master Thesis, Department of Solid Mechanics, Linkping University, March 2001.

Dhia, H.B., Durville, D., Calembour, an implicit method based on and enriched kinematical thin-plate model for sheet-metal forming simulation, Journal of Materials Processing Technology, vol. 50: 70-80, 1995.

DiPaolo, B.P., Monteirob, P.J.M., Gronsky, R. Quasi-Static Axial Crush Response of a Thin-Wall, Stainless Steel Box Component. International Journal of Solids and Structures 41, no. 14, 2004, 3707-3733.

Dipaolo, B.P., Tom J.G. A Study on an Axial Crush Configuration Response of Thin-Wall, Steel Box Components : The Quasi-Static Experiments International journal of solids and structures 43, no. 25-26, 2006, 7752-7775.

Fang, H., Horstemeyer, M. F., Global response approximation with radial basis functions, Engineering Optimization, Vol. 38, No 4, pp 407 – 424, 2006

179

Faruque, O., Saha, N. Extruded Aluminum Crash Can Topology for Maximizing Specific Energy Abdorption. SAE technical paper series, 2008.

Fonseca, M., Fleming, P.J., Genetic Algorithms for Multiobjective Optimization: Formulation, Discussion and Generalization, Proceedings of the 5th International Conference on Genetic Algorithms San Francisco, CA, USA: Morgan Kaufmann Publishers Inc., pp. 416--423, 1993.

Francois, M., A Plasticity Model with Yield Surface Distortion for Non-Proportional Loading, International Journal of plasticity, Vol 17, 2001, pp. 703-717.

Gholipour, J., Worswick, M. J., Oliveira, D.A., Application of damage models in bending and hydroforming of aluminum alloy tube, SAE International, paper # 2004-01-0835, 2004.

Grantab, R., Interaction between Forming and Crashworthiness of Advanced High Strength Steel S-Rails, PhD dissertation, University of Waterloo, Canada, 2006.

Haftka, R.T., An Improved Computational Approach for Multilevel Optimum Design, Journal of Structural Mechanics, Vol. 12, No. 2, 1984, pp. 245-261.

Halquist, J., LS-DYNA user's manual version 971, Livermore Software Technology Corporation 2006.

Han, J., Papalambros, P.Y., A Sequential Linear Programming Coordination Algorithm for Analytical Target Cascading, Journal of Mechanical Design, FEBRUARY 2010, Vol. 132, pp. 1-8.

Hanssen A. G., Langseth M., and Hopperstad, O. S., Static and Dynamic Crushing of Square Aluminum Extrusions With Aluminum Foam Filler, International Journal of Impact Engineering, Vol.24, No.4, 2000, pp.347-383.

Hanssen, A. G., Langseth, M., Hopperstad, O. S., Optimum Design For Energy Absorption of Square Aluminum Columns With Aluminum Foam Filler, International Journal of Mechanical Sciences, Vol. 43, No.1, 2001, pp. 153-176.

Hibbitt, H.D., Marcal, P.V., Rice, J. R., A finite element formulation for problems of large strain and large displacement, International Journal of Solids and Structures, Vol. 6, pp. 1069–1086, 1970.

Horstemeyer, M. F., From Atoms to Autos A New Design Paradigm Using Microstructure-Property Modeling Part 1: Monotonic Loading Conditions, Sandia National Laboratory, March 2001, SAND2000–8662

Horstemeyer, M., Potirniche, G., & Marin, E. B., Chapter 3. Mesoscale-Macroscale Continuum Modeling: Crystal Plasticity. In S. Yip, Springer (Eds.), Handbook for Materials Modeling, The Netherland: 3300 AA Dordrecht.

Hu, W., Yao, L.G. Hua, Z.Z., Optimization of sheet metal forming processes by adaptive response surface based on intelligent sampling method, Journal of Materials Processing Technology, Vol. 197, No. 1-3, pp. 77-88, 2008

Jetteur, P., Implicit integration algorithm for elastoplasticity in plane stress analysis, Engineering with Computers, vol. 3: 251-253, 1986.

Jones, N., Wierzbicki, T. (ed), Structural Failures, John Wiley, New York, 1989.

Kaufman, M., Gaines, D., Kundrick, K., Liu, S.D., Integration of chassis frame forming analysis into performance models to more accurately evaluate crashworthiness. SAE Proceedings, paper no. 980551, 1998.

Kellicut, A., Cowell, B., Kavikondala, K., T. Dutton, S. Iregbu, R. Sturt, Application of the results of forming simulation in Crash Models. In: Numisheet'99 conference proceedings, Besancon, France, p. 509–14, 1999.

Kim, H.M., Chen, W., Wiecek, M. M., Lagrangian Coordination for Enhancing the Convergence of Analytical Target Cascading, AIAA JOURNAL Vol. 44, No. 10, October 2006

Kim, H.S. New Extruded Multi-cell Aluminum Profile for Maximum Crash Energy Absorption and Weight Efficiency. Thin-Walled Structures 40, no. 4, 2002, 311-327.

Kim, H.S., New extruded multi-cell aluminum profile for maximum crash energy absorption and weight efficiency, Thin-Walled Structures, Vol. 40, No. 4, pp. 311-327, 2002

Kim, M.K., Michelena, N.F., Papalambros, P.Y., and Jiang, T., Target Cascading in Optimal System Design, Journal of Mechanical Design, Vol. 125, 2003, pp. 474-480.

Kim, Y.J., Yang, D.Y., A Formulation for Rigid-plastic Finite Element Method Considering Work-Hardening Effect, International Journal of Mechanical Science, Vol. 27, pp. 487-495, 1985.

Kirsch, U., Multilevel Approach to Optimum Structural Design, ASCE Journal of the Structural Division, Vol. 98, 1975, pp. 956-974.

Kirsch, U., Reiss, M., and Shamir, U., Optimal design by partitioning into subsystems, ASCE Journal of the Structural Division. Vol. 98, No. ST1, pp. 249-267

Kocks, U.F., Argon, A. S., Ashby, M. F.Thermodynamics and kinetics of slip, 1975, Pergamon Press.

Kocks, U.F., Tome, C.N., and Wenk. H.-R., (1998) Texture and Anisotropy, Cambridge University Press, first edition.

Kokkolaras M. , Fellini, R. , Kim, H. M., Papalambros, P. Y., From Product Platform and Product Family Design: Methods and Applications, in Product Platform and Product Family Design: Methods and Applications, Editors: T. W. Simpson, Z. Siddique, R. Jianxin Jiao, Springer, 2005

Konak, A. Coit, D.W., Smith, A.E., Multi-objective optimization using genetic algorithms: A tutorial, Reliability Engineering & System Safety, Vol. 91, No. 9, Special Issue - Genetic Algorithms and Reliability, pp. 992-1007, 2006.

Kothari, M., and Anand, L., (1998), Elasto-Viscoplastic Constitutive Equations For Polycrystalline Metals: Application to Tantaluni, Journal of the Mechanics and Physics of Solids, 46:51-83.

Krishnamachari, R., 1996. A Decomposition Synthesis Methodology for Optimal Systems Design, Doctoral Dissseration, Department of Mechanical Engineering and Applied Mechanics, University of Michigan, Ann Arbor.

Kröner, E., On the plastic deformation of polycrystals, acta metallurgica, Vol 9, 1961, pp. 155–161.

Krusper, A., Influences of the Forming Process on the Crash Performance - Finite Element Analysis, Master Thesis, Department of Structural Mechanics, Chalmers University of Technology, May 2003.

Lee, S., Kwon, Y.N., Kang, S.H., Kim, S.W., Lee, J.H., Forming limit of AZ31 alloy sheet and strain rate on warm sheet metal forming, Journal of Materials Processing Technology, Vol. 201, No. 1-3, pp. 431-435, 2008.

Li, K.P., Carden, W.P., and Wagoner R.H., Simulation of Springback, International Journal of Mechanical Sciences, Vol. 44 pp. 103-122, 2002.

Lin, Z., Liu, G., Study on the effects of numerical parameters on the precision of springback prediction. Proceedings of the 6th International LS_DYNA User's Conference, Session 13C, Dearbon, MI, 2000.

M. Langseth, and O.S. Hopperstad, Static and Dynamic Axial Crushing of Square Thin-Walled Aluminum Extrusions, International Journal of Impact Engineering, Volume 18, Issues 7-8, October-December 1996, pp. 949-968.

Marin E. B. , On the Formulation of Crystal Plasticity Model, Sandia Report, Sandia National Laboratory, ,SAND2006-4170, 2006

Marin E. B., Dawson, P.R., On modeling the elasto-viscoplastic response of metals using polycrystal plasticity, Computer Methods in Applied Mechanics and Engineering,1998, Vol, 165, pp.1- 21.

Marin E. B., Dawson, P.R.,, Elastoplastic finite element analysis of metal deformations using polycrystal constitutive models, Computer Methods in Applied Mechanics and Engineering, 1998, Vol. 165, pp. 23 - 41.

MATLAB documentation R2008, MathWorks Inc.

Mayer, R., Theoretical effects of hydroforming on crashworthiness of straight sections. ASME Applied Mechanics Division. 255, 591-603, 2004.

McDowell D.L., H.J. Choi, J. H. Panchal, R. Austin, J. K. Allen, and F. Mistree, Plasticity-Related Microstructure-Property Relations for Materials Design, Key Engineering Materials, Vol 340-341, pp. 21-30, 2007.

MD Nastran R3 Quick Reference Guide, MSC.Software Corporation, 2008, Santa Ana, CA, USA

Meyers, M.A., Vohringer, O., Kad, B.K., Xue, Q., Fu, H.-H., (2002), Constitutive description of Dynamic Deformation: Physically-Based Mechanisms, Material Science and Engineering, Vol. A322, 194-216.

Michelena, N.F., Kim, H.M., and Papalambros, P.Y., A System Partitioning and Optimization Approach to Target Cascading, Proceedings of the 12th International Conference on Engineering Design, Munich, Germany, 1999.

Michelena, N.F., Park, H., and Papalambros, P.Y., Convergence Properties of Analytical Target Cascading, AIAA Journal, Vol. 41, No. 5, 2003, pp. 897-905.

Moussouni, F., Kreuawan, S., Brisset, S., Gillon, F., Brochet, P. and Nicod, L., Analytical Target Cascading for Optimal Design of Railway traction System, EngOpt 2008 - International Conference on Engineering Optimization, Rio de Janeiro, Brazil, 01 - 05 June 2008.

Najafi, A. & Rais-Rohani, Hammi Y., Multi-Attribute Integrated Forming-Crush Simulation Optimization Using Internal State Variable Model, 1st World Congress on Integrated Computational Materials Engineering, July 10-14, 2011, Seven Springs, PA

Najafi, A. & Rais-Rohani, M., Mechanics of Axial Plastic Collapse in Multi-Cell, Multi-Corner Crush Tubes, Thin-Walled Structures, Jan 2011, Vol. 49, No. 1, Pages 1-12

Najafi, A. & Rais-Rohani, Sequential Multi-Attribute Process-Performance Simulation and Optimization of Thin-Walled Components, 16th Design for Manufacturing and the Life Cycle Conference (DFMLC), August 28-31, 2011, Washington, DC.

Najafi, A. Rais-Rohani, M., Mechanics of axial plastic collapse in multi-cell, multi-corner crush tubes, Thin-Walled Structures, Vol. 49, No. 1, pp. 1-12, 2011.

183

Najafi, A., & Rais-Rohani, M., Influence of Cross-Sectional Geometry on Crash Characteristics of Crush Tubes, proceedings of 49th AIAA/ASME/ASC/AHS/ASC Structures, Structural Dynamics and Materials Conference, Schaumburg, Il: Apr 2008.

Najafi, A., Axial Collapse Of Thin-Walled, Multi-Corner Single- and Multi-Cell Tubes, MSc Thesis, Department of Aerospace Engineering, Mississippi State University, 2009

Najafi, A., Marin, E., Rais-Rohani, M., Influence of Anisotropic Texture on Crushing Behavior of Square Tubes. 52nd AIAA/ASME/ASCE/AHS/ASC Structures, Structural Dynamics and Materials Conference, April 2011.

Noels, L., Stainier, L., Ponthot, J.P., "Combined implicit/explicit time integration algorithms for the numerical simulation of sheet metal forming". Journal of Computational and Applied Mathematics, vol. 168: 331-339, 2004.

Oden, J.T., Kikuchi, N., Song, Y. J., Penalty-Finite Element Methods for the Analysis of Stokesian Flows, Computer Methods in Applied Mechanics and Engineering, Vol. 31, pp. 297-326, 1982.

Oden, J.T., Pires, E.B., Numerical Analysis of Certain Contact Problems in Elasticity with Non-classical Friction Laws, Computers & Structures, Vol. 16. pp. 481-485, 1983.

Oliveira, D.A., Worswick, M.J., Grantab R., Williams B., Mayer R., Effect of forming process variables on the crashworthiness of aluminium alloy tubes. International Journal of Impact Engineering, Vol. 32 No. 5, pp.826–846, 2006.

Olson, G.B., Computational design of hierarchically structured materials. Science 277(5330). pp. 1237-42, 1997

Ortiz, M., Popov, E. P., Distortional Hardening Rules for Metal Plasticity Journal of Engineering Mechanics-ASCE 109 No. 4, 1983, 1042-1057

Otubushin, A., Detailed Validation of A Non-Linear Finite Element Code Using Dynamic Axial Crushing of A Square Tube, International Journal of Impact Engineering, May 1998, Volume 21, No. 5, pp. 349-368.

Parrish, A.E., Rais-Rohani, M., Najafi, A., Crashworthiness Optimization of Vehicle Structures Made of a Lightweight Magnesium Alloy. 7th AIAA Multidisciplinary Design Optimization Specialist Conference, Denver, CO: AIAA, 2001.

Raabe D, Roters F. Using texture components in crystal plasticity finite element simulations. International Journal of Plasticity, 2004;20, pp. 339–61.

Raabe, D., Klose P, Engl B, Imlau K-P, Friedel F, Roters F. Concepts for integrating plastic anisotropy into metal forming simulations. Advanced Engineering Materials, 2002, Vol 4, pp.169–80.

184

Raabe, D., Wang, Y., Roters F. Crystal plasticity simulation study on the influence of texture on earing in steel. Computational Materials Science 2005, 34, pp.221–34.

Rebel, G., Park, K.C., Felippa, C.A., A Contact Formulation Based on Localized Lagrange Multipliers: Formulation and Application to Two dimensional Problems. International Journal for Numerical Methods in Engineering, Vol. 54, pp. 263-297, 2002.

Regueiro, R.A., Bammann, D.J., Marin, E.B. and Garikipati, K., A nonlocal phenomenological anisotropic finite deformation plasticity model accounting for dislocation defects. Journal of Engineering Materials and Technology 124, 2002, pp. 380–387.

Renaud, J.E. and Gabriele, G.A., Using the Generalized Reduced Gradient Method to Handle Equality Constraints Directly in a Multilevel Optimization, Advances in Design Automation-1989, DE Vol. 19-2, presented at the 15th Design Automation Conference, Montreal, Quebec, Canada, Sep 1989, pp.7-14.

Roters, F., Eisenlohr, P., Hantcherli, L., Tjahjanto, D.D., Bieler, T.R., Raabe, D. ,Overview of constitutive laws, kinematics, homogenization and multiscale methods in crystal plasticity finite-element modeling: Theory, experiments, applications, Acta Materialia 58, 2010, 1152–1211.

Ryou H., Chung K., Yoon J., Han C., Incorporation of Sheet-Forming Effects in Crash Simulations Using Ideal Forming Theory and Hybrid Membrane and Shell Method Journal of Manufacturing Science and Engineering, Vol. 127, No. 1, pp. 182–192, 2005

Simo, J.C., Hughes, T.J.R., Computational inelasticity, Springer, New York, 2000.

Simo, J.C., Laursen, T.A., An Augmented Lagrangian Treatment of Contact Problems Involving Friction. Computers & Structures, Vol. 42, pp. 97-116, 1992.

Simunovic S., Aramayo G., Steel Processing Properties and their effect on Impact Deformation of Lightweight Structures, Computer Science and Mathematics Division, Computational Materials Science Group, American Iron and Steel Institute, 2002

Sobieszczanski-Sobieski, J., A Linear Decomposition Method for Large Optimization Problems—Blueprint for Development, NASA TM 83248, 1982.

Sobieszczanski-Sobieski, J., James, B. and Dovi, A., Structural Optimization by Multi-Level Decomposition, AIAA Journal, Vol. 23, No. 11, 1985, pp. 1775-1782.

Sobieszczanski-Sobieski, J., James, B., and Riley, M.F., Structural Sizing by Generalized, Multilevel Decomposition, AIAA Journal, Vol. 25, No. 11, 1987, pp. 139-145.

Sobieszczanski-Sobieski, J., Sizing of Complex Structures by the Integration of Several Different Optimal Design Algorithms, AGARD LS-70, Sep 1974, pp. 4.1-4.19.

Stephan, B.,Wohlmuth B., An overlapping domain decomposition method for the simulation of elastoplastic incremental forming processes, International journal for numerical methods in engineering, Vol. 77, No9, pp. 1224-1246, 2009.

Sun, G., Li, G., Gong, Z., Cui, X., Yang, X., Li, Q., Multiobjective robust optimization method for drawbead design in sheet metal forming, Materials & Design, Volume 31, Issue 4, Design of Nanomaterials and Nanostructures, pp. 1917-1929, 2010.

Tang, S.C., Elasto-plastic and Large Deformation Analysis of Thin Shells by the Deformation Theory of Plasticity, Computers & structures, Vol. 6, pp. 297-303, 1976.

Tang, S.C., Large Elasto-plastic Strain Analysis of Flanged Hole Forming. Computers & Structures, Vol. 13, pp.363-370, 1981.

Taylor G. I., Plastic strain in metals, Journal of the Institute of Metals 62 (1938), pp. 307–324.

Thareja, R., and Haftka, R.T., Numerical Difficulties Associated with Using Equality Constraints to Achieve Multi-level Decomposition in Structural Optimization, Proceedings of the 27th IAA/ASME/ASCE/AHS/ASC Structures, Structural Dynamics, and Materials Conference, San Antonio, TX, 1986.

van den Boogaard A.H., Meinders, T., Huétink J., Efficient implicit finite element analysis of sheet forming processes, International Journal for Numerical Methods in Engineering, Vol 56, No 8, pp 1083–1107, 2003.

van Hoek, T., The History influence of Forming on the Predicted Crash Performance of a Truck Bumper MSc thesis, Eindhoven University of Technology,2006.

Vanderplaats, G.N., Yang, Y.J., and Kim, D.S., Sequential Linearization Method for Multilevel Optimum, AIAA Journal, Vol. 28, No. 2, 1990, pp. 290-295.

Wang, G., Shan, S., Review of Metamodeling Techniques in Support of Engineering Design Optimization, Journal of Mechanical Design, Vol. 129, No. 4, pp. 370–380, 2007.

Wang, N-M., Budiansky, B., Analysis of sheet metal stamping by finite element method. Journal of Applied Mechanics, Transaction ASME Vol 45, pp. 73–82, 1978.

Wei, L., Yuying, Y., Multi-objective optimization of sheet metal forming process using Pareto-based genetic algorithm, Journal of Materials Processing Technology, Vol. 208, No. 1-3, 21, pp. 499-506, 2008.

Wierzbicki, T., Schneider, F. Energy Equivalent Flow Stress in Crash Calculations. Impact and Crashworthiness laboratory, MIT, 1999

Wierzbicki, W., and Abramowicz T., On the Crushing Mechanics of Thin Walled Structures, Journal of Applied Mechanics, Vol. 50, 1983, pp.727-734.

186

Williams, B.W., Oliveira, D.A., Worswick, M.J., Mayer, R., Crashworthiness of high and low pressure hydroformed straight section aluminum tubes. In: Proceedings of SAE World Congress, paper No. 2005-01-0095, 2005.

Williams, B.W., Simha, C.H.M., Abedrabbo, N., Mayer, R., Worswick, M.J., Effect of anisotropy, kinematic hardening, and strain-rate sensitivity on the predicted axial crush response of hydroformed aluminum alloy tubes, International Journal of Impact Engineering, Vol. 37, No. 6, Impact Loading of Lightweight Structures, pp. 652-661, 2010.

Wriggers, P., Computational Contact Mechanics, Springer; 2nd edition, 2006

Xie C. L., Nakamachi E. Investigations of the formability of BCC steel sheets by using crystalline plasticity finite element analysis. Material Design, 2002;23:59–68

Xu, W.L., Ma, C.H., Li, C. H., Feng, W. J., Sensitive factors in springback simulation for sheet metal forming, Journal of Materials Processing Technology, Vol 151, pp. 217–222, 2004.

Yang, D.Y., Jung, D.W., Song, I.S., Comparative Investigation into Implicit, Explicit, and Iterative Implicit/Explicit Schemes for the Simulation of SheetMetal Forming Processes, Journal of Materials Processing Technology, vol. 50: 39-53, 1995.

Yang, D.Y., Yoo, D.J., Song, I.S., Investigation into Tool Surface Forming Process, Journal of Materials Processing Technology, Vol. 45, pp. 267-273, 1994.

Zhang, X., Cheng, G. A Comparative Study of Energy Absorption Characteristics of Foam-Filled and Multi-Cell Square Columns. International Journal of Impact Engineering 34, no. 11, 2007, pp.1739-1752.

187

APPENDIX A

SOURCE CODE FOR PREPROCESSING

188

A.1   GEN_INP.f file

```fortran
      program erd_mat_ls

      OPEN(UNIT=2,FILE='PARAM_INP.txt')
      OPEN(UNIT=3,FILE='doe.txt')
      OPEN(UNIT=4,FILE='doe.out')
      READ(3,*)tmx1,tmx2,tmx3,tmx4,tmx5,tmx6,tmx7
          WRITE(2,9)
    9      FORMAT('*PARAMETER')
          WRITE(2,10) tmx1
   10      FORMAT('W= ',E12.5)
           WRITE(2,20) tmx2
   20      FORMAT('H= ',E12.5)
           WRITE(2,30) tmx3
   30      FORMAT('CR= ',E12.5)
           WRITE(2,40) tmx4
   40      FORMAT('THK= ',E12.5)
           WRITE(2,50) tmx5
   50      FORMAT('HF= ',E12.5)
           WRITE(2,60) tmx6
   60      FORMAT('PV= ',E12.5)
           WRITE(2,70) tmx7
   70      FORMAT('PFC= ',E12.5)
           WRITE(2,80)
   80      FORMAT('DFC = PFC')
           WRITE(2,90)
   90      FORMAT('HFC = PFC')
           WRITE(2,100)
  100      FORMAT('HFR = 1000.0')
           WRITE(2,110)
  110      FORMAT('WPT = 298')
      CLOSE(2)
      DO mm=1,50
         READ(3,*)tx1,tx2,tx3,tx4,tx5,tx6,tx7
         WRITE(4,800)tx1,tx2,tx3,tx4,tx5,tx6,tx7
  800    FORMAT(E12.5,',',E12.5,',',E12.5,',',E12.5,',',E12.5,
     *   ',',E12.5,',',E12.5)
      ENDDO
      CLOSE(3)
      CLOSE(4)

      END
```

189

A.2   PARAM_INP.txt generated by GEN_INP.f

```
*PARAMETER
**---------------------------------------**
**----------   Process Parameters
**---------------------------------------**
****-------------------------------------**
** CONSISTENT UNITS= mm, s, N, MPa,E-9
**   W        = Width (mm)   40<W<70
**   H        = Height(mm)   20<H<35
**   CR       = Corner Radious (mm) 2.5<CR<7.5
**   THK      = Nominal Thickness (mm) 0.5<THK<2.5
**   WPT      = Workpiece Temprature (K)
**   HF       = Maximum Holder Force (N)
**   HFR      = Holder Force Rate (N/s) 10000<HF<10000
**   PV       = Punch Velocity (mm/s) 2000<PV<10000
**   PFC      = Punch-Blank Friction Coeficient
**   DFC      = Die-Blank Friction Coeficient
**   HFC      = Holder-Blank Friction Coeficient
****-------------------------------------**
**---------------------------------------**

W=      40
H=      20
CR=      2.5
THK=      0.5
HF=      10000
PV=      2000
PFC=      0.1
DFC = PFC
HFC = PFC
HFR = 1000.0
WPT = 298
```

A.3   Shell script source code for main.sh

```
for runlevel in 1 2 3 4 5 6 7 8 9 10 11 12 13 14 15 16 17 18 19 20 21 22 23 24 25 26 27 28 29 30 31 32 33 34 35 36
do
  mkdir MXMN${runlevel}
 g95 GEN_INP.f
./a.out
mv doe.out doe.txt
cp  rap_pbs.dat STMP.inp SPBK.inp CRSH.inp PARAM_INP.txt stmpprinaao.f spbkprinaao.f crshprin.f MXMN${runlevel}
cd MXMN${runlevel}
## rm STMP.lck
## qsub rap_pbs.dat
## nohup abaqus job=STMP double inter&
cd ..
rm a.out core
done
```

APPENDIX B

SIMULATIONS INPUT DECK

B.1 Input deck for forming simulation

```
*Heading
** Job name: NOPARTstmp Model name: INTSTMP
** Generated by: Abaqus/CAE 6.9-1
*Preprint, echo=NO, model=NO, history=NO, contact=NO
** ----------------------------------------------------------------
*INCLUDE,INPUT=PARAM_INP.txt
*PARAMETER
  DIE_WALLp = W/2+THK/2
  DIE_WALLp_1=DIE_WALLp+THK/2
  DIE_WALLn = -W/2-THK/2
  DIE_WALLn_1 = DIE_WALLn+THK/2
     THKB2_20 = -20-THK/2
        DLYp = 20+THK
        DLYn = -DLYp
     TMFORC = 1.0/HFR
    TOTALTM = H/PV
      ENDTM = TOTALTM+TMFORC
         C1 = CR-THK/2
        C11 =-C1
         C2 = -20.+CR-THK/2
         C3 = 15.-CR+THK/2
         C4 = W/2-CR-THK/2
       C4_2 = W/2-CR-THK
       C4_1 = 20-CR
         C5 = -C4
         C6 = 15.+THK
         C7 = -C6
         C8 = 15.+2*THK
      C9=-20.+THK/2-3/2*THK
      C10=15.+2*THK+THK/2-3/2*THK
      C12=C7-THK-3/4*THK+3/2*THK
   DLYp THK=DLYp-THK+3/2*THK
     THK4B = THK/2
   BLTHK4B = THK/2-THK/2
  BLTHK4Bn =-THK+3/2*THK-THK/2
    THK4Bn =-THK+3/2*THK
     THKB2 = THK/2
   THKB2_1 = THK/4
      THK3 = THK+THK/2-3/2*THK
   PU_WALLp = W/2-THK/2
   PU_WALLn = -PU_WALLp
        HFn =-HF
        PVn =-PV
   BLK_by_P = 2.0
       PREM1 = int(2.0*CR*3.14+2.0*(H-2*CR)+(W-2*CR))
   BLKSPAN = PREM1*BLK_by_P
   BLKSPNB2 = BLKSPAN/2
     nedjel = 125
       EL_L = BLKSPAN/nedjel
     PREMint = int(2.0*CR*3.14+2.0*(H-2*CR)+(W-2*CR)+2*EL_L)
       NEL  = int(PREMint/(2*EL_L))
   CENTER_EL = 63
 BLKX1=BLKSPNB2-0*EL_L
 BLKX2=BLKSPNB2-1*EL_L
 BLKX3=BLKSPNB2-2*EL_L
 BLKX4=BLKSPNB2-3*EL_L
 BLKX5=BLKSPNB2-4*EL_L
 BLKX6=BLKSPNB2-5*EL_L
 BLKX7=BLKSPNB2-6*EL_L
 BLKX8=BLKSPNB2-7*EL_L
 BLKX9=BLKSPNB2-8*EL_L
 BLKX10=BLKSPNB2-9*EL_L
 BLKX11=BLKSPNB2-10*EL_L
 BLKX12=BLKSPNB2-11*EL_L
```

```
ST1=15+0*nedjel+CENTER_EL-NEL
ST2=15+1*nedjel+CENTER_EL-NEL
ST3=15+2*nedjel+CENTER_EL-NEL
ST4=15+3*nedjel+CENTER_EL-NEL
ST5=15+4*nedjel+CENTER_EL-NEL
ST6=15+5*nedjel+CENTER_EL-NEL
ST7=15+6*nedjel+CENTER_EL-NEL
ST8=15+7*nedjel+CENTER_EL-NEL
ST9=15+8*nedjel+CENTER_EL-NEL
ST10=15+9*nedjel+CENTER_EL-NEL
ST11=15+10*nedjel+CENTER_EL-NEL
ST12=15+11*nedjel+CENTER_EL-NEL
ST13=15+12*nedjel+CENTER_EL-NEL
ST14=15+13*nedjel+CENTER_EL-NEL
ST15=15+14*nedjel+CENTER_EL-NEL
ST16=15+15*nedjel+CENTER_EL-NEL
ST17=15+16*nedjel+CENTER_EL-NEL
ST18=15+17*nedjel+CENTER_EL-NEL
ST19=15+18*nedjel+CENTER_EL-NEL
ST20=15+19*nedjel+CENTER_EL-NEL
ST21=15+20*nedjel+CENTER_EL-NEL
ST22=15+21*nedjel+CENTER_EL-NEL
ST23=15+22*nedjel+CENTER_EL-NEL
ST24=15+23*nedjel+CENTER_EL-NEL
ST25=15+24*nedjel+CENTER_EL-NEL
ST26=15+25*nedjel+CENTER_EL-NEL
ST27=15+26*nedjel+CENTER_EL-NEL
ST28=15+27*nedjel+CENTER_EL-NEL
ST29=15+28*nedjel+CENTER_EL-NEL
ST30=15+29*nedjel+CENTER_EL-NEL
ST31=15+30*nedjel+CENTER_EL-NEL
ST32=15+31*nedjel+CENTER_EL-NEL
EN1=14+0*nedjel+CENTER_EL+NEL-1
EN2=14+1*nedjel+CENTER_EL+NEL-1
EN3=14+2*nedjel+CENTER_EL+NEL-1
EN4=14+3*nedjel+CENTER_EL+NEL-1
EN5=14+4*nedjel+CENTER_EL+NEL-1
EN6=14+5*nedjel+CENTER_EL+NEL-1
EN7=14+6*nedjel+CENTER_EL+NEL-1
EN8=14+7*nedjel+CENTER_EL+NEL-1
EN9=14+8*nedjel+CENTER_EL+NEL-1
EN10=14+9*nedjel+CENTER_EL+NEL-1
EN11=14+10*nedjel+CENTER_EL+NEL-1
EN12=14+11*nedjel+CENTER_EL+NEL-1
EN13=14+12*nedjel+CENTER_EL+NEL-1
EN14=14+13*nedjel+CENTER_EL+NEL-1
EN15=14+14*nedjel+CENTER_EL+NEL-1
EN16=14+15*nedjel+CENTER_EL+NEL-1
EN17=14+16*nedjel+CENTER_EL+NEL-1
EN18=14+17*nedjel+CENTER_EL+NEL-1
EN19=14+18*nedjel+CENTER_EL+NEL-1
EN20=14+19*nedjel+CENTER_EL+NEL-1
EN21=14+20*nedjel+CENTER_EL+NEL-1
EN22=14+21*nedjel+CENTER_EL+NEL-1
EN23=14+22*nedjel+CENTER_EL+NEL-1
EN24=14+23*nedjel+CENTER_EL+NEL-1
EN25=14+24*nedjel+CENTER_EL+NEL-1
EN26=14+25*nedjel+CENTER_EL+NEL-1
EN27=14+26*nedjel+CENTER_EL+NEL-1
EN28=14+27*nedjel+CENTER_EL+NEL-1
EN29=14+28*nedjel+CENTER_EL+NEL-1
EN30=14+29*nedjel+CENTER_EL+NEL-1
EN31=14+30*nedjel+CENTER_EL+NEL-1
EN32=14+31*nedjel+CENTER_EL+NEL-1
```

```
ST1o= 1000015+0*nedjel+CENTER_EL-NEL
ST2o= 1000015+1*nedjel+CENTER_EL-NEL
ST3o= 1000015+2*nedjel+CENTER_EL-NEL
ST4o= 1000015+3*nedjel+CENTER_EL-NEL
ST5o= 1000015+4*nedjel+CENTER_EL-NEL
ST6o= 1000015+5*nedjel+CENTER_EL-NEL
ST7o= 1000015+6*nedjel+CENTER_EL-NEL
ST8o= 1000015+7*nedjel+CENTER_EL-NEL
ST9o= 1000015+8*nedjel+CENTER_EL-NEL
ST10o= 1000015+9*nedjel+CENTER_EL-NEL
ST11o= 1000015+10*nedjel+CENTER_EL-NEL
ST12o= 1000015+11*nedjel+CENTER_EL-NEL
ST13o= 1000015+12*nedjel+CENTER_EL-NEL
ST14o= 1000015+13*nedjel+CENTER_EL-NEL
ST15o= 1000015+14*nedjel+CENTER_EL-NEL
ST16o= 1000015+15*nedjel+CENTER_EL-NEL
ST17o= 1000015+16*nedjel+CENTER_EL-NEL
ST18o= 1000015+17*nedjel+CENTER_EL-NEL
ST19o= 1000015+18*nedjel+CENTER_EL-NEL
ST20o= 1000015+19*nedjel+CENTER_EL-NEL
ST21o= 1000015+20*nedjel+CENTER_EL-NEL
ST22o= 1000015+21*nedjel+CENTER_EL-NEL
ST23o= 1000015+22*nedjel+CENTER_EL-NEL
ST24o= 1000015+23*nedjel+CENTER_EL-NEL
ST25o= 1000015+24*nedjel+CENTER_EL-NEL
ST26o= 1000015+25*nedjel+CENTER_EL-NEL
ST27o= 1000015+26*nedjel+CENTER_EL-NEL
ST28o= 1000015+27*nedjel+CENTER_EL-NEL
ST29o= 1000015+28*nedjel+CENTER_EL-NEL
ST30o= 1000015+29*nedjel+CENTER_EL-NEL
ST31o= 1000015+30*nedjel+CENTER_EL-NEL
```

```
EN1o= 1000014+0*nedjel+CENTER_EL+NEL-1
EN2o= 1000014+1*nedjel+CENTER_EL+NEL-1
EN3o= 1000014+2*nedjel+CENTER_EL+NEL-1
EN4o= 1000014+3*nedjel+CENTER_EL+NEL-1
EN5o= 1000014+4*nedjel+CENTER_EL+NEL-1
EN6o= 1000014+5*nedjel+CENTER_EL+NEL-1
EN7o= 1000014+6*nedjel+CENTER_EL+NEL-1
EN8o= 1000014+7*nedjel+CENTER_EL+NEL-1
EN9o= 1000014+8*nedjel+CENTER_EL+NEL-1
EN10o= 1000014+9*nedjel+CENTER_EL+NEL-1
EN11o= 1000014+10*nedjel+CENTER_EL+NEL-1
EN12o= 1000014+11*nedjel+CENTER_EL+NEL-1
EN13o= 1000014+12*nedjel+CENTER_EL+NEL-1
EN14o= 1000014+13*nedjel+CENTER_EL+NEL-1
EN15o= 1000014+14*nedjel+CENTER_EL+NEL-1
EN16o= 1000014+15*nedjel+CENTER_EL+NEL-1
EN17o= 1000014+16*nedjel+CENTER_EL+NEL-1
EN18o= 1000014+17*nedjel+CENTER_EL+NEL-1
EN19o= 1000014+18*nedjel+CENTER_EL+NEL-1
EN20o= 1000014+19*nedjel+CENTER_EL+NEL-1
EN21o= 1000014+20*nedjel+CENTER_EL+NEL-1
EN22o= 1000014+21*nedjel+CENTER_EL+NEL-1
EN23o= 1000014+22*nedjel+CENTER_EL+NEL-1
EN24o= 1000014+23*nedjel+CENTER_EL+NEL-1
EN25o= 1000014+24*nedjel+CENTER_EL+NEL-1
EN26o= 1000014+25*nedjel+CENTER_EL+NEL-1
EN27o= 1000014+26*nedjel+CENTER_EL+NEL-1
EN28o= 1000014+27*nedjel+CENTER_EL+NEL-1
EN29o= 1000014+28*nedjel+CENTER_EL+NEL-1
EN30o= 1000014+29*nedjel+CENTER_EL+NEL-1
EN31o= 1000014+30*nedjel+CENTER_EL+NEL-1
EN32o= 1000014+31*nedjel+CENTER_EL+NEL-1
** PART INSTANCE: BLKHOLDERLEFT-1
**
*System
<DIE_WALLn>,<THKB2>,0.,<DIE_WALLn_1>,<THKB2>,0.
<DIE_WALLn>,<THKB2_1>,0.
*Node
      1,          -5.,          -5.,        130.
*Element, type=MASS, elset=MASSForElm1
1, 1
*Mass, elset=MASSForElm1
0.05,
*Element, type=ROTARYI, elset=RotForElm2
2, 1
*RotaryI, elset=RotForElm2
0.05, 0.05, 0.05, 0., 0., 0.
*Surface, type=CYLINDER, name=BLKHOLDERLEFTU
<DIE_WALLn>, <THK3>, 0., 74., <THK3>, 0.
<DIE_WALLn>, <THK3>, 150.
START,         -150.,          0.
 LINE,           -5.,          0.
 CIRCL,           0.,         -5.,         -5.,         -5.
 LINE,           0.,         -30.
** ------------------------------------------------------------
**
** PART INSTANCE: BLKHOLDERIGHT-1
**
*System
<DIE_WALLp>,<THKB2>,0.,<DIE_WALLp_1>,<THKB2>,0.
<DIE_WALLp>,<THKB2_1>,0.
*Node
      2,           5.,          -5.,        130.
*Element, type=MASS,elset=MassForElem35
```

```
3, 2
*Element, type=ROTARYI,elset=RotForElem46
4, 2
*Mass, elset=MassForElem35
0.05,
*RotaryI, elset=RotForElem46
0.05, 0.05, 0.05, 0., 0., 0.
*Surface, type=CYLINDER, name=BLKHOLDERIGHTU
<DIE_WALLp>, <THK3>, 0., 126., <THK3>, 0.
<DIE_WALLp>, <THK3>, 150.
START,             0.,         -30.
 LINE,             0.,          -5.
 CIRCL,            5.,           0.,           5.,          -5.
 LINE,           150.,           0.
** --------------------------------------------------------------
**
** PART INSTANCE: DIELEFT-1
**
*System
<DIE_WALLn>,-20.,0.,<DIE_WALLn_1>,-20.,0.
<DIE_WALLn>,<THKB2_20>,0.0
*Node
        3,            -5.,          -15.,          130.
*Element, type=MASS, elset=MassForElem79
7, 3
*Element, type=ROTARYI, elset=RotForElem810
8, 3
*Mass, elset=MassForElem79
0.05,
*RotaryI, elset=RotForElem810
0.05, 0.05, 0.05, 0., 0., 0.
*Surface, type=CYLINDER, name=DIELEFTU
<DIE_WALLn>, <C9>, 0., 74., <C9>, 0.
<DIE_WALLn>, <C9>, 150.
START,            0.,          30.
 LINE,            0.,         <C2>
 CIRCL,         <C11>,        -20.,         <C11>,        <C2>
 LINE,         -150.,         -20.
** --------------------------------------------------------------
**
** PART INSTANCE: DIERIGHT-1
**
*System
<DIE_WALLp>,-20.,0.,<DIE_WALLp_1>,-20.,0.
<DIE_WALLp>,<THKB2_20>,0.
*Node
        4,             5.,          -15.,          130.
*Element, type=MASS, elset=MassForel11
11, 4
*Element, type=ROTARYI, elset=RotForEl12
12, 4
*Mass, elset=MassForel11
0.05,
*RotaryI, elset=RotForEl12
0.05, 0.05, 0.05, 0., 0., 0.
*Surface, type=CYLINDER, name=DIERIGHTU
<DIE_WALLp>, <C9>, 0., 126., <C9>, 0.
<DIE_WALLp>, <C9>, 150.
START,          150.,         -20.
 LINE,         <C1>,         -20.
 CIRCL,          0.,         <C2>,       <C1>,      <C2>
 LINE,           0.,          30.
** --------------------------------------------------------------
**
** PART INSTANCE: PUNCH-1
**
*System
0.,<C4>,0.,<THKB2>,<C4>,0.
0.,<C4_1>,0.0
*Node
      5,           0.,           15.,          130.
```

```
*Element, type=MASS, elset=MassForel13
13, 5
*Element, type=ROTARYI, elset=RotForEl14
14, 5
*Mass, elset=MassForel13
0.05,
*RotaryI, elset=RotForEl14
0.05, 0.05, 0.05, 0., 0., 0.
*Surface, type=CYLINDER, name=PUNCHU
0., <C10>, 0., 150., <C10>, 0.
0., <C10>, 150.
START,    <PU_WALLn>,          -30.
 LINE,    <PU_WALLn>,          <C3>
  CIRCL,       <C5>,           <C6>,       <C5>,          <C3>
  LINE,        <C4>,           <C6>
  CIRCL,    <PU_WALLp>,        <C3>,       <C4>,          <C3>
 LINE,     <PU_WALLp>,          -30.
** -------------------------------------------------------------
**
** PART INSTANCE: BLANK-B
*System
0.,<THKB2>,-125.,<THKB2>,<THKB2>,-125.
**      0.,         <THK>,       -125.,          <THK>,         <THKB2>,        -125.
*Node
      6,<BLKX1>,          <BLTHK4B>,         250.
      7,<BLKX2>,          <BLTHK4B>,         250.
      8,<BLKX3>,          <BLTHK4B>,         250.
      9,<BLKX4>,          <BLTHK4B>,         250.
     10,<BLKX5>,          <BLTHK4B>,         250.
     11,<BLKX6>,          <BLTHK4B>,         250.
     12,<BLKX7>,          <BLTHK4B>,         250.
*Element, type=S4R, ELSET=TOPBLANK
     15,      6,      7,    133,    132
     16,      7,      8,    134,    133
     17,      8,      9,    135,    134
     18,      9,     10,    136,    135
     19,     10,     11,    137,    136
     20,     11,     12,    138,    137
     21,     12,     13,    139,    138
     22,     13,     14,    140,    139
     23,     14,     15,    141,    140
     24,     15,     16,    142,    141
     25,     16,     17,    143,    142
     26,     17,     18,    144,    143
     27,     18,     19,    145,    144
     28,     19,     20,    146,    145
     29,     20,     21,    147,    146
     30,     21,     22,    148,    147
     31,     22,     23,    149,    148
     32,     23,     24,    150,    149
     33,     24,     25,    151,    150
     34,     25,     26,    152,    151
     35,     26,     27,    153,    152
     36,     27,     28,    154,    153
     37,     28,     29,    155,    154
     38,     29,     30,    156,    155
     39,     30,     31,    157,    156
```

```
*Nset, nset=BLANK-B__PICKEDSET2, generate
    6,  26591,      1
*Elset, elset=BLANK-B__PICKEDSET2, generate
   15,  26264,      1
** Section: Section-1-_PICKEDSET2
*Shell Section, elset=CRUSH_OBU, material=MATERIAL-1, controls=EC-1
<THK>, 5
*Shell Section, elset=OBLL, material=MATERIAL-1, controls=EC-1
<THK>, 5
*Shell Section, elset=OBLR, material=MATERIAL-1, controls=EC-1
<THK>, 5
** ----------------------------------------------------------------
**
** PART INSTANCE: BLKHOLDERLEFT-A
**
*System
<DIE_WALLn>,0.,0.,<DIE_WALLn_1>,0.,0.
*Node
2000001,          -5.,          -5.,         130.
*Element, type=MASS,elset=MassFor9390
2000001, 2000001
*Element, type=ROTARYI,elset=RotFor9391
2000002, 2000001
*Mass, elset=MassFor9390
0.05,
*RotaryI, elset=RotFor9391
0.05, 0.05, 0.05, 0., 0., 0.
*Surface, type=CYLINDER, name=BLKHOLDERLEFTL
<DIE_WALLn>, <THK4Bn>, 0., 74., <THK4Bn>, 0.
<DIE_WALLn>, <THK4Bn>, -150.
START,       -150.,           0.
 LINE,         -5.,           0.
 CIRCL,         0.,          -5.,          -5.,          -5.
 LINE,          0.,         -30.
** ----------------------------------------------------------------
**
** PART INSTANCE: BLKHOLDERIGHT-A
**
*System
<DIE_WALLp>,0.,0.,<DIE_WALLp_1>,0.,0.
*Node
   2000002,           5.,          -5.,         130.
*Element, type=MASS, elset=MassFor9392_4
2000003, 2000002
*Element, type=ROTARYI, elset=MassFor9393_5
2000004, 2000002
*Mass, elset=MassFor9392_4
0.05,
*RotaryI, elset=MassFor9393_5
0.05, 0.05, 0.05, 0., 0., 0.
*Surface, type=CYLINDER, name=BLKHOLDERIGHTL
<DIE_WALLp>, <THK4Bn>, 0., 126., <THK4Bn>, 0.
<DIE_WALLp>, <THK4Bn>, -100.
START,         0.,         -30.
 LINE,         0.,          -5.
 CIRCL,         5.,           0.,           5.,          -5.
 LINE,       150.,           0.
** ----------------------------------------------------------------
**
** PART INSTANCE: DIELEFT-A
**
*System
<DIE_WALLn>,<DLYp>,0.,<DIE_WALLn_1>,<DLYp>,0.
*Node
   2000003,          -5.,         -15.,         130.
*Element, type=MASS, elset=MassFor9396_8
2000005, 2000003
*Element, type=ROTARYI, elset=MassFor9397_9
2000006, 2000003
*Mass, elset=MassFor9396_8
0.05,
*RotaryI, elset=MassFor9397_9
0.05, 0.05, 0.05, 0., 0., 0.
```

```
*Surface, type=CYLINDER, name=DIELEFTL
<DIE_WALLn>, <DLYp_THK>, 0., 74., <DLYp_THK>, 0.
<DIE_WALLn>, <DLYp_THK>, -150.
START,              0.,            30.
 LINE,              0.,            <C2>
 CIRCL,            <C11>,         -20.,            <C11>,           <C2>
 LINE,            -150.,         -20.
** ----------------------------------------------------------------
**
** PART INSTANCE: DIERIGHT-A
**
*System
<DIE_WALLp>,<DLYp>,0.,<DIE_WALLp_1>,<DLYp>,0.
*Node
   2000004,            5.,            -15.,           130.
*Element, type=MASS, elset=MassFor9400
2000007, 2000004
*Element, type=ROTARYI, elset=MassFor9401
2000008, 2000004
*Mass, elset=MassFor9400
0.05,
*RotaryI, elset=MassFor9401
0.05, 0.05, 0.05, 0., 0., 0.
*Surface, type=CYLINDER, name=DIERIGHTL
<DIE_WALLp>, <DLYp_THK>, 0., 126., <DLYp_THK>, 0.
<DIE_WALLp>, <DLYp_THK>, -150.
START,            150.,          -20.
 LINE,            <C1>,          -20.
 CIRCL,             0.,          <C2>,      <C1>,    <C2>
 LINE,              0.,           30.
** ----------------------------------------------------------------
**
** PART INSTANCE: PUNCH-A
**
*Node
   2000005,            0.,             15.,           130.
*Element, type=MASS, elset=MassFor9402
2000009, 2000005
*Element, type=ROTARYI, elset=MassFor9403
2000010, 2000005
*Mass, elset=MassFor9402
0.05,
*RotaryI, elset=MassFor9403
0.05, 0.05, 0.05, 0., 0., 0.
*Surface, type=CYLINDER, name=PUNCHL
0., <C12>, 0., 150., <C12>, 0.
0., <C12>, -150.
START,     <PU_WALLn>,          -30.
 LINE,     <PU_WALLn>,          <C3>
 CIRCL,        <C5>,            <C6>,     <C5>,          <C3>
 LINE,         <C4>,            <C6>
 CIRCL,    <PU_WALLp>,          <C3>,     <C4>,          <C3>
 LINE,     <PU_WALLp>,          -30.
** ----------------------------------------------------------------
**
** PART INSTANCE: BLANK-1
**
*System
0.,<THKB2>,-125.,<THKB2>,<THKB2>,-125.
*Node
1000006,<BLKX1>,                  <BLTHK4Bn>,        250.
1000007,<BLKX2>,                  <BLTHK4Bn>,        250.
1000008,<BLKX3>,                  <BLTHK4Bn>,        250.
1000009,<BLKX4>,                  <BLTHK4Bn>,        250.
1000010,<BLKX5>,                  <BLTHK4Bn>,        250.
```

```
*Nset, nset=BLANK-1__PICKEDSET2, generate
1000006, 1026591,      1
*Elset, elset=BLANK-1__PICKEDSET2, generate
1000015, 1026264,      1
****((((((((((((((((((((((((((((((((((((((((((((((((((((((((((((
*Shell Section, elset=CRUSH_OBL, material=MATERIAL-1, controls=EC-1
<THK>, 5
*Shell Section, elset=OBUL, material=MATERIAL-1, controls=EC-1
<THK>, 5
*Shell Section, elset=OBUR, material=MATERIAL-1, controls=EC-1
<THK>, 5
*Elset, elset=BLANKH, generate
 15, 26264,      1
*Elset, elset=BLANKD, generate
 1000015, 1026264,      1
*Surface, type=ELEMENT, name=BLANKD
BLANKD
*Surface, type=ELEMENT, name=BLANKH
BLANKH
**
**
*Rigid Body, ref node=4, analytical surface=DIERIGHTU
*Rigid Body, ref node=2000003, analytical surface=DIELEFTL
*Rigid Body, ref node=2000004, analytical surface=DIERIGHTL
*Rigid Body, ref node=3, analytical surface=DIELEFTU
*Rigid Body, ref node=2, analytical surface=BLKHOLDERIGHTU
*Rigid Body, ref node=5, analytical surface=PUNCHU
*Rigid Body, ref node=1, analytical surface=BLKHOLDERLEFTU
*Rigid Body, ref node=2000002, analytical surface=BLKHOLDERIGHTL
*Rigid Body, ref node=2000001, analytical surface=BLKHOLDERLEFTL
*Rigid Body, ref node=2000005, analytical surface=PUNCHL
**
*********************************************
*ELSET, ELSET=CRUSH_OBL, GENERATE
<ST1>,<EN1>,1
<ST2>,<EN2>,1
<ST3>,<EN3>,1
<ST4>,<EN4>,1
<ST5>,<EN5>,1
```

```
*ELSET, ELSET=ELTOBO
tie_top,tie_bot
*Nset, nset=tiedobj, elset=ELTOBO
*Nset, nset=CRUSH_OBU, elset=CRUSH_OBU
*Nset, nset=CRUSH_OBL, elset=CRUSH_OBL
*Nset, nset=BC_CRUSH, GENERATE
26466,26591,1
1026466,1026591,1
** ELEMENT CONTROLS
**
*Section Controls, name=EC-1, hourglass=RELAX STIFFNESS, second order accuracy=YES
1., 1., 1.
*Amplitude, name=AMP-1
          0.,          0.,         0.01,             1.
**
** MATERIALS
**
*Material, name=MATERIAL-1
*Density
 1.738e-09,
*Elastic
45000., 0.33
*Plastic,rate=0
2.25E+02,0.0
2.39E+02,0.0227565
2.51E+02,0.0280123
2.62E+02,0.0334448
2.71E+02,0.039026
2.80E+02,0.0446936
2.87E+02,0.0505404
2.93E+02,0.0565043
2.95E+02,0.0628393
2.98E+02,0.0691321
3.01E+02,0.0755729
*plastic,rate=4300
3.15E+02,0.0
3.36E+02,0.0234699
**
*Surface Interaction, name=DIE_FC
*Friction
 <DFC>,
*Surface Interaction, name=HOLDER_FC
*Friction
 <HFC>,
*Surface Interaction, name=PUNCH_FC
*Friction
 <PFC>,
*Nset, nset=BLANKEDG,GENERATE
6,26466,126
131,26591,126
1000006,1026466,126
1000131,1026591,126
*Nset, nset=DIES
 3,4,2000004,2000003
*Nset, nset=HOLDERS
 1,2,2000001,2000002
*Nset, nset=PUNCHES
 5,2000005
*Nset, nset=PUNCHET
 5
*Nset, nset=PUNCHEB
 2000005
*Nset, nset=HOLDERTOP
 1, 2
*Nset, nset=HOLDERBOT
2000001,2000002

** --------------------------------------------------------------
**
** STEP: Step-2
**
*Step, name=Step-2
*Dynamic, Explicit
, <TMFORC>
*Bulk Viscosity
0.06, 1.2
```

201

```
*Dynamic, Explicit
, <TMFORC>
*Bulk Viscosity
0.06, 1.2
** Mass Scaling: Semi-Automatic
**              Whole Model
*Fixed Mass Scaling, factor=100.
**
** BOUNDARY CONDITIONS
**
** Name: Blank Type: Displacement/Rotation
*Boundary
BLANKEDG, 2, 2
** Name: DIE Type: Displacement/Rotation
*Boundary
DIES, 1, 1
DIES, 2, 2
DIES, 3, 3
DIES, 4, 4
DIES, 5, 5
DIES, 6, 6
** Name: Holder Type: Displacement/Rotation
*Boundary
HOLDERS, 1, 1
HOLDERS, 3, 3
HOLDERS, 4, 4
HOLDERS, 5, 5
HOLDERS, 6, 6
** Name: PunchSTEP1 Type: Displacement/Rotation
*Boundary
PUNCHES, 1, 1
PUNCHES, 2, 2
PUNCHES, 3, 3
PUNCHES, 4, 4
PUNCHES, 5, 5
PUNCHES, 6, 6
**
** LOADS
 **======================================
 ** Name: Load-1    Type: Concentrated force
 *Cload, amplitude=AMP-1
 HOLDERTOP, 2, <HFn>
 ** Name: Load-2    Type: Concentrated force
 *Cload, amplitude=AMP-1
 HOLDERBOT, 2, <HF>
 **======================================
 ** INTERACTIONS
 **
 ** Interaction: INT-1-1
 *Contact Pair, interaction=HOLDER_FC, mechanical constraint=KINEMATIC, cpset=INT-1-1
 BLANKD, BLKHOLDERLEFTU
 ** Interaction: INT-1-2
 *Contact Pair, interaction=HOLDER_FC, mechanical constraint=KINEMATIC, cpset=INT-1-2
 BLANKH, BLKHOLDERLEFTL
 ** Interaction: INT-2-1
 *Contact Pair, interaction=DIE_FC, mechanical constraint=KINEMATIC, cpset=INT-2-1
 BLANKD, DIELEFTU
 ** Interaction: INT-2-2
 *Contact Pair, interaction=DIE_FC, mechanical constraint=KINEMATIC, cpset=INT-2-2
 BLANKH, DIELEFTL
 ** Interaction: INT-3-1
 *Contact Pair, interaction=PUNCH_FC, mechanical constraint=KINEMATIC, cpset=INT-3-1
 BLANKD, PUNCHU
 ** Interaction: INT-3-2
 *Contact Pair, interaction=PUNCH_FC, mechanical constraint=KINEMATIC, cpset=INT-3-2
 BLANKH, PUNCHL
 ** Interaction: INT-4-1
 *Contact Pair, interaction=HOLDER_FC, mechanical constraint=KINEMATIC, cpset=INT-4-1
 BLANKD, BLKHOLDERIGHTU
 ** Interaction: INT-4-2
 *Contact Pair, interaction=HOLDER_FC, mechanical constraint=KINEMATIC, cpset=INT-4-2
 BLANKH, BLKHOLDERIGHTL
 ** Interaction: INT-5-1
 *Contact Pair, interaction=DIE_FC, mechanical constraint=KINEMATIC, cpset=INT-5-1
 BLANKD, DIERIGHTU
 ** Interaction: INT-5-2
```

```
*Restart, write, number interval=1, time marks=NO
**
** FIELD OUTPUT: F-Output-1
**
*Output, field, variable=ALL
**
** HISTORY OUTPUT: H-Output-1
**
*Output, history, variable=ALL
*Output, history, frequency=10
*Contact Output, cpset=INT-1-1
CAREA, CFN1, CFN2, CFN3, CFNM
**
** HISTORY OUTPUT: H-Output-3
**
*Contact Output, cpset=INT-1-2
CAREA, CFN1, CFN2, CFN3, CFNM
**
** HISTORY OUTPUT: H-Output-4
**
*Contact Output, cpset=INT-2-1
CAREA, CFN1, CFN2, CFN3, CFNM
**
** HISTORY OUTPUT: H-Output-5
**
*Contact Output, cpset=INT-2-2
CAREA, CFN1, CFN2, CFN3, CFNM
**
** HISTORY OUTPUT: H-Output-6
**
*Contact Output, cpset=INT-3-1
CAREA, CFN1, CFN2, CFN3, CFNM
**
** HISTORY OUTPUT: H-Output-7
**
*Contact Output, cpset=INT-3-2
CAREA, CFN1, CFN2, CFN3, CFNM
**
 **
 ** STEP: Step-3
 **
*Step, name=Step-3
*Dynamic, Explicit
, <TOTALTM>
*Bulk Viscosity
0.06, 1.2
** Mass Scaling: Semi-Automatic
**                 Whole Model
*Fixed Mass Scaling, factor=100.
**
** BOUNDARY CONDITIONS
**
** Name: Blank Type: Displacement/Rotation
*Boundary, op=NEW
BLANKEDG, 2, 2
** Name: DIE Type: Displacement/Rotation
*Boundary, op=NEW
DIES, 1, 1
DIES, 2, 2
DIES, 3, 3
DIES, 4, 4
DIES, 5, 5
DIES, 6, 6
** Name: Holder Type: Displacement/Rotation
*Boundary, op=NEW
HOLDERS, 1, 1
HOLDERS, 3, 3
HOLDERS, 4, 4
HOLDERS, 5, 5
HOLDERS, 6, 6
** Name: PunchSTEP1 Type: Displacement/Rotation
*Boundary, op=NEW
** Name: PunchSTEP2 Type: Displacement/Rotation
*Boundary, op=NEW
PUNCHES, 1, 1
PUNCHES, 3, 3
PUNCHES, 4, 4
, PUNCHES, 5, 5
```

203

```
*Cload, op=NEW
*Cload, op=NEW
**--------------------------------------
*Cload, op=NEW
HOLDERTOP, 2, <HFn>
*Cload, op=NEW
HOLDERBOT, 2, <HF>
**======================================
*Boundary, op=NEW, type=VELOCITY
PUNCHET, 2, 2, <PVn>
*Boundary, op=NEW, type=VELOCITY
PUNCHEB, 2, 2, <PV>
**======================================
** INTERACTIONS
**
**
**
** LOADS
**
** OUTPUT REQUESTS
**
*Restart, write, number interval=1, time marks=NO
**
** FIELD OUTPUT: F-Output-2
**
*Output, field, variable=ALL
**
** HISTORY OUTPUT: H-Output-2
**
*Output, history, variable=ALL
*Output, history, frequency=10
*Contact Output, cpset=INT-1-1
CAREA, CFN1, CFN2, CFN3, CFNM
**
** HISTORY OUTPUT: H-Output-3
**
*Contact Output, cpset=INT-1-2
```

B.2 Input deck for springback simulation

```
*Heading
** Job name: INTSPBK Model name: INTSTMP
** Generated by: Abaqus/CAE 6.9-1
*Preprint, echo=NO, model=NO, history=NO, contact=NO
**
*INCLUDE,INPUT=PARAM_INP.txt
*PARAMETER
        EL_L = 2.0
        PREM = int(2.0*CR*3.14+2.0*(H-2*CR)+(W-CR))
        NEL  = int(PREM/(2*EL_L))
 CENTER_EL = 37
**
** PARTS
**
**
*Import,STEP=2,STATE=YES, update=yes
CRUSH_OBU,OBLL,OBLR,CRUSH_OBL,OBUL,OBUR
*Amplitude, name=AMP-1
            0.,          0.,         0.01,          1.
**
** MATERIALS
**
*Material, name=Material-1
**CONDUCTIVITY
**156.,
**SPECIFIC HEAT
**452.,
*Density
 1.738e-08,
*Elastic
45000., 0.33
*Plastic,rate=0
2.25E+02,0.0
2.39E+02,0.0227565
2.51E+02,0.0280123
2.62E+02,0.0334448
2.71E+02,0.039026
2.80E+02,0.0446936
2.87E+02,0.0505404
**Nset, nset=Ybound, GENERATE
*Nset, nset=Ybound
100,1000100,37,1000037,26560,1026560,26497,1026497
**68,26528,126
**1000068,1026528,126
**1013172,1013298,
**13172,13298
**    6,   131, 26466, 26591
*Nset, nset=Zbound
1013235,1013110,1013235,1013110
*Nset, nset=Xbound
1000068, 1026528,68, 26528
**
** PREDEFINED FIELDS
**
** Name: Predefined Field-1   Type: Initial State
** ----------------------------------------------------------------
**
** STEP: Step-1
**
**Step, name=Step-1, amplitude=STEP
*Step, name=Step-1, nlgeom=YES
*Static, stabilize=0.0002, allsdtol=0.05, continue=NO
1., 1., 1e-05, 1.
**Coupled Temperature-Displacement,STABILIZE,ALLSDTOL, CONTINUE=YES
**Coupled Temperature-Displacement, creep=none, deltmx=5.
**1., 1., 1e-08, 1.
**
** BOUNDARY CONDITIONS
**
** Name: BC-1 Type: Temperature
**Boundary
**_PickedSet43, 11, 11, 298.
** Name: BC-6 Type: Displacement/Rotation
*Boundary, fixed
Xbound, 1, 1
*Boundary, fixed
Ybound, 2, 2
```

```
*Output, field, variable=ALL
*EL FILE, ELSET=CRUSH_OBU, POSITION=CENTROIDAL
STH
*EL FILE, ELSET=CRUSH_OBL, POSITION=CENTROIDAL
STH
*EL FILE, ELSET=CRUSH_OBU, POSITION=CENTROIDAL
SINV
*EL FILE, ELSET=CRUSH_OBL, POSITION=CENTROIDAL
SINV
**NODE FILE, NSET=tiedobj,FREQUENCY=2
**COORD
*NODE FILE, NSET=CRUSH_OBU,FREQUENCY=1
COORD
*NODE FILE, NSET=CRUSH_OBL,FREQUENCY=1
COORD
**EL PRINT, ELSET=CRUSH_OBL, POSITION=CENTROIDAL,SUMMARY=YES
**PEEQMAX
**EL PRINT, ELSET=CRUSH_OBU, POSITION=CENTROIDAL,SUMMARY=YES
**PEEQMAX
***NODE PRINT, NSET=tiedobj, SUMMARY=YES
**U
**
** HISTORY OUTPUT: H-Output-1
**
```

B.3   Input deck for crush simulation

```
**
** PART INSTANCE: PART-1-1
**
*Import, step=1,state=yes, update=YES
CRUSH_OBL,CRUSH_OBU
** --------------------------------------------------------------
**
** PART INSTANCE: Part-2-1
**
*System
          0.,           0.,           130.,           1.,           0.,           130.
          0.,0.,          129.
*Surface, type=CYLINDER, name=Part-2-1_Surf-3
0., 0., 130., 100., 0., 130.
0., -100., 130.
START,          -95.,                0.
 LINE,           95.,                0.
*System
*Node,nset=RigidWall-1-RefPt_
3000000,           0.,           -100.,           130.
*Rigid Body, ref node=RigidWall-1-RefPt_, analytical surface=Part-2-1_Surf-3
*Nset, nset=_PickedSet250
3000000,
*Nset, nset=_PickedSet251
3000000,
*Nset, nset=_PickedSet253
3000000,
** Constraint: Constraint-1
*Amplitude, name=AMP-1
          0.,           0.,           0.01,           1.
**
** MATERIALS
**
*Material, name=MATERIAL-1
*Density
 1.738e-09,
*Elastic
45000., 0.33
*Plastic,rate=0
2.25E+02 0.0
```

```
**
*Tie, name=TIECONT, adjust=yes, position tolerance=<THK>
BOTBLK, TOPBLK
*Surface, type=ELEMENT, name=BOTBLK, MAX RATIO
tie_top,
*Surface, type=ELEMENT, name=TOPBLK, MAX RATIO
tie_bot,
*Surface, type=ELEMENT, name=BLKU, MAX RATIO
BLANKD
**CRUSH_OBL,
*Surface, type=ELEMENT, name=BLKL, MAX RATIO
BLANKH
**CRUSH_OBU,
*ELSET, ELSET=BLANKL
CRUSH_OBL
*ELSET, ELSET=BLANKU
CRUSH_OBU
*Surface, type=ELEMENT, name=BLANKU, MAX RATIO
BLANKU
**CRUSH_OBU,
*Surface, type=ELEMENT, name=BLANKL, MAX RATIO
BLANKL
**CRUSH_OBL,
*Surface Interaction, name=IntProp-1
*Friction
0.,
*Surface Interaction, name=IntProp-2
*Friction
 0.1,
**
** PREDEFINED FIELDS
**
** Name: Predefined Field-1   Type: Initial State
** --------------------------------------------------------------
```

```
*Step, name=Step-1
*Dynamic, Explicit
, 0.025
*Bulk Viscosity
0.06, 1.2
** Mass Scaling: Semi-Automatic
**                Whole Model
*Fixed Mass Scaling, factor=100.
**
** BOUNDARY CONDITIONS
**
** Name: BC-1 Type: Displacement/Rotation
*Boundary
_PickedSet250, 1, 1
_PickedSet250, 2, 2
_PickedSet250, 4, 4
_PickedSet250, 5, 5
_PickedSet250, 6, 6
** Name: BC-2 Type: Velocity/Angular velocity
*Boundary, type=VELOCITY
_PickedSet251, 3, 3, -5000.
** Name: BC-3 Type: Displacement/Rotation
*Boundary
BC_CRUSH, 1, 1
BC_CRUSH, 2, 2
BC_CRUSH, 3, 3
BC_CRUSH, 4, 4
BC_CRUSH, 5, 5
BC_CRUSH, 6, 6
**
** INTERACTIONS
*Contact Pair, interaction=IntProp-2, mechanical constraint=PENALTY, cpset=Int-1
Part-2-1_Surf-3, BLKU
*Contact Pair, interaction=IntProp-2, mechanical constraint=PENALTY, cpset=Int-2
Part-2-1_Surf-3, BLKL
*Contact Pair, interaction=INTPROP-1, mechanical constraint=PENALTY, cpset=Int-2
BLANKU,BLANKL
*Contact Pair, interaction=INTPROP-1, mechanical constraint=PENALTY, cpset=Int-2

** OUTPUT REQUESTS
**
```

APPENDIX C

POST-PROCESSING CODES

C.1 Stamping response extraction stmpaao.f

```fortran
      SUBROUTINE ABQMAIN
C=================================================================
C This program must be compiled and linked with the command:
C     abaqus make job=fprin
C Run the program using the command:
C     abaqus fprin
C=================================================================
C
C  Purpose:
C
C    This program computes the principal stresses and strains and their
C    directions from stress and strain values stored in an ABAQUS
C    results file (.fil).
C
C  Input File names: `FNAME.fil', where FNAME is the root file name of
C                               the input file.
C
C  Output File name:  pvalue.dat
C
C=================================================================
C
C  Variables used by this program and ABAQUS subroutine SPRIND :
C
C   NDI    -- Number of direct components in stress/strain tensor.
C   NSHR   -- Number of shear components in stress/strain tensor.
C   NDIP1  -- NDI + 1
C   ARRAY  -- Real array containing values read from results file
C             (.fil). Equivalenced to JRRAY.
C   JRRAY  -- Integer array containing values read from results file
C             (.fil). Equivalenced to ARRAY.
C   FNAME  -- Root file name of input file (w/o .fil extension).
C   NRU    -- Number of results files (.fil) to be read.
C   LRUNIT -- Array containing unit number and format of results files:
C             LRUNIT(1,*) --> Unit number of input file.
C             LRUNIT(2,*) --> Format of input file.
C   LOUTF  -- Format of output file:
C             0 --> Standard ASCII format.
C             1 --> ABAQUS results file ASCII format.
C             2 --> ABAQUS results file binary format.
C   JUNIT  -- Unit number of file to be opened.
C   JRCD   -- Error check return code.
C             .EQ. 0 --> No errors.
C             .NE. 0 --> Errors detected.
C   KEY    -- Current record key identifier.
C   JELNUM -- Current element number.
C   INTPN  -- Integration point number.
C   LSTR   -- Indicates type of principal value (stress/strain) and
```

```fortran
C    LSTR   -- Indicates type of principal value (stress/strain) and
C              ordering used:
C                  For calculation of principal value (stress/strain):
C                     1 --> stress.
C                     2 -->  strain.
C                  For calculation of directions:
C                     1 -->  stress.
C                     2 -->  strain.
C    S      -- Array containing stress tensor.
C    PS     -- Array containing principal stresses.
C    ANPS   -- Array containing directions of principal stresses.
C    E      -- Array containing strain tensor.
C    PE     -- Array containing principal strains.
C    ANPE   -- Array containing directions of principal strains.
C
C===================================================================
C
C  The use of ABA_PARAM.INC eliminates the need to have different
C  versions of the code for single and double precision.
C  ABA_PARAM.INC defines an appropriate IMPLICIT REAL statement
C  and sets the value of NPRECD to 1 or 2, depending on whether
C  the machine uses single or double precision.
C
C===================================================================
C
      INCLUDE 'aba_param.inc'
      DIMENSION  ARRAY(513), JRRAY(NPRECD,513), LRUNIT(2,1)
      EQUIVALENCE (ARRAY(1), JRRAY(1,1))
C
C===================================================================
      DIMENSION S(6), E(6), PS(3), PE(3), ANPS(3,3), ANPE(3,3),RN(4)
      CHARACTER  FNAME*80
C
C===================================================================
C  Get the name of the results file.
C
C===================================================================
      FNAME='STMP'
      PRIN1=0
      PRIN2=0
      AA_phi=0
      BB_phi=0
      AA_xi=0
      BB_xi=0
       df = 0
       dw = 0
      INN=0
```

211

```fortran
C=====================================================================
      OPEN(UNIT=9,FILE='STMP.txt',STATUS='NEW')
C
      NRU = 1
      LOUTF = 0
      LRUNIT(1,1) = 8
      LRUNIT(2,1) = 2
C
      CALL INITPF(FNAME,NRU,LRUNIT,LOUTF)
C
      JUNIT = 8
C
      CALL DBRNU(JUNIT)
C
C=====================================================================
C  Read records from the results (.fil) file and process the data.
C  Cover a maximum of 10 million records in the file.
C
C=====================================================================
      DO 1000 K100 = 1, 100
      DO 1000 K1 = 1, 99999
         CALL DBFILE(0,ARRAY,JRCD)
         IF (JRCD .NE. 0) GO TO 1001
         KEY = JRRAY(1,2)
C
C=====================================================================
C  Get the heading (title) record.
C
C=====================================================================
         IF (KEY .EQ. 1922) THEN
C            WRITE(9,1100) (ARRAY(IXX),IXX=3,12)
C 1100       FORMAT(1X,10A8)
C
C=====================================================================
C  Get the current step and increment number.
C
C=====================================================================
         ELSE IF (KEY .EQ. 2000) THEN
C            WRITE(9,1200) JRRAY(1,8), JRRAY(1,9)
C 1200       FORMAT(1X,'** STEP ',I2,'    INCREMENT ',I3)
            RES_INC=JRRAY(1,9)
C
C=====================================================================
C  Get the element and integration point numbers, JELNUM and INTPN,
C  and the location of INTPN (0--at int.pt., 1--at centroid,
C  4--nodal average) and the number of direct and shear components
C  in the analysis.
C
```

212

```fortran
c      4--nodal average) and the number of direct and shear components
c      in the analysis.
c=====================================================================
        ELSE IF (KEY .EQ. 1) THEN
            JELNUM = JRRAY(1,3)
            INTPN  = JRRAY(1,4)
            LOCATE = JRRAY(1,6)
            NDI    = JRRAY(1,8)
            NSHR   = JRRAY(1,9)
            NDIP1  = NDI + 1
c=====================================================================
c      Get the stress tensor.
c
c=====================================================================
c
c
c=====================================================================
c      Get the plastic strain tensor.
c
c=====================================================================
        ELSE  IF (KEY .EQ. 22) THEN
            DO 30 IXX = 1, NDI
              E(IXX) = ARRAY(IXX+2)
 30         CONTINUE
            DO 40 IYY = NDI + 1, NSHR + NDI
              E(IYY) = ARRAY(IYY+2)
 40         CONTINUE
c
c
c=====================================================================
c      Calculate the principal strains and corresponding principal
c      directions in unsorted order.
c=====================================================================
            LSTR = 2
            CALL SPRIND(E,PE,ANPE,LSTR,NDI,NSHR)
            IF (ABS(PE(1)).GT.PRIN1)  THEN
                PRIN1=ABS(PE(1))
                PRIN1_1=PE(1)
            END IF
            IF (ABS(PE(2)).GT.PRIN2)  THEN
                PRIN2=ABS(PE(2))
                PRIN2_2=PE(2)
            END IF
        df=df+(PE(1)-AA_phi*PE(2)-BB_phi)**2
        dw=dw+(AA_xi*PE(2)+BB_xi-PE(1))**2
        ELSE  IF (KEY .EQ. 107) THEN
            IF (RES_INC.NE.0) THEN
            DO 50 IXX = 1, 4
              RN(IXX) = ARRAY(IXX+2)
 50         CONTINUE
                INN=1+INN
            WRITE(9,2203) (RN(IZZ), IZZ = 1, 4)
C 2203       FORMAT(4X,'NODENUMBER= ',I8,'  X = ',E12.5,'  Y = ',E12.5,'  Z = ',E12.5)
 2203        FORMAT(I8,',',E12.5,',',E12.5,',',E12.5)

            END IF

        END IF
 1000   CONTINUE
 1001   CONTINUE
            WRITE(9,2206) INN,df, dw
 2206        FORMAT(I8,'df = ',E12.5,'dw = ',E12.5)


      CLOSE (UNIT=9)

      RETURN
      END
```

213

C.2 Springback response extraction spbkaao.f

```fortran
      SUBROUTINE ABQMAIN
C====================================================================
C This program must be compiled and linked with the command:
C     abaqus make job=fprin
C Run the program using the command:
C     abaqus fprin
C====================================================================
C
C  Purpose:
C
C     This program computes the principal stresses and strains and their
C     directions from stress and strain values stored in an ABAQUS
C     results file (.fil).
C
C  Input File names: `FNAME.fil', where FNAME is the root file name of
C                                 the input file.
C
C  Output File name:  pvalue.dat
C
C====================================================================
C
C  Variables used by this program and ABAQUS subroutine SPRIND :
C
C   NDI    -- Number of direct components in stress/strain tensor.
C   NSHR   -- Number of shear components in stress/strain tensor.
C   NDIP1  -- NDI + 1
C   ARRAY  -- Real array containing values read from results file
C             (.fil). Equivalenced to JRRAY.
C   JRRAY  -- Integer array containing values read from results file
C             (.fil). Equivalenced to ARRAY.
C   FNAME  -- Root file name of input file (w/o .fil extension).
C   NRU    -- Number of results files (.fil) to be read.
C   LRUNIT -- Array containing unit number and format of results files:
C             LRUNIT(1,*) --> Unit number of input file.
C             LRUNIT(2,*) --> Format of input file.
C   LOUTF  -- Format of output file:
C             0 --> Standard ASCII format.
C             1 --> ABAQUS results file ASCII format.
C             2 --> ABAQUS results file binary format.
C   JUNIT  -- Unit number of file to be opened.
C   JRCD   -- Error check return code.
C             .EQ. 0 --> No errors.
C             .NE. 0 --> Errors detected.
C   KEY    -- Current record key identifier.
C   JELNUM -- Current element number.
C   INTPN  -- Integration point number.
C   LSTR   -- Indicates type of principal value (stress/strain) and
```

214

```
C    LSTR    -- Indicates type of principal value (stress/strain) and
C                ordering used:
C                  For calculation of principal value (stress/strain):
C                    1 -->  stress.
C                    2 -->  strain.
C                  For calculation of directions:
C                    1 -->  stress.
C                    2 -->  strain.
C    S       -- Array containing stress tensor.
C    PS      -- Array containing principal stresses.
C    ANPS    -- Array containing directions of principal stresses.
C    E       -- Array containing strain tensor.
C    PE      -- Array containing principal strains.
C    ANPE    -- Array containing directions of principal strains.
C
C=====================================================================
C
C  The use of ABA_PARAM.INC eliminates the need to have different
C  versions of the code for single and double precision.
C  ABA_PARAM.INC defines an appropriate IMPLICIT REAL statement
C  and sets the value of NPRECD to 1 or 2, depending on whether
C  the machine uses single or double precision.
C
C=====================================================================
C
      INCLUDE 'aba_param.inc'
      DIMENSION  ARRAY(513), JRRAY(NPRECD,513), LRUNIT(2,1)
      EQUIVALENCE (ARRAY(1), JRRAY(1,1))
C
C=====================================================================
      DIMENSION S(6), E(6), PS(3), PE(3), ANPS(3,3), ANPE(3,3),RN(4)
      CHARACTER  FNAME*80
      character*13 para1
      character*13 para2
C
C=====================================================================
C  Get the name of the results file.
C
C=====================================================================
      WRITE(6,*) 'Enter the name of the input file (w/o .fil):'
      READ(5,'(A)') FNAME
      FNAME='SPBK'
      VMS0=0
      STHX=0
C      STHN=100
      STHN=0.0
      distV=0
      distVX=0
```

```fortran
      EV_tot=0.0
      EA_tot=0.0
      JTOTELEM=0
C
C====================================================================
C  Open the output file.
C
C====================================================================
      OPEN(UNIT=9,FILE='SPBKold.txt',STATUS='NEW')
      OPEN(UNIT=15,FILE='TH.txt',STATUS='NEW')
C
      NRU = 1
      LOUTF = 0
      LRUNIT(1,1) = 8
      LRUNIT(2,1) = 2
C
      CALL INITPF(FNAME,NRU,LRUNIT,LOUTF)
C
      JUNIT = 8
C
      CALL DBRNU(JUNIT)
C
C====================================================================
C  Read records from the results (.fil) file and process the data.
C  Cover a maximum of 10 million records in the file.
C
C====================================================================
      DO 1000 K100 = 1, 100
      DO 1000 K1 = 1, 99999
         CALL DBFILE(0,ARRAY,JRCD)
         IF (JRCD .NE. 0) GO TO 1001
         KEY = JRRAY(1,2)
C
C====================================================================
C  Get the heading (title) record.
C
C====================================================================
      IF (KEY .EQ. 1922) THEN
C         WRITE(9,1100) (ARRAY(IXX),IXX=3,12)
C 1100    FORMAT(1X,10A8)
C
C====================================================================
C  Get the current step and increment number.
C
C====================================================================
      ELSE IF (KEY .EQ. 2000) THEN
C         WRITE(9,1200) JRRAY(1,8), JRRAY(1,9)
C 1200    FORMAT(1X,'** STEP ',I2,'    INCREMENT ',I3)
```

216

```fortran
            STP_INC=JRRAY(1,9)
C
C=====================================================================
C  Get the element and integration point numbers, JELNUM and INTPN,
C  and the location of INTPN (0--at int.pt., 1--at centroid,
C  4--nodal average) and the number of direct and shear components
C  in the analysis.
C
C=====================================================================
          ELSE IF (KEY .EQ. 1) THEN
              JELNUM = JRRAY(1,3)
              INTPN  = JRRAY(1,4)
              LOCATE = JRRAY(1,6)
              NDI    = JRRAY(1,8)
              NSHR   = JRRAY(1,9)
              NDIP1  = NDI + 1
CC            IF(LOCATE.LE.1) THEN
CC              WRITE(9,1201) JELNUM, INTPN ,NDI,NSHR
CC 1201        FORMAT(2X,'ELEMENT NUMBER = ',I8,5X,
CC   1                    'INT. PT. NUMBER = ',I2,5X,
CC   2                    'NDI/HSHR = ',2I2)
CC            ELSEIF(LOCATE.EQ.4) THEN
CC              WRITE(9,1191) JELNUM, NDI,NSHR
CC 1191        FORMAT(2X,'NODE NUMBER = ',I8,5X,
CC   1                    'NDI/HSHR = ',2I2)
CC            END IF
C
C=====================================================================
C  Get the VON MISES stress.
C
C=====================================================================
          ELSE  IF (KEY .EQ. 12) THEN
CC            WRITE(9,1202)
CC 1202        FORMAT(3X,'VON MISES STRESS:')
              VMS = ARRAY(3)
CC            WRITE(9,1203) VMS
CC 1203        FORMAT(4X,'VMS = ',E12.5)
            IF (VMS.GT.VMS0) VMS0=VMS
          ELSE  IF (KEY .EQ. 27) THEN
CC            WRITE(9,1202)
CC 1202        FORMAT(3X,'VON MISES STRESS:')
            lmt=0.10000E+01
            IF (STP_INC.EQ.lmt) THEN
              STH = ARRAY(3)
CC            WRITE(9,1203) VMS
CC 1203        FORMAT(4X,'VMS = ',E12.5)
              JTOTELEM=JTOTELEM+1
              WRITE(15,1202) STH
1202          FORMAT(4X,E12.5)
            END IF

            IF (STH.GT.STHX) STHX=STH
            IF (STH.LT.STHN) STHN=STH
          ELSE  IF (KEY .EQ. 78) THEN
            E_VOL=ARRAY(3)
            WRITE(9,1204) E_VOL
1204        FORMAT(4X,'E_VOL=',E12.5)
            E_Area= E_VOL/STH
            EA_tot=E_Area+EA_tot
            EV_tot=E_VOL+EV_tot
          ELSE  IF (KEY .EQ. 107) THEN
              WRITE(9,2202)
2202          FORMAT(3X,'NODAL COORDINATES:')
            DO 30 IXX = 1, 4
              RN(IXX) = ARRAY(IXX+2)
 30         CONTINUE
              INN=1+INN
            WRITE(9,2203) (RN(IZZ), IZZ = 1, 4)
2203          FORMAT(4X,'NODENUMBER= ',I8,'  X = ',E12.5,'  Y = ',E12.5,'  Z = ',E12.5)
2203          FORMAT(I8,',',E12.5,',',E12.5,',',E12.5)
```

217

```fortran
          END IF
1000 CONTINUE
1001 CONTINUE
          WRITE(9,2206) INN,VMS, STHX,EV_tot
C         WRITE(9,2206) JTOTELEM,VMS, STHX,EV_tot
2206      FORMAT('TOTAL_NODE = ',I8,/,
     1           'VMS_MAX = ',E12.5,/,
     2           'STH_MEAN = ',E12.5)

      CLOSE (UNIT=9)
      CLOSE (UNIT=15)
      OPEN(UNIT=17,FILE='STMP.txt',STATUS='OLD')
      OPEN(UNIT=18,FILE='SPBKold.txt',STATUS='OLD')
      OPEN(UNIT=15,FILE='TH.txt',STATUS='OLD')
      OPEN(UNIT=19,FILE='SPBK.txt',STATUS='NEW')
      eof=INN
        PORINC=INN/STP_INC
        PORINC=INT(PORINC)
        STINC=(STP_INC-1)*PORINC
      do 4001 m=1,STINC
        iglobal=0
        read(18,2215,end=4001)cordn2,xcord2,ycord2,zcord2
!        read(18,end=4001)para2
2215      FORMAT(I8,E12.5,E12.5,E12.5)
4001 CONTINUE
      do 5001 m=STINC+1,INN
        read(18,2220,end=5001)cordn2,xcord2,ycord2,zcord2
!        read(18,end=5001)para2
        read(17,2220,end=5002)cordn1,xcord1,ycord1,zcord1
!        read(17,end=5002)para1
2220      FORMAT(I8,E12.5,E12.5,E12.5)
            distX=xcord2-xcord1
            distY=ycord2-ycord1
            distZ=zcord2-zcord1
C           WRITE(19,2221) cordn1,cordn2, distX,distY,distZ
C 2221      FORMAT(I8,',',I8,',',E12.5,',',E12.5,',',E12.5)
          distV=SQRT(distX**2+distY**2+distZ**2)
          IF (distV.GT.distVX) distVX=distV
        if(para1.eq.'TOTAL_NODE = ')   GO TO 5002
        if(para2.eq.'TOTAL_NODE = ')   GO TO 5002
5001 CONTINUE
5002 CONTINUE
      CLOSE (UNIT=17)
      CLOSE (UNIT=18)
      do 6001 m=1,JTOTELEM
        read(15,2229,end=6001)THICK
2229      FORMAT(4X,E12.5)
2229      FORMAT(4X,E12.5)
          STHN=STHN+(THICK/STHX-1)**2
C         WRITE(19,5202)THICK,STHN,STHX
C 5202      FORMAT(4X,',',E12.5,',',E12.5,',',E12.5)
6001 CONTINUE
      CLOSE (UNIT=15)
          WRITE(19,5206) JTOTELEM,VMS, STHN,distVX,EV_tot
C         WRITE(9,2206) JTOTELEM,VMS, STHX,distV,EV_tot
5206      FORMAT(I8,',',E12.5,',',E12.5,',',E12.5,',',E12.5)
      CLOSE (UNIT=19)
      RETURN
      END
```

218

C.3   Crush response extraction CRSH.py

```python
# -*- coding: mbcs -*-
#
# Abaqus/CAE Release 6.10-2 replay file
# Internal Version: 2010_07_13-11.28.21 102888
# Run by ali on Sat Nov  6 21:05:31 2010
#

# from driverUtils import executeOnCaeGraphicsStartup
# executeOnCaeGraphicsStartup()
#: Executing "onCaeGraphicsStartup()" in the site directory ...
from abaqus import *
from abaqusConstants import *
session.Viewport(name='Viewport: 1', origin=(0.0, 0.0), width=291.501556396484,
    height=229.247512817383)
session.viewports['Viewport: 1'].makeCurrent()
session.viewports['Viewport: 1'].maximize()
from caeModules import *
from driverUtils import executeOnCaeStartup
executeOnCaeStartup()
session.viewports['Viewport: 1'].partDisplay.geometryOptions.setValues(
    referenceRepresentation=ON)
Mdb()
#: A new model database has been created.
#: The model "Model-1" has been created.
session.viewports['Viewport: 1'].setValues(displayedObject=None)
o1 = session.openOdb(
    name='CRSH.odb')
session.viewports['Viewport: 1'].setValues(displayedObject=o1)
#: Model: CRSH.odb
#: Number of Assemblies:         1
#: Number of Assembly instances: 0
#: Number of Part instances:     2
#: Number of Meshes:             2
#: Number of Element Sets:       13
#: Number of Node Sets:          15
#: Number of Steps:              1
odb = session.odbs['CRSH.odb']
xy1 = xyPlot.XYDataFromHistory(odb=odb,
    outputVariableName='Total force due to contact pressure: CFN3     BLKL/PART-2-1 SURF-3',
#: Number of Steps:         1
odb = session.odbs['CRSH.odb']
xy1 = xyPlot.XYDataFromHistory(odb=odb,
    outputVariableName='Total force due to contact pressure: CFN3     BLKL/PART-2-1_SURF-3',
    steps=('Step-1', ), suppressQuery=True)
c1 = session.Curve(xyData=xy1)
xy2 = xyPlot.XYDataFromHistory(odb=odb,
    outputVariableName='Total force due to contact pressure: CFN3     BLKU/PART-2-1_SURF-3',
    steps=('Step-1', ), suppressQuery=False)
c2 = session.Curve(xyData=xy2)
xyp = session.XYPlot('XYPlot-1')
chartName = xyp.charts.keys()[0]
chart = xyp.charts[chartName]
chart.setValues(curvesToPlot=(c1, c2, ), )
session.viewports['Viewport: 1'].setValues(displayedObject=xyp)
xy1 = session.xyDataObjects['_temp_1']
xy2 = session.xyDataObjects['_temp_2']
xy3 = sae60Filter(xyData=xy1+xy2, timeScaleFactor=10)
xyp = session.xyPlots['XYPlot-1']
chartName = xyp.charts.keys()[0]
chart = xyp.charts[chartName]
c1 = session.Curve(xyData=xy3)
chart.setValues(curvesToPlot=(c1, ), )
xyp = session.xyPlots['XYPlot-1']
chartName = xyp.charts.keys()[0]
chart = xyp.charts[chartName]
x0 = chart.curves['_temp_4']
session.writeXYReport(fileName='abaqus.rpt', appendMode=OFF, xyData=(x0, ))
xQuantity = visualization.QuantityType(type=NONE)
yQuantity = visualization.QuantityType(type=NONE)
session.XYDataFromFile(name='XYData-1',
    fileName='abaqus.rpt',
    xField=1, yField=2, skipFrequency=500,
    sourceDescription='Read from abaqus.rpt',
    contentDescription='field 1 vs. field 2', axis1QuantityType=xQuantity,
    axis2QuantityType=yQuantity, )
x0 = session.xyDataObjects['XYData-1']
session.writeXYReport(fileName='CRSH.rpt', xyData=(x0, ))
```

219

C.4   Shell scripts for extracting multiple responses of simulations

For stamping case the AssemSTMP.sh script is :

```
for runlevel in 1 2 3 4 5 6 7 8 9 10 11 12 13 14 15 16 17 18 19 20 21 22 23 2
do
  id1=$[10+$runlevel]
  cp stmpprinaao2.f MXMN${runlevel}
  cd MXMN${runlevel}
  rm STMP.txt
  abaqus make job=stmpprinaao2.f
  abaqus stmpprinaao2
  mv STMP.txt fort.$id1
  cp fort.$id1 ..
  cd ..

done
```

For springback case the AssemSPBK.sh script is :

```
for runlevel in 1 2 3 4 5 6 7 8 9 10 11 12 13 14 15 16 17 18 19 20
do
  id1=$[10+$runlevel]
  cp stmpprinaao.f spbkprinaao.f MXMN${runlevel}
  cd MXMN${runlevel}
  rm SPBKold.txt SPBK.txt TH.txt
  abaqus make job=stmpprinaao.f
  abaqus stmpprinaao
  abaqus make job=spbkprinaao.f
  abaqus spbkprinaao
  mv SPBK.txt fort.$id1
  cp fort.$id1 ..
  cd ..

done
```

220

For crush case the AssemCRSH.sh script is :

```
for runlevel in 1 2 3 4 5 6 7 8 9 10 11 12 13 14 15 16 17 18 19 20
do
  id1=$[10+$runlevel]
  cp CRSH.py MXMN${runlevel}
  cd MXMN${runlevel}
  rm fort.$id1
  abaqus cae noGUI=CRSH.py
  mv CRSH.rpt fort.$id1
  cp fort.$id1 ..
  cd ..

done
```

221